

REPORT DOCUMENTATION PAGE		READ INSTRUCTIONS BEFORE COMPLETING FORM
1. REPORT NUMBER SIO REFERENCE 85-32	2. GOVT ACCESSION NO.	3. RECIPIENT'S CATALOG NUMBER
4. TITLE (and Subtitle) MEASUREMENTS OF ACOUSTIC BACKSCATTER OF THE DEEP SEA FLOOR USING A DEEPLY TOWED VEHICLE		5. TYPE OF REPORT & PERIOD COVERED Summary
		6. PERFORMING ORG. REPORT NUMBER MPL-U-50/85
7. AUTHOR(s) Marco Weydert		8. CONTRACT OR GRANT NUMBER(s) N00014-82-K-0147 NOAA-83-SAC-00659 NSF DAR 15593
9. PERFORMING ORGANIZATION NAME AND ADDRESS University of California, San Diego, Marine Physical Laboratory of the Scripps Institution of Oceanography, San Diego, CA 92152		10. PROGRAM ELEMENT, PROJECT, TASK AREA & WORK UNIT NUMBERS
11. CONTROLLING OFFICE NAME AND ADDRESS Office of Naval Research, Department of the Navy, 800 North Quincy Street, Arlington, VA 22217		12. REPORT DATE December 1985
		13. NUMBER OF PAGES 187 pages
14. MONITORING AGENCY NAME & ADDRESS (if different from Controlling Office)		15. SECURITY CLASS. (of this report) UNCLASSIFIED
		15a. DECLASSIFICATION/DOWNGRADING SCHEDULE
16. DISTRIBUTION STATEMENT (of this Report) Document cleared for public release; distribution unlimited.		
17. DISTRIBUTION STATEMENT (of the abstract entered in Block 20, if different from Report)		
18. SUPPLEMENTARY NOTES		
19. KEY WORDS (Continue on reverse side if necessary and identify by block number) acoustic backscatter, deep tow, manganese nodule, Patton Escarpment		
20. ABSTRACT (Continue on reverse side if necessary and identify by block number) In 1983 in area of Cu-Ni rich manganese nodules at 14°40'N, 126°25'W (site 'E') was intensively studied with the Deep-Tow of the Scripps Institution of Oceanography, and 16 box cores were collected. Deep-Tow studies of the Thirtymile-Bank off the California Coast and the deep sea at the foot of the Patton Escarpment followed. The nodule coverage at site 'E' varies from 0% to 80%. The nodule sizes vary between 1 and 13 cm. The nodule size distributions are best modeled by a Gaussian distribution. The three main		

nodule axes are related to each other at 1:0.8:0.5. The average density of individual nodules is $2.0 \pm 0.04 \text{ g/cm}^3$ and the volumes increase on the average with the 2.8 power of the third root of the product of the three radii. Changes of the thickness of the upper acoustic unit of the sediment column correlate with changes in nodule coverage and concentration.

The acoustic backscatter has been measured for frequencies of 4.5, 9, 15, 28, 60, 112 and 163 kHz and grazing angles from normal incidence to 50° . The backscatter increases as the square of the frequency for sediments. The backscatter of the deep sea sediments at the foot of the Patton escarpment exceeds the backscatter of the sediments at site 'E' by several dB (depending on the frequency and on the grazing angle). The backscatter from manganese nodules depends on the nodule coverage and on the frequency and exceeds that of sediments, but is less than that from the Thirtymile-Bank phosphorites. In nodule fields the backscatter comes at normal incidence from the first Fresnel zone for frequencies from 4.5 to 60 kHz and increases as the square of the coverage. The width and the asymmetry of the covariance change when the nodule coverage changes. A computer model with ellipsoidal targets relates the backscatter to the target strengths of the nodules and reproduces the covariance. It is concluded that it is possible to distinguish acoustically between different deep sea sediment types and to assess manganese nodule resources. The optimal frequencies are between 15 and 60 kHz.



LIBRARY
RESEARCH REPORTS DIVISION
NAVAL POSTGRADUATE SCHOOL
MONTEREY, CALIFORNIA 93940

MEASUREMENTS OF ACOUSTIC BACKSCATTER OF THE DEEP SEA FLOOR USING A DEEPLY TOWED VEHICLE

A Technique to Investigate the Physical and Geological
Properties of the Deep Sea Floor and to Assess
Manganese Nodule Resources

Dissertation Thesis

Marco Weydert

Sponsored by the
National Science Foundation
Grant NSF DAR 15593
the National Oceanic and Atmospheric Administration
Grant NOAA-83-SAC-00659
and the
Office of Naval Research
Contract N00014-82-K-0147

de SIO REFERENCE 85-32 ~

December 1985

*Reproduction in whole or in part is permitted
for any purpose of the U.S. Government.*

Document cleared for public release;
distribution unlimited.

MPL-U-50/85 ~

MARINE PHYSICAL LABORATORY
of the Scripps Institution of Oceanography
San Diego, California 92152

UNIVERSITY OF CALIFORNIA, SAN DIEGO
MARINE PHYSICAL LABORATORY OF THE
SCRIPPS INSTITUTION OF OCEANOGRAPHY
SAN DIEGO, CA 92152

**MEASUREMENTS OF ACOUSTIC BACKSCATTER
OF THE DEEP SEA FLOOR USING A DEEPLY TOWED VEHICLE**

A Technique to Investigate the Physical and Geological
Properties of the Deep Sea Floor and to Assess
Manganese Nodule Resources

Dissertation Thesis

Marco Weydert

Sponsored by the
National Science Foundation
Grant NSF DAR 15593
the National Oceanic and Atmospheric Administration
Grant NOAA-83-SAC-00659
and the
Office of Naval Research
Contract N00014-82-K-0147

SIO REFERENCE 85-32

December 1985

K. M. Watson, Director
Marine Physical Laboratory

MPL-U-50/85

Table of Contents

	Page
List of figures	vi
List of tables	viii
Acknowledgements	ix
Vita	x
Abstract	xii
Introduction	1
 I. GEOLOGY	
1.1. Manganese nodule area	6
1.2. Thirtymile Bank	44
1.3. Base of Patton Escarpment	49
Appendix	59
 II. IN SITU BACKSCATTER MEASUREMENTS	
2.1 Introduction	61
2.2 Instrumentation	64
2.3 Data collection and processing	109
2.4 Environment	115
2.5 Reflectivity and backscatter of sea floor	119
2.6 Relationships between nodule characteristics reflectivity and backscatter	158
Appendix	167
 III. SIMULATIONS	
3.1. Introduction	170
3.2. Simulation description	172
3.3. Results	175
3.4 Conclusion	177
IV. Conclusion	181
References	183

List of figures

Figure		Page
Chapter I		
1-1	Locations of manganese nodule study sites	7
1-2	Bathymetry of site 'E' with box cores and outcrops	9
1-3	Bathymetry cross sections in the east and in the west	10
1-4	Volcanic lobes on side scans	11
1-5	Sample sub-bottom profiles	14
1-6	Fish tracks during camera runs	16
1-7	Sample photographs of sediments at site 'E'	17
1-8	Examples of typical nodule coverage	18
1-9	Sample box cores	19
1-10	Frequency of occurrence of longest length	25
1-11	Logarithm of number of manganese nodules as a function of size	27
1-12	Frequency of average horizontal diameter on probability paper	29
1-13	Frequency of average horizontal diameter	31
1-14	Frequencies of axes ratios	33
1-15	Manganese nodule volumes as a function of length	35
1-16	Bathymetry, nodule coverage and size during camera runs	39
1-17	Bathymetry, nodule coverage and size during camera runs	40
1-18	Ship track at Thirtymile Bank	47
1-19	Map with Thirtymile Bank and Patton Escarpment	48
1-20	Photographs of sea floor at Thirtymile Bank	49
1-21	Bathymetry at station at foot of Patton Escarpment	52
1-22	Fish track at foot of Patton Escarpment	53
1-23	Photographs of sea floor at foot of Patton Escarpment	54
1-24	Air gun record at DSDP site 469	56
1-25	Sub-bottom profiles near fault at base of Patton Escarpment	57
Chapter II		
2-1	Geometry for calibrations	62
2-2	Schematics of transducer arrays	65
2-3	Backscatter electronics	68
2-4	Calibration pulses	76
2-5	Voltage transmitting response	79
2-6	Current transmitting response	80
2-7	XY-beampatterns of free transducers	81
2-8	XY-beampatterns on fish	82
2-9	XZ-beampatterns of free transducers	83
2-10	XZ-beampatterns on fish	84
2-11	XY-beampatterns at 4.5 kHz	86
2-12	Transmitting XY-beampatterns at 9 kHz	87
2-13	Receiving XY-beampatterns at 9 kHz	88
2-14	Two-way XY-beampatterns at 9 kHz	89
2-15	XY-beampatterns at 15 kHz	90
2-16	XY-beampatterns at 28 kHz	91

2-17	XY-beampatterns at 60 kHz	92
2-18	XY-beampatterns at 112 kHz	93
2-19	XY-beampatterns for one transducer at 163 kHz	94
2-20	XY-beampatterns for two transducers at 163 kHz	95
2-21	Set-up for temperature calibrations	99
2-22	Geometry of backscatter experiment	110
2-23	Simplified flow diagram of backscatter programs	114
2-24	Bottom loss versus backscatter coefficients	127
2-25	Envelope distributions	129
2-26	Samples of raw signal and covariances	137
2-27	Samples of raw signal and covariances	138
2-28	Samples of low-passed backscatter coefficients	140
2-29	Backscatter coefficients as a function of frequency	141
2-30	Relative backscatter coefficients as a function of frequency	143
2-31	Relative backscatter coefficients as a function of the grazing angle	145
2-32	Relative backscatter coefficients as a function of the grazing angle	146
2-33	Theoretical covariance	151
2-34	FIR filter	153
2-35	Intensities, width and asymmetry of covariances	155
2-36	Fish track during backscatter measurements at site 'E'	156
2-37	Reflectivity of hard and nodule spheres	160
2-38	Nodule spacing	166

Chapter III

3-1	Horizontal target strengths of individual nodules	171
3-2	Samples of simulated backscatter	174
3-3	Samples of simulated backscatter	175
3-4	Covariances	179

List of tables

Table		Page
Chapter I		
1-1	Longest length	24
1-2	Definitions, means and variances of some probability functions	26
1-3	Average horizontal diameter	30
1-4	Ratios of medium over longest lengths	32
1-5	Ratios of vertical to longest length	32
Chapter II		
2-1	Spacing between reference pulses	69
2-2	Transmit pulses, reference pulses and bandwidths	72
2-3	Transmitting and receiving responses for transducers on vehicle	77
2-4	Transducer response for free transducers	78
2-5	Effective beamwidths on Fish 5	97
2-6	<i>S/V + Rec.Sen.</i> for temperatures of 20° C and 1° C	101
2-7	Changes of transducer response with temperature and pressure	104
2-8	Noise measurements in the laboratory	107
2-9	Grazing angle on sea floor and at the transducer	117
2-10	Bottom loss as computed from Hamilton 1974	125
2-11	Reflected intensity versus scattered intensity	128
2-12	First Fresnel zones	158
2-13	Backscatter coefficients as a function of nodule coverage	162
2-14	Backscatter coefficients as a function of nodule coverage	163
Chapter III		
3-1	Backscatter coefficients and target strength	176
3-2	Backscatter as a function of the nodule density	180

ACKNOWLEDGMENTS

This work would not have been possible without the collaboration of many people. Especially the skills and the patience of my teachers, the Deep Tow engineers, the ships' captains and the crews from the R/V Melville, New Horizon and Thomas Washington were essential to the success of this project. I am very indebted to F. N. Spiess, V. C. Anderson and D. E. Boegeman for their leadership, help and advice throughout my studies at the Scripps Institution of Oceanography. K. Watson and G. Arrhenius made many helpful suggestions. C. Lowenstein and R. Lawhead operated and maintained the computers at sea, and they managed to teach me how to use them. R. Goddard and D. Princehouse made their REVGEN computer program available. D. Alexandrou installed REVGEN on the VAX of the Marine Physical Laboratory, and, together with W. Hodgkiss made many comments on how to use it together with the existing signal processing routines. J. Jain, R. Elder, T. Clary, and Len Orysiek and his staff proved invaluable in the calibrations of the backscatter transducers. W. Siapno's photographs and charts revealed themselves a great guide for the Echo 1 expedition. J. Griffith and P. Rapp drafted many of the figures, while E. Ford fought - and won many a battle with the wordprocessor.

I'd like to apologize to all those I have not mentioned by name, and thank them as well for the great experience the last 5 years have been.

And, above all, none of this could have been done without the funding by NSF grant number DAR 80-15593, NOAA grant number 83-SAC-00659, a grant from the Scripps Industrial Associates, and ONR grant number N00014-82-K-0147.

VITA

29 September 1954 — Born — Fiels, Luxembourg

1979 Diploma in Physics, Federal Institute of Technology, Zurich (Switzerland)
1979-1980 Teaching Physics and Mathematics, Zurich (Switzerland)
1980-1985 graduate student, Scripps Institution of Oceanography, California (USA)

PUBLICATIONS

F.N. Spiess, Wilson, G., Hessler, R. and Weydert M., " Environmental effects of deep sea dredging ", Technical Report MPL-U-49/85, Marine Physical Laboratory, Scripps Institution of Oceanography.

M. Weydert, "Manganese nodule distributions at a site in the eastern North Pacific", Marine Mining (submitted).

M. Weydert, "Acoustic backscatter of marine manganese nodules", Journal of the Acoustical Society of America, December 1985.

F. N. Spiess and M. Weydert, "Cruise report Rama leg 1, MANOP sites C & R", Scripps Institution of Oceanography Reference 84-8, 1984.

F.N. Spiess, R. Hessler, G. Wilson, M. Weydert and P. Rude, " Echo I cruise report", Scripps Institution of Oceanography Reference 84-3, 1984.

ABSTRACTS

M. Weydert, "Acoustic properties of single manganese nodules", EOS Transactions of the American Geophysical Union, vol.65, No45, 1984.

F. N. Spiess and M. Weydert, "Variability and acoustic reflectivity over a manganese nodule field", Journal of the Acoustical Society of America, vol.74, suppl.1, p.121, 1984.

FIELDS OF STUDY

Major Field: Oceanography

Studies in Underwater Acoustics.

Professors Victor C. Anderson and Fred N. Spiess

Studies in Geology

Professors Albert E. Engel and Joseph R. Curray

Studies in Physical Oceanography

Professors Myrl C. Hendershott and Douglas L. Inman

ABSTRACT OF THE DISSERTATION

Measurements of Acoustic Backscatter
of the Deep Sea Floor using a Deeply Towed Vehicle.
A Technique to Investigate the Physical and Geological
Properties of the Deep Sea Floor and to
Assess Manganese Nodule Resources.

by

Marco Weydert

Doctor of Philosophy in Oceanography

University of California, San Diego, 1985

Professor Fred N. Spiess, Chairman

In 1983 an area of Cu-Ni rich manganese nodules at $14^{\circ} 40'N$, $126^{\circ} 25'W$ (site 'E') was intensively studied with the Deep-Tow of the Scripps Institution of Oceanography, and 16 box cores were collected. Deep-Tow studies of the Thirtymile-Bank off the Californian Coast and the deep sea at the foot of the Patton Escarpment followed. The nodule coverage at site 'E' varies from 0% to 80%. The nodule sizes vary between 1 and 13 cm. The nodule size distributions are best modeled by a Gaussian distribution. The three main nodule axes are related to each other as 1:0.8:0.5. The average density of individual nodules is $2.0 \pm 0.04 g/cm^3$ and the volumes increase on the average with the 2.8 power of the third root of the product of the three radii. Changes of the thickness of the upper acoustic unit of the sediment column correlate

with changes in nodule coverage and concentration.

The acoustic backscatter has been measured for frequencies of 4.5, 9, 15, 28, 60, 112 and 163 kHz and grazing angles from normal incidence to 5° . The backscatter increases as the square of the frequency for sediments. The backscatter of the deep sea sediments at the foot of the Patton escarpment exceeds the backscatter of the sediments at site 'E' by several dB (depending on the frequency and on the grazing angle). The backscatter from manganese nodules depends on the nodule coverage and on the frequency and exceeds that of sediments, but is less than that from the Thirtymile-Bank phosphorites. In nodule fields the backscatter comes at normal incidence from the first Fresnel zone for frequencies from 4.5 to 60 kHz and increases as the square of the coverage. The width and the asymmetry of the covariance change when the nodule coverage changes. A computer model with ellipsoidal targets relates the backscatter to the target strengths of the nodules and reproduces the covariance. It is concluded that it is possible to distinguish acoustically between different deep sea sediment types and to assess manganese nodule resources. The optimal frequencies are between 15 and 60 kHz.

CHAPTER 0 INTRODUCTION

0.A Objectives

Manganese nodules cover millions of square kilometers of the ocean floor, totalling several thousand million tons of manganese, iron, copper, cobalt and nickel. For the last twenty-five years, the manganese nodule deposits -especially those rich in cobalt, nickel and copper- have attracted a lot of attention from the mining industry. While efforts in the USA and Europe have concentrated on scientific studies of the areas, construction of small prototype miners and the design of mining vessels, the Japanese have already developed full-scale prototype exploration, mining and processing equipment (Hiroe, et al., 1984, Katsuya, et al., 1984, Mitsui, et al., 1984).

Only acoustic techniques can be used to survey large areas of the deep sea floor within a reasonable time. They can be used to determine nodule distribution characteristics (patchiness, sizes, number of nodules per area) and topography. Photographic techniques do better than acoustics only when one wants to resolve individual nodules. In fact, the clarity of sea water in most of the areas is such that it is possible to take pictures showing 35 square meters of the sea floor and resolving every single nodule. Sea floor photography at depths of 4 to 5 km is, however, a slow process, and only a 10 meter wide and a few km long strip can be covered within an hour. Towed (deep or shallow) and shipboard acoustic systems allow one to measure the nodule characteristics over a larger swath and to increase the ship's speed at the same time.

A first objective of the present study was to develop an acoustic system mounted on the deep tow vehicle (a fish) of the Marine Physical Laboratory of the Scripps Institution of Oceanography (Spiess and Lonsdale, 1982), with which the

acoustic backscatter properties (coefficients and statistical properties) of the deep sea floor in manganese nodule areas could be measured in situ, and to relate these to the nodule distributions and bottom characteristics.

A second objective of this study was to measure the acoustic backscatter of the sea floor in different areas, all grazing angles and frequencies from a few kHz up to 160 kHz.

0.B Historical Background

Lord Rayleigh's studies of the propagation of sound in fluids (Rayleigh, 1896) were followed by a rather quiet period which lasted to the eve of World War II. The search for enemy submarines revealed the importance of underwater sound acoustics to the military. Numerous investigators studied sound propagation in the ocean during the early 1940's. The results of their work are summarized in a series of technical reports by the Division 6 of the US Navy, published in 1969 as a book (Navy,1969). Besides the reports on sound transmission, several chapters have been dedicated to the reflection of sound from the ocean floor at various frequencies and grazing angles. These measurements revealed that different geological environments behaved differently acoustically, and that rock and sand bottoms reflect better than sand and mud or mud bottoms. The relationship between acoustical and geological properties was used to predict the acoustic behaviour of a region from available geological information. This resulted in the sediment charts prepared for submarine operations. (The Application of Oceanography to sub-surface Warfare, Summary Technical Report of the National Defence Research Committee,1946).

Since World War II, work on underwater acoustics has been substantial. One category of investigators was mainly concerned with sound transmission and sound reflections from the sea floor (Liebermann,1948; Urick,1954; Urick and Saling,1962;

Mackenzie,1960; McKinney and Anderson,1964; Jones, et al.,1964, Clay and Rona,1965; Hastrup,1970). A second category was more interested in the implications of the acoustics for the geologic environment. (Hill,1952; Hamilton,et al.,1956; Shumway,1960; Sarmiento and Kirby,1962; Richards,1962; Nafe and Drake,1963; Breslau,1967; Hamilton, 1970a-c, 1974). Breslau was the first one to successfully predict the broad distribution of sediment types over the areas he studied, using a 12 kHz shipboard echosounder.

Several authors (Mc Kinney and Anderson, 1964, Urick, 1954) have studied the acoustic backscatter at shallow water sites at several grazing angles. This work has been summarized by Urick (Urick,1983) for environments ranging from gravel and sand to mud.

Jitkovskii and Volovova (1967) showed that the frequency dependence of the backscatter depends strongly on the roughness of the sea floor for frequencies from 1 to 30 kHz and grazing angles from 50 to 80 degrees.

A third category of investigators has been preoccupied by computer modeling of the deep sea floor reverberation. General programs to simulate bottom reverberation have been developed (Goddard and Princehouse, 1985). Magnuson (Magnuson,1983) and Ma (Ma, 1983) have studied the statistics and the reverberation from manganese nodules. Their models are based on elastic spheres with the same impedance as manganese nodules. A major development in this field was the use of the T-matrix approach to study the scattering from different bodies, developed by Waterman (Waterman,1969) and refined since by Varadan and Varadan (Varadan and Varadan,1980).

Recently, Weydert (Weydert,1985) studied the echo of individual manganese nodules.

0.C Experimental approach

The work at sea was carried out in an area where large variations in nodule coverage could be expected on the scale of a couple of kilometers. Several suitable areas had been studied by scientists during the Deep Ocean Environmental Study project (DOMES) (Bischoff and Piper, 1979) and the Manganese Nodule Project of the National Science Foundation (MANOP) (Spiess and Greenslate, 1976, Karas, 1978, Spiess and Weydert, 1984) while others had been investigated by companies interested in the mining of manganese nodules. The area which was finally selected for the acoustic backscatter measurements was the Ocean Mining Associates trial mining site. ¹⁾ which is located just south of DOMES site 'C' (figure 1) (Bischoff and Piper, 1979). This permitted the Deep-Tow group and a group of biologists (headed by F.N. Spiess and R. Hessler respectively) to conduct at the same time an environmental impact study on the effects of deep sea mining (Spiess, et al., 1984). It was particularly fortunate that it could be arranged that the R/V T. Washington drove over the area at the end of the Pascua 5 expedition in May 1983. Thus the seabeam multi-beam echosounder of the Scripps Institution of Oceanography could be used to provide the Deep Tow group with a topographic map and 12 kHz reflectivity measurements of the area ²⁾ (Spiess, et al., 1984, de Moustier, 1985). In June 1983, the in situ backscatter measurements could be carried out with the transponder navigated Deep-Tow of the MPL, SIO, after a Deep-Tow site survey had been made collecting photographs and side scan imagery, followed by box coring (Spiess, et al., 1984). A specially built set of transducer arrays to measure the acoustic backscatter at selected frequencies (4.5, 9, 15, 28, 60, 112 and 163 kHz) had been mounted on the

1) I am very grateful to Bill Siapno, Deep Sea Ventures Inc., for his support. Deep Sea Ventures supplied the Deep-Tow group of the MPL, SIO with photographs and maps of the area prior to our expedition. They made also video tapes of the sea floor available.

2) I thank C. de Moustier for the sea beam work.

stern of the deep tow vehicle. This permitted the measurements of the backscatter up to several hundred meters aft and at angles from normal to near grazing.

On a subsequent expedition (Echo 2) two more areas were studied with the same system to complement the environments found at the manganese nodule site: the Thirtymile Bank off Southern California (phosphorites and relict sediments) and the deep sea floor at the foot of the continental rise off Southern California (silty clay).

In the following chapter 1, the geology of all three study areas will be discussed. In chapter 2, the in situ backscatter measurements are presented, together with a detailed description of the tedious calibrations of the backscatter system. The results of a computer simulation will be reported in chapter 3 and compared to the in situ measurements.

CHAPTER I

GEOLOGY

1.1 Geology of the Manganese Nodule Area

SITE DESCRIPTION

a) General area

The manganese nodule area studied on Echo 1 (site 'E') is located in the eastern equatorial Pacific on the west flank of the East Pacific Rise at $14^{\circ}40'N$, $125^{\circ}25'W$ (figure 1-1). The water depth is about 4500 m. Site E is located on the boundary between the red clay and the siliceous ooze regions of the north central Pacific, just below the calcite compensation depth.

Site E lies on 25 million years old crust between the Clipperton and Clarion fracture zones which define a major structural block of the eastern Pacific floor, with the present spreading axis more than 2000 km to the East. Several hundred km east of the area is the relatively rugged relief of the Mathematicians Seamounts. The regional slope is gentle and the relief is occasionally interrupted by clusters of seamounts and small escarpments, which have been attributed to normal faulting. Detailed examination of abyssal hill terrain by Luyendyk (Luyendyk, 1970) has shown that the topographic units are mostly formed by small normal faults, 10-50 m high, and are strongly lineated parallel to the spreading axis.

In the last ten years, the area has been extensively studied during the Deep Ocean Mining Environmental Study (DOMES site 'C' is just 70 km north-west of our site 'E') and the Deep Sea Drilling Project (DSDP holes 159 and 160 are two hundred kilometers to the east and west respectively), as well as by the Ocean Mining

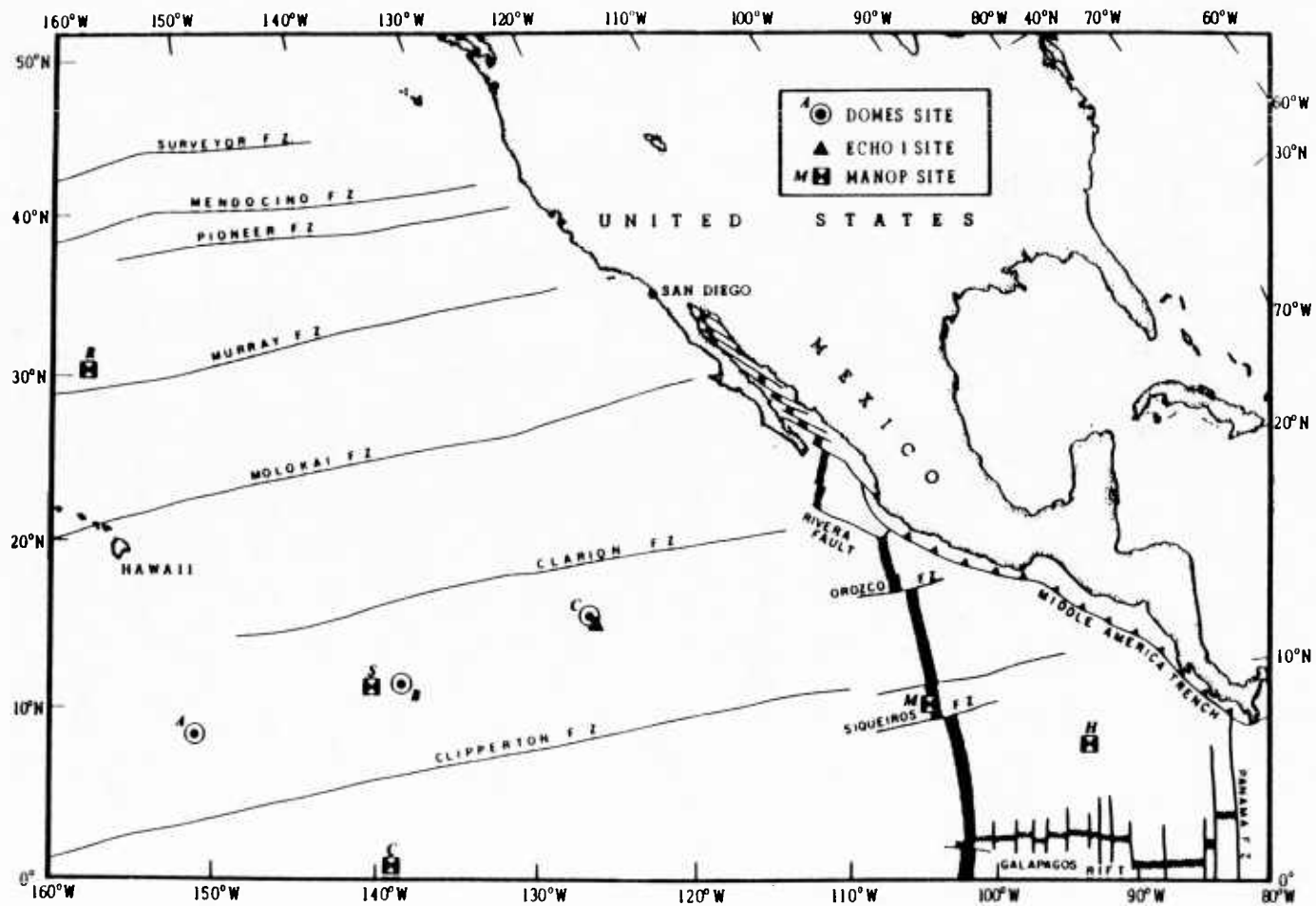


Figure 1-1. Locations of manganese nodule study sites

Map of the eastern North Pacific and the Americas showing the position of site 'E' with respect to the East Pacific Rise, some major fracture zones and other major manganese nodule study areas (DOMES sites A, B and C, and MANOP sites R, S, C, M and H) Site 'E' has been indicated by ▲, the DOMES sites by ⊙ and the MANOP sites by ☒.

Associates (Bischoff and Piper, 1979; Heath and Van Andel, 1973). From the DOMES and DSDP data, as well as from the R/V T. Washington 3.5 kHz profiles collected on Pascua Leg 5, we know that the area is blanketed by a sediment layer of 80-250 m thickness with common basement outcrops. DSDP holes 159 and 160 (Heath and Van Andel, 1973) show that the oldest sediments are Oligocene, approximately 25 million years old, while the near surface sediments are Miocene. DSDP reports suggest that the density of the near surface sediments is 1.3 g/cm^3 with a grain density varying from 2.59 to 2.88 g/cm^3 . The sound velocity has a range of 1.40 to 1.52 km/sec and averages 1.47 and 1.48 km/sec at the DSDP sites 160 and 159 respectively.

Acoustic reflectors could not be distinguished with the 3.5 kHz data collected on Pascua leg 5 because of poor data quality. Three main acoustic reflectors were distinguished at DOMES site C (Bischoff and Piper, 1979, p. 323). Unfortunately, the poor quality of the Pascua 5 data does not permit one to see if they can be traced to site 'E'.

b) Site E

The bathymetry is best illustrated in the map in figure 1-2 (topography modified from de Moustier, 1985). The general trend of the topographic features is roughly North-South. The Deep-Tow area is bounded by depressions to the East and West. The central part is rather flat with gentle slopes to the East and a small conical hill in the North-West. The southern part appears a little steeper. At $14^{\circ} 41' \text{N}$, $125^{\circ} 29' \text{W}$ the area is faulted and relicts of volcanic activity were observed on the 110 kHz side scan displays as the fish passed the area on 20 June 1983 between 15:00 and 16:00 GMT (figures 1-2 and 1-3). Poorly sedimented volcanic lobes cover the middle part of the hill (figure 1-4), while the lower part appears as uniform as the surrounding area. At least 3 other comparable local highs can be seen in figure 1-2. No

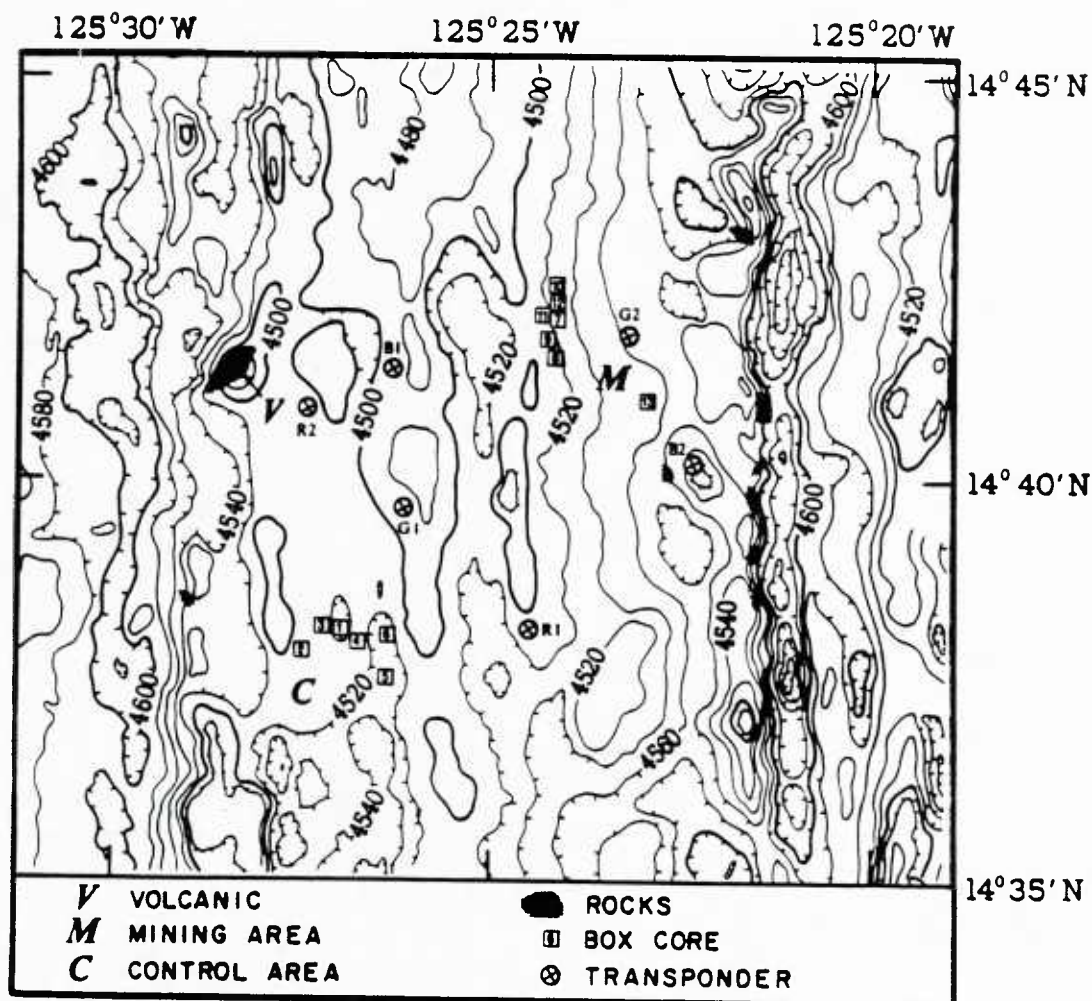


Figure 1-2. Bathymetry of site 'E' with box cores and outcrops

Bathymetry of site 'E' with 20 m contours, box core positions and outcrops. The topography (modified from de Moustier, 1985) was obtained with the SIO Seabeam multi-beam echosounding system. Depths are in uncorrected meters. The box core positions have been determined using Deep Tow bathymetry and transponder navigation. The 'Control Area' (6 box cores) is to the lower left, the 'Mining Area' (6 box cores) in the upper center. The numbers 1 to 13 correspond to box cores H347 to H359. The hatched areas represent outcrops observed with the Deep Tow side looking sonars and sub-bottom profiler

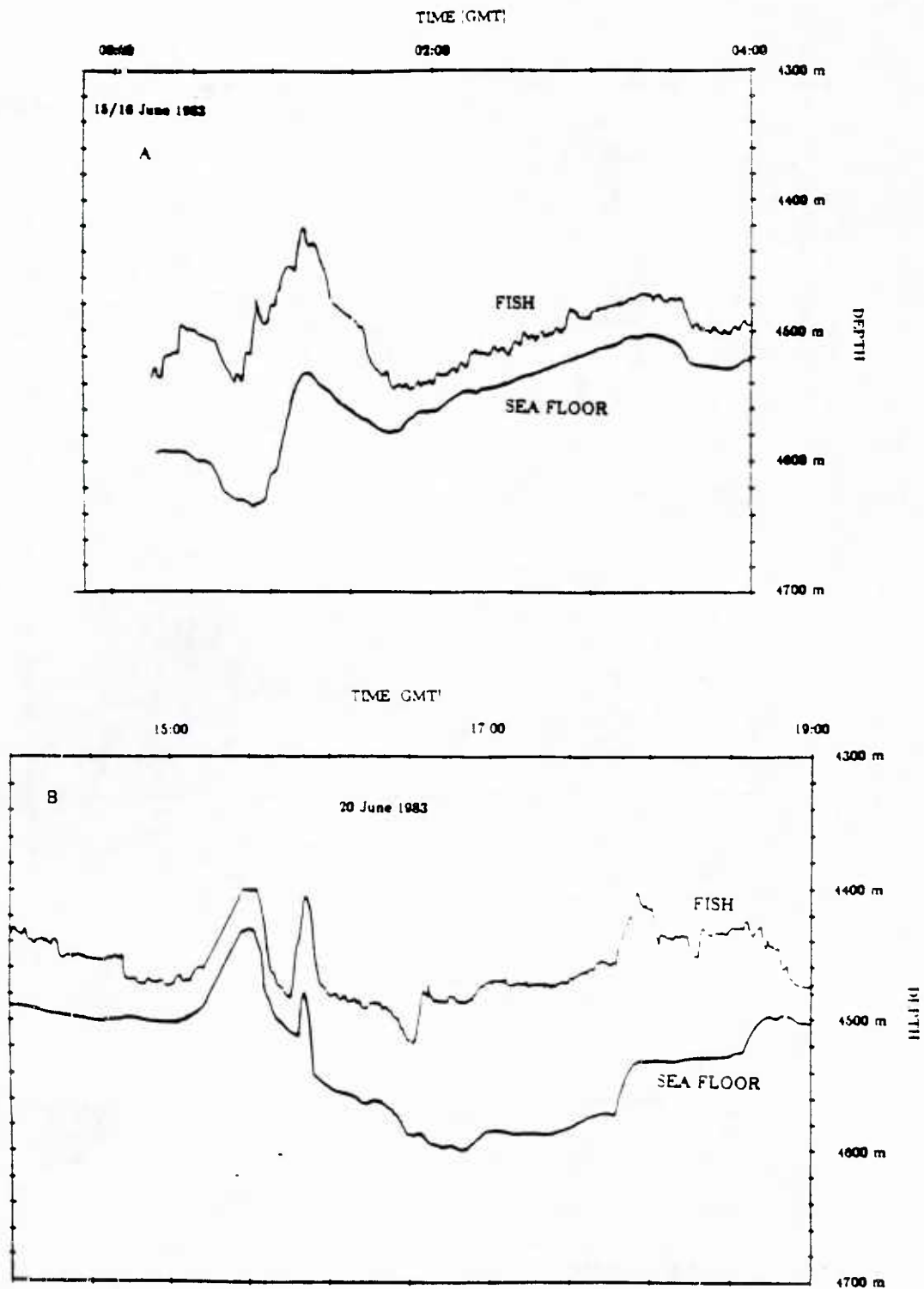


Figure 1-3. Bathymetry cross sections

Bathymetry cross sections (lower line) at eastern side (A) and western side (B) of site 'E' as determined with the Deep Tow echo sounder and pressure gauge. The upper line is the fish depth. Note that the vehicle made a 180° turn in B.

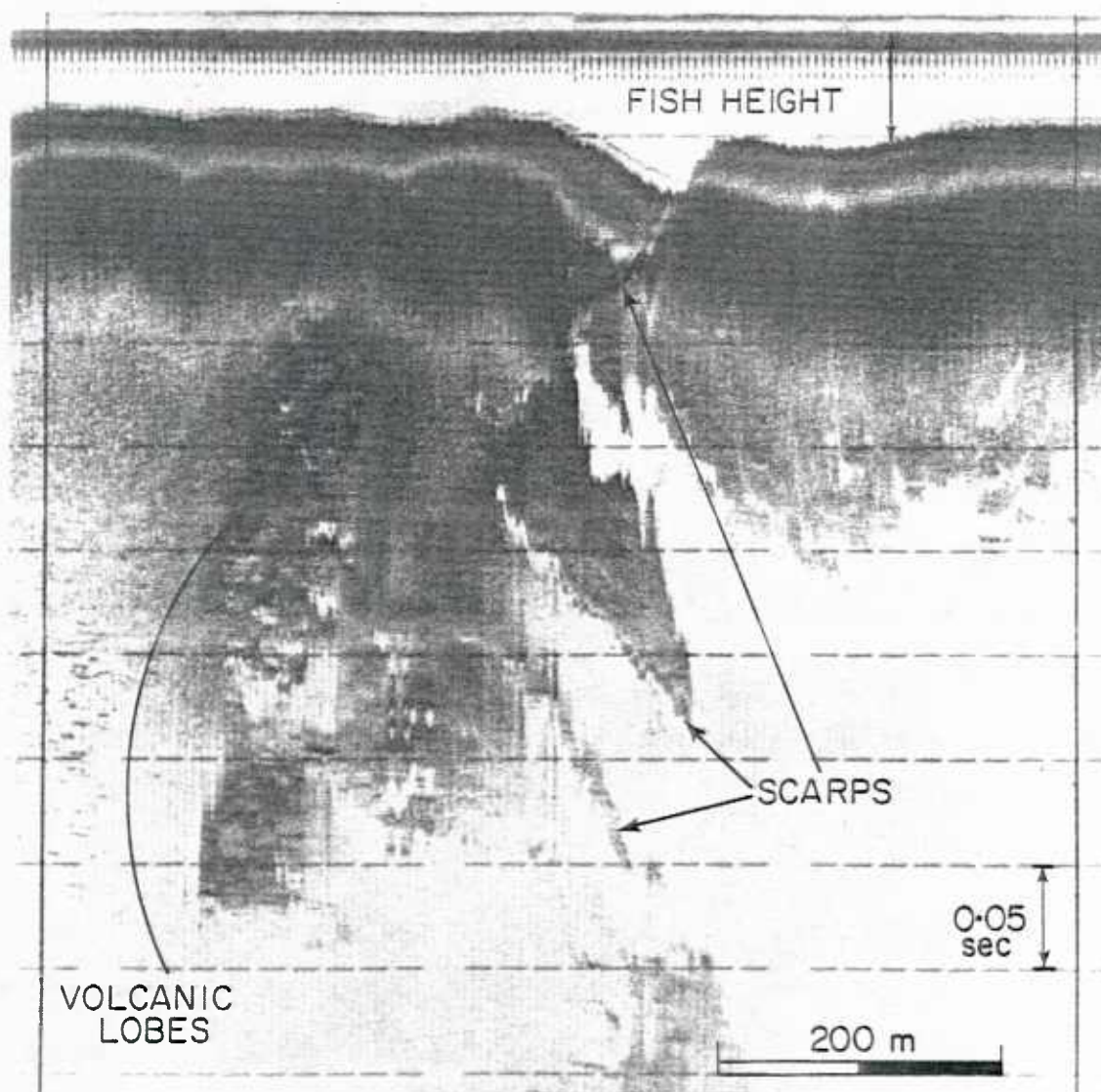


Figure 1-4. Volcanic lobes

Volcanic lobes as seen on 110 kHz side scan records when the fish crossed the hill in the northwest of the Deep Tow area (compare figure 1-2).

bathymetry cross sections made with the deep tow system are available for these, however.

Six to twelve sub-bottom reflectors could be distinguished in the upper 0.050 seconds of sediments (2-way travel time). The observed sediments can be divided into three major acoustic units: The uppermost unit is acoustically transparent (although some scattering can be recognized) and contains a set of 4 well defined acoustic reflectors. Its thickness varies from nothing to 50 m, with some 35 m in the flat central part of the area (figure 1-5.A). It is the only unit which can be traced throughout the area although it is occasionally interrupted by rock outcrops. The second acoustic unit is transparent, except for 5 weak reflectors, and it is some 25 m thick in the flat center. Acoustic unit 3 appears to be similar to unit 2. Often the little energy which penetrates to that depth makes it difficult to recognize weaker reflectors. It appears, however, that its terminal reflector is rather diffuse. When this reflector shoals near outcrops, no lower reflector appears. This suggests that this last visible reflector is the acoustic basement (basalt). The thickness of unit 3 reaches a maximum of 35 m, with 20-25 m in the flat central area. Thus the total sediment column is about 85 m thick in the center. This is less than the 110 m observed at DOMES site 'C' and DSDP holes 159 and 160. Unfortunately, it is not possible to trace these units to DSDP hole 160 and DOMES site 'C' for lack of adequate 3.5 kHz profiles. In the very flat central portion of site 'E', the acoustic sub-bottom reflectors are parallel to the sea floor (figure 1-5.A). Reflectors shoal as they approach topographic highs or rock outcrops, and get deeper in topographic lows (figure 1-5.B). The thickness of the sedimentary layers they define changes accordingly i.e. they increase or decrease as one approaches lows or highs respectively. This is observable for small scale topographic changes as well as for the depression in the east (figure 1-5.B and C). Although no strong currents were observed during the

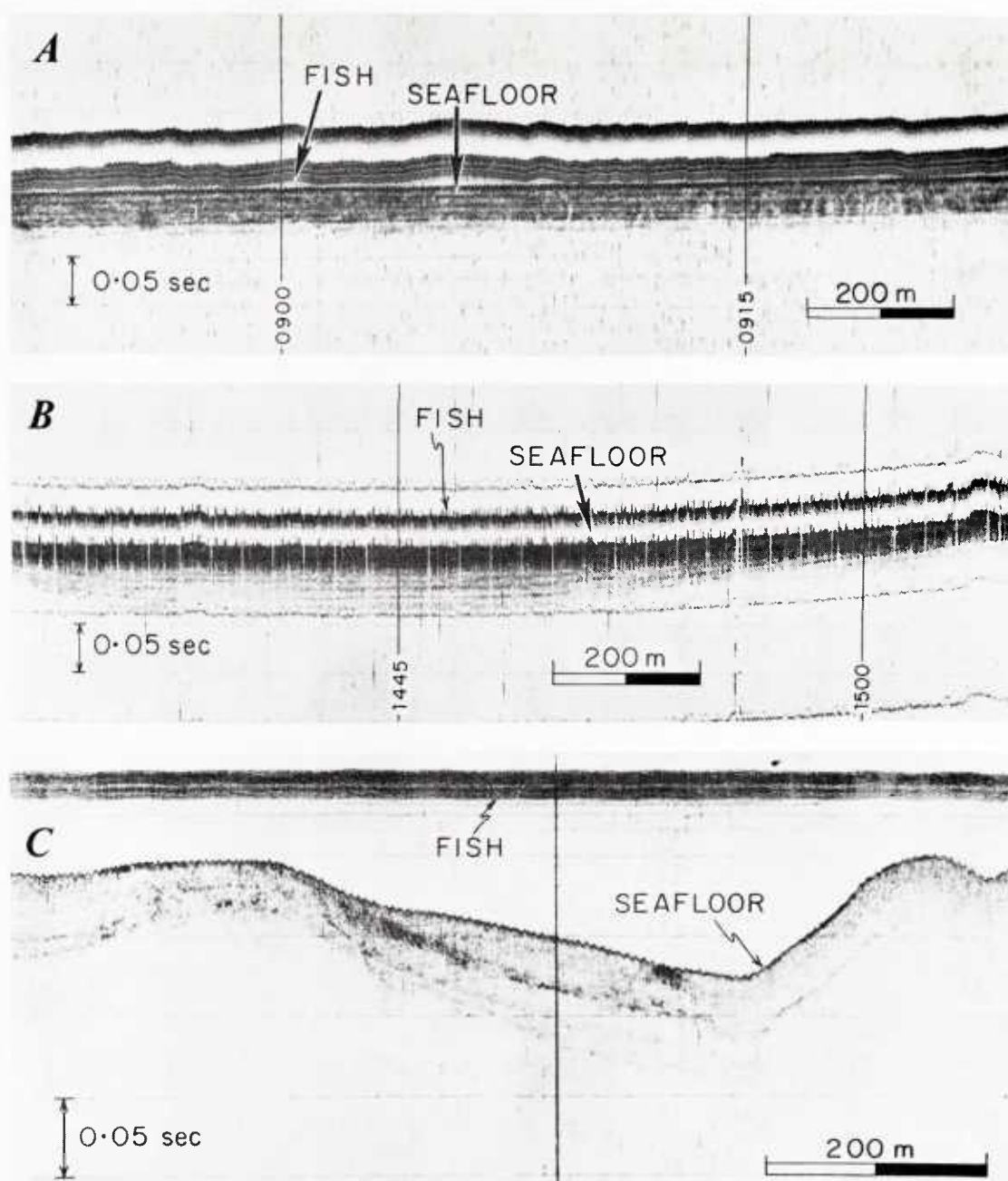


Figure 1-5. Sample sub-bottom profiles

A) Sub-bottom profile as observed in the flat, central part of site 'E' (compare figures 1-2 and 1-6) The sea floor is the uppermost straight line, followed downward by the parallel sub-bottom reflectors. The spacing between horizontal scale lines is 0.050 seconds (2-way travel time). The two vertical time-marks are 15 minutes apart. During that time the vehicle traveled approximately 750 m.

B) Sub-bottom profile as observed during the camera run 1-4 on 11 June 1983 at about 15 00 GMT near the eastern edge of the survey area (compare figures 1-2 and 1-6). Note that the spacing between the sub-bottom reflectors increases as the sea floor gets deeper. This is typical of small and large depressions in the area. The extra lines are the returns from the "fast down echo sounder" used to control the height of the fish during camera runs.

C) Sub-bottom profile as observed on 10 June 1983 at 19 45 GMT on the eastern edge of site 'E'.

mining operations or during the Echo 1 expedition, deep ocean currents are a likely agent redistributing the sediments (Johnson, 1971), eventually combined with gravitational forces working on the soupy top layer observed in all box cores on Echo 1 (see below). Once the sediments are in place, compaction reduces the sediment column, preserving topographic lows as the compaction is the more effective the more sediments it can work on.

Photographs taken by the Deep-Tow group (figures 1-6, 1-7 and 1-8) and by the Ocean Mining Associates show that the flat central portions of the site are well, but not uniformly covered with manganese nodules. The depressions to the east, southeast and west have fewer nodules, sometimes no nodules at all. The biological activity is substantial as illustrated by the mud accumulations and tracks photographed on Echo 1 (figure 1-8; figure 4 in Spiess et al., 1984).

PHYSICAL CHARACTERISTICS of NODULES

a) General description

While on many previous expeditions box cores were generally spaced too far apart to collect nodules from the same population, both the "Control Area" and the "Mining Area" of Echo 1 had been selected after viewing the Deep-Tow photographs so that each of them looked homogeneous with respect to nodule diameter, shape and coverage. This allowed us to make some statistical analyses of the size, mass and volume of the nodules.

On a previous expedition (Vulcan 1) to MANOP Site "H" the nodules recovered by nine box cores had been measured by B. Finney. The data are shown here for comparison although the latter box cores had been spread over a larger area.

From the sixteen 0.25 m^2 box cores taken on Echo 1 (figure 1-9), 13 have been available for detailed geological and physical studies. They are divided into 3

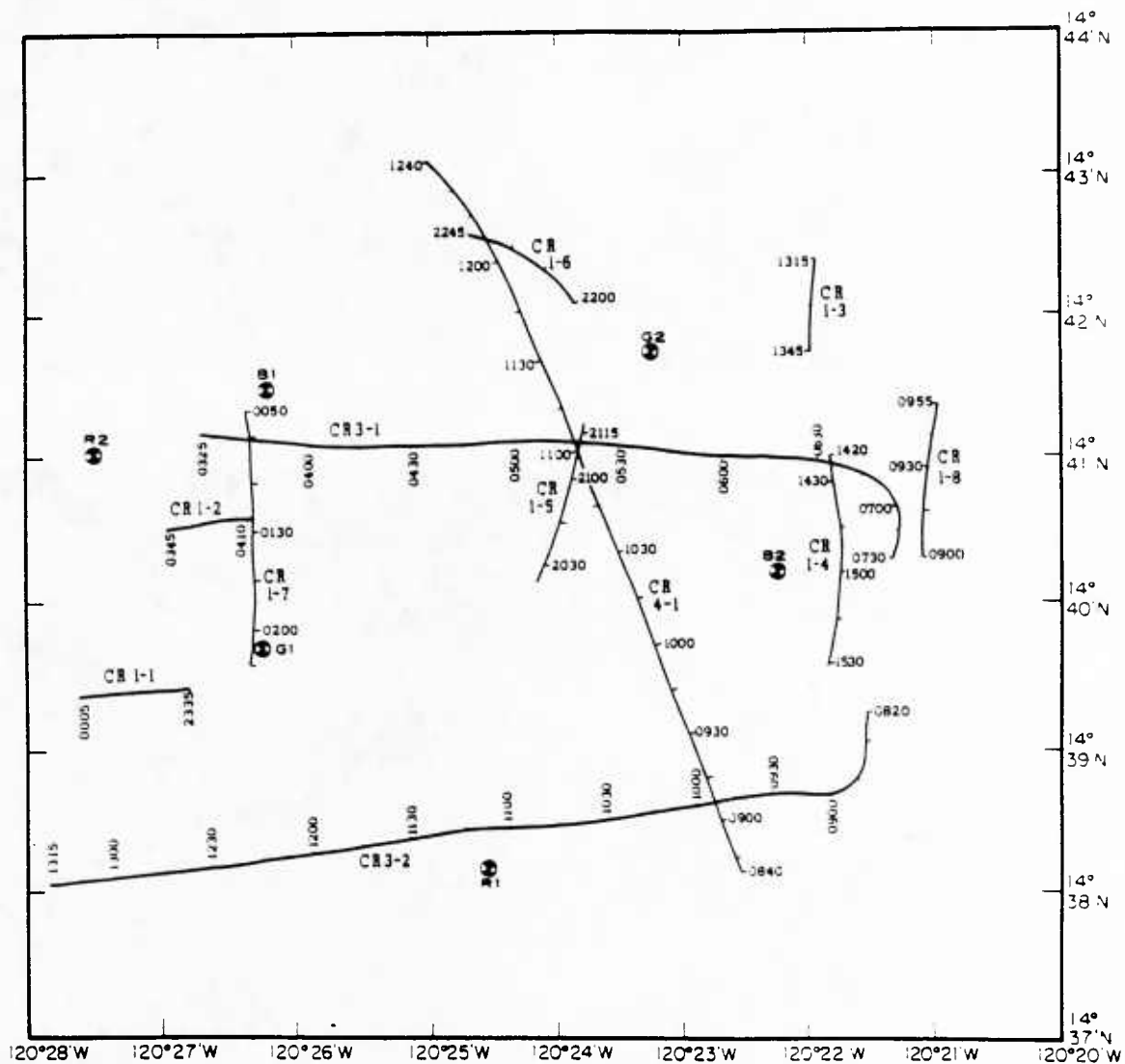


Figure 1-6. Deep tow tracks during camera runs

The positions of the Deep-Tow vehicle are shown for the times of the camera runs. The spacing between tick marks is 15 minutes. The coordinates are in meters east and north of 13°34'N, 125°30'W. The transponder positions permit matching with figure 1-2.

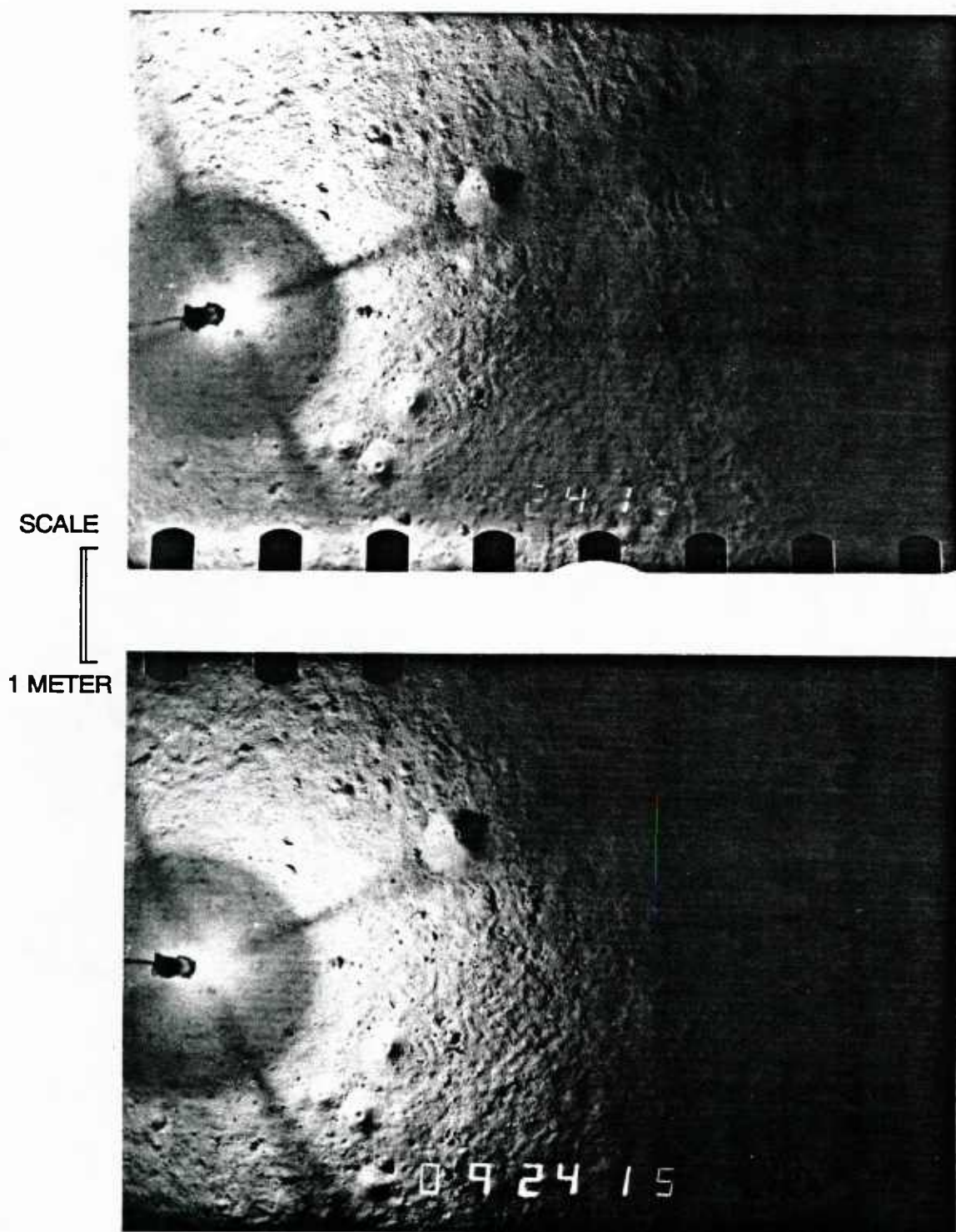


Figure 1-7. Sample photographs of sediments of site 'E'

Stereo photographs of nodule free sea floor in south-east of site 'E'. Note the roughness of the bottom.

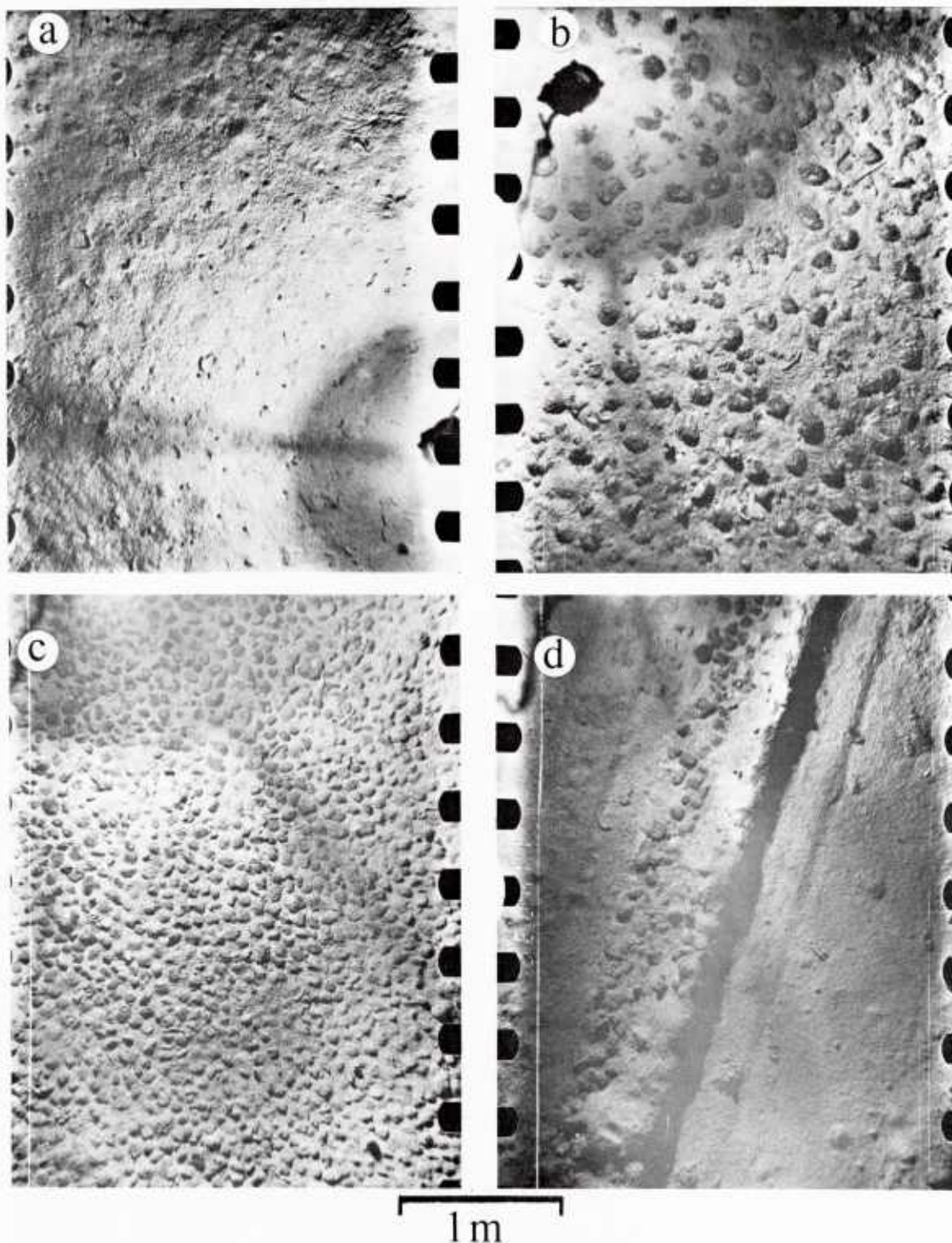
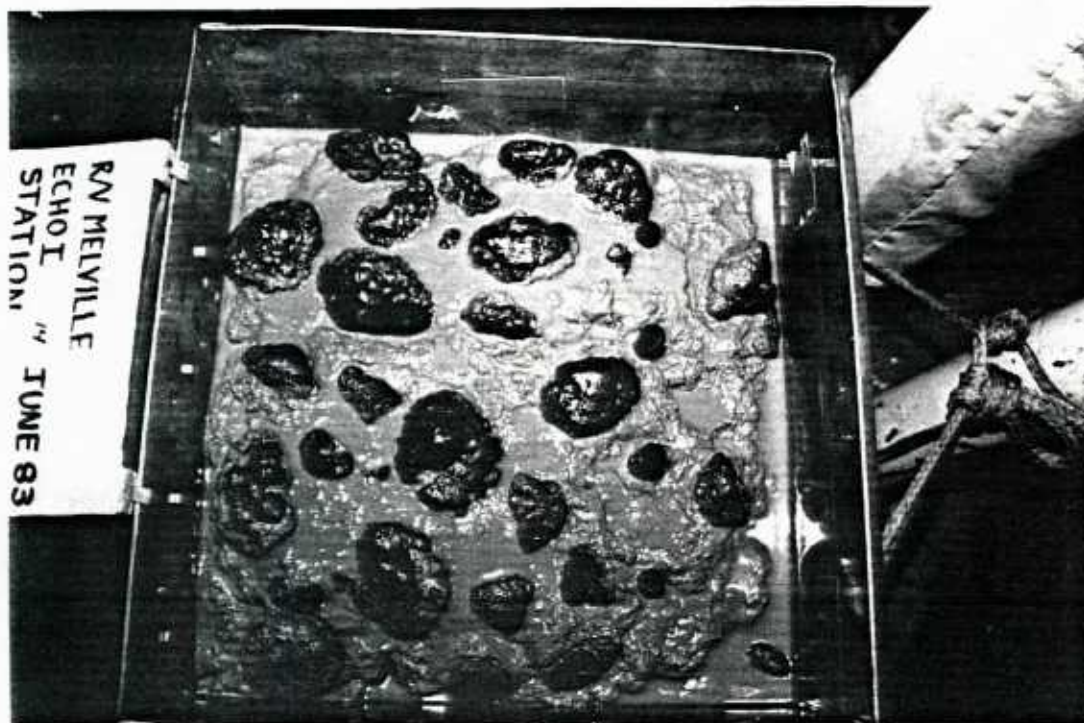


Figure 1-8. Examples of typical nodule coverage

Examples of (a) low, (b) medium, and (c) high nodule coverage at site 'E'. The fourth photograph shows a mining track in the Mining Area. Note that the shadows increase as one gets farther away from the strobe light.



BC H354



BC H352

Figure 1-9. Sample box cores

Surface of 2 box cores taken on Echo 1. The box is 50 cm x 50 cm. Box core H354 is from the Mining Area H352 is from the Control Area. The nodules penetrate the soupy upper sediments for 1-2 cm.

different groups (figure 1-2): Cores H347 - H352 come from the 'Control Area' in the South-West corner ($14^{\circ} 37'N$, $125^{\circ} 28'W$), Cores H353 - H358 come from the 'Mining Area' in the upper center ($14^{\circ} 42'N$, $125^{\circ} 24'W$), and core H359 comes from the transition zone to the East. The "Mining Area" is the area which had been selected by the Ocean Mining Associates to test their manganese nodule mining equipment. The "Control Area" was selected on Echo 1 to compare the biological activity of an undisturbed area with that of the Mining Area.

The box cores were mostly undisturbed when they arrived on board the R/V Melville and contained relatively cold water i.e. no or little surface water. Surface sediment is 75-95% pelagic clay with the remainder being siliceous (as determined by the author using smear slides on board the R/V Melville). The top few cm of each of the 16 box cores taken on Echo 1 are still fluid. Below this soupy sediment layer is a firm unmottled yellowish brown layer averaging 8 cm in thickness, followed by a lower mottled unit (Spiess et al., 1984). The 16 cores taken on Echo 1 contained between 3 and 117 manganese nodules each. The nodules were split between the biologists and the geologists using a random selection technique. About 50% of the nodules were refrigerated with box core sea water and preserved in air tight plastic bags for geological and acoustical studies. The nodules from box core H359 were never exposed to air and curated together with their own box core sea water.

Nodules cored at Site 'E' are ellipsoidal or discoidal with very irregular surface texture (figure 1-9). Rounded bulges on the smooth and lustrous top surface deviate up to 0.5 cm from the mean surface. These bulges are especially pronounced on the larger nodules. The bottom surface is granular, flatter and lacks small scale bumps. Well developed fissures found on the bottom surface penetrate the concretion and terminate a few mm below the top surface. X-ray studies indicate that the tops are mostly disordered manganates, whereas the bottoms are more crystalline

(Arrhenius, et al., 1985). Both, a fixed 10-Å-manganate (β -10-Å-manganate) and a partly expanding 10-Å-manganate (α -10Å-manganate) have been identified. The latter collapses upon dehydration to a fixed 7-Å-manganate (birnessite). No detailed studies of the composition of the nodules collected on Echo 1 have been made. Previous studies indicate that the nodules of this area have a composition similar to that of the nodules at DOMES site 'C' (Bischoff and Piper, 1979, p. 651).

The aspect ratios of the nodules vary from 1 to approximately 0.2. As will be shown in detail, the minor horizontal axis is in general a little shorter than the longest (horizontal) axis, while the vertical axis is on the average only 50% of the longest axis of the nodule.

The nodules from the Mining Area (60-80% coverage) are 5.0 ± 1.5 cm in length (longest axis) and 66 - 114 per box core (0.25 m^2). Those from the Control Area (50% coverage) are 6.75 ± 2.0 cm in length and 30 - 48 per box core. Box core H359 had 10 nodules ranging from 6.6 to 12.7 cm in size and one pushed down or buried nodule of 2.0 cm. (The surface of this small one is all granular like that of buried nodules. It was, however, found near the edge of the box corer and can thus not be identified as 'buried'.)

Deep Tow photos show that the nodules sampled by the box corer are representative for their respective areas. Their sizes will be discussed in detail below.

12 buried nodules were identified in the box cores of the Mining Area, while only 7 nodules were buried in the Control Area box cores. All buried nodules have a very fragile granular surface which is as delicate as and resembles the bottom surface of the surface nodules. X-ray studies of the crystal structure of a single buried nodule (which had been preserved together with the surrounding sediments in an air-tight plastic bag) have revealed that both the top and the bottom contain the fixed 10-Å-

manganate and no observable 7-Å-phase. This suggests that the entire surface of the buried nodules is similar to the underside of the outcropping nodules. The observation of the fixed 10-Å-manganate was done 20 months after collection of the samples. Continuing analysis (Arrhenius, et al., 1985) showed that during this time period expanding 10-Å-manganates convert irreversibly to the non-expanding (fixed) polymorph. This makes the interpretation of the X-rays on the buried nodules difficult. Most of these nodules were found at depths of 5 to 25 cm.

b) Measurements

For some 500 nodules the 3 principal axes, the weight in air and the weight in water were determined. The 3 principal axes are defined as follows:

vertical axis (z-axis) = vertical as on the ocean bottom
 major horizontal axis (x-axis) = longest horizontal axis
 minor horizontal axis (y-axis) = axis perpendicular to vertical axis
 and to major horizontal axis

In order to assure high measurement accuracy of the axes, the nodules were carefully placed between adjustable, machined wooden boards. The spacing of these boards was then measured with a caliper to an accuracy of 0.5 mm or better. The two horizontal axes were measured simultaneously. Then the nodule was rotated 90 degrees around the x-axis and the vertical axis was measured. From these measurements, a "computed volume" can be calculated by assuming the nodules are ellipsoids:

$$V = \frac{4\pi}{3} \frac{a b c}{8} \quad (1-1)$$

where a, b and c are the respective axes. The measurement error propagates as

$$\left(\frac{\Delta V}{V} \right)^2 = \left(\frac{\Delta a}{a} \right)^2 + \left(\frac{\Delta b}{b} \right)^2 + \left(\frac{\Delta c}{c} \right)^2 \quad (1-2)$$

and is estimated to be 5% or less. On the average this volume is some 20% larger

than the measured volume of a nodule. This can be attributed to the large bumps on the surface of the nodules at this site.

The weights in 2°C sea water and in air were determined with a beam balance. Before the weight in air W_{air} could be determined, all water on the balance and, just prior to weighing, excess surface water on the nodules was removed with a paper towel. The accuracy of the beam balance is 0.1 g. From these measurements the volume of the nodules V_{nodule} can be determined by Archimedes's principle:

$$(M_{nodule} - V_{nodule} \rho_{sea\ water}) g = W_{sea\ water} \quad (1-2a)$$

$$V_{nodule} = \frac{W_{air} - W_{sea\ water}}{\rho_{sea\ water} g} \quad (1-2b)$$

where g is the gravitational acceleration, M_{nodule} is the mass of the nodule, $W_{sea\ water}$ is the weight of the nodule in sea water and $\rho_{sea\ water}$ is the density of sea water. Neglecting the measurement error of the density (<1 per mil) the measurement error is

$$\begin{aligned} \frac{\Delta V}{V} &= \frac{\sqrt{2} \Delta W_{air}}{W_{air} - W_{water}} \\ &= \frac{0.2}{W_{air} - W_{water}} \\ &< 3\% \end{aligned} \quad (1-3)$$

The density of a nodule ρ_{nodule} is defined by

$$\rho_{nodule} = \frac{M_{nodule}}{V_{nodule}} \quad (1-4)$$

where M is the mass and V is the measured volume. The error propagates as (neglecting again the error of $\rho_{sea\ water}$)

$$\frac{\Delta \rho_{nodule}}{\rho_{nodule}} = \frac{\Delta W_{air}}{W_{air} - W_{water}} \left[1 + \left(\frac{W_{water}}{W_{air}} \right)^2 \right]^{1/2} \quad (1-5)$$

This is $<10\%$ in the worst case, and $<5\%$ for over 90% of the nodules.

c) Nodule sizes, masses and volumes

c.1 Longest axis

After the box cores H348 and H352 had failed the F-test for the "Control Area" (the probability that they were drawn from the same population as the other 4 box cores is less than 1%), a "Reduced Control Area" (RCA) was defined with the 4 remaining box cores. (It is not surprising that the 2 box cores failed the F-test as the nodule coverage changes substantially in their respective vicinities). Figure 1-10 shows the distribution of the nodule sizes for 3 mm size classes. Table 1-1 lists the first four moments for the 1 mm size classes (The third and fourth moments have been normalized by the third and fourth power of the standard deviation respectively.).

area	number	mean	variance	st. dev.	3rd moment	4th moment
		[mm]	[mm ²]	[mm]		
RCA	79	68.0	234	15.3	-0.29	2.13
mining	243	50.0	214	14.6	0.53	2.97
MANOP H	141	48.5	264	16.3	0.57	3.05

Table No. 1-1 : Longest length

After a graphical comparison of the common probability distributions, those in table 1-2 were selected for a closer inspection.

In previous works, the authors (Karas, 1978; Magnuson, 1983; Ma, 1982), often linked the size distributions of nodules to Rayleigh or Bernoulli distributions (table 1-2). It is possible to find suitable parameters for the Bernoulli distribution if one chooses the interval size very carefully (M. Karas chose 17.8 mm for MANOP site S), but the rms-error is large, as the fits deviate substantially from the data for the nodules exceeding the most frequent length. A fit with a Rayleigh distribution is practically impossible, as the variance and the square of the mean are related by

$$\sigma^2 = (4/\pi - 1)\bar{x}^2 \quad (1-6)$$

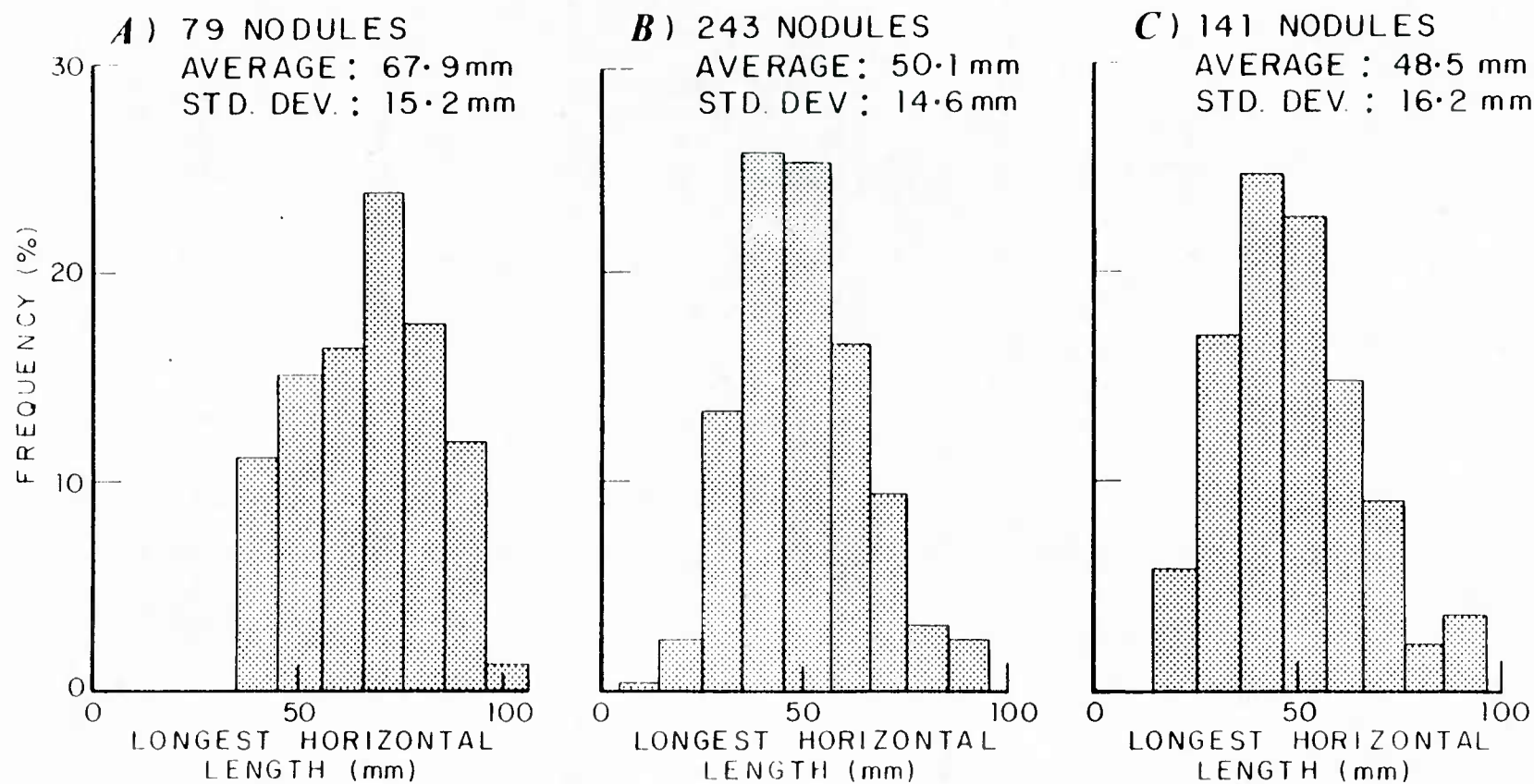


Figure 1-10. Frequency of occurrence of longest length

Frequency of occurrence of longest horizontal length for the Reduced Control Area (A), the Mining Area (B) and MANOP site II (C)

where σ^2 = variance and \bar{x} = mean. This means that

$$\sigma = \sqrt{(4/\pi-1)} \bar{x} = 0.52\bar{x}. \quad (1-7)$$

Table 1-1 shows that this is not the case at Site 'E' nor at MANOP site H.

Name	Definition	Mean	Variance
Bernoulli	$B(N, x, p) = \frac{N!}{x!(N-x)!} p^x (1-p)^{N-x}$ $N+1$ = number of size classes	Np	$Np(1-p)$
Poisson	$P(x, \lambda) = \frac{\lambda^x e^{-\lambda}}{x!}$	λ	λ
Gaussian	$Y(x, \sigma, \mu) = \frac{1}{\sigma\sqrt{2\pi}} e^{-x^2/2\sigma^2}$	μ	σ^2
Rayleigh	$R(x, \alpha) = \frac{x}{\alpha^2} e^{-x^2/2\alpha^2} H(o)$ H = Heaviside step function	$\alpha \frac{\sqrt{\pi}}{\sqrt{2}}$	$2\alpha^2 - \bar{x}^2$
Beta	$B(x, b, c) = \frac{\Gamma(b+c+2)}{\Gamma(b+1)\Gamma(c+1)} x^b (1-x)^c$ $0 \leq x \leq 1$ $b > -1$ $c > -1$ Γ = gamma-function	$\frac{b+1}{b+c+2}$	$\frac{(b+1)(c+1)}{(b+c+2)^2(b+c+3)}$
Gamma	$\gamma(x, \alpha, \beta) = \frac{1}{\Gamma(\alpha+1)\beta^{\alpha+1}} x^\alpha e^{-x/\beta}$ $x > 0$ $\alpha > -1$ $\beta > 0$ Γ = gamma-function	$\beta(\alpha+1)$	$\beta^2(\alpha+1)$

Table No. 1-2 : Definitions, Means and Variances of some probability functions
(for a discussion of these functions and the associated physical models.
see Bendat and Piersol 1971, and Harris 1966)

A plot of the logarithm of the frequency of occurrence versus the longest length shows that the numbers of nodules with diameters exceeding the most frequent

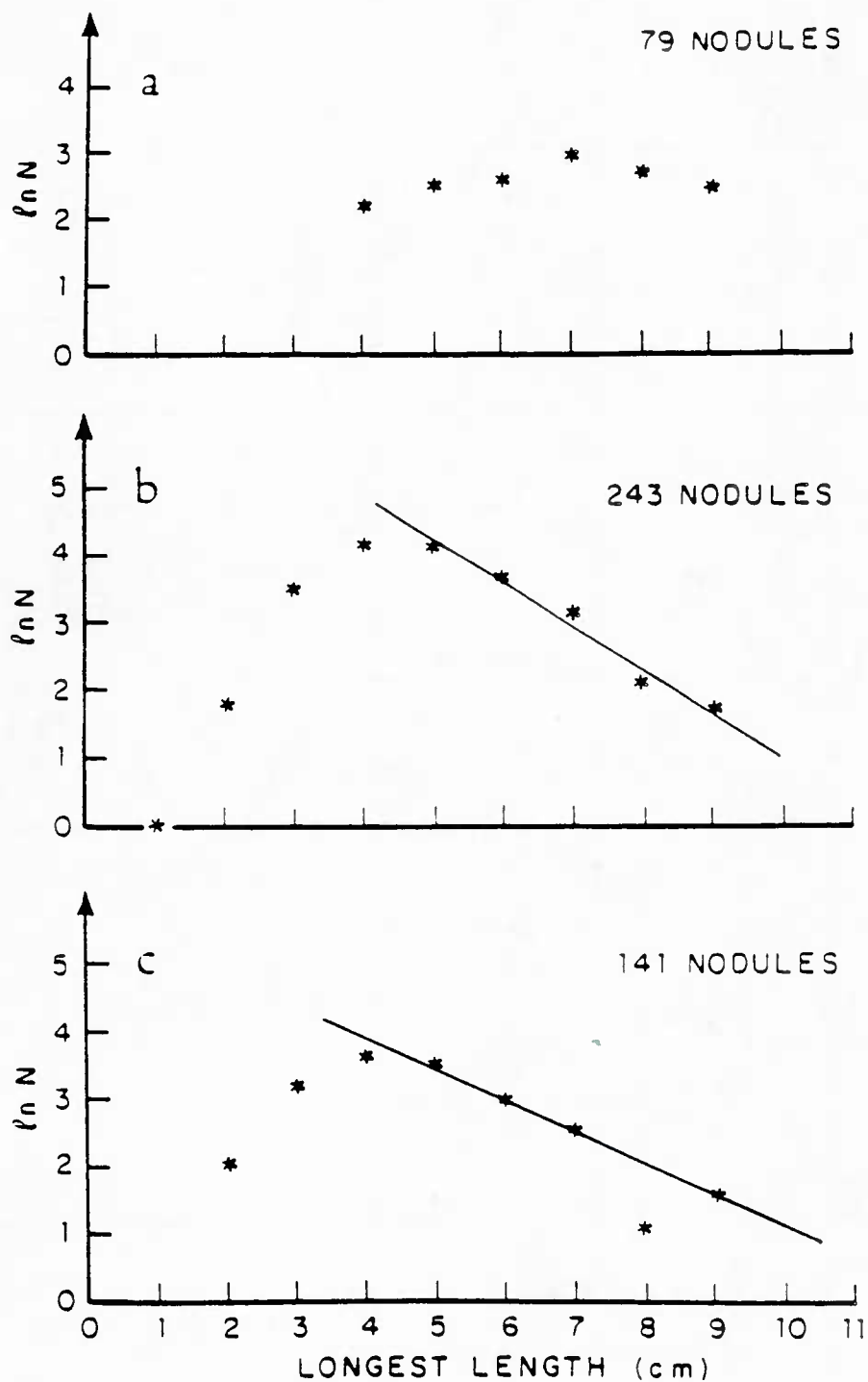


Figure 1-11. Logarithm of number of manganese nodules

Plots of the natural logarithm of the number of manganese nodules for 1 cm size classes. (a = Reduced Control Area, b = Mining Area, c = MANOP site H)

diameter fall on a straight line i.e. that the number of nodules with sizes exceeding the most frequent one decays exponentially with size (figure 1-11). Unfortunately, this does not describe the nodules with smaller axes. A distribution of the form

$$f(x) = g(x)e^{-\alpha x} \quad (1-8)$$

where $e^{-\alpha x}$ decays much faster for large x than $g(x)$ increases, is given by the gamma density function (see table 1-2).

For the RCA, the Mining Area and MANOP site H, the first 4 moments of the longest lengths were computed (table 1-1).¹ A look at the third and fourth moments and the plots in figures 1-10 and 1-12 suggest that a Gaussian distribution will probably be a valid approximation. Using the computed means (\bar{x}) and standard deviations (σ) as parameters, the Gaussian and gamma distributions give satisfactory fits for all 3 areas. Both two-parameter densities can be better adapted by using a least-squares fit to choose the parameters. A simple-minded test on a PDP 11/23 computer allowed for a reduction of the rms error of up to 25%.

A χ^2 -test was made to test the hypothesis that the probability distribution is a gamma-function. The hypothesis had to be rejected at the 30% significance level. A χ^2 -test for a Gaussian shows that the probability distribution is Gaussian at the 80% significance level for MANOP site 'H', a 50% significance level for the RCA and the 80% significance level for the Mining Area. Hence it must be admitted that the frequency of occurrence of the longest length can be best modeled by a Gaussian.

Unfortunately, there are too few nodules available from the transition zone to extend this hypothesis to the transition zone or any areas with large nodules. Although nodules smaller than 5 mm were not retained, the data indicate that micro-

¹ I thank Bruce Finney, Graduate School of Oceanography at the Oregon State University, Corvallis, Oregon, for making his measurements from the Vulcan 1 expedition available (MANOP site H).

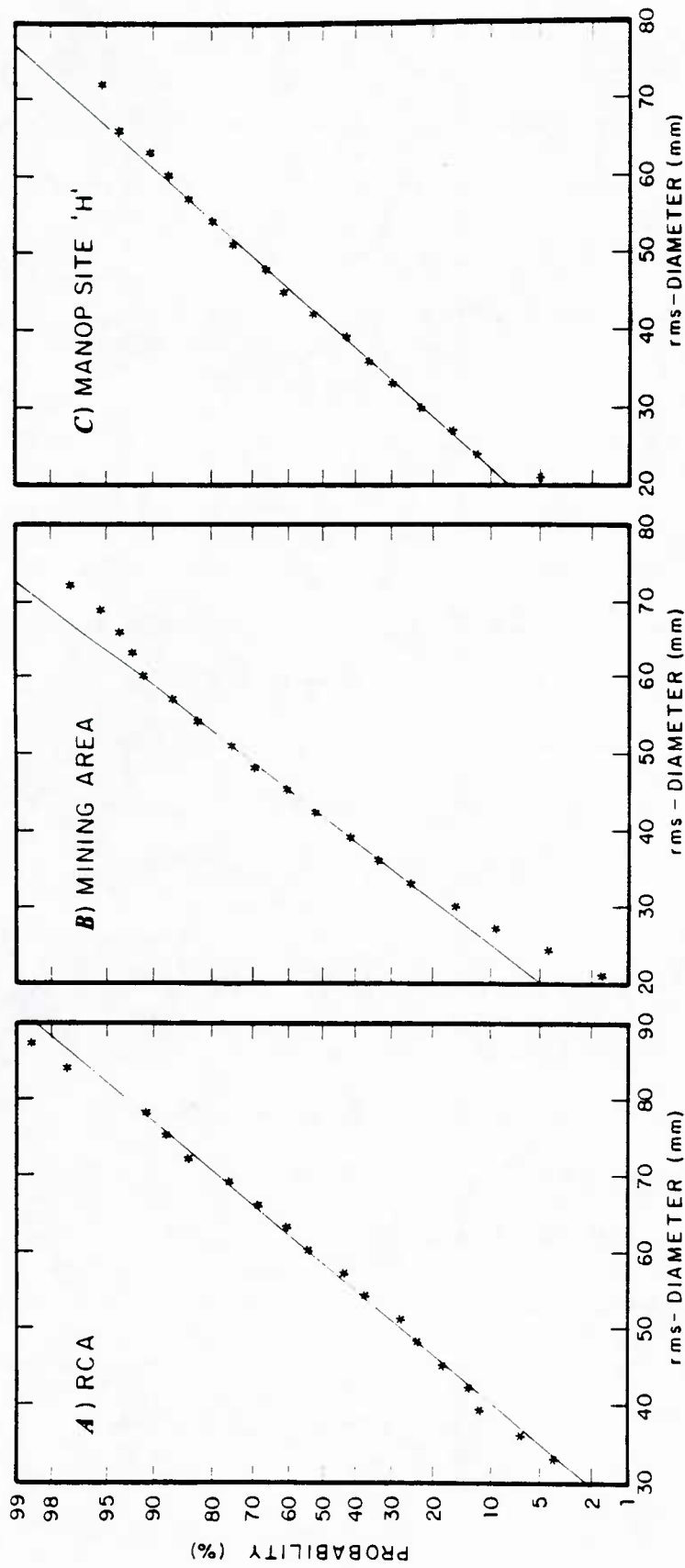


Figure 1-12. Frequency of average horizontal diameter on probability paper

Frequency of occurrence of average horizontal diameter on Gaussian probability paper for the (A) Control area, (B) Mining area, (C) MANOP site 'H'. Note the deviations from the Gaussian at both ends.

nodules form a separate population.

c.2 Average horizontal diameter

For acoustical measurements, it is important to know the average horizontal diameter D_{av} defined by

$$D_{av} = \sqrt{xy} \quad (1-9)$$

where x is the longest horizontal axis and y is the shorter horizontal axis. The same analysis as for the longest horizontal axis has been done, and the results have been summarized in figure 1-13 and the table below:

area	average $\pm \sigma$	Gaussian rms	Gamma rms
Mining	44.5 ± 13.0 mm	0.006 mm	0.014 mm
RCA	60.0 ± 13.5 mm	0.010 mm	0.015 mm
MANOP H	44.0 ± 15.5 mm	0.007 mm	0.014 mm

Table No. 1-3 : Average horizontal diameter

The rms errors for comparisons of the data with a Gaussian and with a gamma distribution have been computed and are shown in table 1-3.

A χ^2 -test shows that the Gaussian is an acceptable probability distribution for the average horizontal diameter for all three areas. The significance levels are 95% for MANOP site 'H', 90% for the Mining Area and 90% for the RCA. Except for the nodules from the Mining Area, a χ^2 -test with a gamma-distribution gives much higher χ^2 values and therefore a lower probability that the γ -distribution is the correct fit. For the Mining Area the χ^2 is the same for both the Gaussian and the gamma distributions.

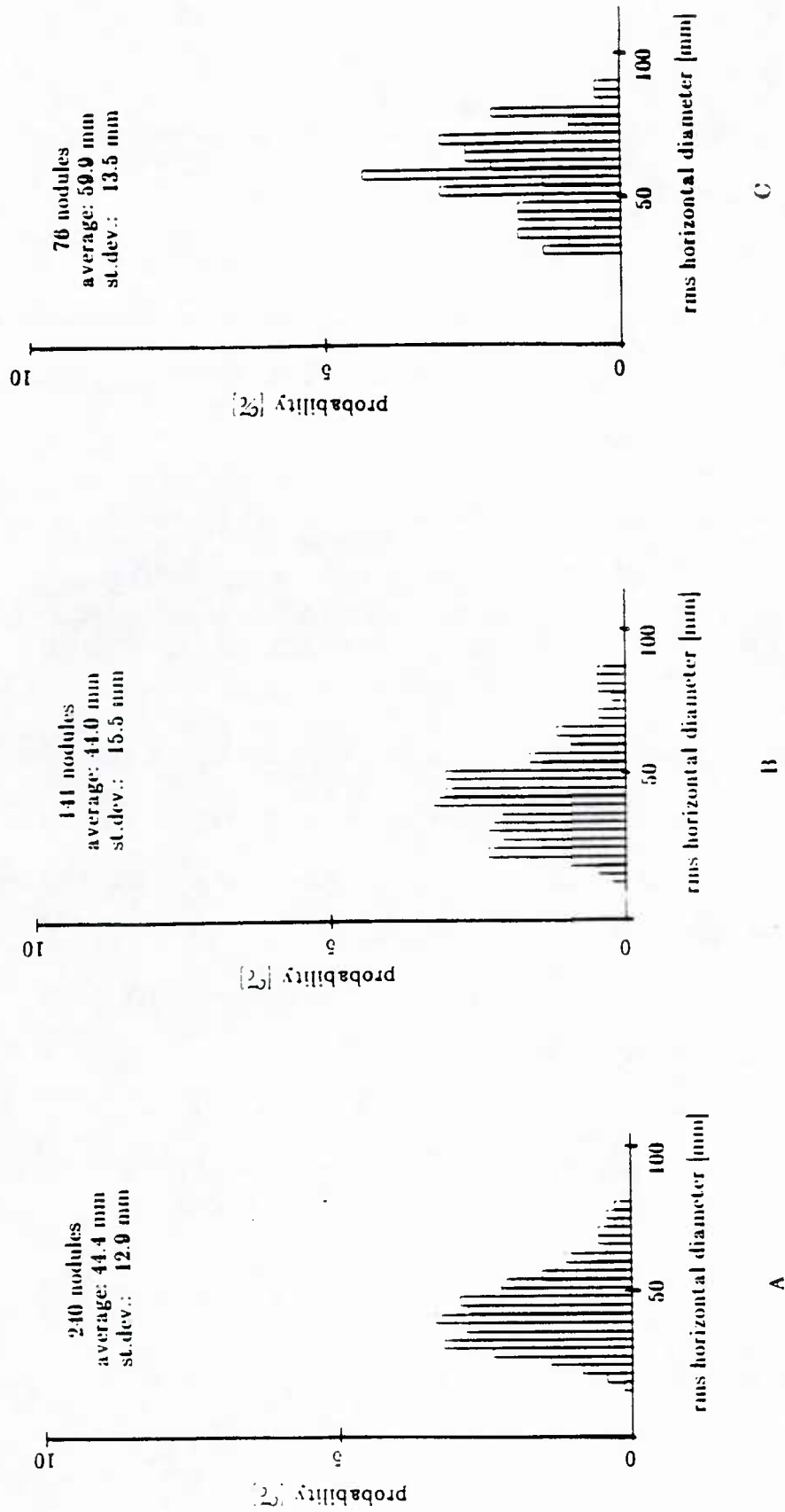


Figure 1-13. Frequency of average horizontal diameter

Frequency of occurrence of the average horizontal diameter for the Reduced Control Area (A), the Mining Area (B) and MANOP site II (C)

c.3 Medium axis

The frequencies of occurrence of the ratio of the medium axis over the longest axis have been plotted in figure 1-14 and the average and standard deviation of those ratios have been computed:

area	average $\pm\sigma$	rms error	number nodules
Mining area	0.79 ± 0.10	0.005	240
RCA	0.77 ± 0.11	0.001	76
MANOP H	0.82 ± 0.12	0.011	141

Table No. 1-4 : Ratios of medium over longest lengths

A fit with a Gaussian with the thus determined averages and standard deviations as parameters leads to the rms-errors indicated in table No. 1-4.

A χ^2 -test shows that a fit with a Gaussian is also here good for the Echo 1 site. The levels of significance are 90% for the Mining Area, 90% for the RCA and 40% for MANOP site 'H'. (Remember that the box cores are not closely spaced at MANOP site 'H' and are shown for comparison only.)

c.4 Vertical axis

The same data reduction as sub c.3 was done for the vertical axis. The results can be found in figure 1-14 and the following table:

area	average $\pm\sigma$	rms-error
Mining area	0.53 ± 0.10	0.006
RCA	0.48 ± 0.09	0.0095
MANOP H	0.53 ± 0.14	0.009

Table No. 1-5 : Ratios of vertical to longest length

The fit with a Gaussian is again good for all 3 areas. The χ^2 -test tells us that the Gaussian can be accepted at the 95% significance level for the Mining Area, 60% for the RCA and 90% for MANOP site 'H'.

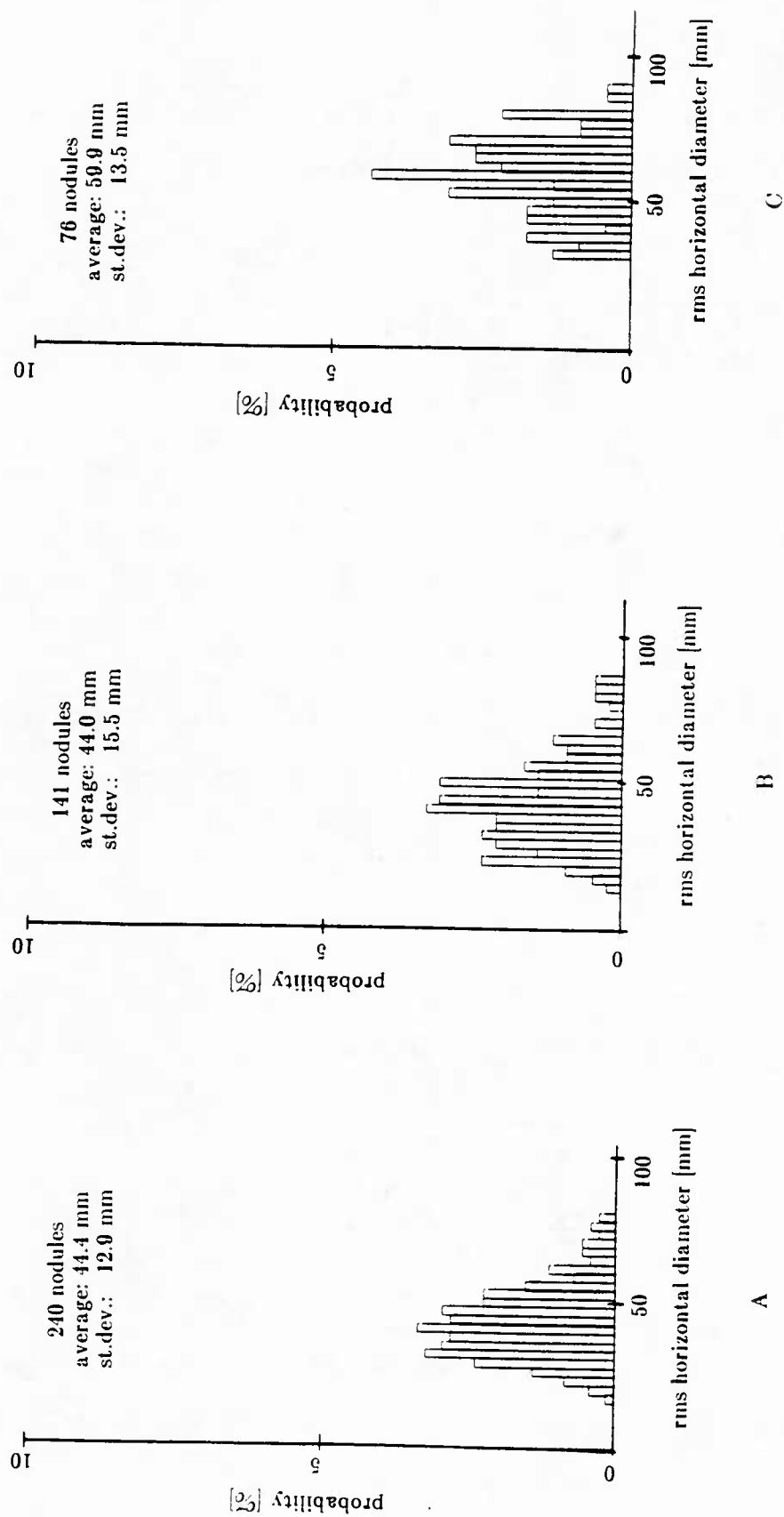


Figure 1-13. Frequency of average horizontal diameter

Frequency of occurrence of the average horizontal diameter for the Mining Area (A), MANOP site 'H' (B) and the Reduced Control Area (C).

c.5 Mass, volume and density

As already stated above, the volume of each nodule was determined by Archimedes's method. Knowing the wet mass, the wet density could be determined with equation (4).

The measured wet density for the nodules of site 'E' is $2.00 \pm 0.04 \text{ g/cm}^3$ (Greenslate, 1977). This is within one standard deviation in agreement with J. Greenslate's constant density of 1.96 g/cm^3 . This result permits one to use the wet mass instead of the volume or vice-versa, whichever quantity can be obtained more easily.

A least squares fit for the nodule volumes was attempted by assuming that

$$V = \nu x^\epsilon \quad (1-10)$$

where V = volume, x = longest length, ϵ and ν are the parameters to be determined. Taking the natural logarithm leads to

$$\ln V = \ln \nu + \epsilon \ln x \quad (1-11)$$

which is a straight line on a $\ln v(\ln x)$ graph. Minimizing the square of the error leads to

$$\epsilon = \frac{\sum \ln V_i \sum \ln x_i - N \sum \ln V_i \ln x_i}{(\sum \ln x_i)^2 - N \sum (\ln x_i)^2} \quad (1-12)$$

$$\ln \nu = \frac{1}{N} [\sum \ln V_i - \epsilon \sum \ln x_i] \quad (1-13)$$

For the Mining Area $\epsilon = 2.35$ and $\nu = 2.1$, while for the Control Area $\epsilon = 2.44$ and $\nu = 1.5$. Figure 1-15 shows the volumes as a function of the longest length and as a function of the volumes calculated with equation (1-1) for the Control Area and the Mining Area. All points with standard deviations are averages over more than 3 nodules, the total number of nodules being 243 for the Mining Area and 90 for the Control Area.

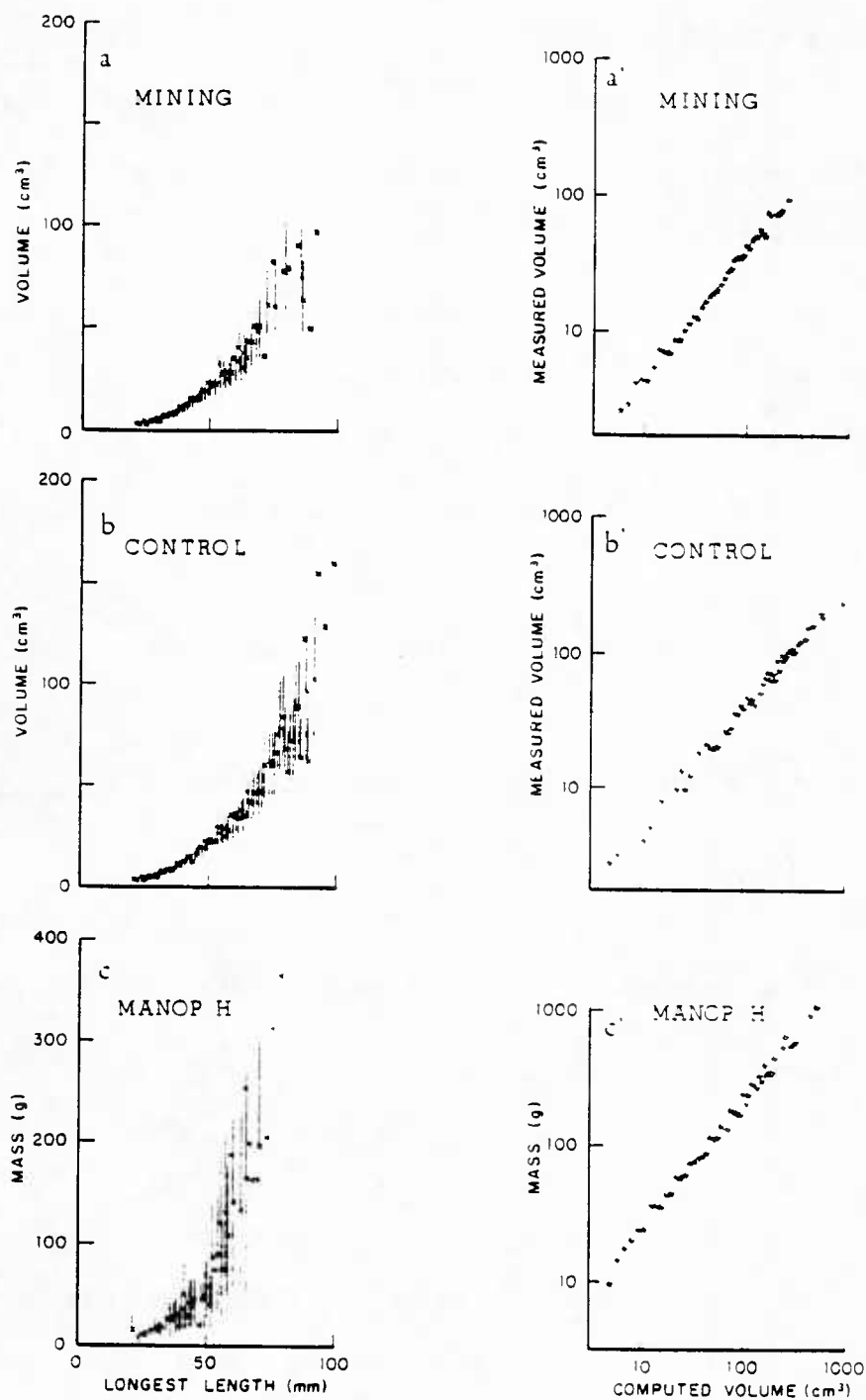


Figure 1-15. Manganese nodule volumes as a function of the nodule length

Averaged volumes of the nodules as a function of the longest length for the Mining area (a) and the Control area (b). The standard deviations are shown if there are more than three nodules of that size. (a') and (b') show the volumes as a function of the product of the three main axes. For MANOP site H, the masses have been plotted instead of the volumes (c and c').

Unfortunately, there are not enough data available to make a reliable estimates of ϵ and ν for the transition zone ($\epsilon = 2.89$ for box core H359).

There are no volume measurements available for MANOP site H. The volumes being directly proportional to the wet masses (page 34), the masses for site H have been plotted as a function of the longest axis (figure 1-15.c).

If the third root of the product of the three axes is used as average length, the volumes are the 2.6th power or the 2.9th power of that average length for the Control Area and the Mining Area respectively (figure 1-15a' and 1-15b'). With the assumption that the wet density is a constant, the 2.7th power is found for MANOP site 'H'.

c.6 Discussion

While the graphical comparison of nodule sizes and axis ratios with probability distributions suggested that Rayleigh, Gamma, Beta and Gaussian probability functions might all fit the data equally well, numerical analyses have shown that a Gaussian gives the best fit for this area if the mean and/or the standard deviations are used as parameters. The deviations from a Gaussian are small enough and are judged to be insignificant for the acoustic assessment of manganese resources. This result will help establish the basics for the modeling of the acoustic backscatter of manganese nodules and possibly of nodule growth. It is likely that the distribution is approximately Gaussian because a large number of independent parameters control nodule growth.

The data presented above suggest that the growth rates in the three orthogonal directions are not independent of each other. Especially for the Mining Area i.e. where a lot of nodules from a well defined homogeneous area are available, the relationship between the two horizontal diameters or between the longest and the

vertical axes are well described by an average ratio and a standard deviation.

The average horizontal diameter as well as the longest length are approximately normally distributed. Deviations from a Gaussian occur at both ends of the size range (figure 1-12). For the RCA, they have to be attributed to sampling errors as there were fewer than 80 nodules available. Sampling errors for the Mining Area and for MANOP 'H' are also possible since a few nodules in the range of 1 mm to 1 cm could change the curve and nodules smaller than 5 mm were not retained. (No nodules of the order of a few mm to 1 cm could be found on Echo 1). This suggests that there is a gap between the micronodules studied on other expeditions to the same area (Arrhenius, 1952; Goldberg and Arrhenius, 1958; Bischoff and Piper, 1979) and that micronodules are unlikely to grow to macronodules. Cross-sections of nodules from site E have revealed that at least some of the nodules have nuclei which are smaller than 1 mm. Further studies and very careful sampling are needed to resolve this problem. Once nodules have reached a certain size, they cannot easily grow bigger. This is reflected in the larger size classes (figure 1-12) and the cut-off with the largest nodule sampled. The reason for this maximum size is unknown. The numerous fissures in the larger nodules and their fragility suggest, however, that the biological activity results in breaking in at least some of the nodules.

d) Nodule coverage

Side looking sonar imagery and photographs provide the primary data on the nodule coverage throughout the area. Since most of the area is rather densely covered, the side looking sonar data can only be used to localize rock outcrops and nodule free zones.

The Deep Tow photographs were analyzed by viewing them with a microscope. The magnification was adjusted so that the 10x10 grid in the field of view

covered 1.5m x 1.5m when the fish was 10m above the bottom. This method allows one to measure the coverage (area actually covered by nodules divided by the total area) within $\pm 10\%$ (percentage points) by weighing the area around the strobe light heavily. Farther away from the strobe light, the shadows become large and it is very difficult to delineate the nodules (figure 1-8). Small scale variations within the area covered by a single frame contribute most of the error. Variations of the camera height of ± 1.5 m introduce an error of about 0.5 cm in the nodule size for the individual picture. On the average, this error is, however small, and an accuracy in nodule dimensions of ± 0.5 cm can be achieved. An average nodule diameter was estimated for each frame and these results, together with the nodule coverage have been superimposed on the bathymetry cross-sections in figures 1-16 and 1-17.

Figures 1-2, 1-6, 1-16 and 1-17 permit one to obtain an idea of the nodule distribution throughout the area. Figure 1-2 shows the relevant box core and transponder positions relative to the sea beam bathymetry. Rock outcrops and scarps have been identified with the side-looking sonars, the 4kHz-subbottom-profiler and two Deep-Tow cameras used as a stereo pair. Figure 1-6 shows the fish positions during the camera runs. Some time marks have been annotated in order identify the positioning of the fish during the camera runs. The spacing between consecutive time marks is 15 minutes. The bathymetry cross-sections for the camera runs are shown in figure 1-16 and 1-17 with time annotations. As the vehicle is traveling with a speed of approximately 3000 m/h, 15 minutes correspond to a distance of 750 m. The nodule coverage and the nodule sizes have been plotted above the bathymetry in figures 1-16 and 1-17.² The times allow for a direct matching of figures 1-6, 1-16 and 1-17. Figures 1-2 and 1-6 can be related by matching the transponder positions.

² Unless otherwise stated all data presented here are Deep-Tow data only. Real time TV data from a previous Ocean Mining Associates expedition have been viewed by the author and are found to be in agreement with the Deep-Tow data.

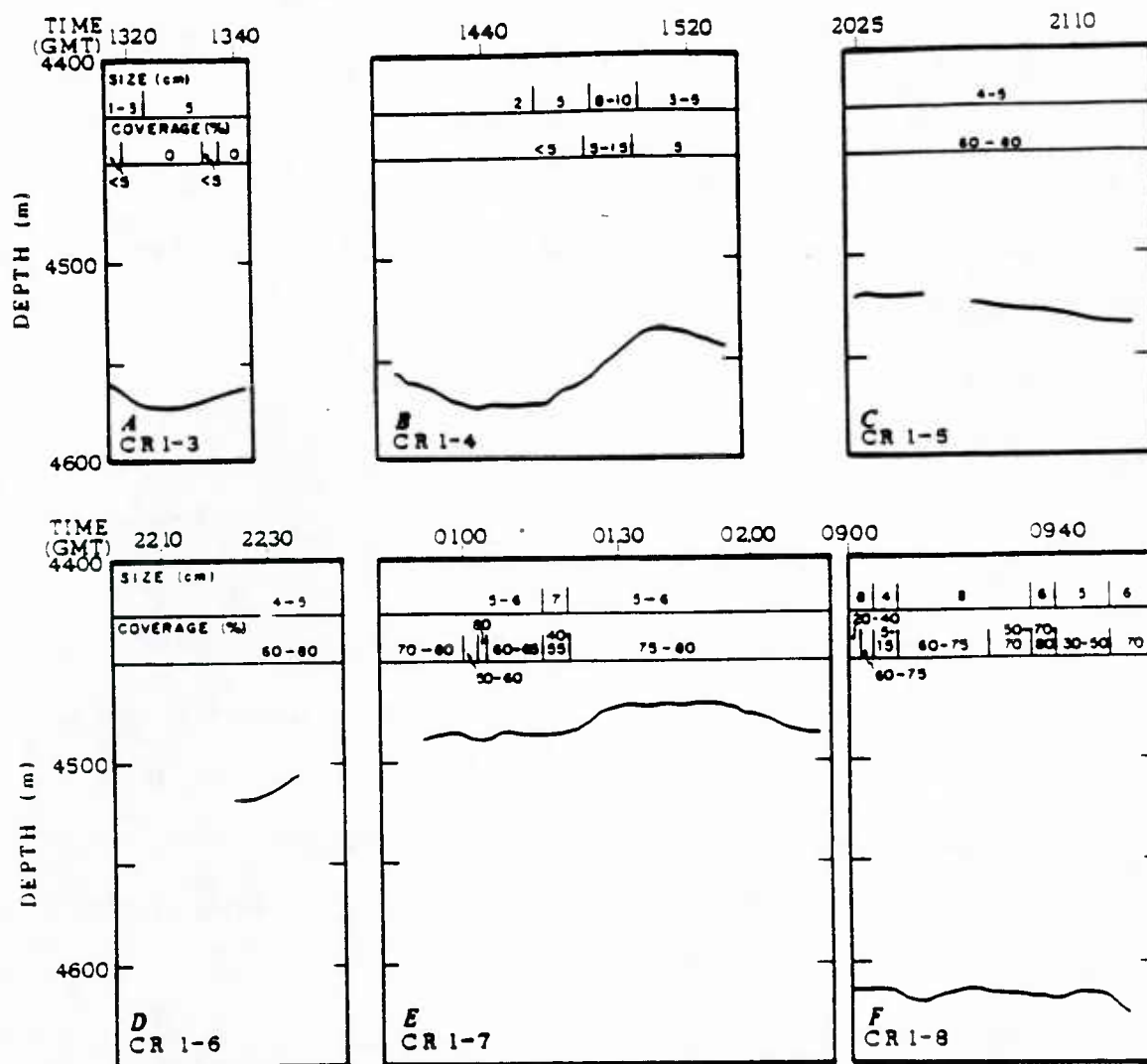


Figure 1-18. Bathymetry, nodule size and coverage during camera runs

Bathymetry (m), nodule coverage (%) and average nodule sizes (cm) during camera runs 1-3 to 1-8. The times are in hours and minutes GMT.

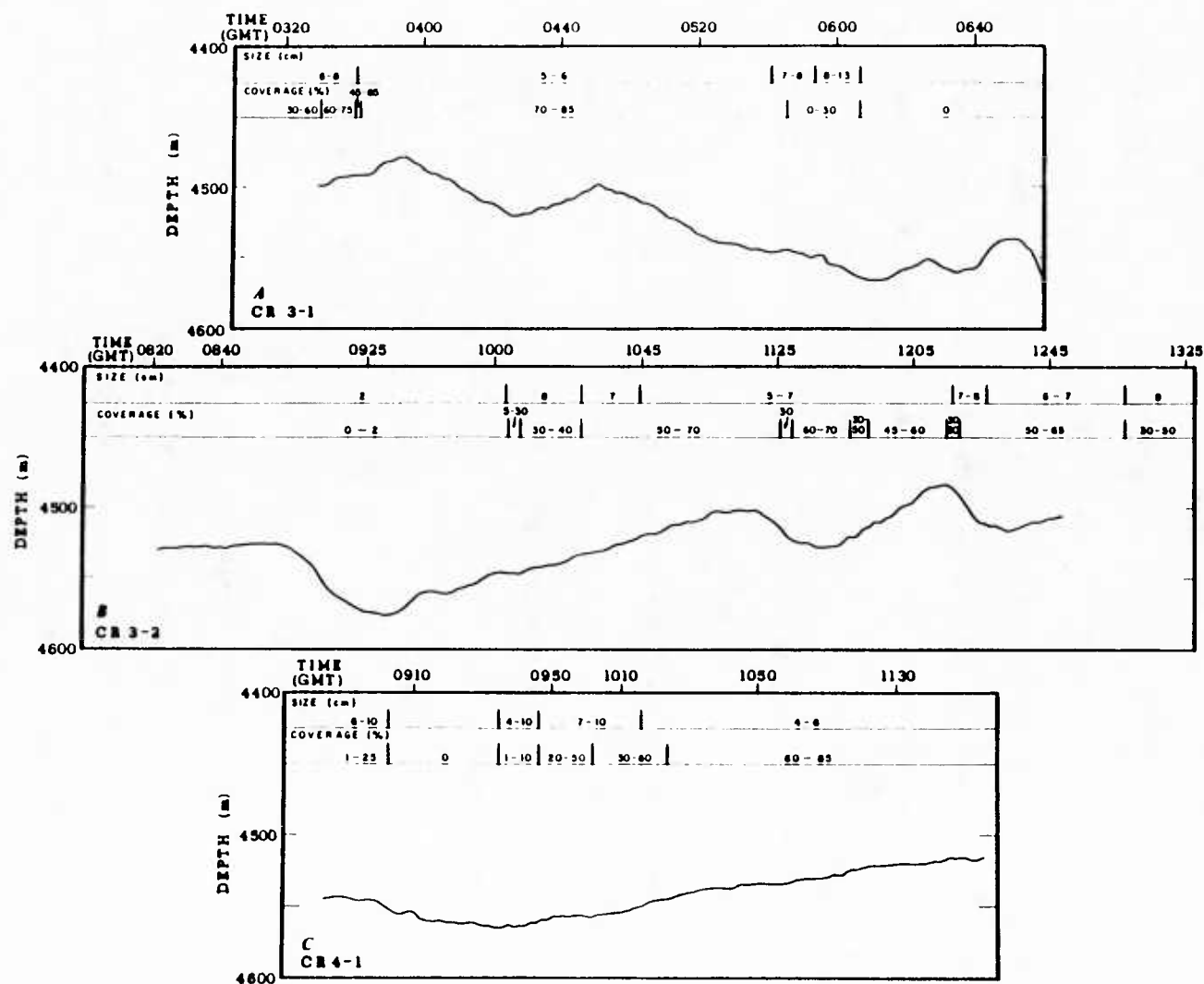


Figure 1-17. Bathymetry, nodule size and coverage during camera runs

Bathymetry (m), nodule coverage (%) and average nodule sizes (cm) during camera runs 3-1 to 4-1. The times are in hours and minutes GMT.

From these figures we see that the central part of the survey area ("Mining Area") appears to be rather uniformly and densely covered by manganese nodules with an average diameter of 5 cm and a coverage of over 60% and a concentration of 20 kg/m^2 . To the east of the Mining Area, there is a transition zone with few, but up to 16cm long and 0.8 kg heavy manganese nodules. Although the coverage is around 20% only, the concentration - as calculated from box core H359 - is 17 kg/m^2 . The nodule coverage drops to zero as one approaches the rocky areas in the east and west. To the south-east there is a sloping nodule-free zone. Ocean Mining Associates data show that between $14^\circ 30' \text{N}$ and $14^\circ 40' \text{N}$, the nodule coverage along $125^\circ 30' \text{W}$ is less than 10% except for two about 300m-patches where it is about 25%. In the RCA, the coverage is generally between 50 and 60%, the concentration 16 kg/m^2 , and the average diameter 6 cm.

As already noted for the MANOP study sites (Spiess and Weydert, 1984; Karas, 1978; Weydert and Zampol, 1985), uniform coverage and size distributions are restricted to gently sloping areas with several tens of meters of sediments and an upper acoustic unit (sedimentary layer defined by the sea floor and the first sub-bottom reflector) of constant thickness. As soon as rocky outcrops appear or the slope exceeds 3 degrees, the coverage generally decreases and variable sizes appear (camera run 3-1 in figure 1-17 and 1-8 in figure 1-16). Local changes in slope are correlated with changes in coverage. Especially depressions of the order of 50-300 m across are related to a reduction in nodule concentration although all of site 'E' is rather flat and well sedimented. The missing nodules and the thicker sedimentary layers are strongly correlated. In the smaller depressions redeposition of sediments removed nearby can result in a sediment blanket on top of the nodules, while in the large depression in the east, sliding and slumping sediments can easily bury nodules in the depression after entraining those from the slopes. This is in agreement with the

observation at several MANOP sites, where the only nodules on steep slopes are those retained by small scale irregularities of rock outcrops (Spiess and Weydert, 1984; Weydert and Zampol, 1985).

Good 4-kHz subbottom profiles are available for camera runs 1-2 to 1-8 only. For parts of the other camera runs it is possible to reconstruct the sub-bottom profiles from previous or later fish profiles collected when the fish crossed the area photographed at an earlier or later time. In all instances where sub-bottom profiles are available, the coverage decreases while the sub-bottom reflectors shoal or deepen. In (small and large) depressions i.e. where the sedimentary layers between the upper sub-bottom reflectors are thickest, the coverage is generally low or nodules are absent altogether (camera runs 3-2 and 4-1 in figure 1-17). No relationship between the nodule distribution and the depth of the upper acoustic reflector could be observed by comparing different areas with acoustic reflectors parallel to the sea floor. From this it can be concluded that nodules grow best on stable sediments, i.e. in areas where sediments are not removed after they had been deposited, and which do not act as sinks for sediments originally deposited in the vicinity. Although M. Karas observed a higher number of nodules at the foot of a slope exceeding 17 degrees (Karas, 1978), there is no evidence at site 'E' of a similar effect for smaller slopes. This suggests that M. Karas actually observed nodules which had rolled down the slope.

There are also rather flat areas where the number of nodules is lower than in the surroundings. Also, in camera run 3-1 (figure 1-17A) the coverage remains constant in the topographic low crossed at 04:30 GMT. No information about the sub-bottom reflectors is available for this part of the survey area so that it is not possible to check if they remain parallel to the sea floor as on camera run 1-4 at 15:00 GMT.

BURIED NODULES

Assuming that nodules exceeding a certain length do have the same probability of being buried and they grow at the same average growth rate g , the number of surface nodules of a size $D > D_o$ is given by

$$\ln N = \ln N_o - \frac{b}{2g}(D - D_o) \quad (1-14)$$

where N is the number of nodules of diameter D per unit area, N_o is the number of smallest nodules (diameter D_o) per unit area, b is the burial rate (nodules per m.y.) and g is the growth rate in mm per m.y. (Heath, 1979). In figure 1-13, a plot of $\ln N$ as a function of the longest horizontal axis for 10 mm intervals with a linear fit is shown. (Average horizontal axes lead to smaller growth rates.) The slope

$$\theta = \frac{b}{2g} = 0.06 \frac{1}{\text{mm.}} \quad (1-15)$$

Assuming a sedimentation rate of 1.5 m/m.y. (Heath and Van Andel, 1973), we find from the Echo 1 box cores

$$\tilde{b} = \frac{\text{number of buried nodules per m.y.}}{\text{total number of nodules}} = \frac{0.03}{0.3} \frac{1}{\text{m.y.}} \quad (1-16)$$

From figure 1-11, $\theta = 0.06$ 1/m.m. Using $b = \tilde{b}$ in θ , we find a growth rate of $g = 0.8$ mm/m.y. This is an unrealistically low growth rate. Assuming the nodules have been growing to an average 60 mm in 25 m.y. (oldest sediment on top of the underlying basalt), we find a minimum growth rate of $60/25 = 2.4$ mm/m.y. As nearly all of the buried nodules were found between 5 and 22cm depth, it is unlikely that box cores which penetrated 45 cm in the sediments, did not reach deep enough to sample the buried nodules adequately. Unless buried nodules disappear or one does not accept Heath's assumption that each nodule has the same probability of being buried, burial cannot be the only process regulating the size distribution. Differential biological activity or unknown physical processes must be responsible for the differential growth

and/or the different sizes of manganese nodules.

Realizing that nodules can grow to over 1 cm in 1 m.y. (nodules in craters at MANOP site 'M' and 6 cm nodules in the caldera of a satellite of the seamount Jasper), it remains a mystery why there are practically no nodules larger than 20 cm. Major burial events like that 60 - 100 thousand years ago at MANOP H (Finney et al., 1984), breaking of the larger nodules or the incapacity of the biota to keep larger nodules at the surface could play a major role here.

CONCLUSION

The nodule coverage and concentration have been studied and related to the bathymetry for site 'E'. It could be shown that there is a strong correlation between changes of the thickness of the upper acoustic unit and changes in nodule coverage and size. A Gaussian with the mean diameter and the standard deviation of the diameter as parameters describes the sizes for a given homogeneous sub-area at site 'E'. Deviations from a normal distribution are small (for acoustic purposes) and must be attributed to upper and lower limits an growth of macro nodules. The three main axes of the nodules are not independent of each other and have average ratios of 1:0.8:0.5. These results will strongly facilitate the use of acoustic multi-frequency techniques to assess the nodule coverage in possible deep sea mining areas (Spiess and Weydert, 1983).

1.2 Thirtymile Bank

1.2.1 Cruise Description

The R/V New Horizon conducted a short Deep Tow survey on the Thirtymile Bank on 9 August 1983 (Echo 2 expedition). The Deep-Tow vehicle was navigated by Loran C navigation supplemented by 12 kHz shipboard echo sounding and Deep-Tow upward and precision downward echo sounding (figure 1-18). Besides the side-looking sonar and backscatter sonars (9 - 163 kHz only), the 4-kHz-subbottom profiler was used continuously and some 200 bottom photographs were taken with television and still cameras.

1.2.2 Site description

The Thirtymile Bank is located in the California Borderland at $32^{\circ} 40'N$, $117^{\circ} 45'W$, some 55 km from the mainland. The bank top is roughly 400 m below the sea surface (figure 1-19). The bank top is in general rather flat, except for two terrace-like steps the fish crossed at 4:45 and 6:45 respectively. The sea floor is highly inhomogeneous, and is formed of outcropping rocks and of sediments which vary in size from coarse sands to muds. The sediments are dominated by pelagic carbonates and contain abundant glauconite and phosphorite, minor amounts of weathered residual or relict grains and little organic matter. (Emery, 1960) The outcropping rocks are metamorphic schists, gneisses and quartzites on the Thirtymile Bank. All Deep-Tow photos show rock fragments. There is an alternation between areas with large phosphorite slabs and mostly angular and subangular fragments (figure 1-20A) and areas with few rounded pebbles and phosphorite nodules, which cover sometimes less than 5% of the sea floor (figure 1-20B). The rounded pebbles and nodules are probably allochthonous. Side-looking sonar records show that the area passed between 5:15 and 5:45 GMT is the only one without scattered rocks. This one must be very limited in

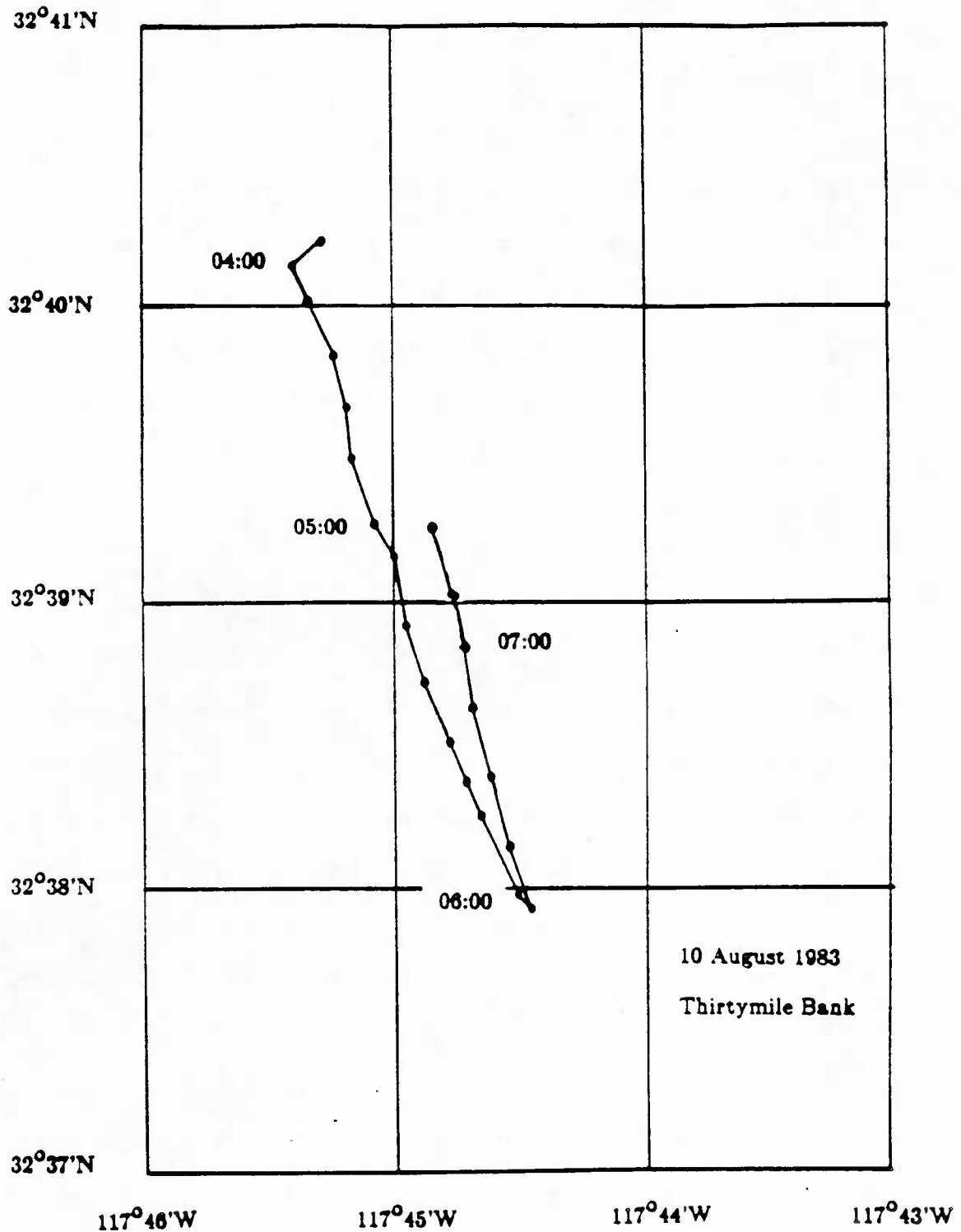


Figure 1-18. Ship track at Thirtymile Bank

Ship track during survey at Thirtymile Bank. The fish is only a short distance behind the ship and follows in this shallow water the ship rather well. The backscatter run was from 4:45 to 6:05 GMT and the camera run from 6:30 to 7:35 GMT.

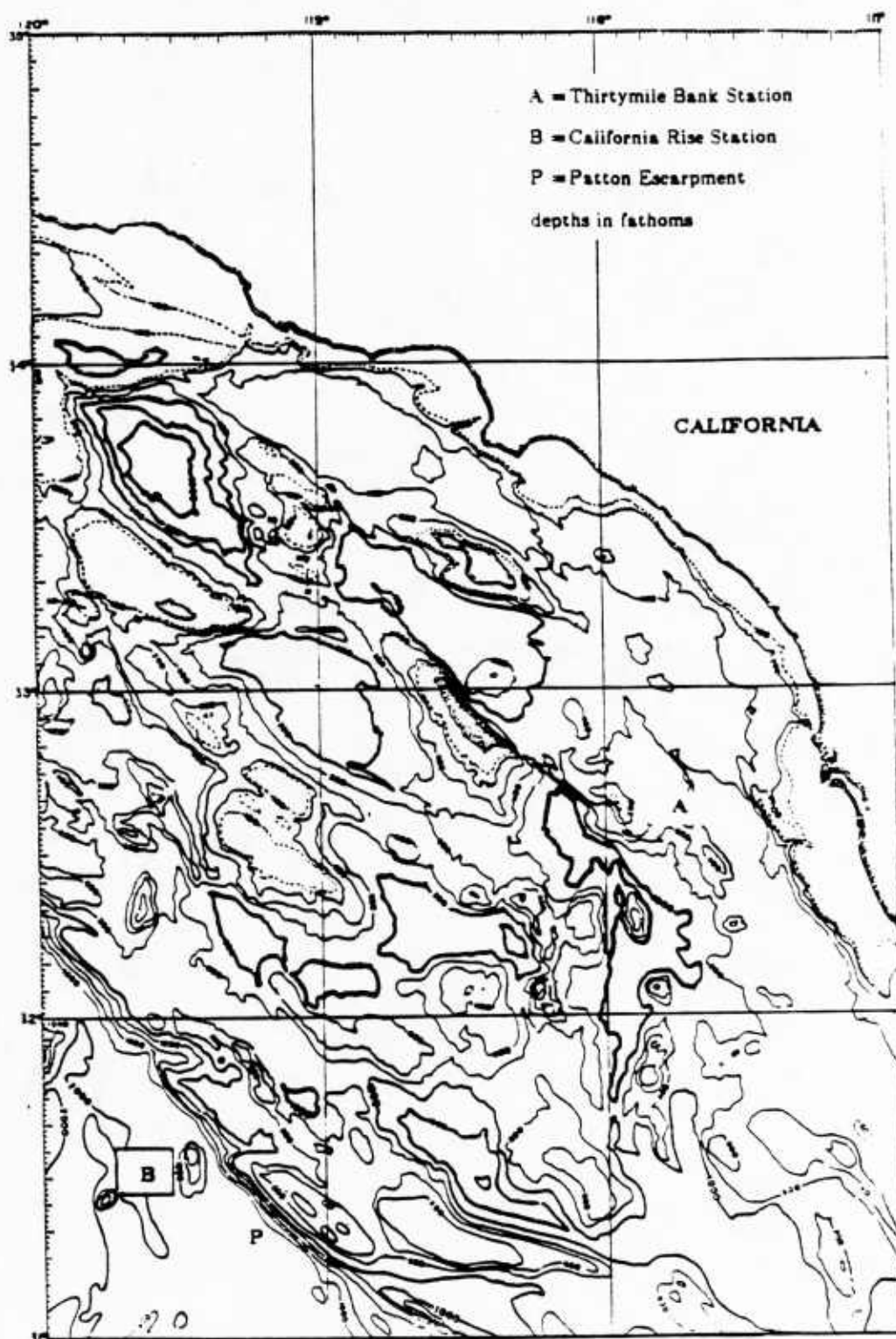


Figure 1-19. Map with Thirtymile Bank and Patton Escarpment

Bathymetry of California Borderland with Thirtymile Bank (A) and California Rise station (B) at foot of Patton Escarpment (P)

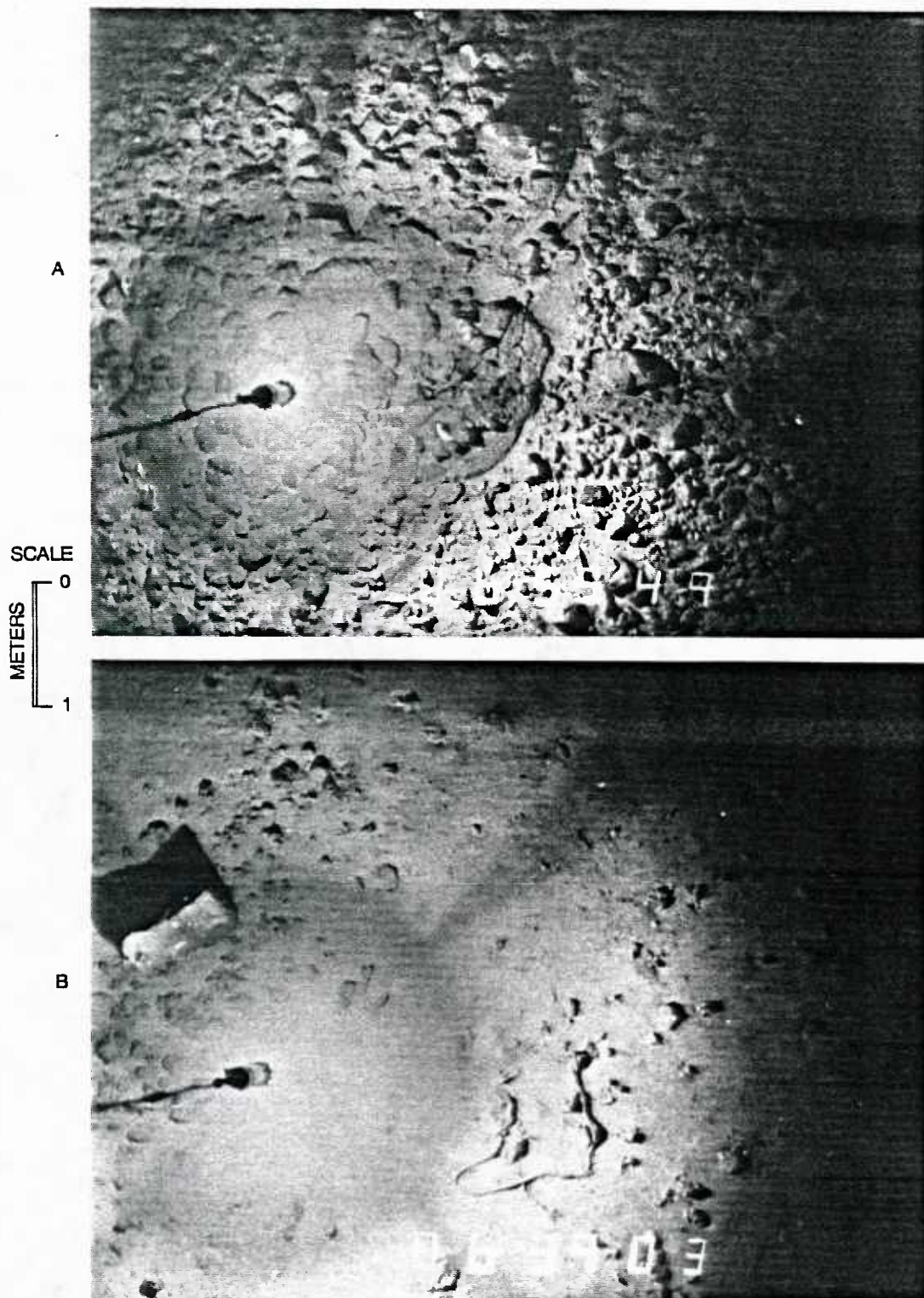


Figure 1-20. Photographs of sea floor at Thirtymile Bank

Deep-Tow photographs of Thirtymile Bank: A) Area densely covered with phosphorite slabs and nodules. Fragments are mostly angular and sub-angular. B) Area with few rather rounded pebbles, interspersed with mud formations of biological origin.

range as the photographs taken a few hundred meters away at 6:30 GMT exhibit very dense phosphorite coverage.

1.3 Base of Patton Escarpment

1.3.1 Cruise description

The last site surveyed with the backscatter system was the deep sea floor at the base of the Patton Escarpment at $31^{\circ} 30'N$, $119^{\circ} 40'W$ (California Rise station, 10 to 12 August 1983)(figures 1-19 and 1-21). Two transponders were launched in a water depth of 3700 m at the foot of the Patton Escarpment (figures 1-21 and 1-22). 500 photographs were collected during a 4-hour camera run to document the sea floor. Two backscatter runs, one at 70 m and one at 30 m above the sea floor followed (figure 1-22). The photographic and backscatter data were supplemented with the usual sub-bottom profiles, side-looking sonar imagery, transponder navigated vehicle position (except for the last lowering where the ship positions were determined using Loran C), vehicle depth and height as well as precision bathymetry along the fish path. Contrary to the Echo 1 expedition and the rest of the Echo 2 expedition, the bathymetry, vehicle depth and vehicle height were not digitized. (The real time grey scale records are available.)

On 26 May 1983, the R/V T.Washington drove over the area of the California Rise station when she came back from the Pascua 5 expedition. Thus it was possible to use the sea beam multi-beam echo sounder of the R/V T.Washington to generate a bathymetry map (figure 1-21 **).

1.3.2 Site Description

The site at the foot of the Patton Escarpment had been selected because the sediments were expected to be intermediate between near-shore sands, silts and carbonates and deep sea clays as those of site 'E'. To the west of the Patton Escarp-

**) I thank P.F. Lonsdale for providing this map.

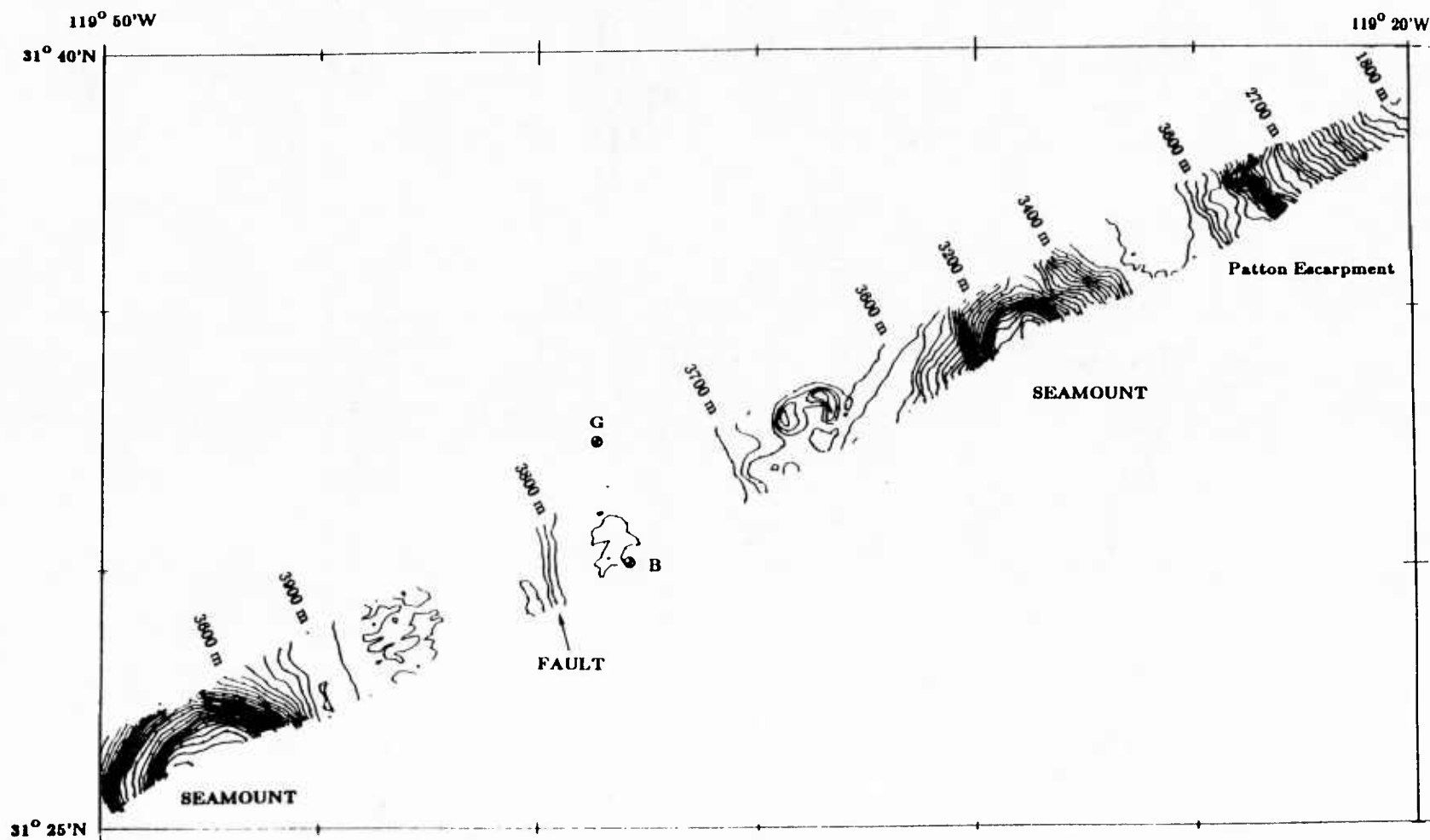


Figure 1-21. Bathymetry at station at foot of Patton Escarpment

Bathymetry of the Patton Escarpment and the Deep-Tow area. The transponder positions are shown. The contour spacing is 50 meters. The Patton Escarpment (continental slope) is in the east, the Deep Tow area with the fault is between the two seamounts.



Fish track at California Rise station at the foot of the Patton Escarpment. The camera runs and the backscatter runs as well as some times (GMT) have been annotated.

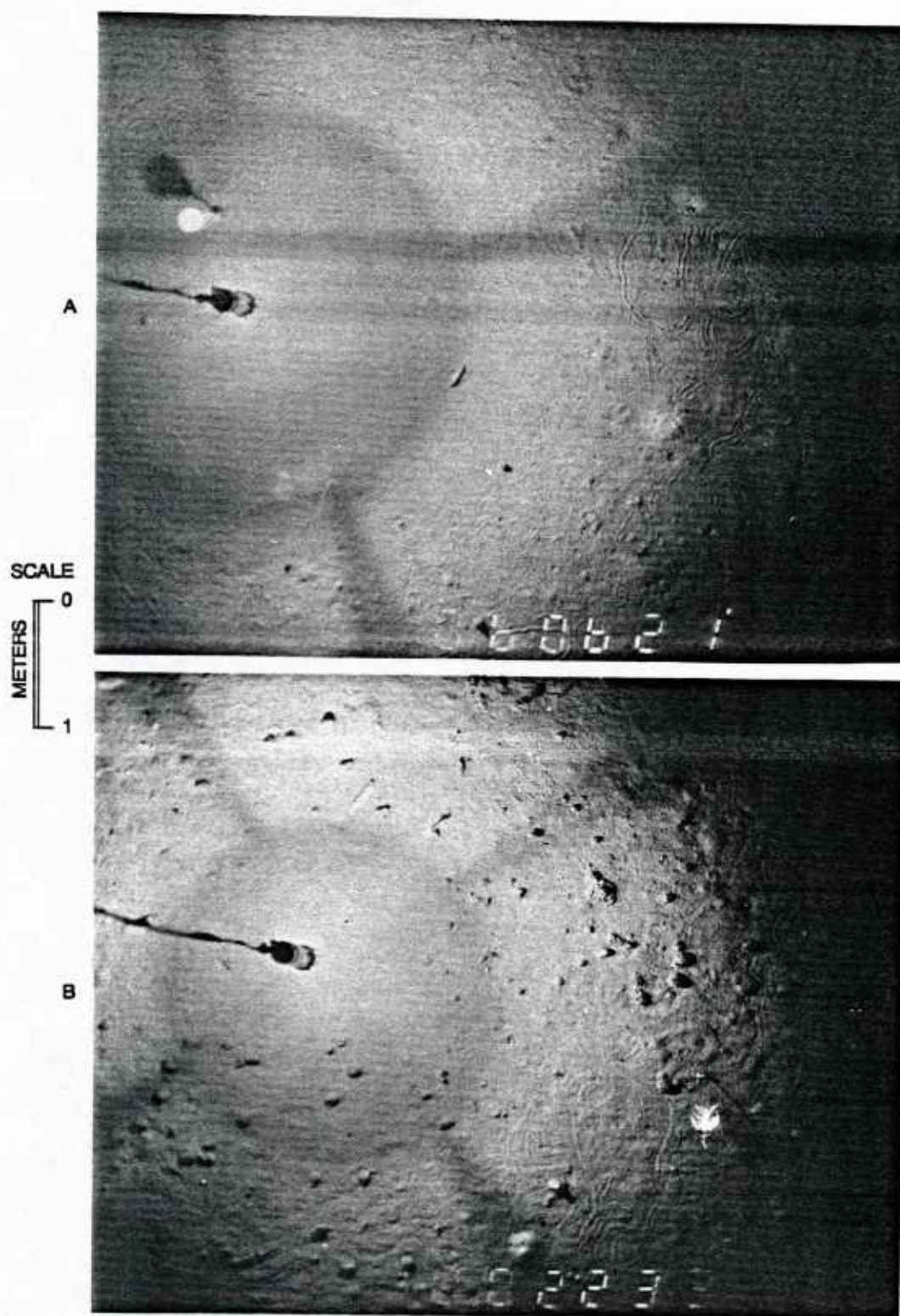


Figure 1-23. Typical photographs of sea floor at foot of Patton Escarpment
The rounded objects in B) are thought to be mud balls of biological origin.

ment, the sea floor is flat, with parallel sub-bottom reflectors and only occasional outcrops and seamounts (figure 1-24 and Yeats and Haq, 1978). DSDP hole 469 is located at the foot of the Patton Escarpment at $32^{\circ} 37'N$, $120^{\circ} 33'W$, in a water depth of 3790 m, at a comparable distance from the Patton Escarpment as the California Rise station (Yeats and Haq, 1978). All previous studies (Emery, 1960, Yeats and Haq, 1978) have found the area to be rather uniformly covered with a mixture of silt and clays. The upper 42 meters cored by DSDP (Quaternary) are silty clay with minor amounts of nannofossil and foraminiferal ooze. Pliocene and lower Miocene sediments follow downward. A sedimentation rate of 25 m/m.y. was estimated for the Quaternary. The sound velocity varies from 1.26 to 1.64 km/sec with an average of 1.50 km/sec. The density of the sediments is between 1.40 and 1.83 g/cm³ with an average of 1.60 g/cm³. In general the upper 42 m are rather uniform and present an excellent survey area for acoustic backscatter measurements.

The California Rise station is located on the deep sea floor half way between two seamounts, one at the N-E and one at the S-W end (figures 1-19 and 1-21). Deep-Tow photographs of the sea floor confirm that the sea floor is smoothly covered with sediments (most likely silts and clays). Common burrows and furrows and occasional rounded, nodule like mud forms can be recognized (figure 1-23). The area is in general flat and the acoustic sub-bottom reflectors are parallel to the sea floor. A strong sub-bottom reflector at a depth of about 10 meters is followed by at least three more reflectors. The acoustic basement could not be reached with the Deep-Tow sub-bottom profiler. In the very center, however, is a fault of unknown age (figures 1-21 and 25). The eastern part of the sea floor is some 200 meters higher than the western part. To the east erosion has thinned the top sedimentary layer. The erosional agent which is most likely a current parallel to the fault has removed the top acoustic layer down to the first strong sub-bottom reflector near the fault i.e. where such a current

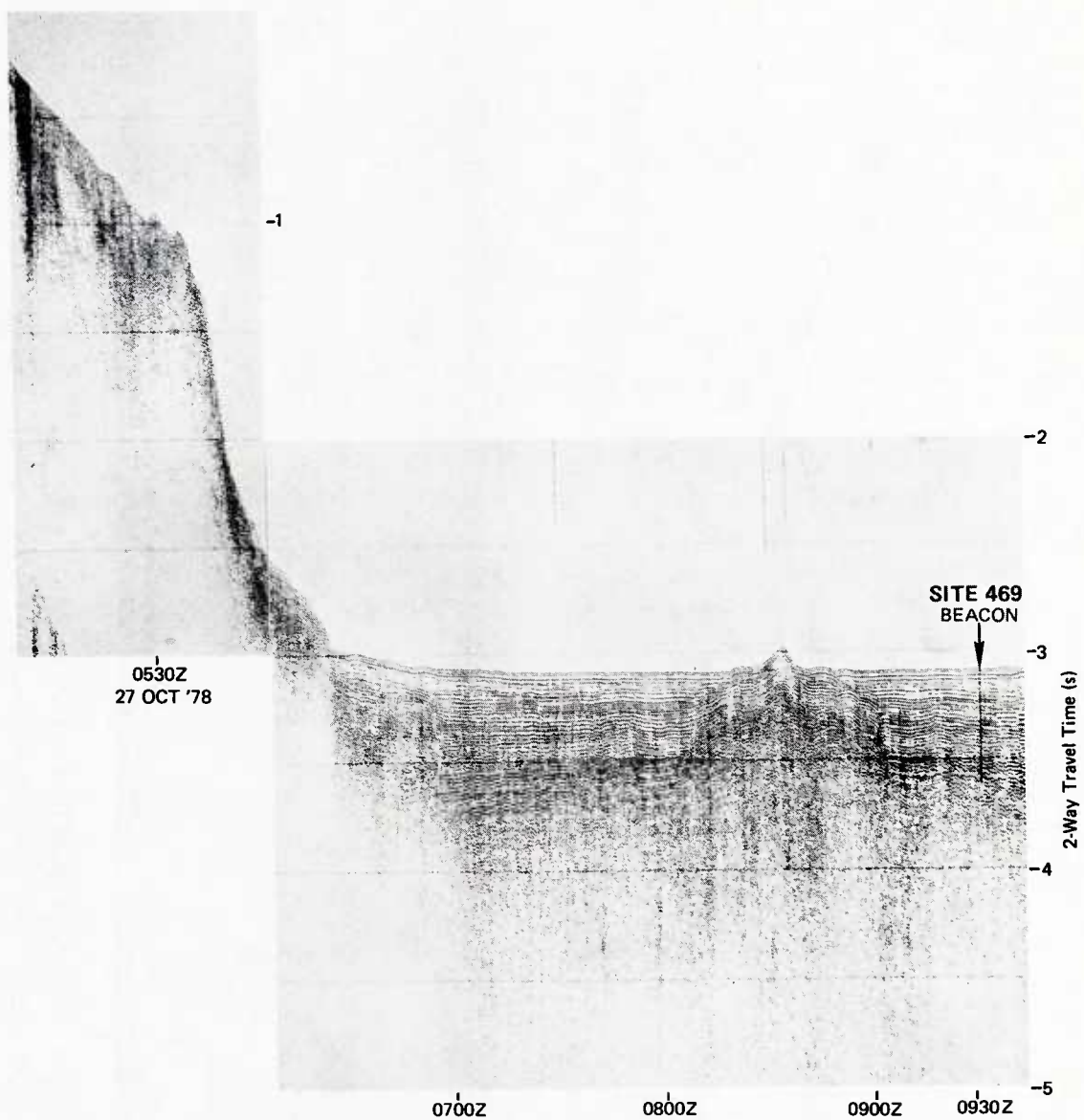


Figure 1-24. Air gun record at DSDP site 469

Air gun record of Glomar Challenger as she approached DSDP site 469 (from Deep Sea Drilling Project).

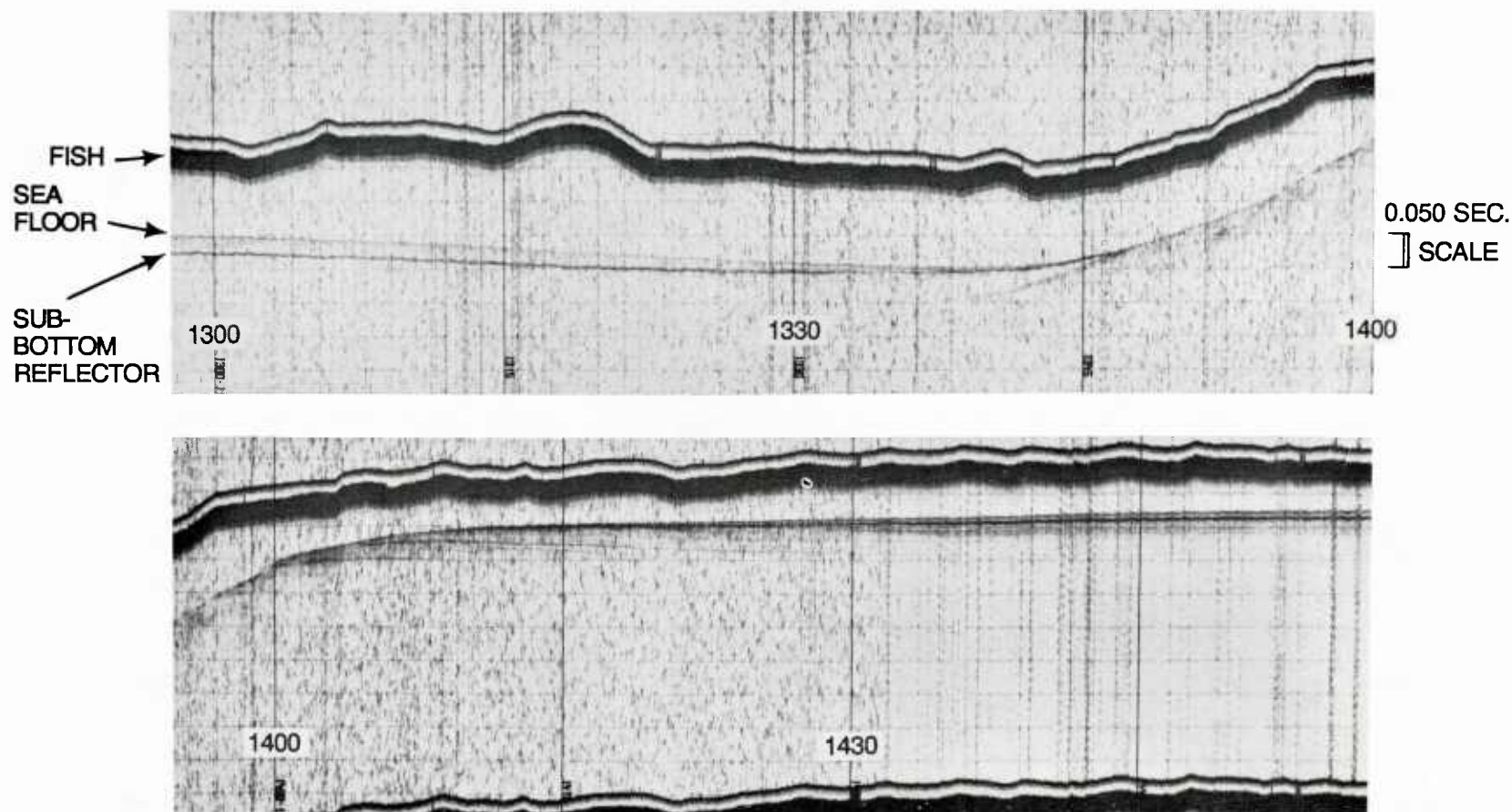


Figure 1-25. Sub-bottom profiles near fault at foot of Patton Escarpment

4 kHz record taken with the Deep-Tow sub-bottom profiler as the fish crossed the fault in the center of the survey area. No acoustic basement can be recognized. The uppermost strong sub-bottom reflector is thought to be made of some material which is a good reflector and difficult to erode (chalk e.g.). A bottom current parallel to the fault is thought to be responsible for the erosion of the upper acoustic unit in the eastern part. Note that the upper acoustic units reach a constant thickness to the east and west.

is expected to be strongest. Further away from the fault, the upper sedimentary layer becomes gradually thicker until it reaches a thickness of about 20 meters to the west and 10 meters to the east. Although it is exposed near the fault, the first major sub-bottom reflector has not been broken by the erosion. This indicates that it is the boundary between the silts and clays and some harder sediments, most likely carbonates (compare Yeats and Haq, 1978).

Appendix 1-1

Chronological Synopsis for expedition Echo 01

04-June-83	1100 GMT	Leave San Diego
06-June-83	17:40 GMT	Test Deep Tow Cable
07-June-83	19:45 GMT	Test Seals of FISH 5
10-June-83	02:00 GMT	Launch 4 Transponders
	10:35 GMT	Launch FISH 5 (lowering 1)
	23:35 GMT	Start Camera run 1
	07:45 GMT	First Miner Tracks on SLS
	09:55 GMT	End Camera Run 1
	12:30 GMT	Start Backscatter(Test)
	16:00 GMT	Start Backscatter(Data)
13-June-83	13:20 GMT	End Backscatter Run 1
	15:05 GMT	FISH 5 on deck
	19:00 GMT	Start Box Coring
15-June-83	03:00 GMT	End Box Coring
	08:45 GMT	Launch FISH 5 (Lowering 2)
	15:00 GMT	Start Backscatter Run 2
16-June-83	04:00 GMT	End Backscatter Run 2
	10:00 GMT	FISH 5 on deck
	20:00 GMT	Launch FISH 5 (lowering 3)
17-June-83	03:25 GMT	Start Camera Run 3
	13:25 GMT	End Camera Run 3
	15:25 GMT	Start Backscatter Run 3
	20:25 GMT	Fish high in water
	20:30 GMT	End Backscatter Run 3
	21:50 GMT	FISH on deck (End lowering 3)
18-June-83	03:00 GMT	Start Box Coring
19-June-83	11:45 GMT	End Box Coring (13 B.C.)
	15:45 GMT	Launch FISH 5 (Lowering 4)
	18:00 GMT	Start Backscatter run 4
20-June-83	08:00 GMT	End Backscatter Run 4
	08:40 GMT	Start Camera Run 4
	12:10 GMT	End Camera Run 4
	13:15 GMT	Start Backscatter Run 5
21-June-83	04:46 GMT	Cable breaks : FISH 5 lost in 4500 m depth
	07:00 GMT	Start Box Coring
	12:00 GMT	End Box Coring
	18:25 GMT	Start Recovery FISH 5
23-June-83	02:30 GMT	FISH 5 back on deck
	08:55 GMT	Start Box Coring
	20:00 GMT	End Box Coring
	20:00 GMT	Recall Transponders
24-June-83	05:45 GMT	Underway to San Diego

Appendix 1-2

Chronology for expedition Echo 02

9 August 1983	15:05 GMT	Underway from San Diego
9 August 1983	19:15 GMT	Arrival Thirtymile Bank
9 August 1983	20:25 GMT	Launch Fish 5
9 August 1983	23:35 GMT	Fish back on board
10 August 1983	03:45 GMT	Start lowering 2
10 August 1983	04:45 GMT	Start backscatter (15 fms)
10 August 1983	06:05 GMT	End backscatter 1
10 August 1983	06:30 GMT	Start camera run 2
10 August 1983	07:34 GMT	End camera run 2
10 August 1983	08:00 GMT	Fish on deck
10 August 1983	19:45 GMT	Arrival at "Cal. Rise"
10 August 1983	20:30 GMT	Launch transponders
11 August 1983	05:58 GMT	Start camera run 3
11 August 1983	09:53 GMT	End camera run 3
11 August 1983	11:46 GMT	Start backscatter 2 (40 fms)
11 August 1983	16:48 GMT	Start backscatter 3 (15 fms)
11 August 1983	19:51 GMT	Fish 5 back on deck
11 August 1983	21:00 GMT	Recall transponders
11 August 1983	23:46 GMT	Lowering 4
12 August 1983	02:10 GMT	Start backscatter 4
13 August 1983	07:43 GMT	calibration at 500 m above bottom
13 August 1983	09:44 GMT	End lowering 4
14 August 1983	00:00 GMT	Start Seamount Survey
27 August 1983	15:45 GMT	End Seamount Survey
28 August 1983	03:00 GMT	Arrival at San Diego

CHAPTER II In situ backscatter measurements

2.1 Introduction

The primary goal of this work was to measure the acoustic properties -especially the backscatter coefficients- of the deep sea floor, and to learn how to determine manganese nodule concentrations acoustically.

The approach for the acoustic survey of nodule fields was to mount 5 transducers (analog side-looking sonars) on the deep tow vehicle "FISH 5" of the Marine Physical Laboratory of the Scripps Institution of Oceanography (figure 2-1). They were designed to operate at a total of 7 frequencies namely 4.5, 9, 15, 28, 60, 112 and 163 kHz. The size of the transducers was chosen so as to fit on the stern of the vehicle and to allow at a range of a few hundred meters for spatial resolutions from a few square meters at 163 kHz up to a few hundred square meters at 4.5 kHz. At the high frequency end, the return should strongly fluctuate in sparsely covered areas, thus making statistical analysis possible.

No attempt was made to resolve individual nodules as this is best done with existing still photography or real time television.

The frequency range must be large enough so that you can easily discriminate between different nodule sizes and coverages. This was well achieved, as a range from 4.5 to 163 kHz allows for a ka (wave number times radius) from 0.1 to 70 for nodules from 1 cm to 20 cm in diameter. Assuming the nodules are hard spheres, 4.5 kHz is always in or at the limit of the region of Rayleigh scattering, while 163 kHz always means geometric scattering.

If the nodule coverage is not prohibitive, it will be possible to see into the sediments with 4.5 kHz and 9 kHz, and to detect buried nodules which cannot be seen

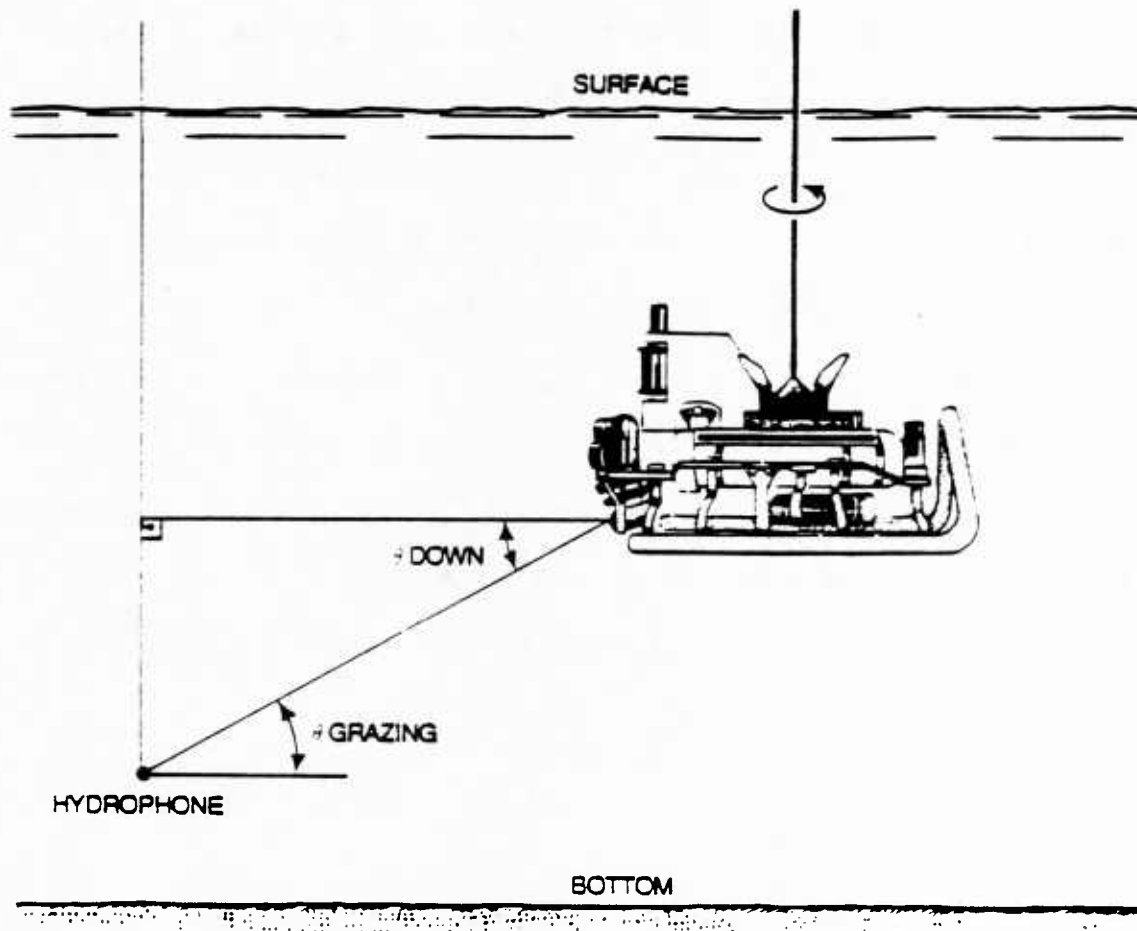


Figure 2-1. Geometry for calibrations

The fish with the backscatter transducers is mounted on a turn table. The standard hydrophone is lowered at a predetermined distance to the depth corresponding to the grazing angle θ . The geometry is such that reflections from the surface or the bottom arrive after the direct pulse.

optically. This is especially interesting where large amounts of nodules are covered by a few cm of sediments.

Measurements of the acoustic backscatter in different parts of the ocean would allow us to determine the backscattering strength as a function of frequency for different deep sea environments.

It was desired (but not achieved) that the beams should be fan shaped and well behaved in the vertical. Thus it would be possible to identify any arrival with a particular range, grazing angle and patch of the sea floor.

The associated electronics (drivers, amplifiers, pulse and frequency generators) were designed to match existing Deep-Tow electronics, although the backscatter electronics were installed in an extra pressure case. Both an adjustable gain and a time-varied gain were built so that the dynamic ranges could be adjusted as a function of time according to the strength of the incoming signal.

2.2 Instrumentation

2.2.1 Description of backscatter transducers

The backscatter transducers are 5 PZT-4-transducer arrays, similar to those used as side-looking sonars, but looking aft. Although all arrays had reasonable sidelobes in the horizontal (plane including longest axis) and smooth vertical beam-patterns in the aft direction before they were mounted on the vehicle, their beam-patterns changed substantially when they were mounted on FISH 5 (chapter 2.2.2.2). They are operated at the already mentioned nominal frequencies of 4.5, 9, 15, 28, 60, 112, 163 kHz. They are mounted with a simple ladder like frame on the stern of FISH 5 (Spiess and Lonsdale, 1982). The transducers are nearer to the center of the fish the lower they have been mounted. (figure 2-2). This configuration allows for minimal interference of the transducers with each other as well as with the deep tow vehicle.

a.) 4.5 and 9 kHz

The transducers ITC 3253-1 to -5 are radially polarized, free flooded 12 cm x 10 cm PZT-4 cylinders which are operated in the k_{31} -mode. They are mounted together as an array shown in figure 2-2.a on a stainless steel plate. The spacing between the centers is 15.5 cm. This configuration was chosen after several others with 4 or 5 transducers had proved to have unsatisfying beam-patterns. After the impedance had been measured as a function of frequency, and several beam-patterns between 4 and 12 kHz were made, the transmission frequencies were chosen as 4474 Hz and 8984 Hz.

While the beam-pattern at 4.5 kHz was good enough to transmit and receive on this array, we decided to use the transducer ITC 6094 to receive at 9 kHz (see sub 60 kHz).

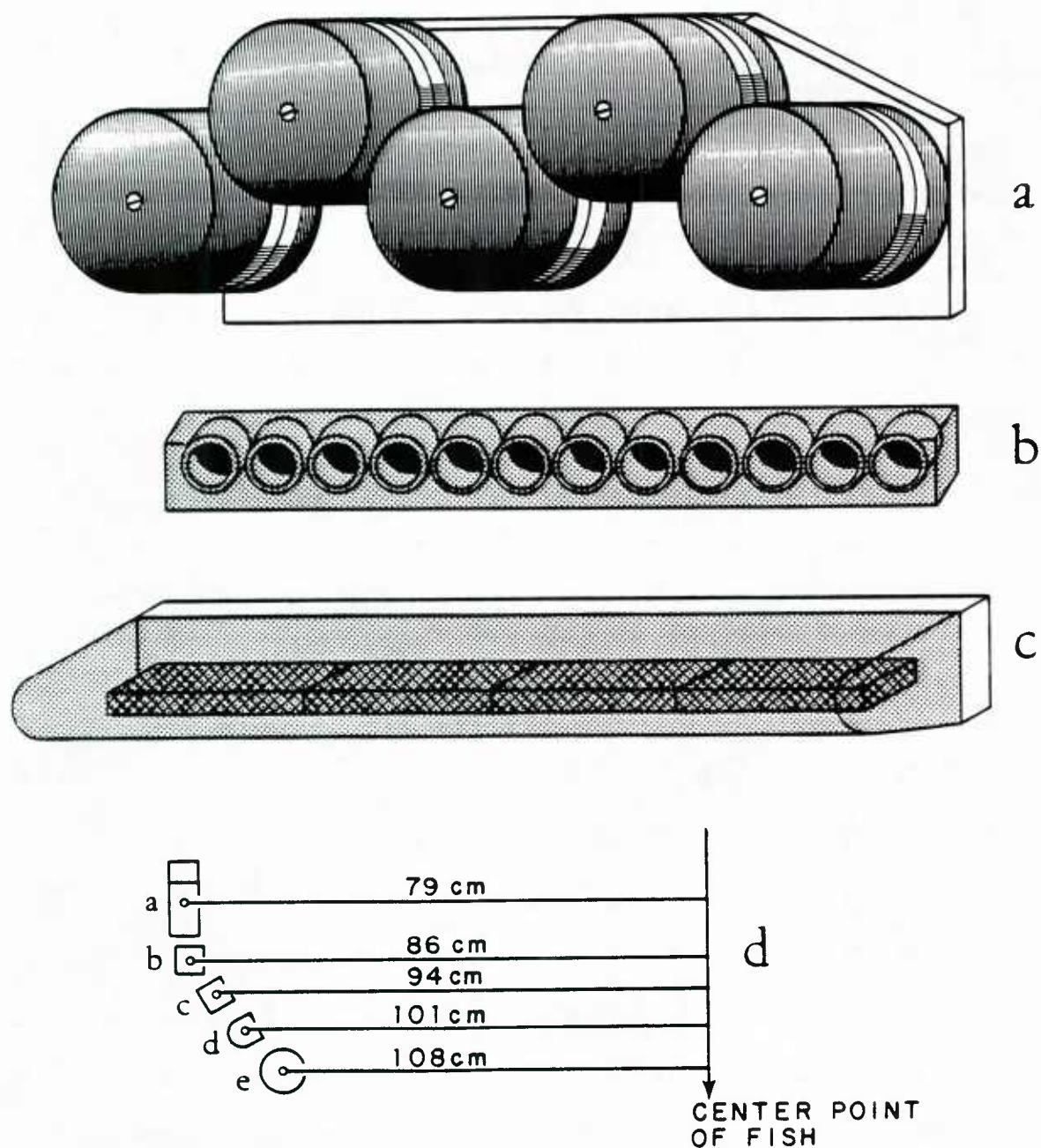


Figure 2-2. Schematics of transducer arrays

a) ITC 3253 S/N 1 to 5. The five PZT-4-transducers with the serial numbers 1-5 are mounted in an array as shown in the figure. Serial number 1 is the middle one in the upper row. This transducer array is used at 4.5 and 9 kHz.

b) ITC 6093 S/N 1. This transducer array is made out of 12 PZT-4 cylinders. It is used at 15 and 28 kHz.

c) The transducers ITC 6094 (60 kHz and 9 kHz), MPL 83-1 (112 kHz) and Teleprobe (163 kHz) are made of PZT-4 bars as shown in this figure.

d) The 5 transducers are mounted on ladder-like frame on the stern of the fish. a) 4.5 and 9 kHz, b) 15 and 28 kHz, c) 60 kHz, d) 163 kHz, e) 112 kHz.

b.) 15 and 28 kHz

The transducer ITC 6093 is a line array of twelve 3.5 cm long PZT-4 cylinders with a diameter of 1.9 cm mounted on a 54.5 cm x 5 cm stainless steel backplate and surrounded by a polyurethane (figure 2-2.b). Each cylinder is radially polarized and operated in the k_{31} -mode. The operating frequencies are 14914 Hz and 27965 Hz. Operating this transducer at lower frequencies would mean a substantial drop in transducer response as the cavity resonance is right below 15 kHz.

c.) 60 kHz

The transducer ITC 6094 is a 53.2 cm x 5 cm line array of forty 1.1 cm x 1.1 cm x 2.5 cm PZT-4 bars. These bars are $\lambda/2$ -resonant in the thickness mode at 60 kHz. The spacing between the reflector plate and the ceramics is $\lambda/4$ (figure 2-2.c). It has been mounted at a downward angle of 30 degrees on the stern of Fish 5 in order to increase the useful power. Its operating frequencies are 59657 Hz and 8984 Hz (latter for receiving only).

d.) 112 kHz

The transducer MPL-83-1 (operated at 111857 Hz) (figure 2-2.c) is made out of eight 7.6 cm x 1.3 cm x 0.6 cm PZT-4 bars, surrounded by an oil pocket inside a polyurethane boot. The backplate is a 1.3 cm x 12.7 cm x 56 cm stainless steel plate.

e.) 163 kHz

The Teleprobe transducers (figure 2-2.c) are 28 cm long PZT-4 bars (one 150 kHz unit and one 160 kHz unit) mounted on a stainless steel backplate. On the expeditions Echo 1 and Echo 2, only the starboard transducer (160 kHz unit) was operated at a frequency of 162702 Hz. Both are tilted 15° downward in order to increase the useful power.

2.2.2 CALIBRATION

The calibration of a transducer is essential to making acoustical measurements. The acoustical power, transmitted or received, has to be related to directions in space and to electrical currents and voltages. This can only be achieved if one knows the transmitting and receiving responses for all frequencies of interest as well as the corresponding beampatterns in three dimensions. In addition, it is important to know the electrical impedance of the transducer if one wants to match the electronics to the transducer. That allows one to get only real, single frequency power into the transducer. Electrical power coming out of a hydrophone is amplified, attenuated and filtered by electronics which also require calibration.

In the following the different calibrations made will be described and their results discussed.

2.2.2.1 CALIBRATION OF ELECTRONICS

2.2.2.1.1. Introduction

In order to relate the output voltage at topside to the sound pressure at the hydrophone, the response of the electronic network must be known in addition to the hydrophone response.

The transducer transforms the incoming sound wave into a voltage, which passes through a TR-switch, some fixed preamplifiers, adjustable time-varied gains (TVG) and adjustable receiver gains, before it is modulated and sent over the 125 kHz channel of the 9000 m long deep tow wire to the the laboratory on board the ship (figure 2-3). At top side, the envelope is generated and digitized.

To keep track of eventual transmit power problems or failures of the electronics, and of the transmit voltage itself, a scaled down version of the transmit pulse

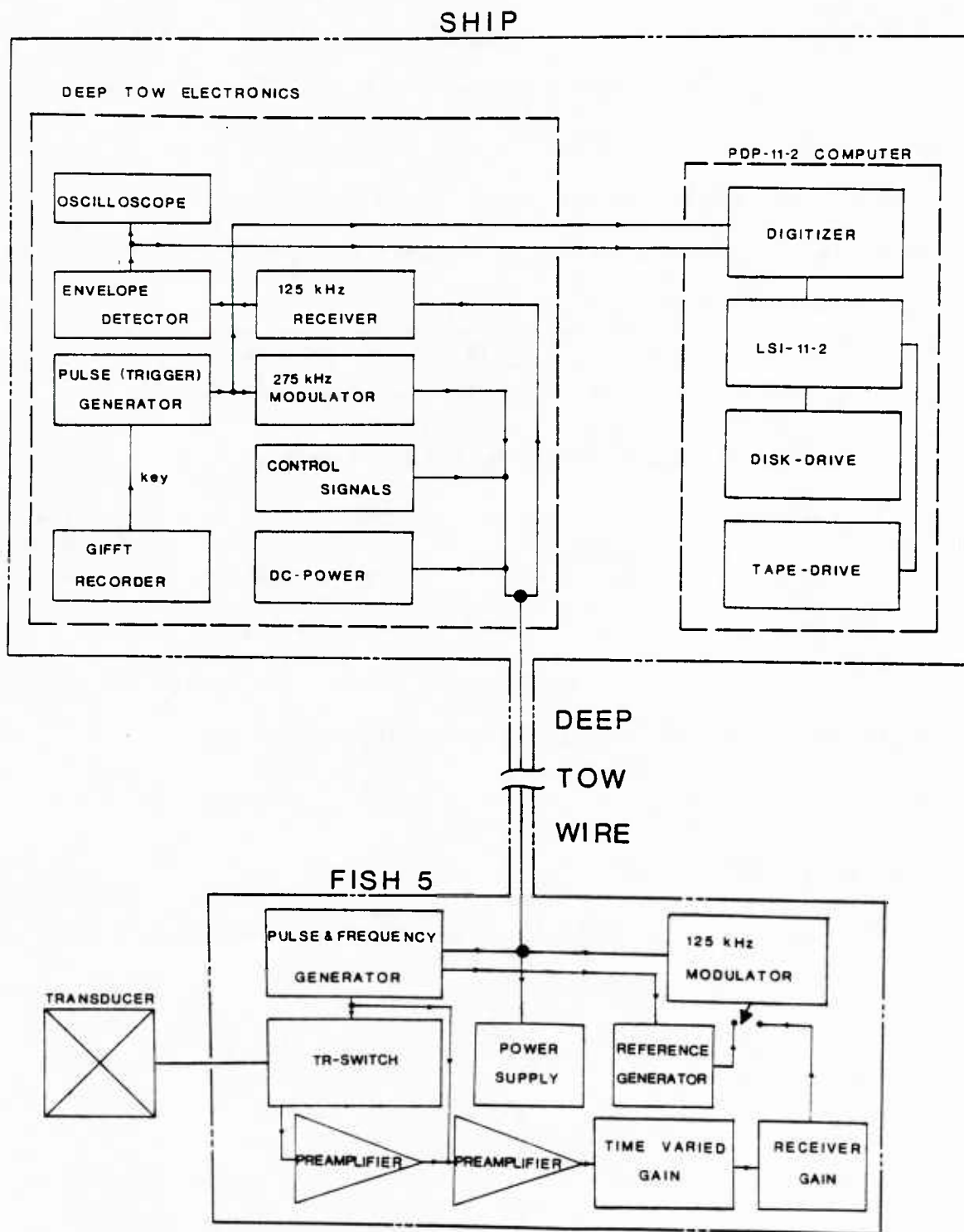


Figure 2-3. Backscatter electronics

The electronics used during the backscatter measurements is sketched here as it is divided into deeply towed electronics (inside pressure cases on FISH-5), shipboard Deep Tow electronics and a PDP-11/2 computer system to record the data. All telemetry and power passes over different channels of a single 9000 m long armoured power cable

is sent up the wire, after it has passed through the second preamplifier, the TVG and the receiver gain (figure 2-3). Both the transmit pulse and the received signal are compared to two identical reference pulses, which are inserted after all the preamplifiers, but before the modulator and the deep tow wire (figure 2-3). The reference pulses are 1 ms wide and identify the frequency by the spacing between them, which are given in table 2-1:

frequency (kHz)	4.5	9	15	28	60	112	163
spacing (ms)	0	1	2	3	4	5	6

Table No. 2-1: Spacing between reference pulses.

Thus two sets of electronic system calibrations must be done for each frequency: 1.) The transmit voltage must be determined as a function of the ratio of its scaled down version to the reference pulse and the adjustable gains (sub 4).

2.) The transducer output voltage must be related to its ratio with the reference pulses as a function of the gain settings (sub 2 & 3).

2.2.2.1.2 TIME-VARIED-GAIN

The time-varied gain control (TVG) is a 10 bit integrated AD7520 (basically an R-2R ladder) with the least significant bit tight high and the other bits controlled by a clocked shift register. The received signal is attenuated by

$$\frac{2^N - 1}{2^{10} - 1} \quad (2-1)$$

where N is the number of bits set. The clock generates pulses at intervals which are integer (1 to 15) multiples of 10 ms. The following attenuations are applied to the received signal, each of them for the same integer multiple of 10 ms: -60.2, -50.7, -43.3, -36.7, -30.4, -24.2, -18.1, -12.1, -6.0, 0.0 dB.

An extra step of -60.2 dB is inserted at the moment the TVG clock starts, while the last step lasts until the next transmission is started.

On the expeditions Echo 1 and 2, the TVG clock has always been started together with the transmit pulse, although a delay can be added.

Three sets of measurements were made to calibrate the TVG:

- 1.) The noise was measured at sea for all TVG steps, with the gains set for the measurements at that time (see chapter on noise).

- 2.) The input voltages were measured in the laboratory for receiver gains of 1/16 or 2/16 and for the 10 TVG steps for output signal/reference ratios of 4, 0, -10, -20 and -25 dB (called table 'A'). To do this, we put a small signal at the operating frequency across the transducer terminals and read the output on the oscilloscope, after the signal had gone through all the gains, the modulator and the deep tow wire. This procedure allowed us to account for the non-linearities, especially those from the modulator.

- 3.) The changes in output levels as a function of the changes in input levels were measured for receiver gains of 1/16 or 2/16 and for TVG = -60.2 dB and TVG = 0 dB at output signal/reference ratios of -25 dB, -20 dB, -15 dB, and then at 1 dB steps from -10 dB to 10 dB (same method as sub 2.)). In general, the system is saturated for output signal/reference ratios exceeding 5 dB (limit of the modulator/demodulator system). Therefore, those data are not used. These last measurements have been regrouped by linear interpolation as changes in input levels as a function of changes in output levels (called table 'B'). This saves a lot of computer time in the data analysis.

From the above data, the input voltage (i.e. the voltage generated by the hydrophone) in dB relative 1 Volt rms is computed by interpolation (appendix 2-1).

2.2.2.1.3 Receiver gain

The receiver gain control is an integrated 10bit AD7520 (essentially an R-2R) ladder, whose 6 least significant bits are tied high, so that the 4 most significant bits allow us to attenuate the signal in steps of 1/16 from 1/16 to 16/16 (-24.1 dB to 0 dB). Measurements showed that this gain is indeed linear. The gains measured at the various steps agree within 0.1 dB with the theoretical values. No new nonlinearities could be observed within the useful input and output voltage ranges.

2.2.2.1.4 Transmit pulse

The ratio of the scaled down transmit pulse and the reference pulse was measured for the transmit voltages and receiver gains listed in table 2-2. All measurements were made with an accuracy of 5% or better. The voltages measured in the laboratory are in good agreement with those found at sea for 4.5, 9, 15 and 28 kHz, while they deviate at 60, 112 and 163 kHz up to 20%, as if the transmit voltages were not a constant. As the voltages used at sea were well within the linear range of the system, including the digitizer of the computer, it had to be assumed that the transmit voltages really changed, which was most likely due to an impedance change with temperature and pressure. The transmit voltage at 60 kHz increased by about 20-25% while the fish was lowered from the surface to 300 meters depth. Subsequent measurements in the laboratory (compare chapter on pressure and temperature calibrations) showed that this change of the transmit voltage is real and that the impedance of the transducer as well as the transmitting response changed when the pressure was increased from 1 bar to 30 bars. The changes for the transducers MPL 83-1 (112 kHz) and Teleprobe (163 kHz) were shown to be within the manufacturer's specifications.

Along with these measurements, the system quality factor Q (number of cycles to rise to full response, center frequency/bandwidth) was determined (table 2-2).

<i>frequency</i>	<i>transmit</i> ¹⁾ <i>reference</i>	<i>transmit</i> ²⁾ <i>reference</i>	<i>transmit voltage</i>	<i>Bandwidth</i> ³⁾	<i>Q</i> ³⁾
4.5 kHz	0.30	0.31	725 V _{pp}	1120 Hz	4
9 kHz	0.64	0.64	1150 V _{pp}	2310 Hz	4
15 kHz	1.18	1.12	1300 V _{pp}	3325 Hz	4
28 kHz	0.75	0.74	875 V _{pp}	6670 Hz	4
60 kHz	1.32	1.51	1250 V _{pp}	9900 Hz	6
112 kHz	0.50	0.57	1140 V _{pp}	10140 Hz	11 ⁴⁾
163 kHz	0.96	1.22	1200 V _{pp}	9780 Hz	16

1) measured in the laboratory in July 1983

2) at sea data from June 1983

3) measured with TVG = -60 dB

4) at 112 kHz the Q changes to 14 when the TVG = 0 dB

Table No. 2-2

2.2.2.2 CALIBRATION OF TRANSDUCERS

2.2.2.2.1. Electrical impedance

We measured the admittance of the transducers as a function of frequency at current levels of a few hundred mA at the Transducer Evaluation Center (TRANSDEC) of the Naval Ocean Systems Center (NOSC) at San Diego. D. Boegeman and his engineers of the MPL, SIO, analyzed the data and built the necessary complex matching networks to drive the transducers efficiently at the selected operating frequencies.

The transmit voltages are measured at the transducer terminals, thus the matching networks need not be considered in the data analysis, and neither the admittance nor the matching networks will be discussed further.

2.2.2.2.2 Transmitting and receiving response

In any acoustic measurement, electrical currents or voltages have to be related to acoustic power. The relationships were determined with the comparison method (Urlick, 1983; Bobber, 1970; ANSI, 1972) at the TRANSDEC of NOSC, San Diego. In principle, acoustic power, transmit current and transmit voltage were measured as functions of the azimuthal angles and selected grazing angles at the already determined operating frequencies. We used a pulsed mode with the backscatter transducers as projectors and the Navy standards F37 (4.5 - 28 kHz), F41 (28 - 163 kHz) and LC10 (all frequencies) as hydrophones. For each geometry several readings were taken and found to be within 0.1 dB from each other. As the F37 was not a good source, we measured the transmitting voltage response S/V (Source level per Volt) and the transmitting current response S/A (Source level per Ampere), and calculated the receiving sensitivity by (see Bobber, 1970)

$$RECEIVING \ SENSITIVITY \ (dB) = S/A(dB) - 294 - 20 \log f \ (Hz). \quad (2-2)$$

where the S/A is in dB reference $1 \mu Pa$ per Volt at 1 meter, and the Rec. Sens. is in dB reference 1 Volt per μPa . A check at 9 kHz and 60 kHz showed that the calculated receiving sensitivity is within 0.5 dB of the measured one, as one expects for reciprocal transducers.

A first set of calibrations was made according to the standards set by the National Standards Institute (ANSI 1972) to verify the transducer quality and to study the interference between the transducers. An array configuration for the transducers used at 4.5 and 9 kHz had to be found. The only satisfying array configuration is the one shown in figure 2-2, where the spacing between the centers of the five cylinders has been selected so as to allow for a well behaved beampattern. For this set of calibrations, the transducers were lowered into the tank either by themselves or together with a couple others mounted on a rigid frame. Later, the transducers were calibrated together with the whole Deep-Tow vehicle so that we could recognize the changes in the beampatterns due to the pressure cases and the frame of the fish. The Deep-Tow vehicle with the backscatter transducers was rotated on a turn table at some 5 m depth, while the standard hydrophone was lowered to the appropriate depth at a distance of up to 22.5 m (figure 2-1). The water depth being more than 10 m, this gave us, at a distance of 20 m, about 0.5 ms pulse between the end of the longest rise time (< 1 ms) and the surface/bottom reflection.

A computer controlled 0.1 ms wide tracking gate was used to sample the envelope of the pulse between 1.0 and 1.1 ms from the beginning of the pulse. The computer program allowed us to keep the position of the gate fixed within the pulse, while we turned the vehicle around its axis. For a typical transducer distance of 1 m between the transducer and the axis of rotation, the gate had to be moved between 0

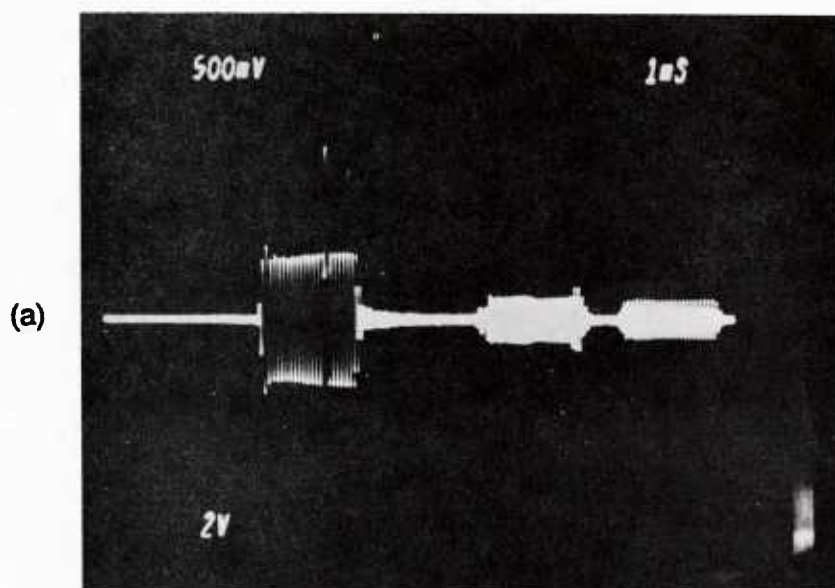
and 2.7 ms with respect to the transmit time.

Several tests were made to check the accuracy of the measurements:

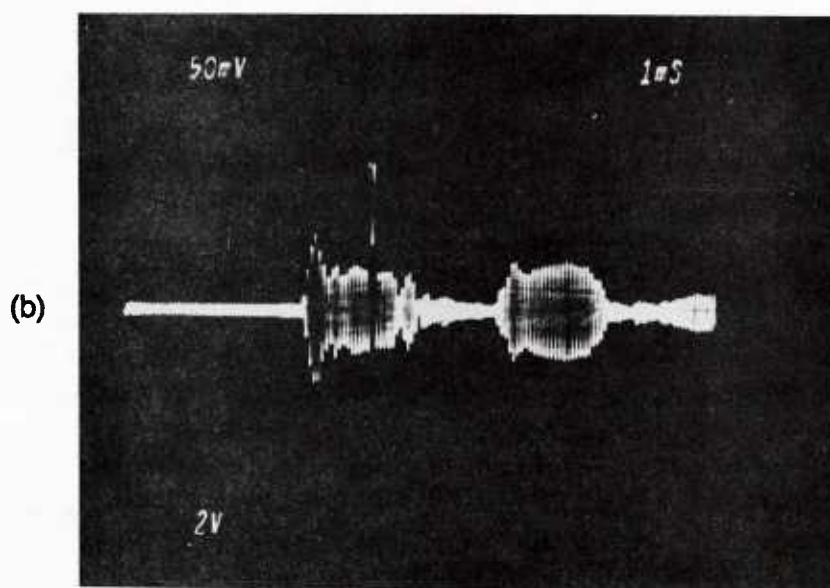
The far field is defined as the region beyond a distance $\pi L^2/4\lambda$, where L is the longest dimension of the transducer, and λ is the acoustic wavelength (ANSI 1972). Unfortunately, the deep tow vehicle is not a baffle, but an assemblage of pressure cases mounted in all directions on a heavy frame (figure 2-1). Thus, reflections from the fish as well as from the other transducers contribute to the acoustic field and can lead to complicated pulse shapes, especially at directions different from straight aft. This is well illustrated in the photo in figure 2-4b.

A repetition of some of the measurements with the hydrophone at distances varying from 8 meters to 22.5 meters from the center of rotation shows that, at least in the horizontal plane through the transducer, there is little change in source level or beam pattern as you change distance within this range (after the usual correction for spherical spreading).

Because of the different reflectors on the fish, it is not evident that the averaging over the 0.1 ms gate leads to a representative number. By moving the gate back and forth within 1.5 ms and 5 ms long pulses (not into the transient part nor into a surface or bottom reflection), we found that the determined source levels always agree within 1 dB at 4.5 kHz and 0.3 dB at the other frequencies. Off axis, the fluctuations are larger at those azimuthal angles where the S/V is 10 dB or more below the on-axis value. These fluctuations are insignificant in this context, as they do not change the effective beamwidth.



23 MARCH 1983
RUN #125
15 kHz
80° DOWN
0° HORIZONTAL



22 MARCH 1983
RUN #123
15 kHz
60° DOWN
88° HORIZONTAL

2.2.2.2.1 Source Levels and Receiving Sensitivities

Frequency	March 83	April 83	3 May 84	4 May 84	average	rms error
4.5 kHz	190.0		188.8	189.3	189.3	0.6
9 kHz	189.2		188.9	189.7	189.4	0.3
15 kHz	181.0		179.2	179.7	180.0	0.8
28 kHz		189.3	188.9	188.6	189.0	0.3
60 kHz			207.2	207.7	207.5	0.3
110 kHz		210.9	209.6	209.8	210.1	0.4
160 kHz			209.0		209.0	-----

Source/Ampere for Backscatter on Fish 5
all units are dB ref 1 uPa/A at 1 m

Frequency	March 83	April 83	3 May 84	4 May 84	average	rms error
4.5 kHz	142.9		141.5	142.5	142.3	0.6
9 kHz	146.5		146.3	147.4	146.8	0.5
15 kHz	140.0		138.6	138.9	139.5	0.7
28 kHz	153.0	153.0	152.7	152.4	152.8	0.3
60 kHz			158.4	158.7	158.6	0.2
110 kHz		165.7	165.4	165.5	165.5	0.2
160 kHz			161.4		161.4	-----

Source/Volt for backscatter mounted on Fish 5
all units are dB ref. 1 uPa/V at 1 m

Frequency	March 83	April 83	4 May 84	4 May 84	average	rms error
4.5 kHz	-177.3		-178.4	-177.7	-177.8	0.5
9 kHz				-199.1	-199.1	-----
15 kHz	-196.5		-198.2	-197.9	-197.5	0.7
28 kHz		-193.7	-194.5	-194.3	-194.2	0.4
60 kHz			-182.3	-181.8	-182.1	0.3
110 kHz		-184.2	-185.4	-185.1	-184.9	0.5
160 kHz			-189.4		-189.4	-----

Receiving Sensitivity for backscatter on Fish 5
all units are dB ref. 1 Volt/micro Pascal

Table 2-3 :Transmitting and Receiving Response for backscatter transducers on vehicle.

- 9 kHz receiving sensitivity on ITC 6094
- all sensitivities are calculated from S/A
- data may be averages over several measurements

The source levels and receiving sensitivities were repeatedly determined on several different days at temperatures from 13° to 20°C and pressures of 1 bar. The measurements were made either on axis or at a point which could be easily related to the on-axis value, knowing the beampattern. The results (corrected for vehicle tilt) are summarized for the operating frequencies in table 2-3. (other frequencies are in figures 2-5 and 2-6). The rms errors are less than 0.8 dB. (The absolute accuracy of TRANSDEC is said to be 1 dB.)

A comparison of these data with those for the free transducers (i.e. not mounted on the Deep-Tow vehicle, table 2-4), show that the on axis transducer response changes up to 4 dB when the transducers are mounted on FISH 5. From this one must conclude that it is essential to calibrate transducers in their installed positions.

frequency	S/V	S/A	Receiving Sensitivity
4.5 kHz	144.3 dB	190.5 dB	-176.3 dB
9 kHz	145.8 dB	188.0 dB	-186.0 dB
15 kHz	139.1 dB	179.5 dB	-198.0 dB
28 kHz	149.8 dB	185.4 dB	-198.0 dB
60 kHz	159.0 dB	208.5 dB	-181.0 dB
112 kHz	163.5 dB	208.5 dB	-186.3 dB
163 kHz	162.6 dB	211.0 dB	-186.2 dB

Table 2-4 : Transducer response for free transducers (single measurements)

2.2.2.2.2 Beampatterns

The following approach was used to determine the directionality of the transducers mounted on the Deep-Tow vehicle (figures 2-7 to 2-10): A set of nearly horizontal beampatterns (XY-beampatterns) was made at nominal grazing angles of 0, 10, 20, 30, 40, 50, 60, 70, 80, and 88°. Therefore the hydrophone (LC-10 or Navy

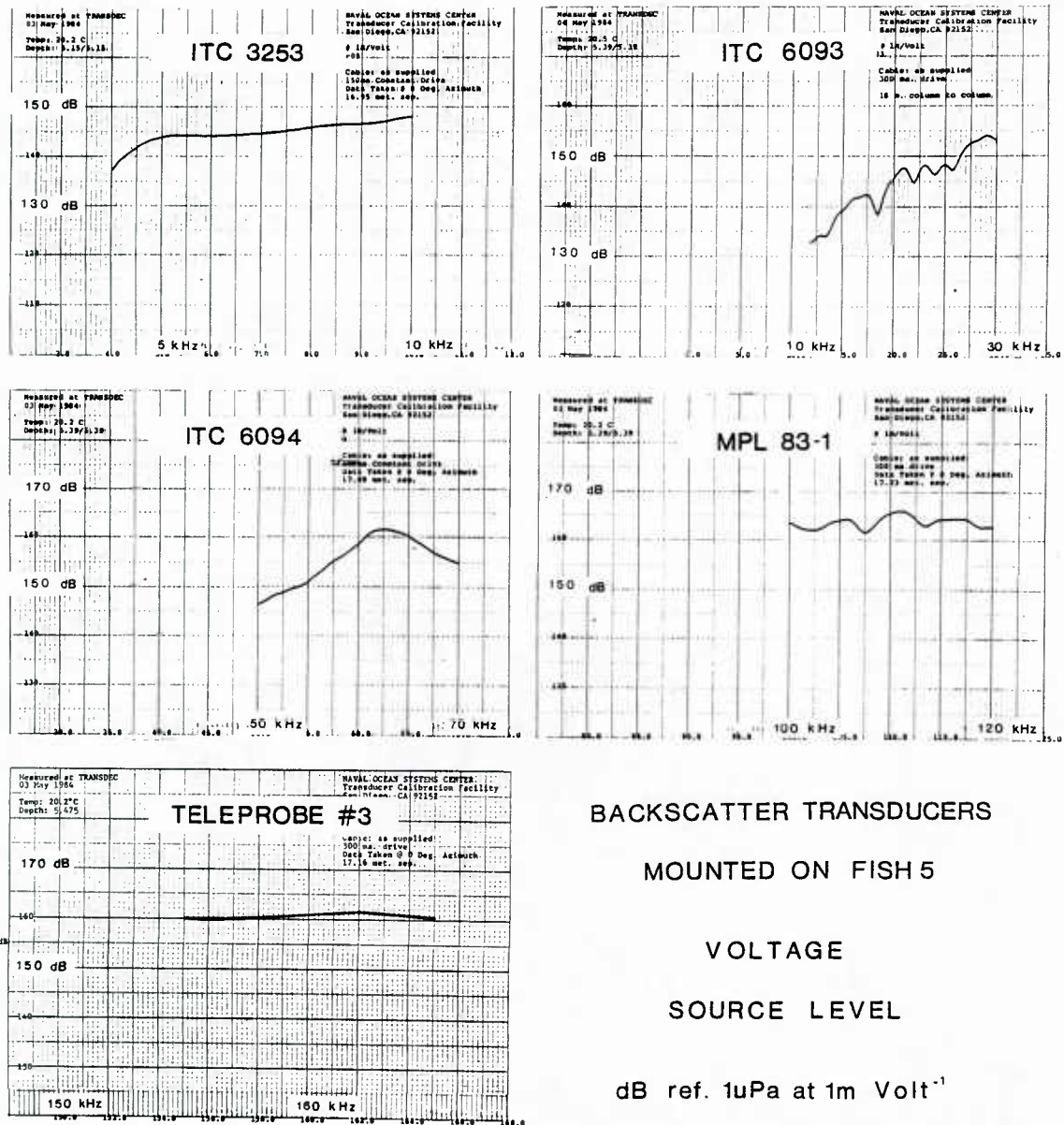


Figure 2-5. Voltage transmitting response

Voltage Source Level (dB ref. 1 micro Pascal per Volt at 1 m) as a function of frequency for the 5 backscatter transducers. The transducers are mounted on the Deep Tow vehicle. Note that the scales differ.

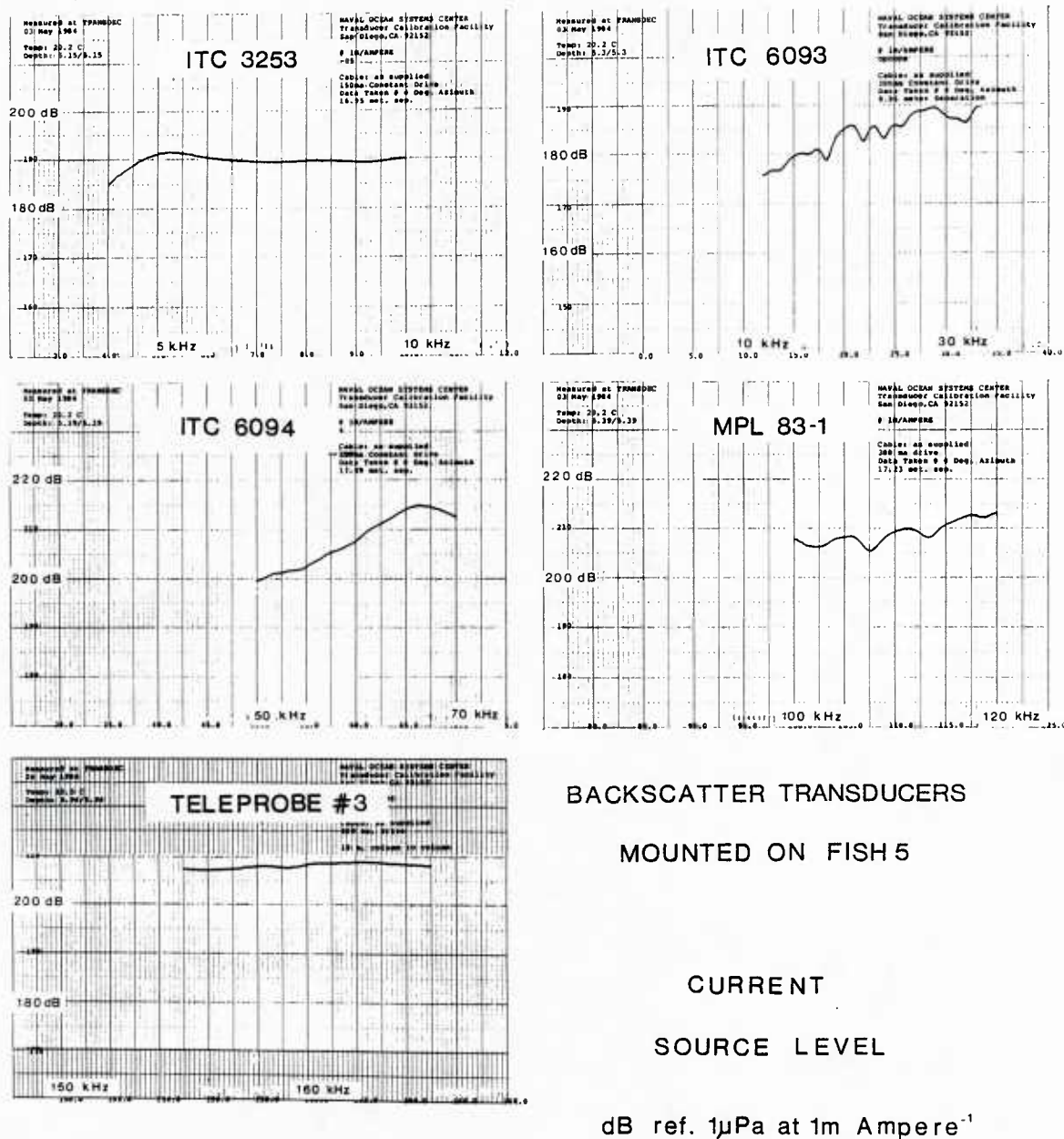


Figure 2-8. Current transmitting response

Current Source Level (dB ref. 1 micro Pascal per Ampere at 1 m) as a function of frequency for the 5 backscatter transducers. The transducers are mounted on the Deep Tow vehicle. Note that the scales differ.

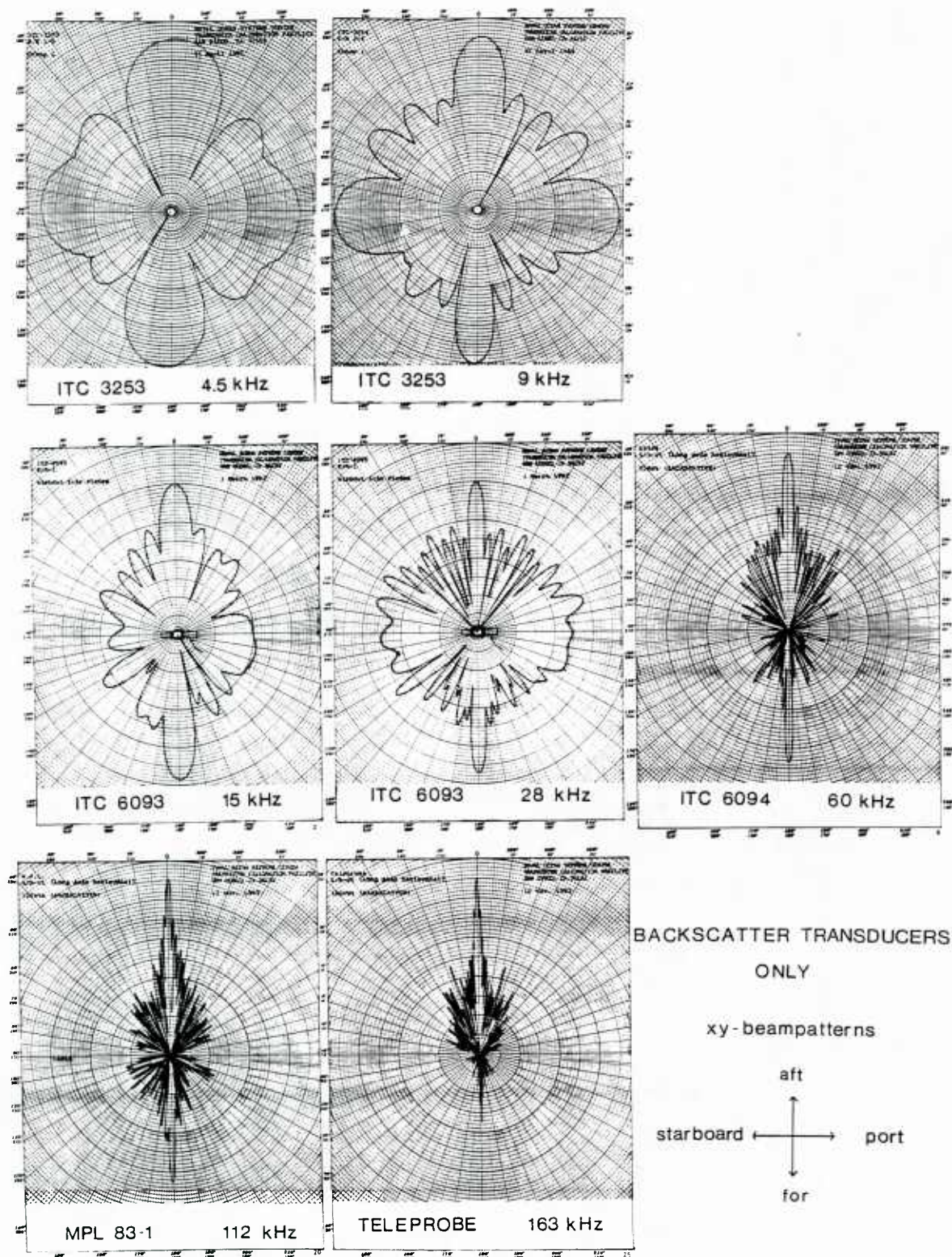


Figure 2-7. XY-beampatterns of free transducers

XY-beampatterns in the transducer plane for the free transducers (i.e. not mounted on the vehicle) at the operating frequencies (1 dB per radial scale line i.e. 50 dB top to center).

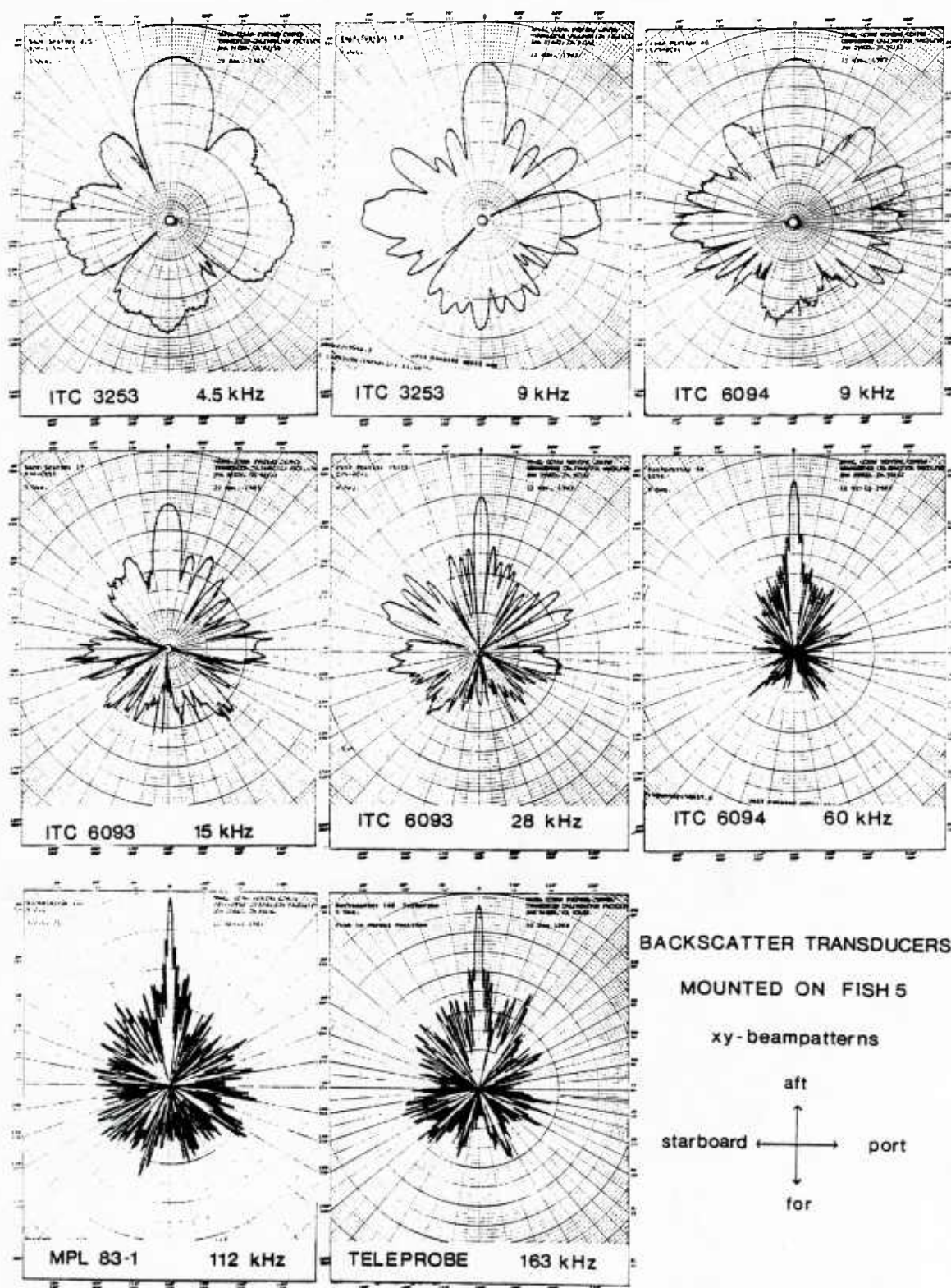


Figure 2-8. XY-beampatterns on fish

XY-beampatterns in the plane through the transducer and the vehicle for the backscatter transducers mounted on the Deep Tow vehicle at the operating frequencies (50 dB top to center).

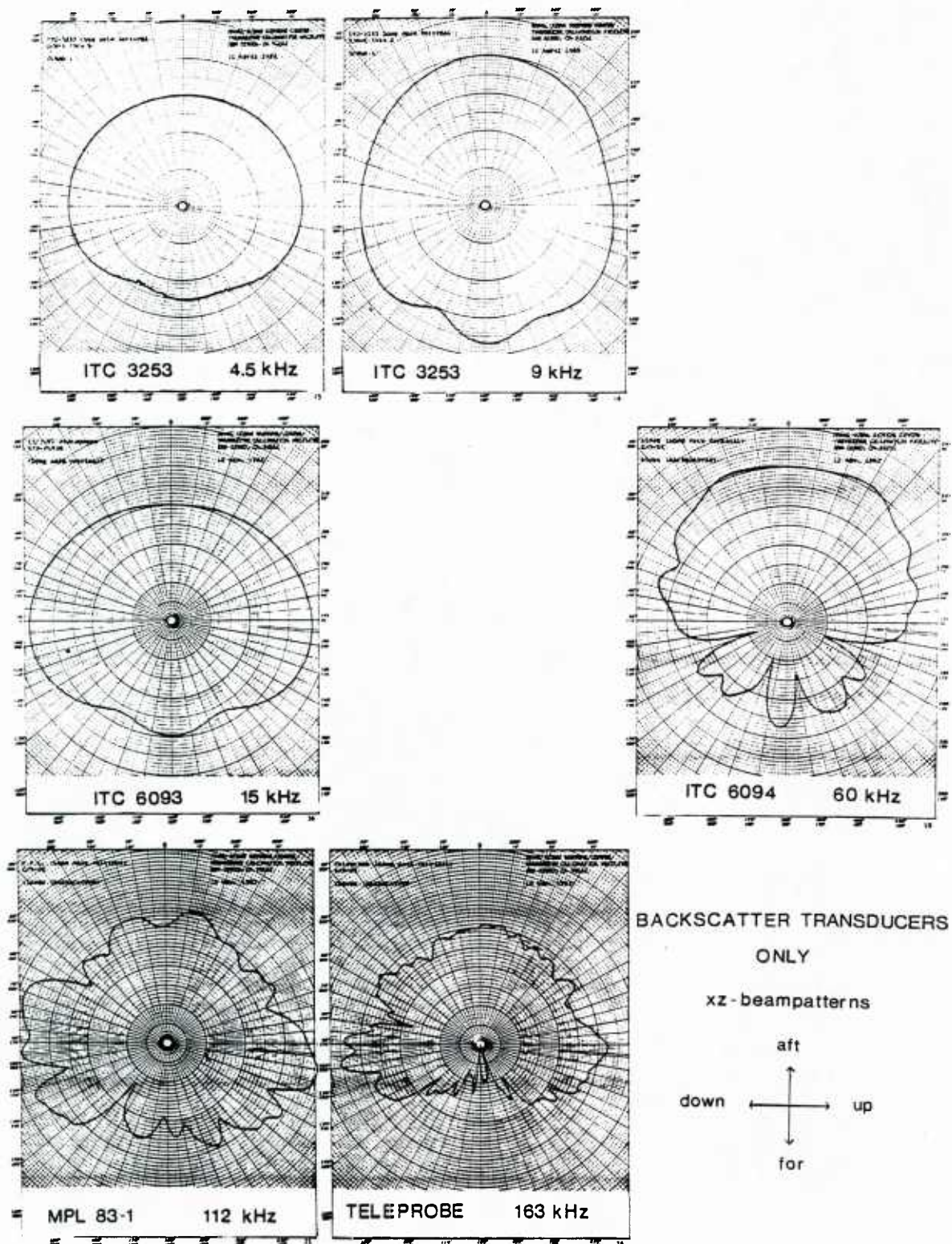


Figure 2-9. XZ-beampatterns of free transducers

XZ-beampatterns in the plane through the center of the transducer for the free transducers (i.e. not mounted on the vehicle) at the operating frequencies (50 dB top to center).

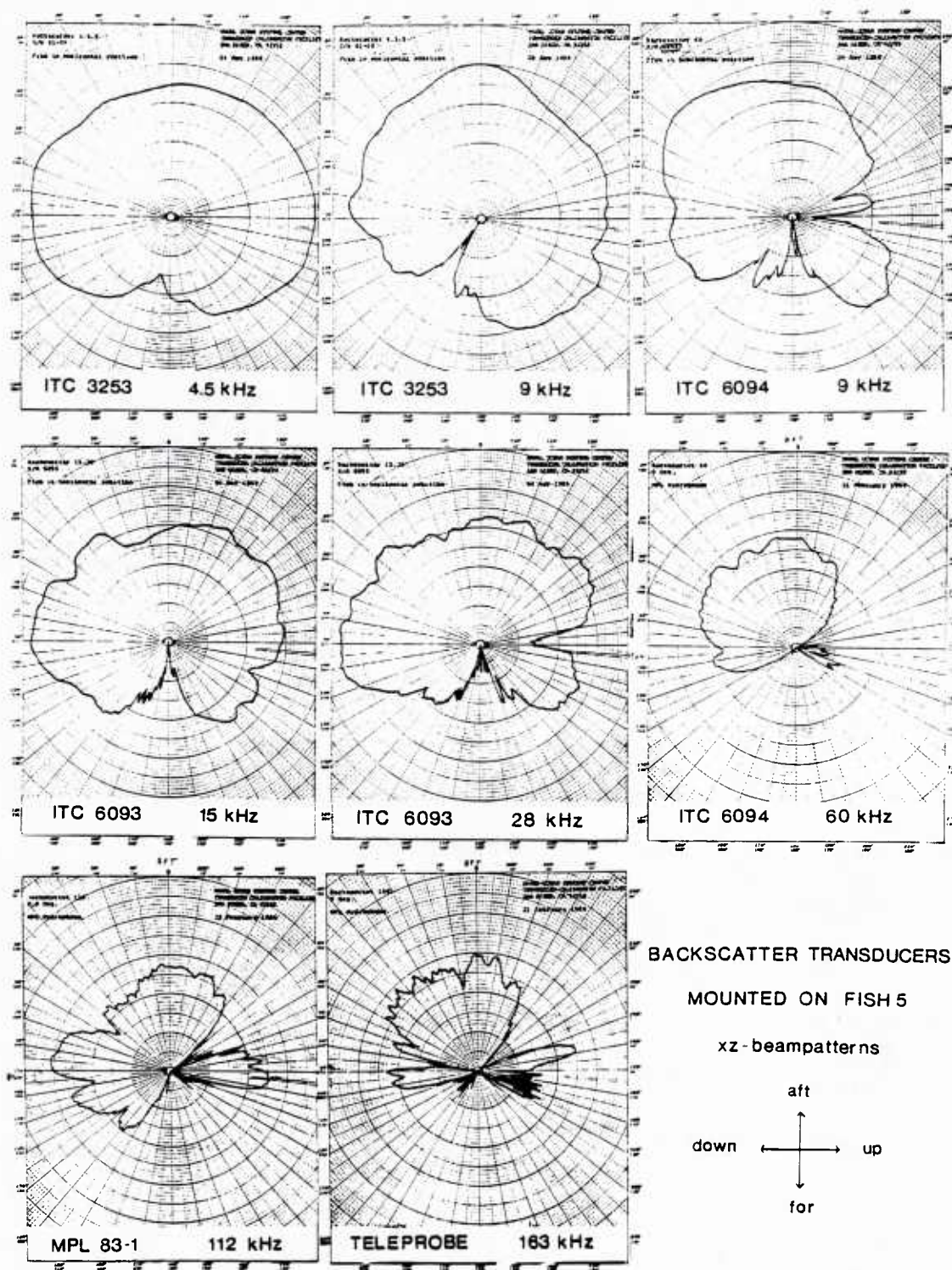


Figure 2-10. XZ-beampatterns on fish

XZ-beampatterns in the plane through the transducer and the vehicle for the backscatter transducers mounted on the deep tow vehicle (50 dB top to center).

standard) was lowered to the appropriate depth, as far away from the fish as possible, without allowing surface or bottom reflections to interfere with the acoustic pulse arriving by the straight line path (figure 2-1). The fish was then rotated around its center of gravity, while the backscatter transducers were used as projectors. The changes in distance between the backscatter transducer and the hydrophone were taken into account by correcting for the spherical spreading before the beampatterns were plotted in dB relative to the maximum of the first beampattern in that series.

Turning the fish means also changing the grazing angle. These changes are small in the aft direction, but increase in the forward direction to up to 10° for grazing angles of 70° or higher. After the changes in distance have been corrected for, the influence on the effective beamwidth is, except for 9 kHz, less than 2%, as the transducer response is higher in the aft than in any other direction.

As one turns the fish and not the transducer, the azimuthal angle in the plots is the sum of the angle of rotation of the fish and the angle under which the hydrophone sees the backscatter transducer (zero = on-axis). For azimuthal angles near 0 or 180 degrees, the deviations are negligible compared to the positioning inaccuracy. At angles of 90 and 270 degrees, they reach a maximum of 3 degrees. This has, however, no substantial influence on the effective beamwidth as the changes occur slowly and essentially off-axis, and are neglected here.

In most instances, the reference was the maximum response at a grazing angle of 0° . That way, all data collected on the same day, for the same transducer and the same frequency have the same reference, and the plots can be compared (figures 2-11 to 2-20).

From these XY-beampatterns, the effective beamwidth for the 2-way-beampattern was computed for each grazing angle by equating the product of the

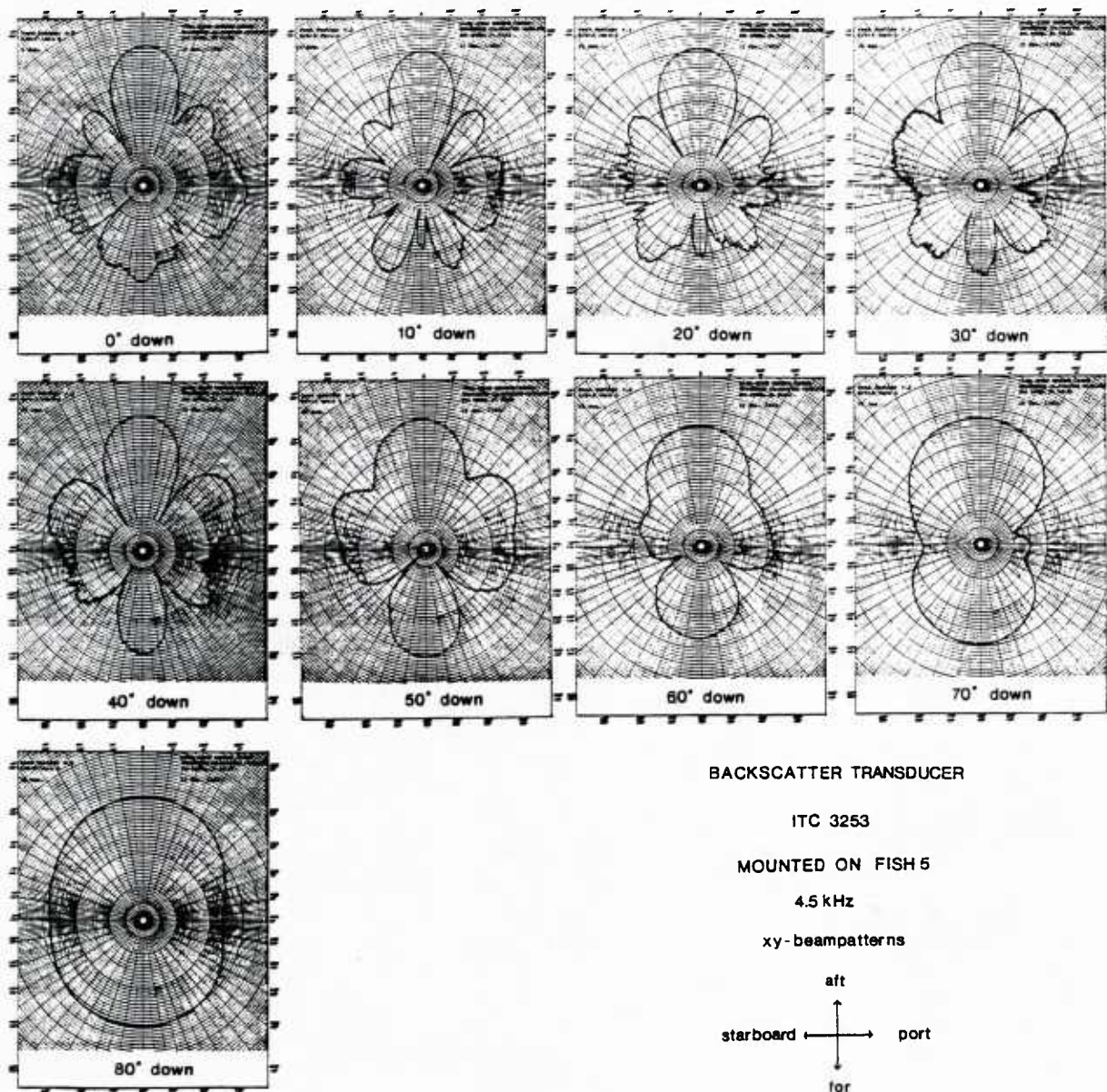


Figure 2-11. XY-beampatterns at 4.5 kHz

One-way XY-beampatterns for grazing angles from 0 to 80°. The transducers and the pressure cases were all mounted on the Deep Tow vehicle and all measurements were made with the same gains so that the changes of the transducer response between different grazing angles are also displayed (one dB per radial scale line i.e. 50 dB from top to center).

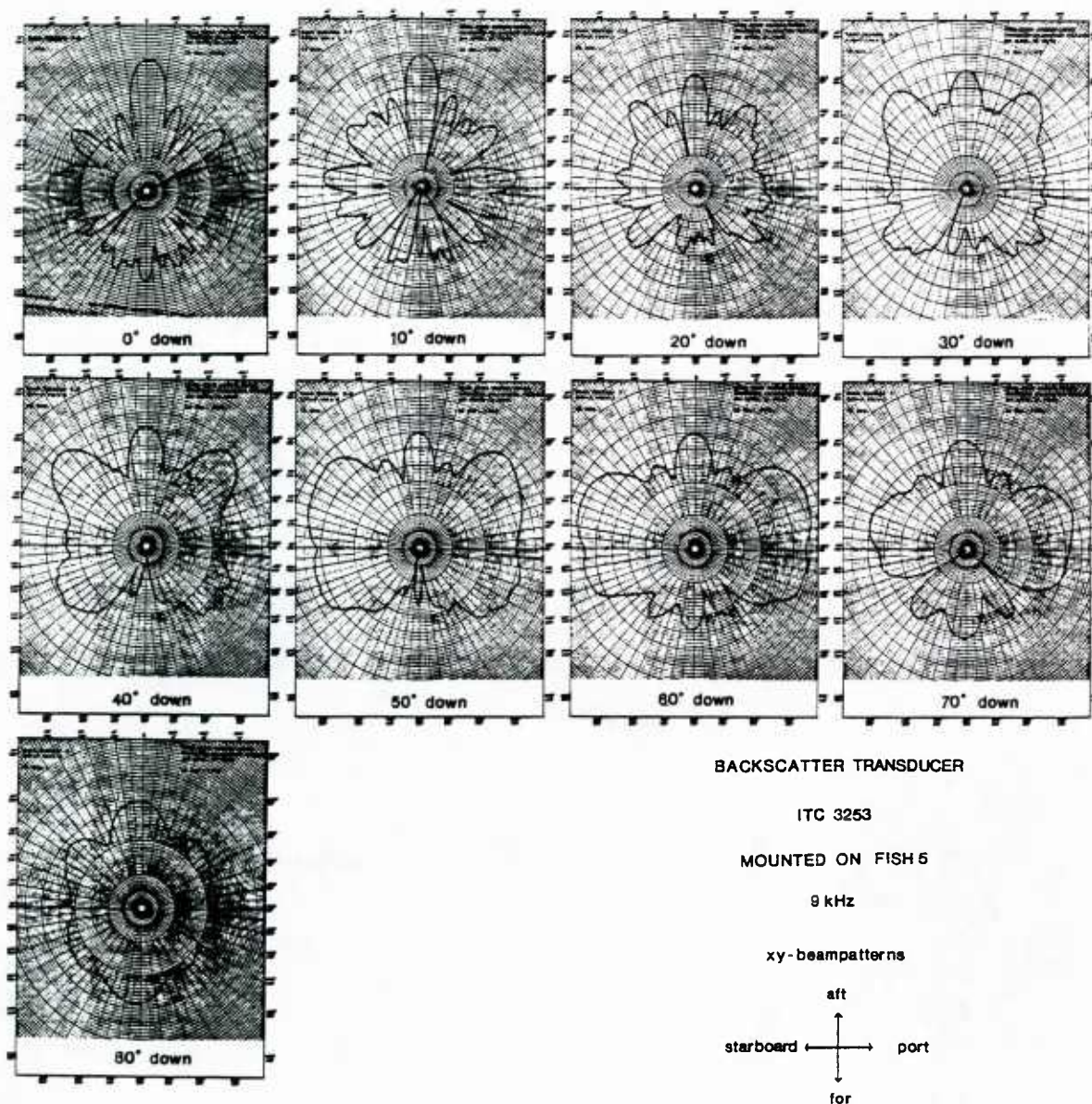


Figure 2-12. Transmitting XY-beampatterns at 9 kHz

One-way XY-beampatterns for grazing angles from 0 to 80° (50 dB top to center). The transducers and the pressure cases were all mounted on the Deep Tow vehicle and all measurements were made with the same gains so that the changes of the transducer response between different grazing angles are also displayed.

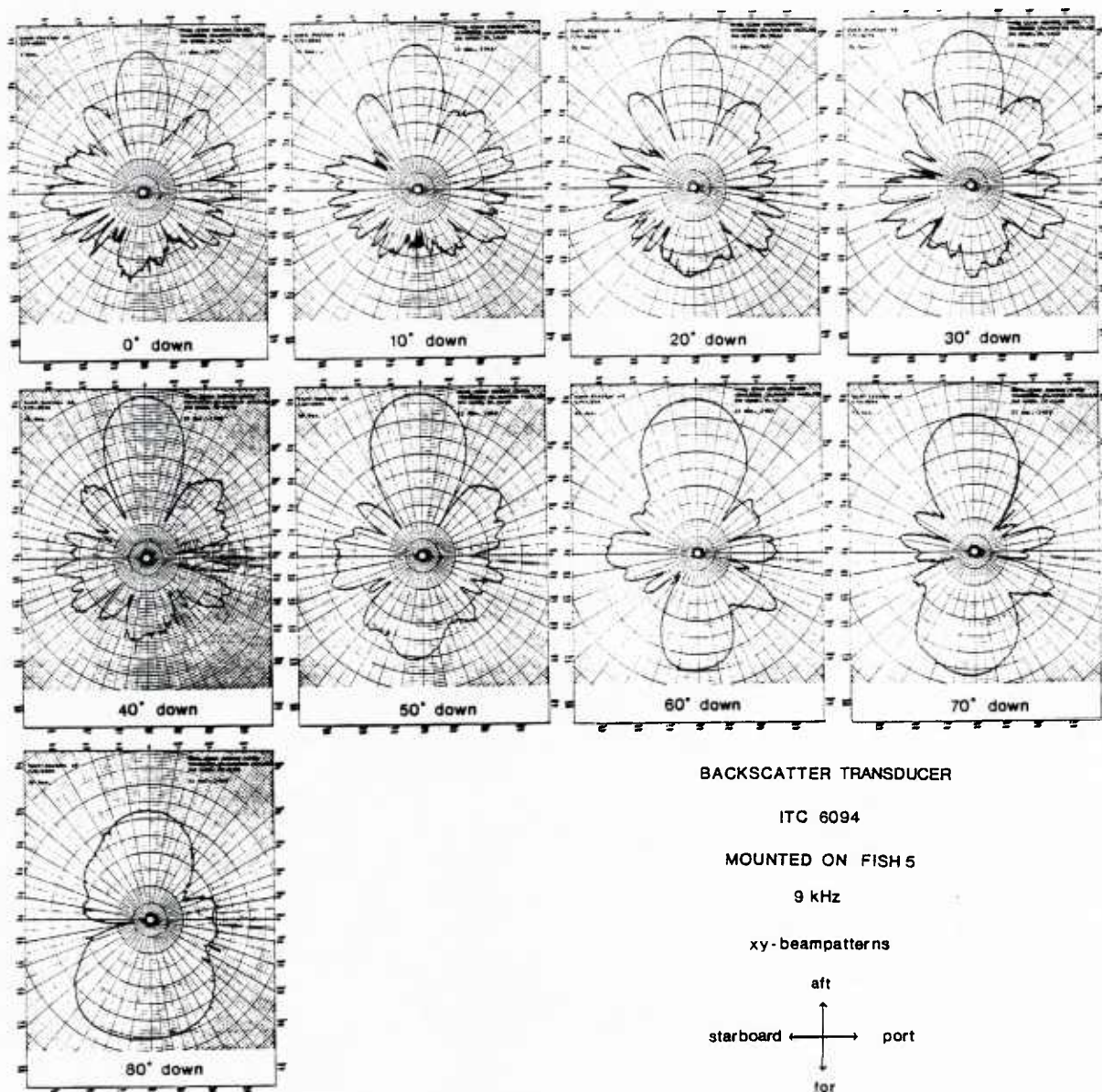


Figure 2-13. Receiving XY-beampatterns at 9 kHz

One-way XY-beampatterns for grazing angles from 0 to 80° (50 dB top to center). The transducers and the pressure cases were all mounted on the Deep Tow vehicle and all measurements were made with the same gains so that the changes of the transducer response between different grazing angles are also displayed.

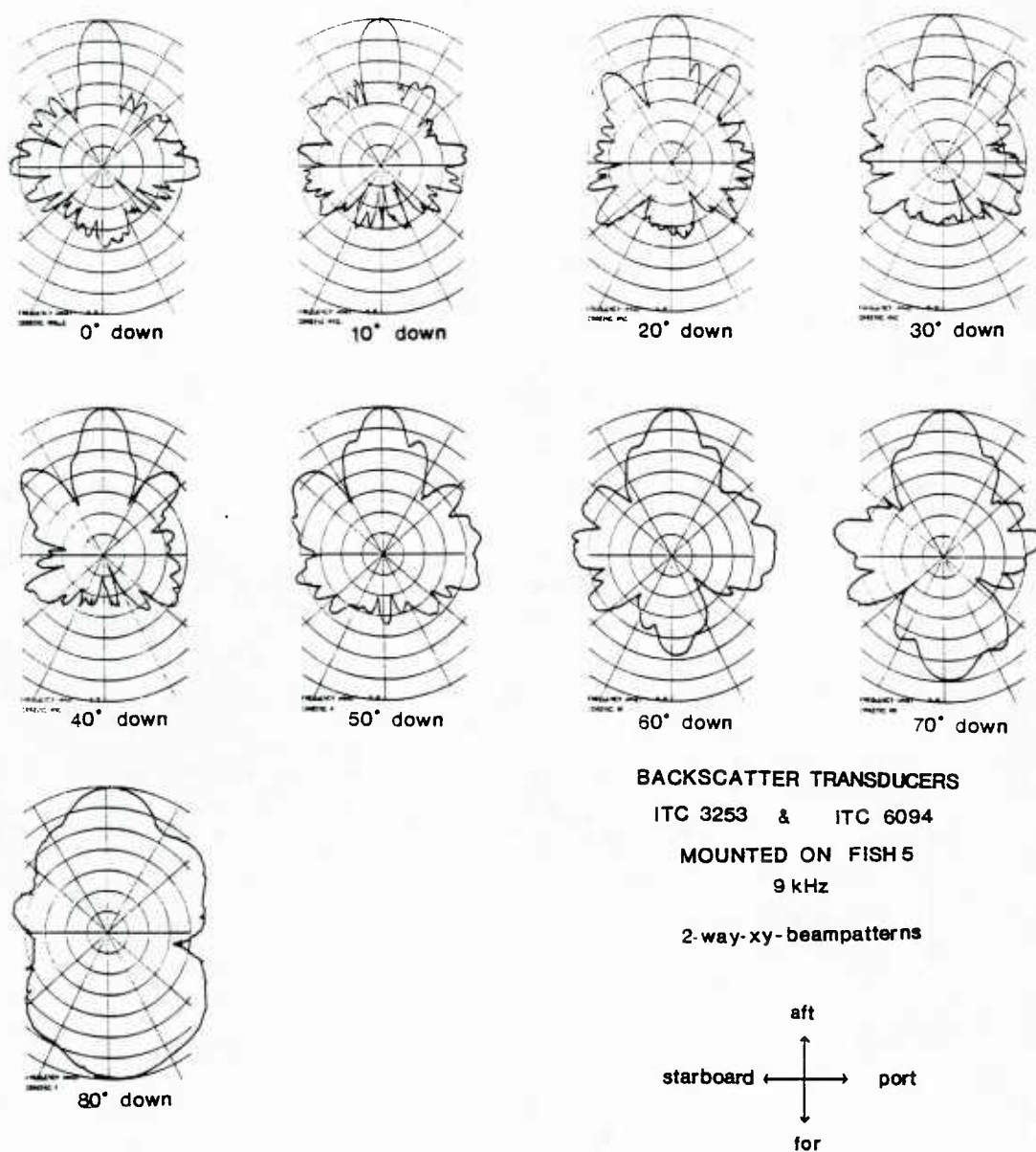


Figure 2-14. Two-way XY-beampatterns at 9 kHz

Two-way XY-beampatterns for grazing angles from 0 to 80° (10 dB per radial scale line). The transducers and the pressure cases were all mounted on the Deep Tow vehicle and all measurements were made with the same gains so that the changes of the transducer response between different grazing angles are also displayed

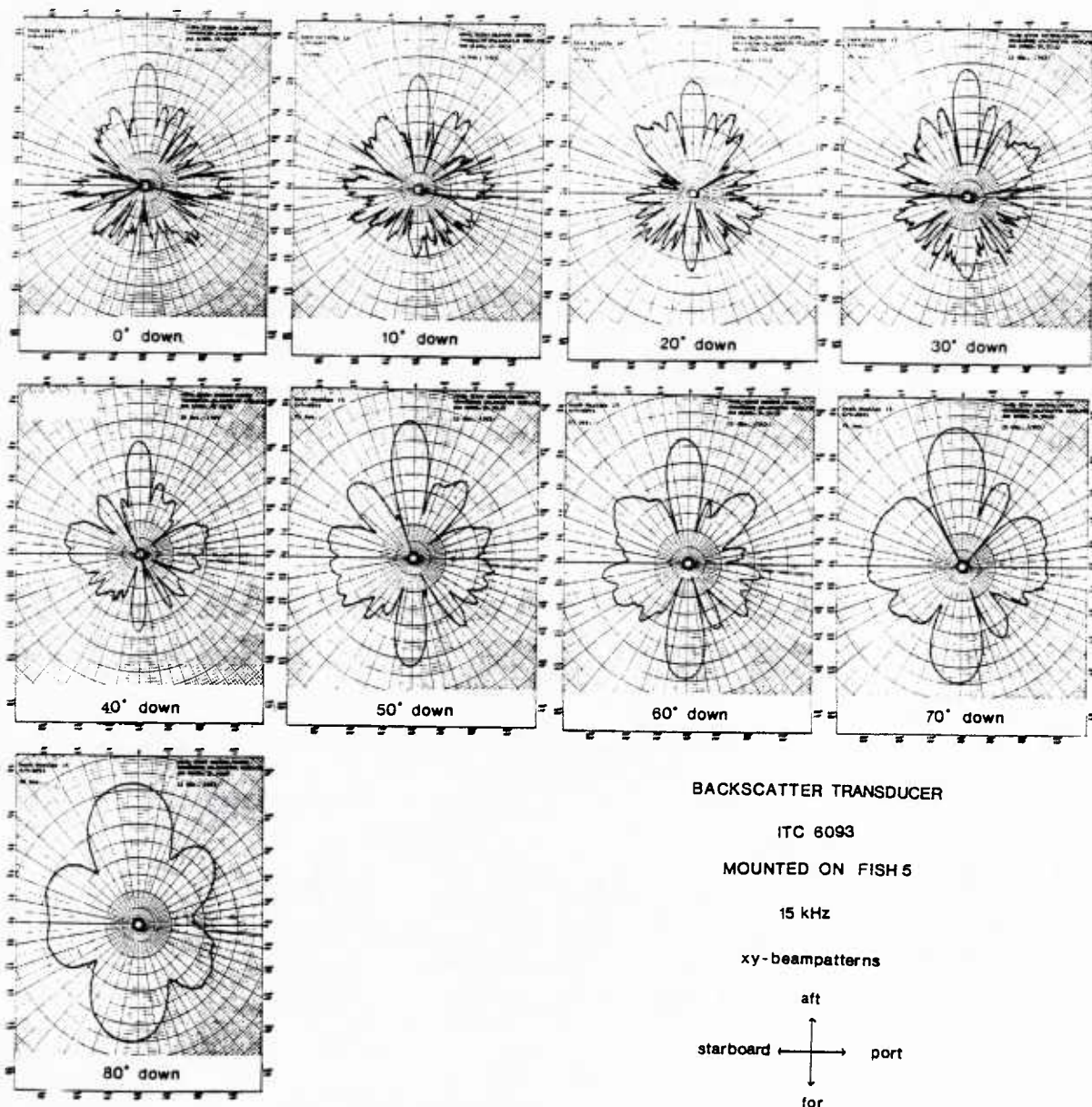


Figure 2-15. XY-beampatterns at 15 kHz

One-way XY-beampatterns for grazing angles from 0 to 80°. The transducers and the pressure cases were all mounted on the Deep Tow vehicle and all measurements (except for a grazing angle of 40°) were made with the same gains so that the changes of the transducer response between different grazing angles are also displayed. Add 6 dB at a grazing angle of 40°.

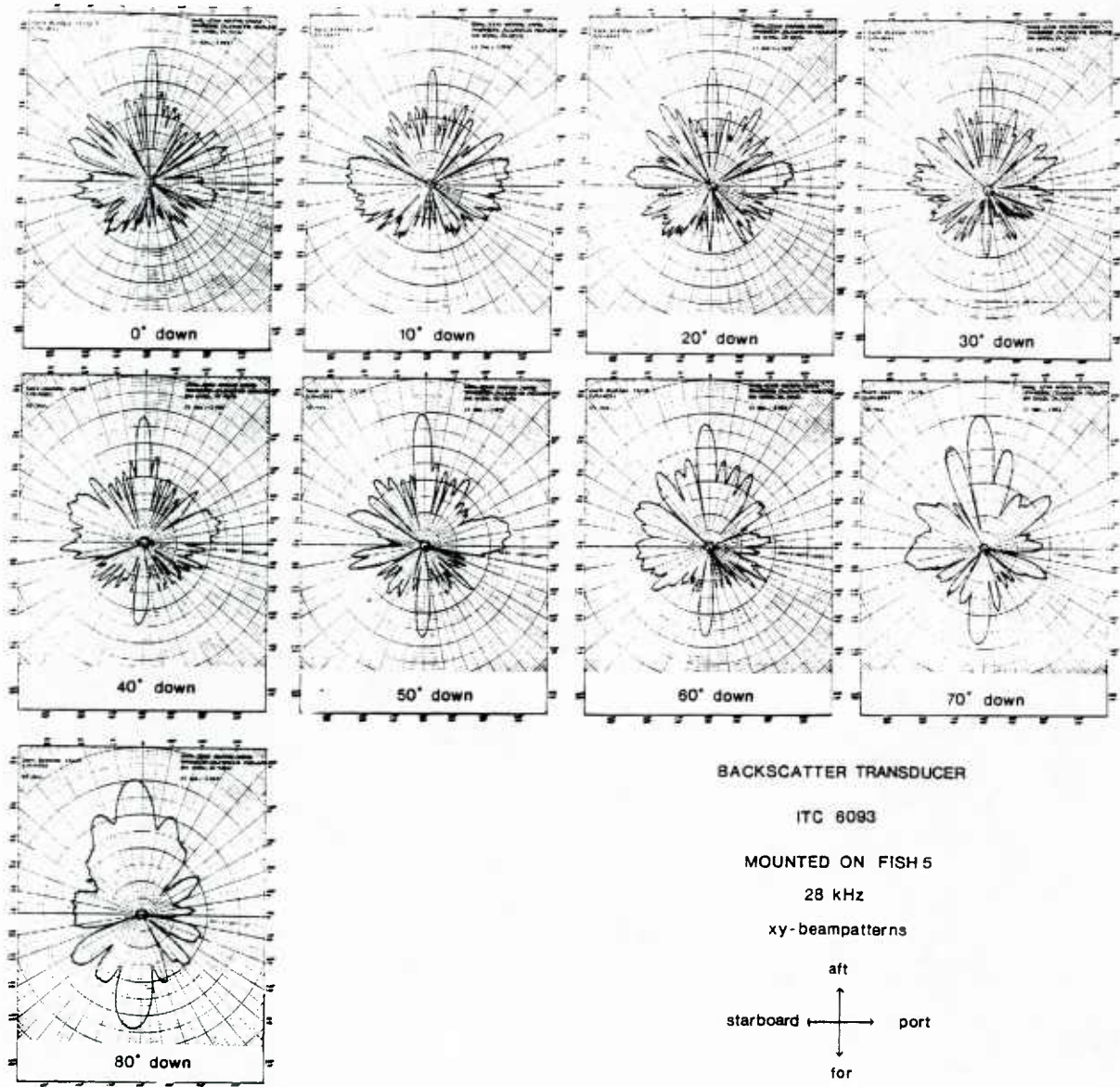
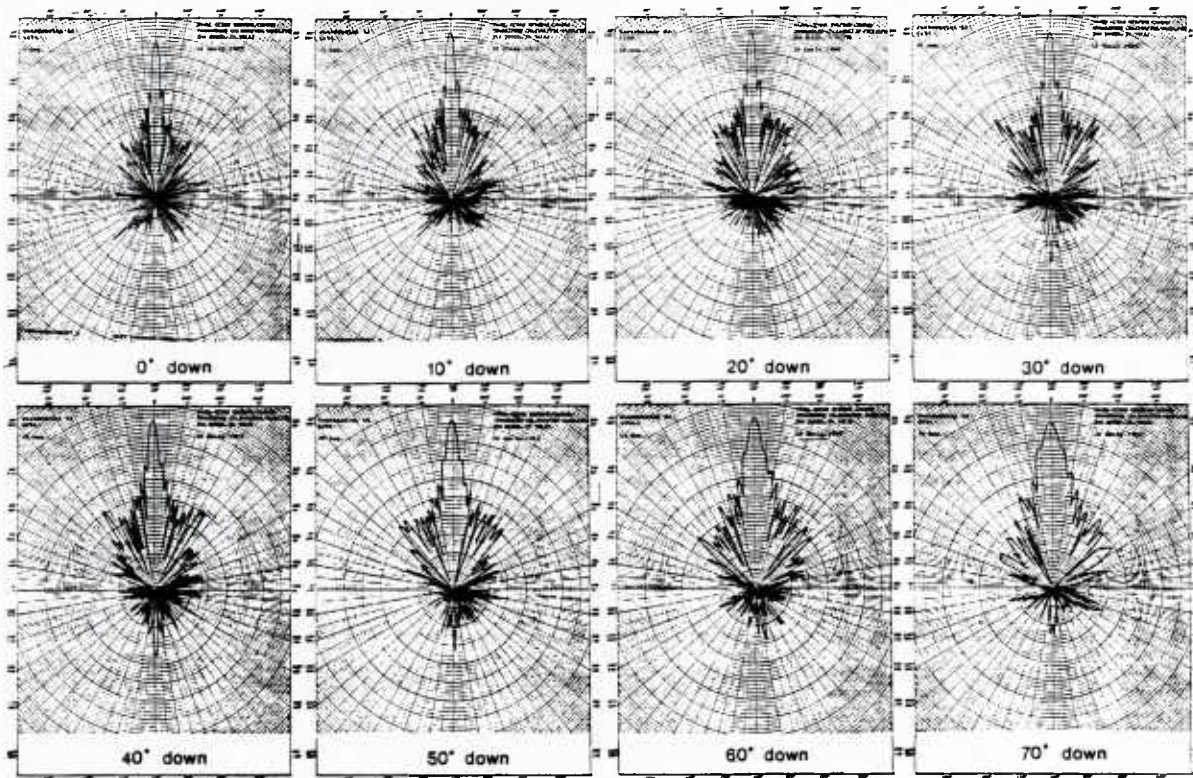


Figure 2-16. XY-beampatterns at 30 kHz

One-way XY-beampatterns for grazing angles from 0 to 80°. The transducers and the pressure cases were all mounted on the Deep Tow vehicle and all measurements were made with the same gains so that the changes of the transducer response between different grazing angles are also displayed.



BACKSCATTER TRANSDUCER

ITC 6094

MOUNTED ON FISH 5

60 kHz

xy-beampatterns

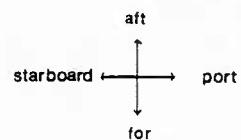


Figure 2-17. XY-beampatterns at 60 kHz

One-way XY-beampatterns for grazing angles from 0 to 80°. The transducers and the pressure cases were all mounted on the Deep Tow vehicle and all measurements were made with the same gains so that the changes of the transducer response between different grazing angles are also displayed.

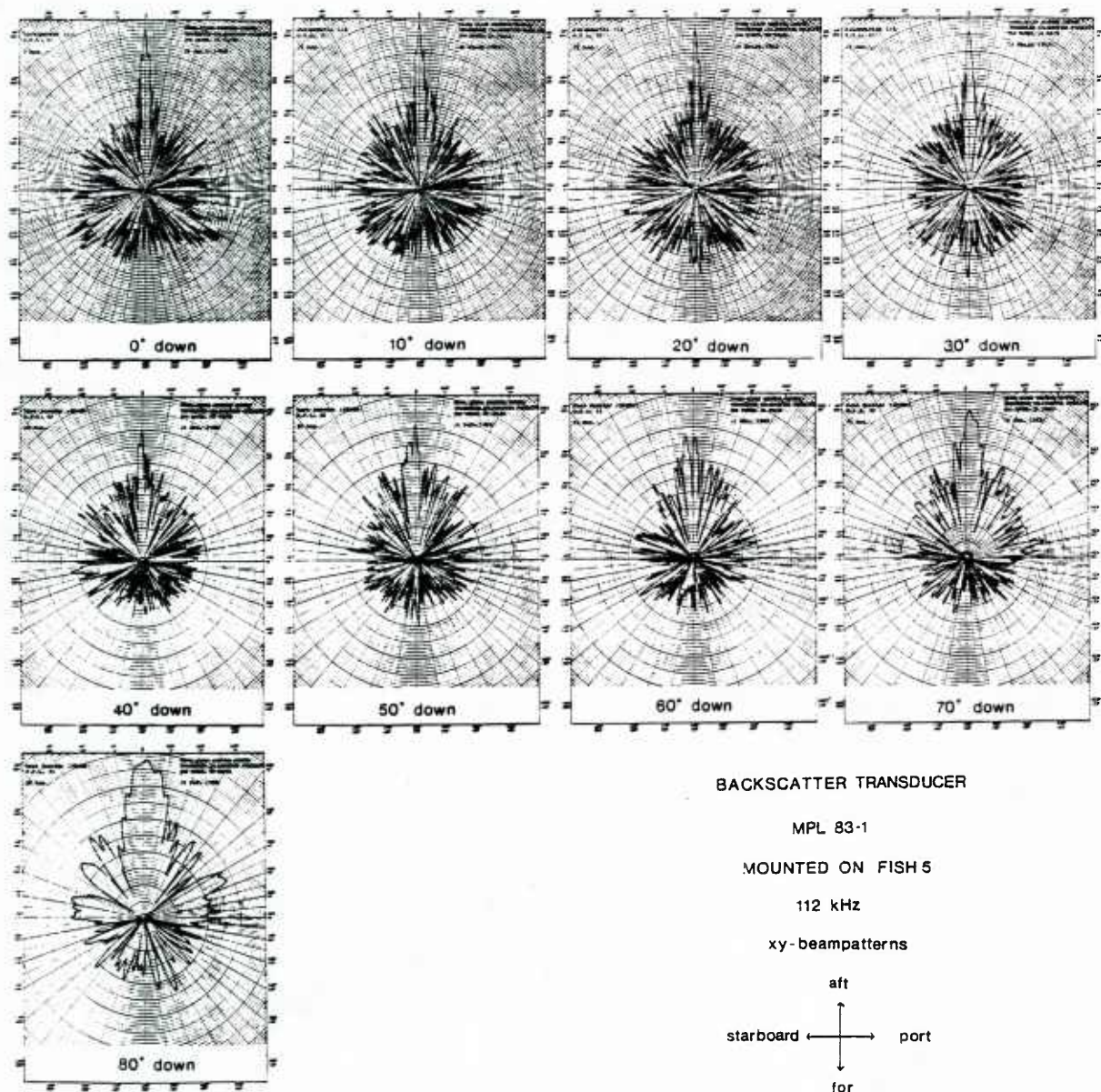
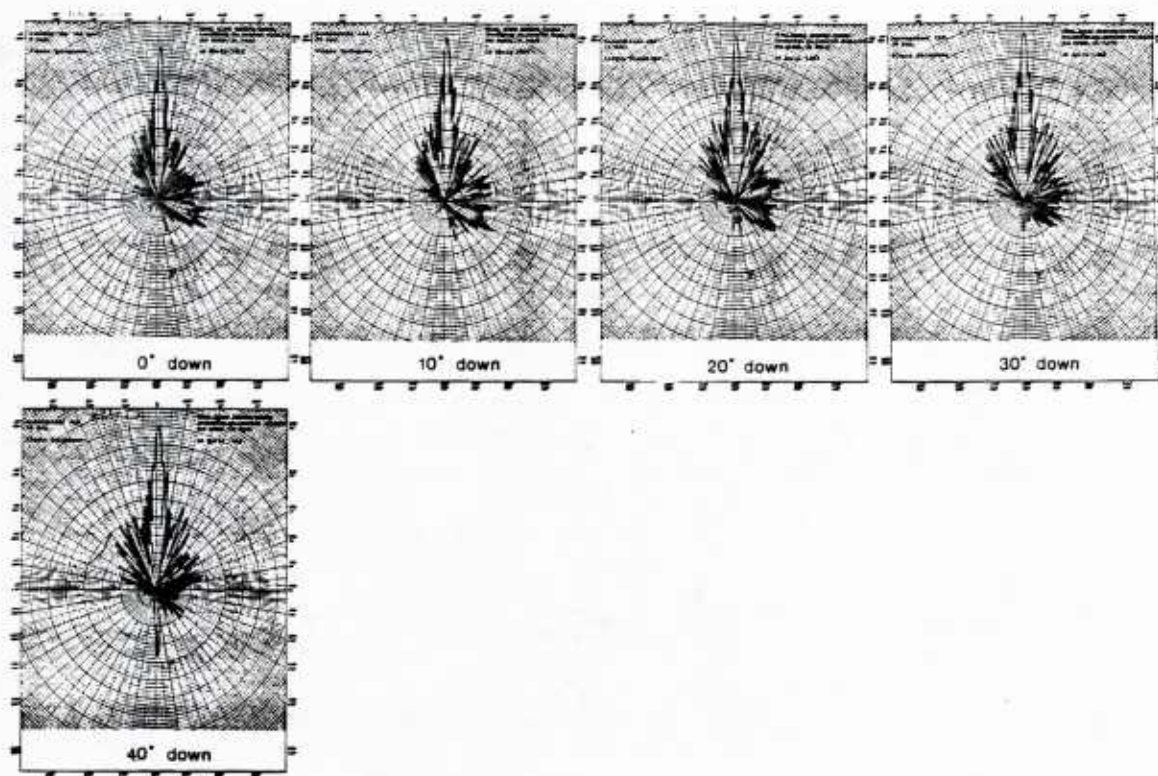


Figure 2-18. XY-beampatterns at 112 kHz

One-way XY-beampatterns for grazing angles from 0 to 80°. The transducers and the pressure cases were all mounted on the Deep Tow vehicle. The measurements at grazing angles of 0, 10, 20, 30° were made with the same gains, those at 40, 50, 60, 70 and 80° were made at another gain setting.



BACKSCATTER TRANSDUCER

TELEPROBE S/N 1

MOUNTED ON FISH 5

163 kHz

xy-beampatterns

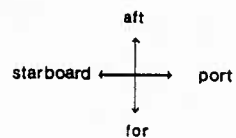


Figure 2-19. XY-beampatterns for one transducer at 163 kHz

One-way XY-beampatterns for grazing angles from 0 to 40°. The transducers and the pressure cases were all mounted on the Deep Tow vehicle and all measurements were made with the same gains so that the changes of the transducer response between different grazing angles are also displayed.

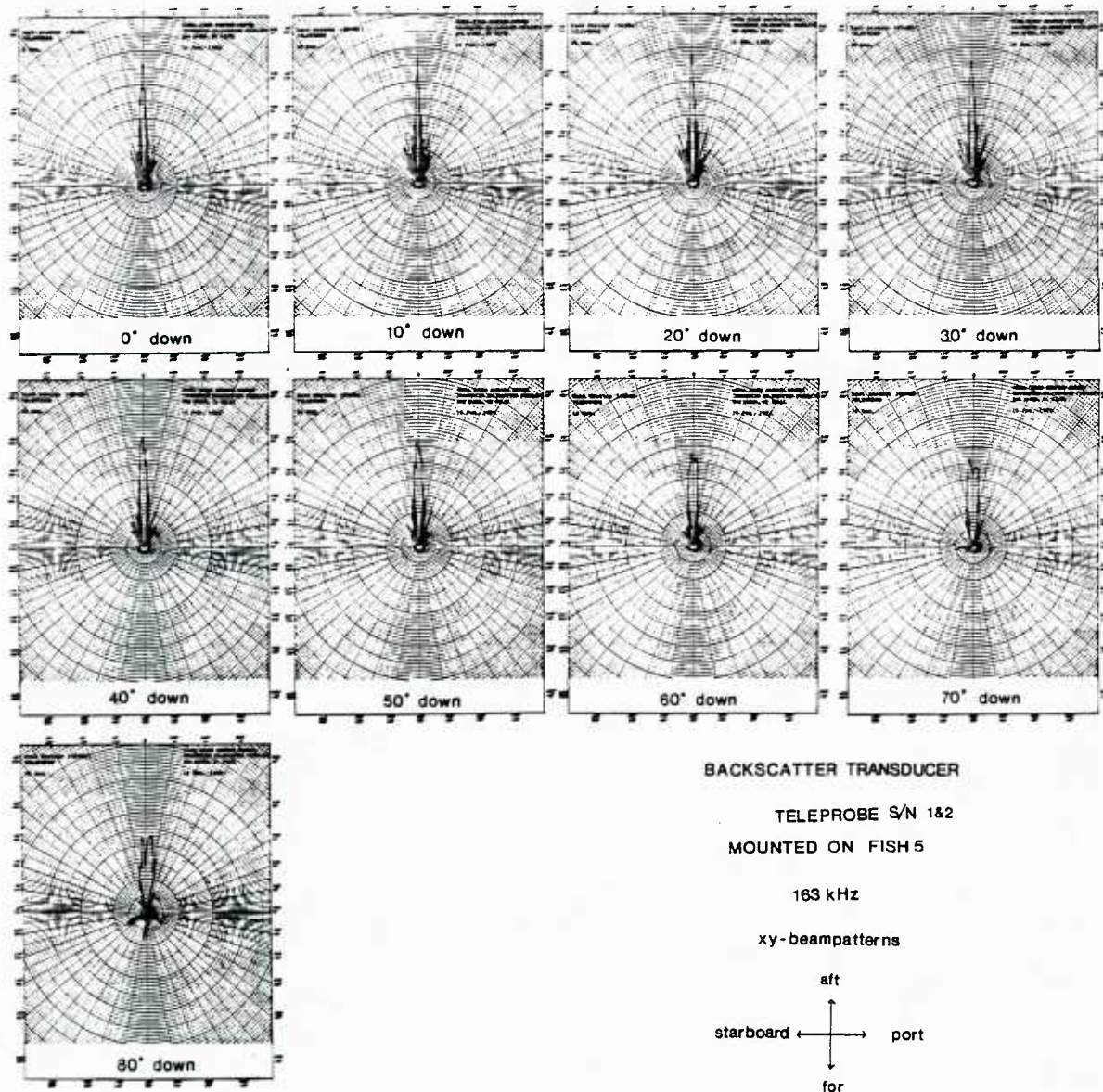


Figure 2-20. XY-beampatterns for two transducers at 163 kHz

One-way XY-beampatterns for grazing angles from 0 to 80° (50 dB top to center). The transducers and the pressure cases were all mounted on the Deep Tow vehicle and all measurements were made with the same gains so that the changes of the transducer response between different grazing angles are also displayed. The Teleprobes S/N 1 and S/N 2 were operated both (compare figure 2-19 for S/N 3 only).

intensities of the real beams with those of an idealized fan-shaped beam

$$\int_0^{2\pi} b(\theta_o, \phi) b'(\theta_o, \phi) d\phi = \int_0^{\Phi_{eff}} 1 \times 1 d\phi = \Phi_{eff} \quad (2-3)$$

where ϕ is the azimuthal angle, θ_o is the selected grazing angle, $b(\theta_o, \phi) = 10^{dB/10}$ and $maximum(b(\theta_o, \phi)) = 1$.

The results are summarized in table 2-5. Tests made at 110 kHz (greatest $\pi L^2/4\lambda$) suggest that all beampatterns (70° and 80° at 163 kHz excepted) are good approximations to far field beampatterns, although those from 60 kHz on upward had to be measured well below the distance $\pi L^2/4\lambda$ for the higher grazing angles.

Realizing during the at sea trials that the transducers ITC 6094 (60 kHz) and Teleprobe (163 kHz) did not work well at normal incidence, it became clear that the beampattern is not as well behaved in the vertical as the cuts made so far suggested. Turning the 1000 kg vehicle on its side on the TRANSDEC turntable allowed us to make a set of XZ-beampatterns. (As the XZ-beampatterns made at azimuthal angles of 1° to 5° agree closely with those for 0°, only the last ones have been reproduced in figure 2-9.) These permitted us now to determine the intervals in which the beampatterns are smooth. Strong changes in effective (XY-)beamwidth have to be expected if the slope of the XZ-beampattern is strong. Another complication was created by the 1° - 2° backlash of the turntable, which prohibited us to define the transducer response within 1 dB whenever the slope is more than 0.5 db/degree. Thus we excluded the following grazing angles in the data analysis :

TELEPROBE: 5° - 15° and 60° - 90°

MPL 83-1 : 50° - 70°

Everywhere else, the following approach was used:

- 1.) The effective beamwidth is linearly interpolated between the two nearest

values from table 2-5.

- 2.) The S/V, S/A and Receiving Sensitivity at 1 bar and 20°C are read from the XZ-beampattern, where the on-axis values come from table 2-3.

grazing angle	0°	10°	20°	30°	40°	50°	60°	70°	80°	90°
frequency										
4.5kHz	17.2°	17.2°	20.1°	21.2°	20.7°	27.5°	34.7°	40.5°	60.6°	
9x9 kHz	20.7°	10.8°	10.9°	12.0°	12.8°	13.5°	15.4°	19.8°	62.3°	
15 kHz	6.9°	7.8°	7.6°	7.8°	8.2°	11.8°	17.9°	14.9°	22.3°	
30 kHz	3.4°	4.2°	4.1°	4.1°	4.2°	4.8°	5.7°			
60 kHz	1.8°	1.7°	1.8°	2.0°	2.0°	2.3°				
110 kHz	0.5°	0.4°	0.4°	1.1°						
160 kHz	1.3°	1.2°	1.2°	1.4°						

Table No. 2-5 : Effective Beamwidth on FISH 5

2.2.2.2.3 Calibrations as a function of temperature and pressure

The calibrations described above were made in a large tank at temperatures between 12° and 20°C. So they do not take into account pressures and temperatures as they are found in the deep sea. Several manufacturers as well as the US Navy have studied the behavior of ceramics (including PZT-4) used as transducer materials on small samples at various temperatures and pressures. Using the data from Channel Industries (manufacturer) in the linear relationship

$$p = \omega^2 E_3^2 k^2 \epsilon_{33}^T Q_M \quad (2-4)$$

(Berlincourt and Kruger, 1964) one sees that the response of prestressed PZT-4 (used for ITC 3253, ITC 6093 and ITC 6094) drops 1-2 dB when one lowers the temperature from 13° to 0°C. All transducers used also shift resonances to lower frequencies as one lowers the temperature. High Q transducers thus can change their response by several dB if one operates near or on resonance.

Data collected by the US Navy and several manufacturers (Hewlett Packard, 1979) on the behavior of transducers and transducer materials under pressure cannot be used in this study as every transducer is built in a different way, uses different secondary materials and behaves differently under pressure changes. A calibration as a function of pressure had to be done for those transducers for which no manufacturer's estimates were available (see below).

The design of the transducers ITC 6093 and the experience of the manufacturer suggested that the transducer response does not change more than 1 to 2 dB with temperature and pressure. The transducers ITC 3253, MPL 83-1 and the Teleprobes were expected to change 1-3 dB maximum.

a.) Calibrations as a function of temperature only

In order to verify the estimates for the different temperatures for the transducer arrays with their backplates, we made the following experiment :

In a 170 cm deep tank filled with UV-sterilized sea water, the transducers were mounted one at a time on a 30 cm high PVC-table on the bottom of the tank (figure 2-21). The transducers were far enough from the bottom so that it was possible to discriminate against the bottom return (and the downward transmission) as long as pulses of less than 0.4 ms were used. The main axis was directed towards the surface, which was - contrary to the bottom - assumed to be a perfect, temperature independent reflector. The electrical cable and the polypropylene ropes to handle the table came off the narrow ends of the table and continued along the bottom for a couple of meters before they came up near the side walls i.e. they had been routed where the acoustic response is substantially lower than on-axis (± 90 degrees in beam-pattern). As the side walls were 2.3 m away, their echo arrived more than one millisecond after the first surface return.

SET-UP FOR TEMPERATURE CALIBRATION

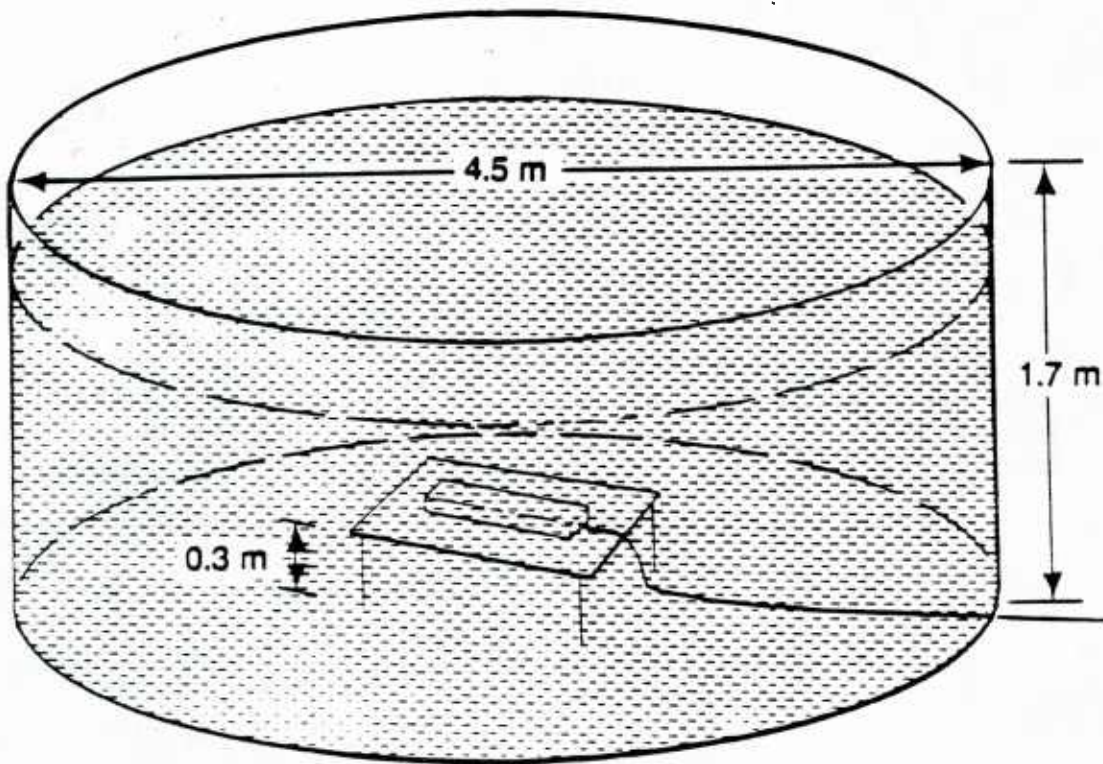


Figure 2-21. Set-up for temperature calibrations

The PVC table with the transducer is in the center of the tank. The transmitted sound is reflected at the water surface and the echo is received on the same transducer.

The control electronics consisted essentially of a frequency generator, a power amplifier, a TR-switch, a simple matching network and a preamplifier. The TR-switch permitted to transmit and receive on the same transducer.

While a pulse was transmitted at a well defined frequency, the transmit current and transmit voltage were measured (with a current probe and an oscilloscope) between the TR-switch and the transducer. The sound was reflected on the surface before it came back to the transducer. The corresponding received voltage was amplified and determined with the oscilloscope. The temperature was varied from 1.2°C to 20°C , and the above described measurements repeated at least once per degree temperature change.

Assuming the beam pattern does not change appreciably, it is thus possible, without any absolute calibrations, to measure changes in the difference of the sum of the source level, the receiving response and the transmission loss as a function of temperature. The spraying of the transducers and the table with alcohol prevented the formation of highly scattering or reflecting air bubbles on the transducer. In addition, the transducer was left at least 24 hours in the tank before the first measurement was made. A closed circuit filter-pump-refrigeration system kept mixing the water until about half an hour before the measurement. It was impossible to do an accurate absolute calibration as we were working in the nearfield of the transducers and did not know what the spreading law was. From a previous experiment (Weydert, 1985) we do know that the xy-beam pattern of the transducer is well behaved and does not change significantly with distance from the transducer as long as you do not get very close to the transducer. The sound velocity changes by about 50m/s (out of 1500m/s) for a temperature change of 10°C , so the wavelength changes a few percent per 10°C , which has no significant influence on that part of the sound field which is of interest here. The sound absorption is less than 0.025 dB per meter at 112 kHz.

Even a doubling or tripling of this value would have no significant influence on the outcome of the measurements as we are looking for changes exceeding 1 dB. So, differences in received/transmitted voltage or current are solely due to the transducer behavior. The results of the experiment are summarized in table 2-6. It can be seen that the ratio of received to transmitted voltage drops or stays the same for all transducers and frequencies as you lower the temperature from 13°C to 1.2°C. The response and impedance changes for different frequencies are different, suggesting that some of the resonance frequencies shifted.

transducer	frequency	high T	low T
ITC 6093	16 kHz	-18.5 dB	-18.6 dB
ITC 6093	28 kHz	-25.8 dB	-25.9 dB
ITC 6094	55 kHz	-35.4 dB	-35.1 dB
ITC 6094	63 kHz	-23.4 dB	-22.8 dB
ITC 6094	71 kHz	-15.7 dB	-18.1 dB
MPL 831	100 kHz	-15.1 dB	-17.5 dB
MPL 831	125 kHz	-13.6 dB	-17.9 dB

Table No. 2-6: $S/V + Rec.Sens.$ for temperatures of 20 and 1 degrees.

b) Calibrations as a function of pressure only

The transducers ITC 3253-1 to -5 (array), ITC 6094 and MPL 83-1 were mounted on a single frame and lowered into the pressure vessel at TRANSDEC. The size of the pressure vessel did not permit to make the measurements inside. The vessel is, however, sufficiently transparent so that the standard can be outside (vessel losses are a few dB). This allowed us to make far field measurements at ambient pressure and at pressures up to 100 bar. Comparisons between the results at pressures of 1 bar and at high pressures yielded the changes in transducer response without the need to correct for the vessel losses (assuming the vessel losses did not change). The impedance measurements did not involve measurements through the vessel and are exact.

The changes of $S/V + Rec. Sens.$ of the ITC 3253 were less than 1 dB for both 4.5 and 9 kHz when the pressure was increased from ambient to 100 bar. The $S/V + Rec. Sens.$ of the transducer MPL 83-1 dropped by 1 - 2 dB and the magnitude of the impedance dropped from 200 Ω to 180 Ω , when the pressure was increased from 1 to 100 bar. As already observed at sea, the transducer ITC 6094 changed its characteristics when the pressure was increased from 1 to 30 bar, but did not change between 30 and 100 bar. The $S/V + Rec. Sens.$ dropped by 4 dB when the pressure was increased. Measurements of the impedance made with and without the matching network confirmed that impedance changes were responsible for the changes in transmitting voltage observed at sea.

For the pressure calibration of the 9 kHz system (ITC 3253 as projector and ITC 6094 as hydrophone) the transducers ITC 3253-4 and ITC 6094 were mounted on a bar and inserted into a cylindrical wave guide which could be pressurized up to 600 bar. Several measurements of the $S/V + Rec. Sens.$ were made at different geometries and pressures up to 530 bar. The $S/V + Rec. Sens.$ increased by 8 ± 0.5 dB when the pressure was increased from 1 bar to 30 bar. Only changes of the order of a few tenths of a dB could be observed at higher pressures. The latter ones are attributed to changes in sound velocity and, subsequently, in the beampattern. Assuming that all the gas bubbles were dissolved, and knowing that the transducers ITC 3253-1 to -5 do not change substantially with pressure, the whole change of $S/V + Rec. Sens.$ must be attributed to changes of the characteristics of the ITC 6094. Since the transmitting voltage monitored at sea at 60 kHz and the transducer response of the ITC 6094 measured in a pressure vessel showed strong changes for pressures below 30 bar only, it is concluded that the changes which occur at depths of 300 meters or more can be neglected. Hence, all the backscatter measurements made at depths exceeding 300 meters can be compared directly i.e. without knowing the absolute calibrations.

The Teleprobe was put into a similar pressure vessel and the echo off a circular stainless steel plate ($\rho c = 40$) was measured as a function of pressure. The $S/V + Rec.Sens.$ decreased 1 dB while the pressure was increased from 1 to 450 bar.

c) Measurements at sea

A temperature and pressure calibration would not be complete without monitoring the parameters at sea. In order to make an in situ calibration and to keep track of eventual power changes, a calibration sphere was towed behind the vehicle. Because the XZ-beampatterns change significantly with the grazing angle, the data collected at sea with the calibration sphere are too unreliable to identify any power changes of the order of 1-2 dB. In addition to recording the echoes off the calibration sphere towed behind the fish, we left the backscatter system operating at the end of lowering 4 on Echo 2 until the fish had been brought nearly to the surface. This allowed us to measure the transmit voltages for pressures and temperatures found near the surface down to 3700 meters. At 2 frequencies (15 and 30 kHz), the calibration sphere allowed to measure the changes in $S/v + Rec.Sen.$ while the fish came up. No changes were observed. The transmit voltage was well recorded for all frequencies. At 60 kHz, the transmit voltage decreased to 85% when the fish moved through the upper 200 meters of the water column. This is in agreement with the measurements made in the TRANSDEC pressure vessel.

d) Conclusions

The changes with temperature and pressure have been summarized in table 2-7. The response of the transducers ITC 3253 does not change more than 2.5 dB when the transducer is cooled down to 1°C and the pressure is increased to 100 bars. The changes of the the ITC 6093 are of the order of 1 dB only. The $S/V + Rec. Sens.$

of the ITC 6094 drops by 3.5 dB at 60 kHz when the pressure is increased from 1 to 100 bars. At 9 kHz, the $S/V + Rec. Sens.$ of the 9 kHz system (ITC 3253 and ITC 6094) increased by 8 dB when the pressure was increased. The change with temperature appears to be insignificant. The transducer MPL 83-1 changes its $S/V + Rec. Sens.$ 1.5 dB when the pressure is increased and 2.5 dB when the temperature is decreased to 1°C. Assuming that these two effects add together, the $S/V + Rec. Sens.$ drops by 4 dB when the pressure is increased to 100 bars and the temperature is lowered to 1°C. The $S/V + Rec. Sens.$ of the Teleprobe 3 increased by 9.5 dB when the pressure was increased to 100 bar and the temperature lowered to 2°C.

frequency	$\Delta response$ 20° - 1°	$\Delta response$ 1 bar - 200 bar	$\Delta total$ surface - deep	error ²⁾
4.5 kHz	-1 dB	-1.5 dB	-2.5 dB	1.5 dB
9.0 kHz	0 dB	+8 dB	+8 dB	4.0 dB
15 kHz	--	--	-1 dB ¹⁾	1.5 dB
28 kHz	--	--	-1 dB ¹⁾	1.5 dB
60 kHz	-0.5 dB	-3 dB	-4.5 dB	1.5 dB
112 kHz	-2.5 dB	-2.0 dB	-4.5 dB	3.0 dB
163 kHz	-1 dB	-1 dB	-2 dB	1.5 dB

-- = no data available

1) = manufacturer's estimate

2) = calibration error for overall response

Table No. 2-7 : Transducer calibrations as a function of T and p

2.2.2.2.3 Conclusion

The backscatter system, including the associated electronics, has been calibrated. While an accuracy of 1 dB could easily be achieved for the calibrations of the electronics, both the description of the sound field generated by the transducers and the description of the response of the transducers to an incoming acoustic wave presented a large number of problems. The response of the electronics has been tabu-

lated (input voltage as a function of the output voltage) and is accurate within 1 dB or better for output signal to reference ratios between -30 and +5 dB. The beampatterns were determined for several grazing angles in the respective xy-planes and for a few azimuthal angles in the corresponding xz-planes. The xz-beampatterns show that no absolute measurement can be made at several grazing angle ranges at frequencies of 60, 112 and 163 kHz. Repetitions of the measurements (at room temperature and a pressure of 1 bar) permitted us to identify and eliminate bad measurements.

The calibrations at temperatures of 1-2°C and pressures up to 100 bar presented a new set of problems which have been described in detail.

Absolute calibration problems and systematic errors aside, it is thought that with the following recipe, the calibration errors contribute less than 1 dB to the error of the backscatter coefficients for 4.5, 15, 30 and 60 kHz, and less than 3 dB for 9, 112 and 163 kHz.

- 1) compute the effective beamwidth at grazing angles of 10,20,30,...,80,88 degrees
- 2) interpolate the effective beamwidths for intermediate grazing angles (and compute effectively insonified area)
- 3) find the on-axis $S/V + Rec.Sens.$ at room temperature and a pressure of 1 bar
- 4) determine the correction for $S/V + Rec.Sens.$ for the grazing angle from the XZ-beampattern
- 5) correct the $S/V + Rec.Sens.$ for the temperature and pressure changes

2.2.3 Noise

System noise, ambient noise and flow noise, all interfere with the acoustic signal we want to measure. In spite of careful design, the backscatter system is very noisy at high receiver gains or high time-varied-gain steps. In order to analyze the backscatter at low signal to noise ratios i.e. at low grazing angles or in nodule free and rock free zones, the noise levels have to be known. Therefore the noise was measured in the laboratory as well as at sea.

a) Noise measurements in the laboratory

For the noise measurements in the laboratory, the same set up was used as for the gain calibrations (figure 2-2). We determined the noise levels at the top side (deep tow control electronics) with the input at the transducer open for a TVG = 0 dB and a TVG = -60 dB with the lowest possible receiver gains. From these measurements, the noise level at the input can be calculated by adding the already measured system gains and subtracting the bandwidth by

$$V_{noise}(1Hz) = \frac{V_{top}}{gain \sqrt{BW}} \quad (2-5)$$

where $V_{noise}(1Hz)$ is the noise at the electronics input reduced to 1 Hz (volts rms), V_{top} is the noise measured at the top side electronics with the gains set to $gain$, and BW is the system bandwidth. The results are summarized in table 2-8. Although these measurements tell us what the lowest recognizable signal level is, they are insufficient, as they were made under idealized conditions. In situ measurements at sea during a full sized deep tow operation are needed if you want to extract signals with low signal to noise ratios.

frequency	output without gains	noise for TVG 0 dB	noise at input ¹
4.5 kHz	-117 dB	1.5 μV	-147 dB
9 kHz	-115 dB	1.5 μV	-148 dB
15 kHz	-117 dB	1.4 μV	-152 dB
30 kHz	-113 dB	2.3 μV	-151 dB
60 kHz	-105 dB	5.6 μV	-145 dB
112 kHz	-107 dB	4.0 μV	-147 dB
163 kHz	-110 dB	3.2 μV	-150 dB

dB = dB ref 1 Volt rms

Receiver DDT0 gain = 2/16 for all frequencies

1) per Hz

Table 2-8 : Noise measurements in the laboratory

b) Noise measurements at sea

On the test expedition Ceres 1 in June 1982, we were able to measure the noise levels on 3 of the 5 transducers. These data were relevant for the design of the whole system, but they have no significance in the data analysis discussed below and will not be discussed further.

During the data collections on Echo 1 and Echo 2, we made new noise measurements in 2 different ways:

- Without changing anything on the gain settings, we stopped transmitting, and listened for 5 minutes to the noise, cycling through the different frequencies as usual.
- We moved the vehicle from the data collection depth slowly higher, so that the first return came in later and later. This method permits to measure the noise levels before the first return without having to turn off the transmit pulse.

In both cases we were able to determine the noise levels for the general operating conditions and for the gains set on that particular run. The digitized noise intensities were averaged for each TVG step, and made available for the data processing in a disk file.

The standard deviations of the averaged rms noise amplitudes are between 25 and 30%. If I_S is the intensity of the signal, I_N is the intensity of the noise, then the intensity of the signal and the noise I_{S+N} is given by

$$I_{S+N} = I_S + I_N \quad (2-6)$$

Equation (2-5) can be rewritten as

$$I_S = I_{S+N} - I_N \quad (2-6')$$

The error in the determination of the signal is then given by

$$(\Delta I_S)^2 = (\Delta I_{S+N})^2 + (\Delta I_N)^2 \quad (2-7)$$

and the relative errors are

$$\left(\frac{\Delta I_S}{I_S} \right)^2 = \left(\frac{\Delta I_{S+N}}{I_S} \right)^2 + \frac{1}{\alpha^2} \left(\frac{\Delta I_N}{I_N} \right)^2 \quad (2-8)$$

If $\alpha \gg 1$, the second term can be neglected and the error of the signal I_S equals the measurement error of I_{S+N} . This leads to an error contribution of 15% for $\frac{I_S}{I_N} = 2$, 9% for $\frac{I_S}{I_N} = 4$, and 3% for $\frac{I_N}{I_S} = 100$.

2.3 Data collection and processing

2.3.1 Experimental set up

After the transponder net had been established at site 'E', photographic and side scan sonar data were collected. These permitted us to assess the nodule coverage, nodule free areas and the mining tracks of the Ocean Mining Associates. So we could optimize the selection of the areas for the backscatter measurements as well as those for the box coring (Spiess et al., 1984), all located with a 2.5 meter rms residual error within the transponder net. After a set of tests of the backscatter equipment, the receiver gains, the time-varied-gain and the pinglengths were adjusted so as to get the best possible signal to noise ratios from high to low grazing angles. After all the electronics had been set up, the transponder navigated fish was towed at a prearranged height (27, 35 or 72 meters) above the sea floor, with vertical excursions of ± 4 meters. Pinging at one frequency after the other, the returned signal was recorded for about 0.8 seconds after each ping i.e. up to a slant range of 600 m. This way, it took 7 full seconds to cycle once through all 7 frequencies. During that time the fish traveled about 5.5 m along the sea floor. Figures 2-22a and 2-22b show the geometry. The sound travels away from the transducer, hits first the bottom at normal incidence (this is right below the vehicle for a flat horizontal bottom), then insonifies one ring sector after the next. For a flat sea floor, at any given time, the backscattered intensity arriving at the hydrophone comes from a well defined sector of the sea floor (associated with a particular grazing angle). If the nodule coverage is low, a substantial amount of acoustic energy penetrates the sea floor at 4.5 and 9 kHz, before it is partially reflected by subbottom reflectors. These reflections add to the surface backscatter and, except at normal incidence, cannot be timed out.

On Echo 2 the above described procedures were followed in general. At the

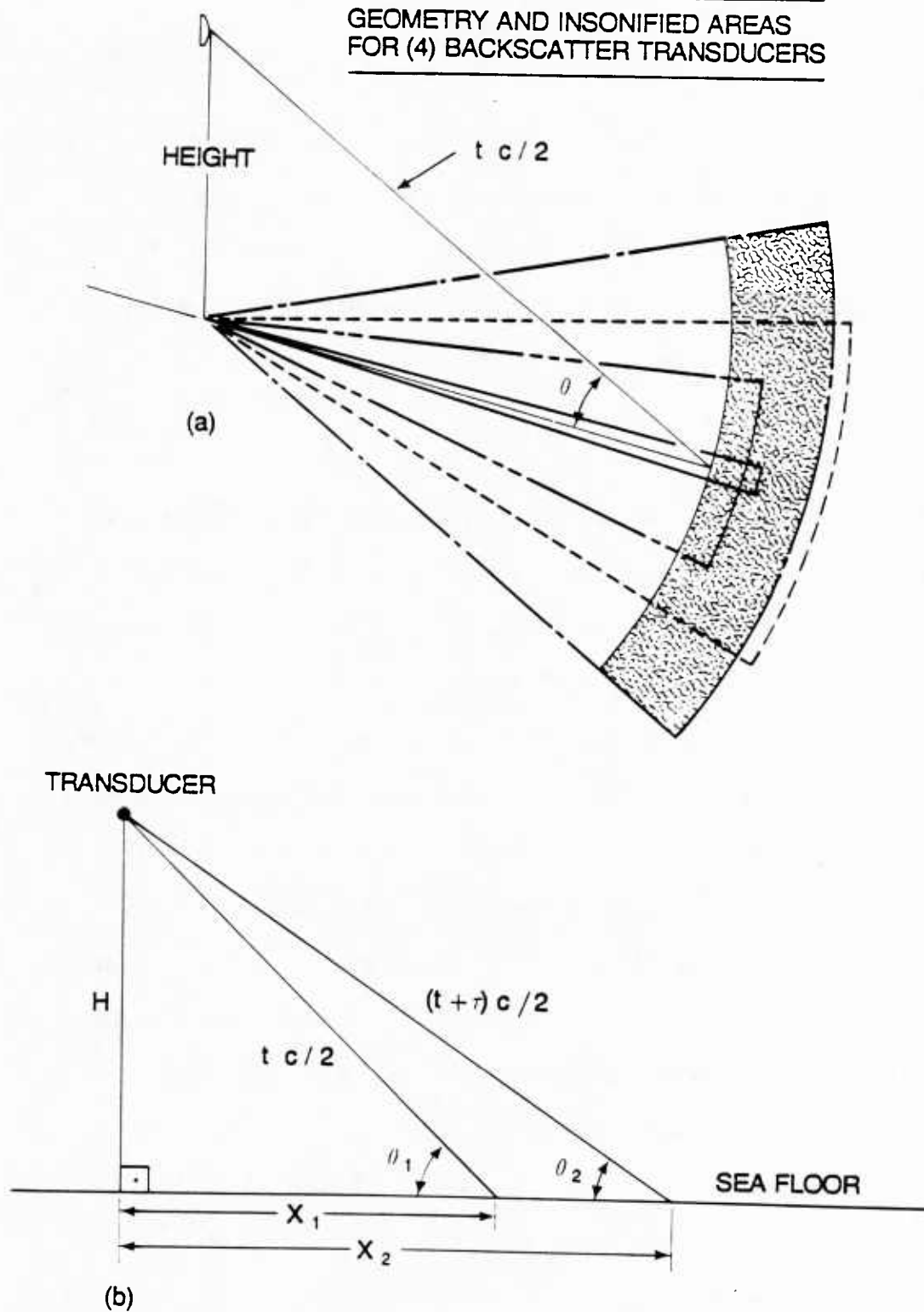


Figure 2-22. Geometry of backscatter experiment

a) insonified areas: The insonified areas depend on the distance to the transducer, the pulse length and the beamwidth. Different beamwidths and pulse lengths give different areas which overlap as indicated.

b) schematics of geometry: The fish with the backscatter transducers is at a height H above the sea floor. At any moment t (time since transmission), the backscattered energy comes from a well defined patch of the sea floor (and range of grazing angles)

Thirtymile Bank the water was shallow enough so that the fish followed the ship's track at a short distance. No transponders were launched and the ship was navigated using Loran C and Navstar. At the foot of the Patton escarpment, the transponders had been recalled before the last lowering (lowering 4) and the ship was navigated along a straight track using Loran C and satellite navigation.

2.3.2 Data recording

As illustrated in figure 2-3, the data are sent from the Deep Tow control electronics to a PDP-11/2 computer system with a 12-bit ADV-11-digitizer, a programmable clock and a standard magnetic tape drive. The control program waits for the time-zero-reference key from the Deep Tow control electronics, starts the digitizing process at the desired digitizing rates at the desired times, converts the digitized voltages into integers from -2048 to 2047 and stores them, together with a 20-word header containing date, time and vehicle pitch, in 2048-word records on magnetic tape. On Echo 1 and Echo 2 another computer recorded at the same time transponder navigation (whenever used), depth from uplooking sonar, ambient pressure, height from downlooking sonar, compass heading and transmissiometer readings, while the returns from the 110-kHz side looking sonars were displayed on a grey scale recorder only. A special parameter file was created by the author for each backscatter run or whenever a parameter was changed. This file contains start and end times of the run, gain settings, pitch scale, pulse lengths and digitizing rates. Partially because of the unsatisfying beampatterns, the received signal in some of the areas varied so much with time and grazing angle, that it was not possible not to overdrive the first return and to measure at the same time the backscatter at low grazing angles. As the nodule coverage varied substantially in the South-North direction where bare mud was followed by a transition zone with few, but large nodules

and a very densely covered area with smaller nodules, it was decided to make 2 backscatter runs along the same path :

A run at 75 meters off the sea floor allowed us to receive the first return without overdriving the system, while the signal was masked by the noise for all grazing less than 60 degrees.

A second run made at a height of 35 meters overdrove the first return (at all frequencies except 60 kHz, where there is a null in the beampattern in the downward direction), but it allowed us to get a good signal to noise ratio at all grazing angles from 75 degrees down to about 5 degrees (20 and 21 June 1983 on Echo 1, 11 and 12 August 1983 on Echo 2).

2.3.3 Computer limitations

The amount of acoustic data collected on the cruises Echo 1 and 2 cannot be processed without a computer system. Even with conventional laboratory computers like PDP-11 or VAX, the processing is very time consuming.

At the time of the Echo 1 expedition, only a PDP-11/2 and a PDP-11/23-Plus computers were available to collect and analyze the data. Both computers were running under the RT-11 operating system, which did not permit the use of programs exceeding about 20k words. This called for a large amount of overlayed subroutines as for parameter inputs from disk files. The acquisition of a faster PDP-11/73 with nearly a Megabyte of memory and a TSX-multi-user operating system permit us to use today much more memory for the post cruise data processing. TSX is, however, not a real time operating system, and can therefore not be used for data collections or real time processing. These are the reasons why the backscatter software pushes the overlaying capability of RT-11 to its limits and takes certain parameter inputs from Winchester disk files, two relatively slow processes.

2.3.4 Data processing

Before the data were processed, the noise levels were determined either from oscilloscope readings or from digital recordings made during the backscatter experiments at sea.

Figure 2-23 shows a simplified flow diagram of the backscatter programs. The 2048-word record containing a short 20-word header with the date, the time and the vehicle pitch, is read from the magnetic tape into the computer memory. The digitizing was always 10 kHz for the first 200 samples (interval before the electronics switches to the TR-switch). After the frequency has been identified by measuring the spacing between the two frequency markers, the parameter file with the gain settings and pulse lengths and the file with the transducer response are read from the disk. A new 64-word header with all the parameters listed in the appendix 2, is created and written into memory together with the first 1984 digitized voltages. Now the data analysis can start: The transmit voltage, the height of the transducer above the bottom, the numbers of the words corresponding to the selected grazing angles or TVG steps can be determined. After the noise levels have been read from a disk file, the digitized voltages are corrected for the noise and vehicle pitch, before the sound pressure levels, backscatter coefficients or other parameters which describe the backscatter are derived with the sonar equations. These are written into formatted disk files and made available as graphs.

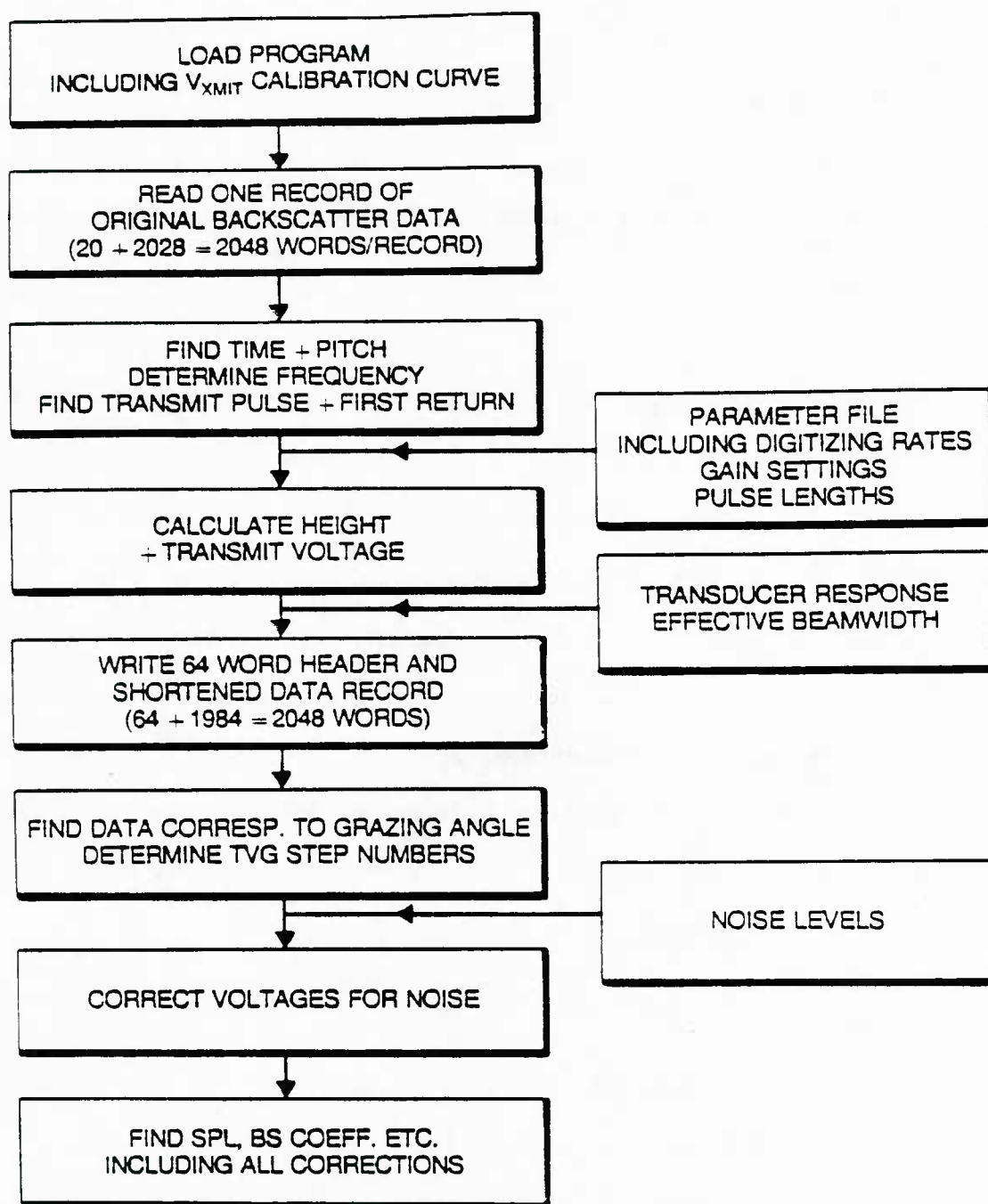


Figure 2-23. Simplified flow diagram of backscatter programs This flow diagram outlines the basic computer programs used to compute the backscatter coefficients

2.4 Environment

2.4.1 Bottom roughness

Nodules stick 2-5 cm out of the sediments. The acoustic wavelength is 0.9 to 33 cm. A criterion for the roughness (Urlick, 1983, p.129) of a surface is given by the Rayleigh parameter R , defined by

$$R = kH\sin\theta \quad (2-9)$$

where H is the rms wave height (crest to trough). In our experiment, R is always greater than 0.33 in nodule-covered areas i.e. there is always some scattering. When $R \gg 1$, there is only scattering.

The roughness of the nodule bare areas at site 'E' is the same as the one for the nodules, but the horizontal scale differs (figure 1-7). The Thirtymile bank is not isotropic with respect to roughness. It varies from an area similar in roughness to site 'E' to an area paved with phosphorites where H is of the order of 10 cm (figure 1-20). The base of the Patton Escarpment can be divided into two areas: one which is smooth on the scale of the wavelengths used, and one which is similar to site 'E' (figure 1-23).

2.4.2 Sound Speed and Ray Bending

The sound speed increases with salinity, pressure and temperature (Urlick, 1983). Let z be the depth coordinate, and x the other coordinate in a vertical xz -plane. Using Fermat's principle for a horizontally stratified ocean, the path of an acoustic ray is given by the variation of the Eikonal

$$I = \int_A^B n(z) ds \quad (2-10)$$

$$n(z) = \frac{c_o}{c(z)} \quad (2-11)$$

is the index of refraction, c_o is the sound speed at the reference level, A and B are the

start and end points respectively. After some algebra and the use of the hypothesis that the sound speed does not change in a horizontal plane, we find that

$$n \cos \theta = \text{constant} \quad (2-12)$$

$$n_1 \cos \theta_1 = n_2 \cos \theta_2 \quad (2-12')$$

From this it follows that the ray paths are bent upward if the sound velocity increases with depth as is the case in the deep ocean. As a result, the grazing angle decreases compared to what it would be if the rays were straight lines, and the path length between two fixed points increases.

The sound speed can be computed as follows: the salinity at the site 'E' is 34.7‰, and the temperature is 1.5°C (J. Reid, personal communication). Using these data in Leroy's simplified pressure equation (Leroy, 1969)

$$p(z) = 1.0052405(1 + 5.28 \cdot 10^{-8} \sin^2 \phi)z + 2.36 \cdot 10^{-8} z^2 \quad (2-13)$$

where p = the pressure in decibars, z = depth in meters and ϕ = latitude, we find a pressure of 4573 decibar at a depth of 4500 m (40 meters above the sea floor), and 4533 decibar at a depth of 4470 m (70 m above the sea floor). Using this in the following equation (Lovett, 1978.eq.3)

$$c = c_o + c_T + c_S + c_p + c_{STP} \quad (2-14)$$

where

$$c_o = 1402.394 \text{ m/s}$$

$$c_T = 5.01132T - 5.513036 \times 10^{-2} T^2 + 2.221008 \times 10^{-4} T^3$$

$$c_S = 1.332947S$$

$$c_p = 1.605336 \times 10^{-2} P + 2.12448 \times 10^{-7} P^2$$

$$c_{STP} = -1.266383 \times 10^{-2} TS + 9.543664 \times 10^{-5} T^2 S$$

$$-1.052396 \times 10^{-8} TP^2 + 2.183988 \times 10^{-13} TP^3$$

$$-2.253828 \times 10^{-13} SP^3 + 2.062107 \times 10^{-8} TS^2 P$$

we find a sound velocity of 1532 m/s at a depth of 4500 m, and 1531 m/s at a depth

of 4470 m. The speed gradient with pressure $dc/dp = 1.8 \times 10^{-2}$ m/s/decibar. Using these results in the equations for the sound rays allows us to compute the grazing angles for the various fish heights.

Equation (2-11) leads to

$$\frac{n_1}{n_2} = \frac{c_2}{c_1} \quad (2-15)$$

Using this in equation (2-12') leads to

$$\cos \theta_2 = c_2/c_1 \cos \theta_1 \quad (2-16)$$

Associating the index 1 with the transducer on the fish, the grazing angle θ_2 on the sea floor can be related to the grazing angle at the transducer (table 2-9).

	height = 35 m	height = 70 m
θ_1	θ_2	θ_2
1.6	0.0	
2.0	1.1	
2.3	1.6	0.0
2.5	1.9	0.9
3.0	2.5	1.9
4.0	3.6	3.3
5.0	4.7	4.4
10.0	9.9	9.7

Table No. 2-9: grazing angle θ_2 on the sea floor as a function of the grazing angle at the transducer θ_1 .

Comparison of the grazing angles at the transducer (θ_1) and at the sea floor (θ_2) as computed with the ray theory for a sound speed gradient of 1.2×10^{-2} m/s/decibar. The heights are the transducer positions above the sea floor .

The ray bending influences also the transmission loss. For a constant sound speed gradient and small grazing angles ($\theta = \sin \theta$), the transmission anomaly is given by

$$H = 10 \log_{10} E/r^2/I = 20 \log_{10} \cos \theta \quad (2-17)$$

where E/r^2 is the inverse square spreading law and I is the energy as determined from the bent rays (Navy, 1969). H is found to be less than -0.15 dB in all cases of interest.

As we listen only for about 0.9 seconds at each transmission, we cannot get to grazing angles below 2.9° at a height of 35 m, and 5.8° at a height of 70 m. This keeps the corrections for the grazing angles well below 0.5° . In the data analysis, corrections are only needed for grazing angles below 15° , as for the higher grazing angles the correction is less than the uncertainty of the measurement of the grazing angle. Both, the deviations from the square spreading law and the increase of the distance between the transducer and a point on the sea floor are negligible.

2.5 Reflectivity and backscatter of the sea floor

2.5.1 Assumptions, sub-bottom reflectors and errors

Processing of acoustic reverberation data is very time consuming, even with the help of fast laboratory computers like the PDP-11/73 with floating point accelerators. This calls for simplifying assumptions about the experimental conditions to reduce the complexity and time involved in the processing of the data. In making such assumptions, it was assumed that the errors involved would be negligible.

In the idealized experiment, a point transducer projects and receives sound in a scattering free, homogeneous and isotropic ocean (compare chapter 2.4 on sound velocity and ray bending). The ocean is bounded at the bottom by a plane, rough sea floor which both reflects and scatters sound. The transducer is far enough above the bottom so that the sound waves hitting the sediment/water interface cannot be distinguished from plane waves. Then one needs to correct only for absorption and spherical spreading (no ray bending!) in order to remove the height of the transducer above the sea floor. These assumptions are generally good in clear deep water without strong currents if the sea floor is in the far field of the transducer. This is the case for all the backscatter transducers, if the height above the sea floor d , fulfills (2-18) for the MPL 83-1 at 112 kHz (worst case)

$$d \gg \frac{\pi a^2}{\lambda} \quad (2-18)$$

where a is half the length of the longest transducer axis and λ is the acoustic wavelength (ANSI S1.20-1972). This required a transducer height of at least 15 meters above the sea floor. It ought to be noted that the transducers are not baffled, and that there are reflectors on the vehicle which interfere with the transmit pulse and with the received signal. This means that the effective sizes of the transducers are larger than their physical sizes, and the vehicle with the transducer must

be farther away from a target for the target to be in the far field. On the Echo expeditions, the minimal height was 35 meters.

This is essentially the model utilized to determine the bottom loss and the backscatter coefficients. It has been refined, however, by using beam pattern information and some sea floor topography.

At frequencies from 15 to 163 kHz (absorption in sediments exceeds 8 dB/m at 15 kHz and increases with frequency), it was assumed that the energy returned by sub-bottom reflectors is negligible and that all the energy received at the transducer comes from reflections and scattering of the sea floor. At 4.5 kHz, it is possible to recognize two subbottom reflectors in a nodule free area at site 'E', one at a depth of 10 meters, the other one at 20 meters. Similar reflectors exist in rock free and nodule free zones as well as in nodule covered zones in other parts of the ocean (Bischoff and Piper, 1979; Spiess, et al., 1984; Spiess and Weydert, 1984). From the 4 kHz 'p'-subbottom profiles collected during and between the camera runs, we know that there are subbottom reflectors throughout site 'E'. In areas which are covered with either rocks or nodules, a much smaller fraction of the energy arriving at the sea floor can penetrate into the sediments than in bare areas. Hence the return from sub-bottom reflectors is much smaller and can probably be neglected. Using the return from the reflectors at 10 meters and 20 meters depth in the south-east corner of site 'E', it can be shown that this error exceeds 3 dB at 4.5 kHz for sparse nodule or rock coverage. This makes it difficult to use a frequency of a few kHz for nodule assessment at intermediate grazing angles, especially as changes in the depth of the upper acoustic reflector correlate with changes in nodule coverage (In some areas, it might enhance the differences though). The normal return and the return from very low grazing angles permit, however, the use of a window to time the return from the sub-bottom reflectors out. This allows one to employ frequencies of a few kHz at normal

incidence. At grazing angles from 20 to 60 degrees, the 4.5 kHz data have to be treated with suspicion for vehicle heights of 30-40 meters above the sea floor. Returns at these grazing angles can arrive at the same time as the returns from the sub-bottom reflectors. In some cases it was possible to estimate the intensity from the sub-bottom reflector and compare it to the intensity at the critical grazing angles. Whenever the intensity returned at some time t (and grazing angle θ) is large compared to the return expected from the sub-bottom reflectors, the data do not need to be rejected.

Three kinds of errors need to be considered: a) absolute errors, b) relative errors at fixed grazing angles i.e. errors to which the individual measurement is subjected, and c) errors at different grazing angles.

a) Absolute measurements are accurate only within the accuracy of the absolute calibration (chapter 2.2). These do not effect the differences between measurements made under the same conditions in different environments or within the same environment.

b) The accuracy of relative measurements at a given grazing angle is influenced by the knowledge of the geometry and the characteristics of the environment. Relative range and absorption errors total less than 0.2 dB (worst case). The changes of the insonified area at a fixed grazing angle are accurate within 0.1 dB. The network response of the electronics has been calibrated with a relative accuracy of 0.2 dB for signal to noise ratios exceeding 6 dB. From this it can be concluded that the comparison of data of the different environments is good within 1 dB (12%) or better for each frequency.

c) The incomplete knowledge of the beampatterns as a function of grazing angle is an exception to this rule. The error in the effective beamwidth and the

transmit response is less than 1 dB for grazing angles of 0, 10, 20, 30, 40 and 50 degrees (chapter 2.2).

2.5.2 Normal incidence

2.5.2.1 Rayleigh coefficient and bottom loss

In this section an attempt is made to parametrize the acoustic bottom loss according to Lord Rayleigh's specular reflection model (Rayleigh, 1896). The sea floor is considered a plane interface between two fluids with densities ρ_1 and ρ_2 and sound velocities c_1 and c_2 respectively. If the rms roughness is smaller than the acoustic wavelength, the assumption of a flat sea floor will be valid. Hamilton has shown that the description of the sea floor as a liquid is good, but that the sediments do propagate shear waves. The fluid model will be incorrect, but not gravely so.

The wave equation in any number of dimensions can be written as

$$\nabla^2 P = \frac{1}{c^2} \frac{\partial^2 P}{\partial t^2} \quad (2-19)$$

If the transducer is far enough from the sea floor so that the transducer can be considered a point source i.e.

$$Height > \pi L^2 / 4\lambda \quad (2-20)$$

where L is the length of the transducer, then the acoustic wave can be considered to propagate radially. For a simple harmonic source of the form

$$P_S = P_o e^{i\omega t} \quad (2-21)$$

the solution to the wave equation becomes in spherical coordinates

$$P = \frac{P_o}{r} e^{-i(kr - \omega t)} \quad (2-22)$$

where $k = 2\pi/\lambda$ is the wave number. If there is some absorption in the medium, then

$$P = P_o e^{-i(kr - \omega t)} \frac{e^{-\frac{\alpha}{2}r}}{r} \quad (2-23)$$

where α is the absorption coefficient. If this wave field is reflected elastically from a plane boundary at a distance H from the transducer (normal incidence), and if the pressure and the normal component of the sound velocity are continuous at the boundary, the reflected wave can be written as

$$P = R_a P_o e^{-ik(2H-\omega t)} \frac{e^{-\frac{\alpha}{2}2H}}{2H} \quad (2-24)$$

where the Rayleigh reflection coefficient R_a is given by

$$R_a = \frac{\rho_2 c_2 - \rho_1 c_1}{\rho_2 c_2 + \rho_1 c_1} \quad (2-25)$$

This can be rewritten as

$$R_a = \frac{Z - 1}{Z + 1} \quad (2-26)$$

where $Z = \frac{\rho_2 c_2}{\rho_1 c_1}$. The acoustic intensity I is given by

$$I = \frac{p^2}{\rho c} \quad (2-27)$$

From this we find

$$I = I_o R_a^2 \frac{e^{-\left(\frac{\alpha}{2}2H\right)^2}}{(2H)^2} \quad (2-28)$$

since both the incident and reflected waves propagate in medium 1. To get the corresponding sonar equation, we take on both sides the logarithm and multiply by 10 to find

$$10 \log I = 10 \log I_o + 20 \log R_a - 20 \log \alpha H - 20 \log 2H \quad (2-29)$$

or

$$EL = SL - BL - TL \quad (2-30)$$

where

$$EL = \text{Echo Level}$$

$$SL = \text{Source Level}$$

$$TL = \text{Transmission Loss}$$

α = absorption coefficient (dB/m).

and the bottom loss BL has been defined by

$$BL = -20 \log R_a \quad (2-31)$$

It is evident that by integration over a pulse length, this equation can be written in terms of energy instead of (peak) intensities as

$$BL = S_{EL} - E_{EL} - TL \quad (2-32)$$

where

BL = Bottom Loss

S_{EL} = Energy transmitted per ping

E_{EL} = total energy received per ping

Both approaches will be used below. For the derivation of the Rayleigh reflection coefficient, it had to be assumed that the incident waves are plane waves and that both the pressure and the normal component of the velocity are continuous. Officer (Officer 1958) has shown that this simple model is a valid approximation for a spherical wave incident on a flat interface if

$$\frac{c_1}{\omega H [c_1^2/c_2^2 - \sin^2\theta]^{3/2}} \ll 1 \quad (2-33)$$

For normal incidence, $\theta = 0$ and equation 2-32 reduces to

$$\frac{\lambda_1}{2\pi H c_1^3/c_2^3} \ll 1 \quad (2-34)$$

where $\omega = 2\pi c_1/\lambda_1$. This requirement was always fulfilled during the Echo 1 surveys. Although it has been shown that the fluid/fluid model is a valid approximation to describe the reflections of a smooth sea floor (Hamilton, 1970) the above theory can completely fail if the roughness is comparable to the acoustic wavelength.

Measurements of the bottom loss made by Breslau at 12 kHz (Breslau, 1967) in 350 meter deep water give an energy based bottom loss of 14 dB and a peak based bottom loss of 18 dB for silty clay at 40° 15'N, 70° 43'W (Martha's Vineyard).

Breslau also established a correlation between the sediment type and porosity and the bottom loss. Subsequent work by Hamilton (Hamilton, 1974) refined Breslau's correlations and permitted to estimate the bottom loss from sediment properties. Using Hamilton's data for ρ_2 and c_2 , one can compute the Rayleigh coefficient R_r and the bottom loss BL using equations 2-24 and 2-30 respectively. The results are summarized in table 2-10. Unfortunately, Hamilton did not study the frequency dependence of the bottom loss.

<i>environment</i>	<i>Bottom Loss</i>
very fine sand	8-9 dB
silt	10-12 dB
silty clay	16-18 dB
clay	17-19dB

Table 2-10: Bottom loss [dB] as computed from Hamilton 1974

The bottom loss as calculated at 4.5 kHz from that data at site 'E' averages 26 dB over the sediments and 22 dB over the nodules. These numbers are substantially higher than those from Hamilton and Breslau. Hamilton worked on a different type of sediments, and did not predict a frequency dependence. Breslau made his measurements at 12 kHz, a frequency at which the return is likely to be mostly back-scattered, and little energy penetrates the bottom (compared to 4.5 kHz).

A simple test can be made to check the validity of the reflection model: The spreading loss for the backscattering is $40\log H + 10\log A$ (A is the effectively insonified area) while the spreading loss for the reflection is $20 \log 2H$. If one of the two mechanisms is strongest, than either the backscatter coefficient or the bottom loss does not change while the height of the transducer is varied.

The bottom loss calculated with (2-32) at site 'E' is a constant for nearly uniform areas and constant fish height. When the vehicle is pulled higher, the bottom loss increases rapidly for frequencies from 9 to 163 kHz (figure 2-24). (only one good

data set over the nodule field).

If the return is composed of scattered energy, then the corrections for spherical spreading and insonified areas have to be used. The changes in returned energy (use the negative of the backscatter coefficient) are less pronounced if the applied correction is spherical spreading for the returns from the manganese nodules, than if those data are treated as reflected energy. From this it can be concluded that at least a large part of the returned energy is scattered energy. As the fish was also moving horizontally, it is difficult to estimate the relative importances of reflected and scattered energy with this method. A different approach will be used below to determine the parts of scattered and reflected energy in the returns.

2.5.2.2 Envelope statistics

Assuming that the incoherent initial process is described by a normal distribution, it can be shown (Anderson, 1984; Ol'shevskii, 1967) that the envelope distribution of the sum of the reflected and scattered return at normal incidence is given by

$$p(R) = 2R \left(1 + \frac{I_R}{I_S}\right) \exp \left[-R^2 \left(1 + \frac{I_R}{I_S}\right) - \frac{I_R}{I_S} \right] J_0 \left(2R \left(1 + \frac{I_R}{I_S}\right)^{1/2} \left(\frac{I_R}{I_S} \right)^{1/2} \right) \quad (2-35)$$

where both I_R and I_S have been normalized by dividing them by their sum $I_R + I_S$, R is the amplitude of the envelope of the sum of the noise and the signal, J_0 is the modified Bessel function of zero order, and $p(R)$ is the generalized Rayleigh distribution. In this form the distribution describes the transition region between the simple form of a Rayleigh distribution

$$\frac{I_R}{I_S} \ll 1 \quad p(R) = 2R \exp(-R^2) \quad (2-36)$$

and a Gaussian

$$\frac{I_R}{I_S} \gg 1 \quad p(R) = \frac{\exp \left[(R-1)^2 \frac{I_R}{I_S} \right]}{\sqrt{2\pi}} \quad (2-37)$$

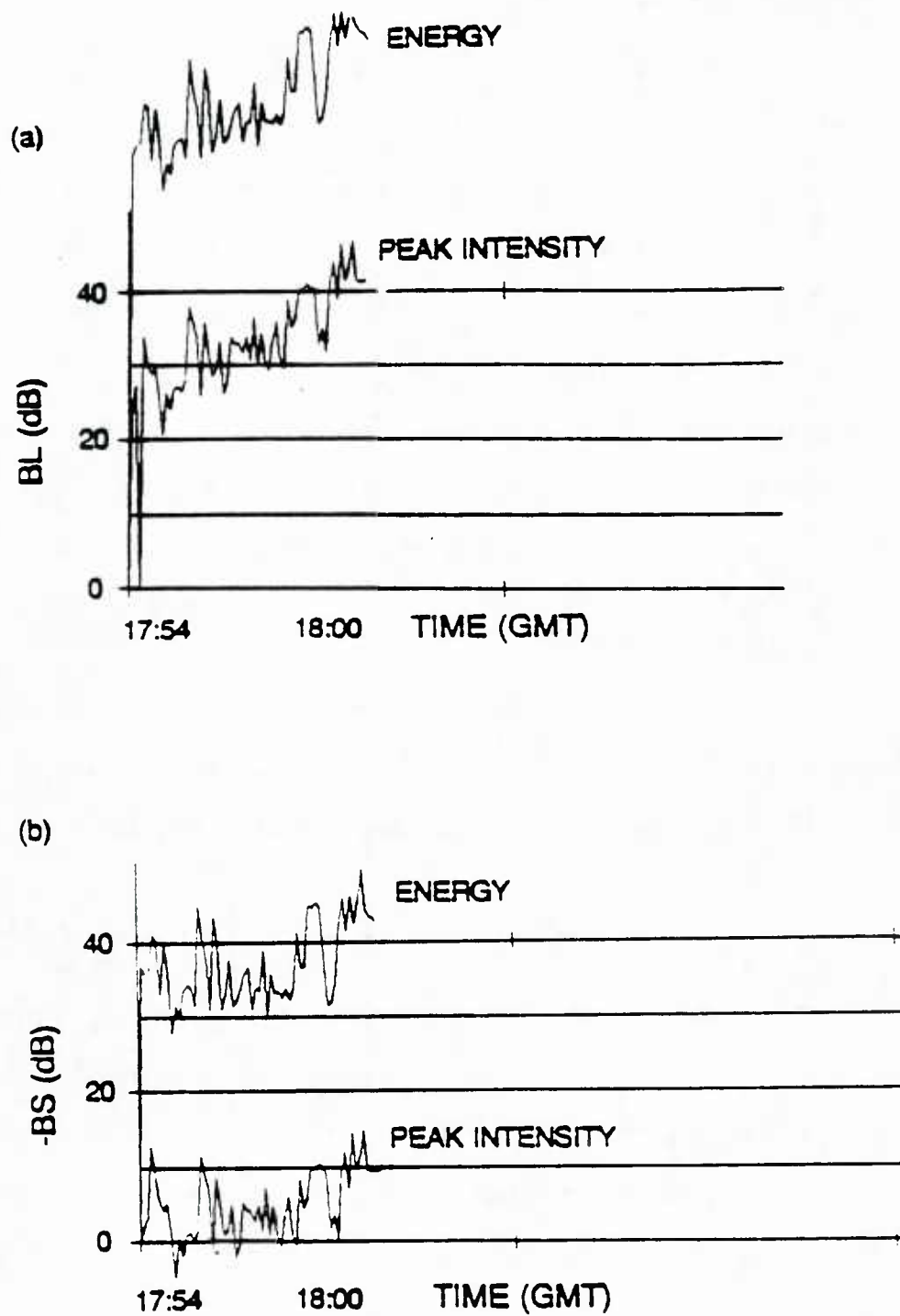


Figure 2-24. Bottomloss versus backscatter coefficients

- a) Bottom loss calculated while the fish is pulled higher
- b) Backscatter coefficients for the same time

This permits one to determine the $\frac{I_R}{I_S}$ ratios by comparing the experimental distribution with the theoretical distribution $p(R)$. Some examples of the envelope distributions are shown on a double logarithmic scale in figure 2-25. The $\frac{I_R}{I_S}$ have been tabulated for 10 minute intervals in table 2-11 for 20/21 June 1983. Mud is from 23:20 - 23:30 GMT, and the transition zone from 23:35 - 23:45 GMT. This simple method permits one to recognize that at 4.5 kHz the nodules do not appear rougher than the mud (the mud might cover nodules, though), while at the higher frequencies they do. While the ratio $\frac{I_R}{I_S}$ is roughly 8 at 4.5 kHz, it becomes less than 0.06 at frequencies exceeding 15 kHz. This means that at frequencies of 15 kHz or more the return from nodule fields is mostly scattered energy, while below 15 kHz there is a substantial amount of reflected energy. At the lower frequencies (9 kHz or lower) the major part of the return at normal incidence is reflected energy.

time (GMT)	4.5 kHz	9 kHz	15 kHz	30 kHz	110 kHz
22:54 - 23:00	4	2	0	--	--
23:00 - 23:10	6	2	1.0	0.5	0
23:10 - 23:20	6	0.5	0	2.0	2.0
23:20 - 23:30	8	6	2.0	2.0	0
23:30 - 23:40	8	2	0	--	--
23:40 - 23:50	4	2	0	0	0
23:50 - 24:00	8	2	2.0	0	0
00:00 - 00:10	8	2	0.5	0	0
00:10 - 00:20	8	4	0	0	0
00:20 - 00:30	8	2	0.5	0	0
00:30 - 00:40	8	2	0	0	0
00:40 - 00:50	8	-	1.0	0	0
00:50 - 01:00	8	4	0	0	0
01:00 - 01:10	12	-	0.5	0	0
01:10 - 01:20	8	-	0	0	0

Table No. 2-11: $\frac{I_R}{I_S}$ for the 75 meter run on 20/21 June 1983 as a function of time and frequency.

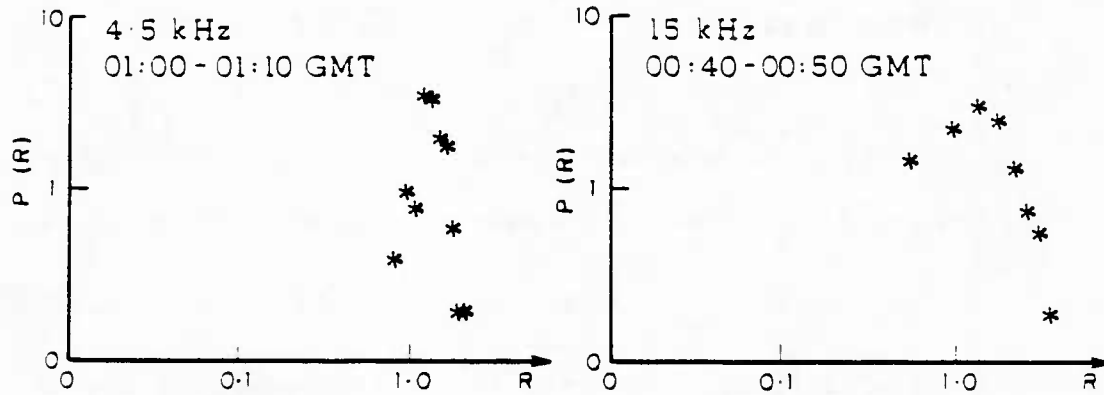


Figure 2-25. Envelope Distributions

Frequency of occurrence of envelopes of backscatter as a function of the amplitude, normalized by the mean. Both axis are logarithmic

From this it can be concluded that over the nodule field, the received intensity is mostly reflected energy at 4.5 kHz, 2/3 of the total reverberation are reflected energy at 9 kHz, and 1/3 at 15 kHz. The received intensities must be corrected by these factors before the backscatter coefficient can be calculated. The sediments at site 'E' appear a little more coherent as is suggested by the higher ratios of reflected to backscattered energy.

It has been shown that the ratio of the reflected to the backscattered return is proportional to the product of the rms-roughness and a two-dimensional correlation area (Stanton, 1984). The available data do not permit to decide which of the two parameters is effected by the change as the roughness of the sediments could well exceed that of the nodules imbedded in the sediments.

2.5.3 Backscattering strength

2.5.3.1 Background

In the following the sonar equations as used for the data analysis of the backscattered signal will be derived and the following simplifying assumptions made:

- 1 - The projector is far enough from the sea floor so that the source can be considered a point source, and that the waves incident on the sea floor are approximately plane waves.
- 2 - The propagation paths are straight lines (see chapter on sound velocity and ray bending). The only sources of attenuation are spherical spreading and absorption. (no volume reverberation)
- 3 - The distribution of scatterers on the sea floor is random and homogeneous within the area insonified at any given instant of time.
- 4 - The number of scatterers within an elemental area dA is large.
- 5 - A short pulse is used i.e. a pulse which is short enough so that the grazing angles under which the backscattering occurs do not change substantially over the area insonified at any given instant of time, and that propagation effects over the elemental area can be neglected.

Consider figure 2-22. If $b(\theta, \phi)$ is the beam pattern of the projector, and I_o is the on-axis intensity at a distance of 1 meter from the projector, the intensity I_{inc} on the sea floor at a distance R and a grazing angle θ_g is given by

$$I_{inc} = \frac{I_o b(\theta, \phi)}{R^2} e^{-\alpha R} \quad (2-38)$$

where α is the absorption coefficient. Let S be the backscattering coefficient defined by

$$S = \frac{I_{BS}}{I_{inc}} \quad (2-39)$$

where I_{BS} is the intensity which is backscattered to the source, measured at a

distance of 1 meter from the scatterer(s). I_{BS} is given by equation (2-40):

$$I_{BS} = e^{-\alpha R} \frac{I_{inc}}{R^2} S dA \quad (2-40)$$

$$= e^{-2\alpha R} \frac{I_o b(\theta, \phi) S}{R^4} dA \quad (2-40')$$

If the voltage response of the hydrophone is X (voltage is proportional to incident incremental pressure) and its beampattern is $b'(\theta, \phi)$, then the output voltage at the hydrophone terminals is given by

$$(V_{rec}^{rms})^2 = X^2 \frac{I_o e^{-2\alpha R}}{R^4} b(\theta, \phi) b'(\theta, \phi) S dA \quad (2-41)$$

where V_{rec}^{rms} is the mean squared output voltage at the receiver terminals.

Assumption 4 allows one to make dA differential and to integrate over the insonified area A . Since the scatterers are randomly and homogeneously distributed (assumption 3), the scattering coefficient S is a constant. Integrating (2-40) over A , we find

$$(V_{rec}^{rms})^2 = X^2 \frac{I_o}{R^4} S e^{-2\alpha R} \int_A b(\theta, \phi) b'(\theta, \phi) dA \quad (2-42)$$

If we define the equivalent plane wave reverberation level RL as 10 times the logarithm of an axially incident plane wave producing the same hydrophone output as the observed reverberation in dB, we find

$$RL = 10 \log \left(\frac{I_o}{R^4} S e^{-2\alpha R} \int_A b b' dA \right) \quad (2-43)$$

Equation (2-43) is exact under the assumptions 1 to 5 and can be extended to volume reverberation by replacing the differential area dA by the differential volume dV and the area A by the volume V . (Keane, 1968)

In the experiments made in the present study, a short pulse was transmitted to measure the acoustic backscatter properties of the deep sea floor. At any given instant of time, the received reverberation signal came from a well defined patch of

the sea floor corresponding to a small range of grazing angles (figure 2-22). Unfortunately, contrary to the volume reverberation where

$$dV = r^2 c \frac{\tau}{2} d\Omega \quad (2-44)$$

and the integral in 2-42 can be easily evaluated by replacing it over an integral over 4π sterads, the integral

$$\Psi = \int b b' dA \quad (2-45)$$

is more problematic.

A transducer at a height H above the sea floor (figure 2-22) transmits a pulse of duration τ at the time zero. At a time $\tilde{t}_0 = \frac{H}{c}$, where c is the sound velocity, the acoustic pulse hits the sea floor. The first echo (normal incidence coherent and incoherent return) arrives at the transducer after a time $t_0 = \frac{2H}{c}$ (90 degree grazing angle). At time $t_0 + \tau$ the whole wave train has hit the sea floor and the last return containing energy from normal incidence is received. From then on, the return comes from a patch of the sea floor determined by the beamwidth, the pulse length, the height of the transducer, and the time since the transmission. If t is the time since the end of the transmission, then all the returns for distances d with

$$\frac{tc}{2} \leq d \leq (t+\tau)\frac{c}{2} \quad (2-46)$$

add together to the signal received at time t . If x_1 and x_2 are defined as in figure 2-22, then the ring insonified at time t by an omnidirectional transducer is given by

$$A_{\text{omni}} = \pi(x_2^2 - x_1^2) \quad (2-47)$$

$$A_{\text{omni}} = \pi(2t\tau + \tau^2)\frac{c^2}{4} \quad (2-48)$$

since

$$t \frac{c}{2} = \sqrt{H^2 + x_1^2} \quad (2-49.a)$$

$$(t + \tau) \frac{c}{2} = \sqrt{H^2 + x_2^2} \quad (2-49.b)$$

For a transducer with an effective beamwidth of $\Delta\phi$ radians, the insonified area is proportional to the beamwidth (figure 2-22b) and is given by

$$A = \pi(2t\tau + \tau^2) \frac{c^2}{4} \frac{\Delta\phi}{2\pi} \quad (2-50)$$

The grazing angle θ_1 and the time t are related by

$$\sin\theta_1 = \frac{H}{t \frac{c}{2}} \quad (2-51)$$

The integral (2-45) can now be replaced by equation 2-50, as for a given grazing angle

$$\begin{aligned} bb' &= 1 & \text{for } -\frac{\Delta\phi}{2} < \phi < \frac{\Delta\phi}{2} \\ bb' &= 0 & \text{otherwise} \end{aligned} \quad (2-52)$$

for an effective beamwidth $\Delta\phi(\theta)$, and (2-42) can be rewritten as

$$RL = 10\log I_o - 40\log R - 10\log e^{-2\alpha R} + 10\log S + 10\log A \quad (2-53)$$

$$RL = SL - 2 TL + BS_A + 10\log A \quad (2-54)$$

where SL is the transmitted energy in dB reference $1 \mu Pa$ at 1 meter, TL is the one-way transmission loss in dB reference 1 meter, BS_A is the backscatter coefficient and A is the effectively insonified area.

After rewriting equation (2-54), the backscatter coefficients can be calculated by

$$BS = 20\log V_{rec}^{rms} - 20\log V_{Xmit}^{rms} + 2TL - (S/V + Rec.Sens.) - 10\log A \quad (2-55)$$

where V_{rec}^{rms} is the rms voltage generated at the transducer terminals by the received signal, V_{Xmit}^{rms} is the rms voltage applied to the projector, S/V is the voltage transmitting response of the projector, $Rec.Sen.$ is the receiving response of the hydrophone, and A is the effectively insonified area.

In order to predict the backscattering strength for different environments, an expression relating S to environmental parameters like the roughness ξ and the impedance

$$z = \frac{\rho_1 c_1}{\rho c} \quad (2-56)$$

where ρc is the impedance of the medium (sea water) and $\rho_1 c_1$ is the average impedance of the sediments of a flat sea floor (see Hamilton 1974 for relationship to porosity and bulk density). Morse and Ingard (Morse and Ingard, 1968) have shown that the scattering of sound incident at a grazing angle θ_i on a patch of rough surface which has also random variations in surface admittance is given by

$$P_s = P_i \frac{e^{ikr}}{\pi r} \frac{\sin \theta_i \sin \theta}{(\sin \theta_i + 1/z)(\sin \theta + 1/z)} \iint \left[ikb(r_o) + k^2 \gamma^2 \xi(r_o) \right] e^{i\mu_x x_o + i\mu_y y_o} dx_o dy_o \quad (2-57)$$

where θ is the grazing angle. The function $b = 1/z - 1/z_o$ is the deviation of the admittance at the point r_o at the surface from the mean value $1/z_o$, and ξ is the normal displacement from the mean shape of the sea floor.

$$\gamma^2 = \cos^2 \theta_i + \cos^2 \theta - \cos \theta_i \cos \theta \cos(\phi_i - \phi) \quad (2-58)$$

where θ and ϕ are the grazing angle and the azimuthal angle under which the sound is scattered. For backscatter this expression reduces to

$$\gamma = 2 \cos \theta_i \quad (2-58')$$

If the two parameters are statistically independent, the intensity of the scattered sound is

$$I_s = 4\pi^2 I_i \frac{A}{r^2} \left| \frac{\sin \theta_i \sin \theta}{(\sin \theta_i + 1/z_o)(\sin \theta + 1/z_o)} \right|^2 \left\{ k^2 |B(k\gamma)|^2 + k^4 \gamma^4 |Z(k\gamma)|^2 \right\} \quad (2-59)$$

where $B(K)$ is the two-dimensional Fourier-transform of $b(r)$, and $Z(k)$ is the two-dimensional Fourier-transform of $\xi(r)$. The first term in braces depends on the impedance variations and in the presence of nodules is defined by the two-dimensional

Fourier-transform of the nodule distribution. The second term describes the roughness. By setting (2-39) and (2-59) equal, the scattering factor S is found to be

$$S = 4\pi^2 \left| \frac{\sin\theta_i \sin\theta}{(\sin\theta_i + 1/z_o)(\sin\theta + 1/z_o)} \right|^2 \left\{ k^2 |B(k\gamma)|^2 + k^4 \gamma^4 |Z(k\gamma)|^2 \right\} \quad (2-60)$$

If the fluctuations of ξ and b are random, their correlation functions will be approximately

$$\gamma_b(d) = \langle b^2 \rangle e^{-\frac{1}{2}(d^2/w_b^2)} \quad (2-61a)$$

$$\gamma_\xi(d) = \langle \xi^2 \rangle e^{-\frac{1}{2}(d^2/w_\xi^2)} \quad (2-61b)$$

Three cases are of interest here:

- environments with different, but constant impedance (different sediment types)
- environments with local changes in impedance (nodules)
- environments with different roughness (different nodule sizes, different sediments)

2.5.3.2 Data reduction

The backscatter coefficients were calculated with equation (2-55) for each digitized sample, after appropriate corrections for the beampatterns and the pitch of the vehicle had been made. It is understood that the reflected energy was subtracted from the total energy for the returns at normal incidence (compare chapter on envelope statistics). These backscatter coefficients were stored on disk or magnetic tape, since their computation was by far the slowest process (many floating point operations and frequent memory swapping). The backscatter coefficients were also displayed graphically. A comparison with the raw signal permitted us to select the grazing angle ranges with valid data (figures 2-26 and 2-27). Then the backscatter coefficients were averaged for each ping over a range of grazing angles using either a

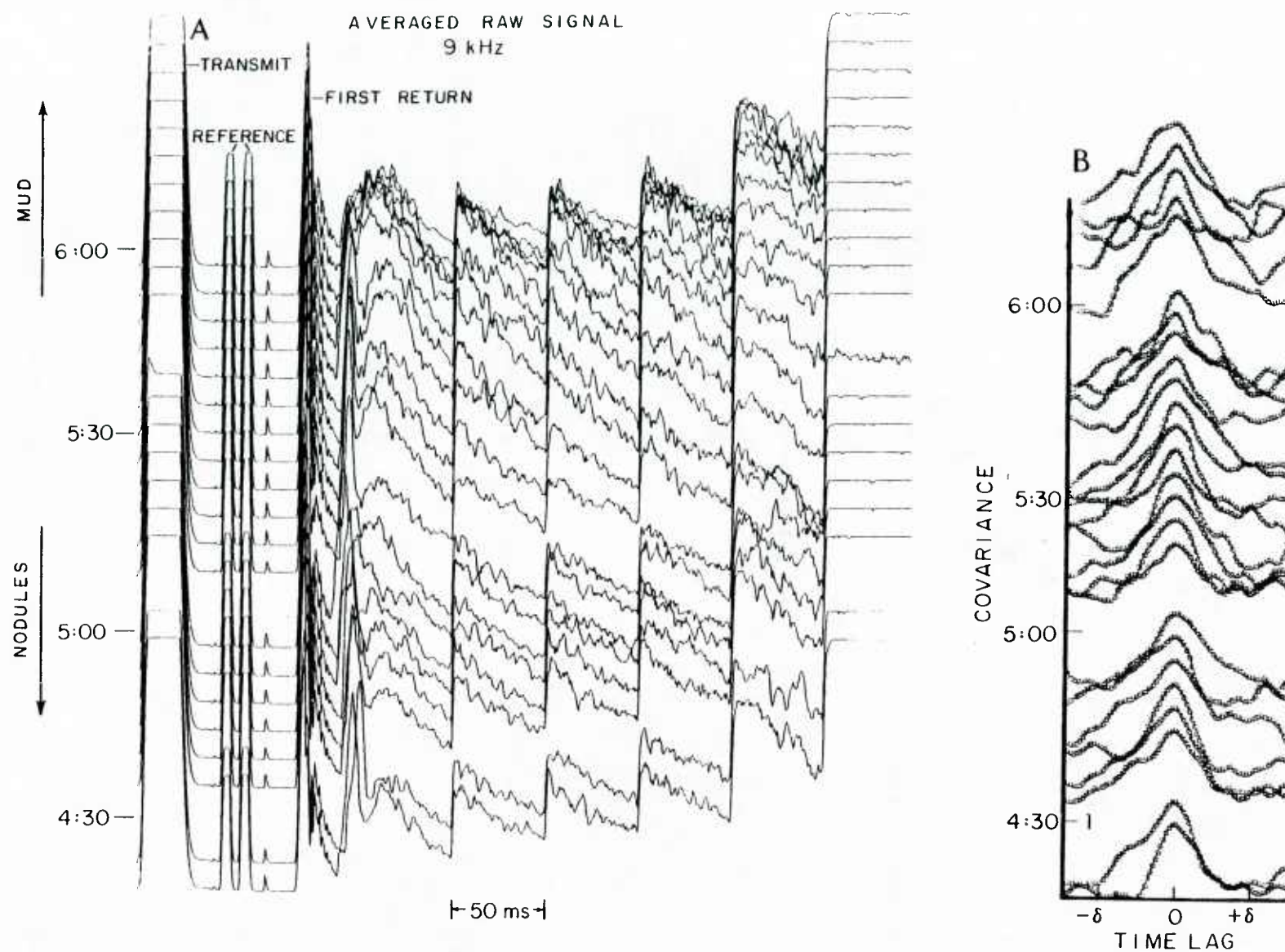


Figure 2-20. Samples of raw signal and covariances

Samples of low-passed raw signals and covariances for 9 kHz. Averages are 43-ping ensemble averages.

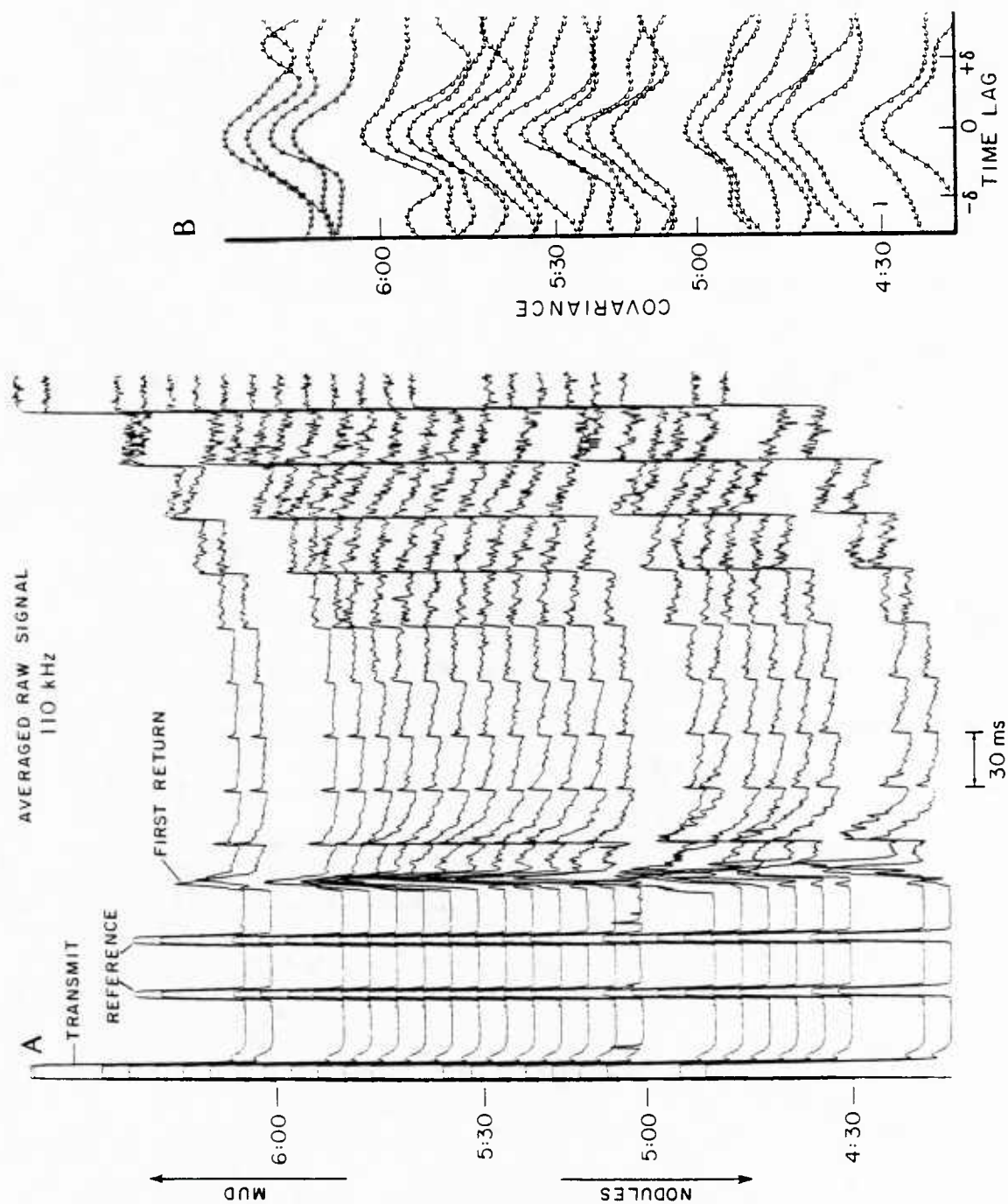


Figure 2-27. Samples of raw signal and covariances

Samples of low passed raw signals and covariances for 110 kHz. Averages are 43-ping ensemble averages

1° or 5° window. From here ensemble averaging over a number of pings at a fixed grazing angle or range of grazing angles could proceed directly. The extension of the homogeneous parts of the sea floor being 50 to 400 meters, it is appropriate to average over 1 to 5 minute intervals which correspond to 8 to 43 pings per frequency. (The fish travels approximately 45 meters per minute). The 68.27% confidence limits for the average backscatter coefficients are better than ± 2 dB for 1 minute intervals and better than ± 1 dB for 10 minute intervals.

A second approach was to ensemble average the raw intensities, subtract the average noise intensity and to apply equation (2-55). At grazing angles of 30° or less only data where the agreement between the two methods was good have been retained.

2.5.3.3 Results

Although the site at the foot of the Patton Escarpment was the last one visited, it will be discussed first as it is comparable to environments studied by other investigators (Urlick, 1983; Jitkovskii and Volovova, 1965). The sea floor is composed of silty clay (chapter 1.3). Its rms-roughness is of the order of a couple of cm (figure 1-23). Figure 2-28 shows the backscatter coefficients (8 ping averages) as a function of the grazing angles for 60 kHz. The backscatter coefficients are constant and equal about -10 dB over a large range of grazing angles. The high frequency oscillations are beam pattern effects. At grazing angles of 20 degrees or higher they can be averaged out with a 5° window. Figure 2-29 shows the frequency dependence of the backscatter coefficients for 15, 28, 60 and 163 kHz at average grazing angles of 30 and 40 degrees and at normal incidence for averages over 80 pings or more.

Figure 2-29 also shows the backscatter coefficients of the sediments at site 'E'. Note that these are always equal or less than those observed at the foot of the

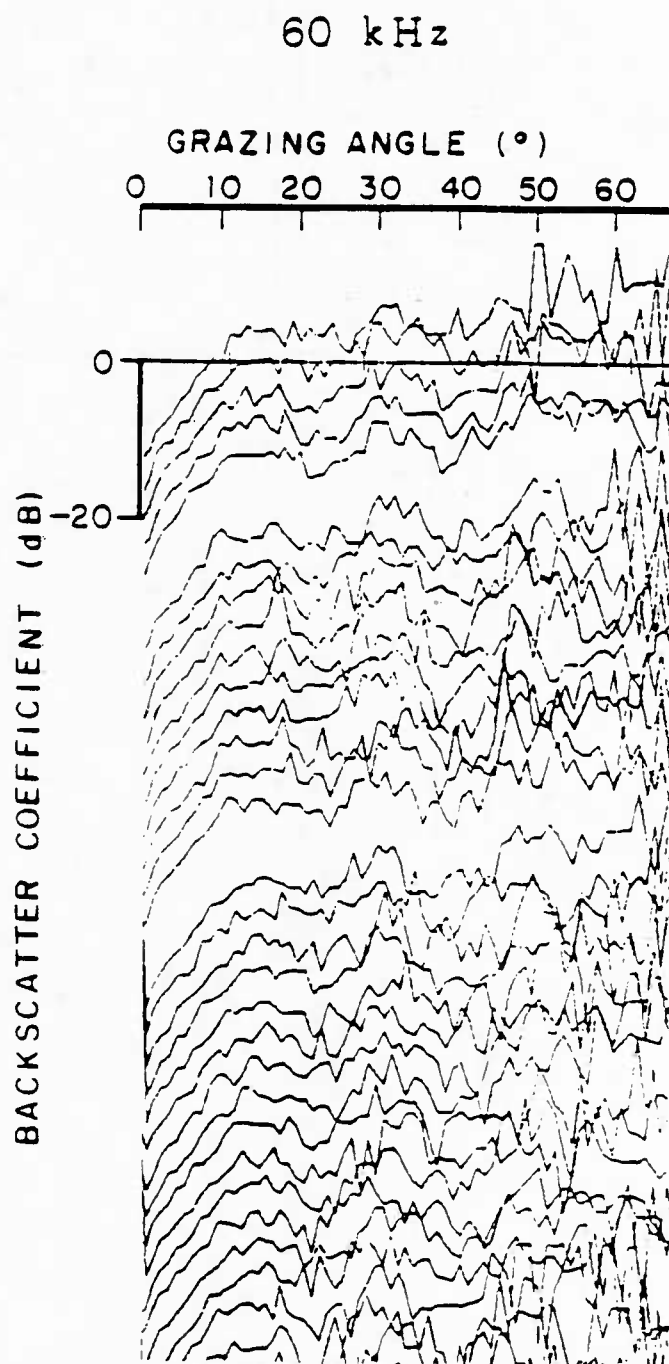


Figure 2-28. Samples of low-passed backscatter coefficients

8-ping averages of the 60 kHz backscatter coefficients as a function of the grazing angle (foot of Patton Escarpment).

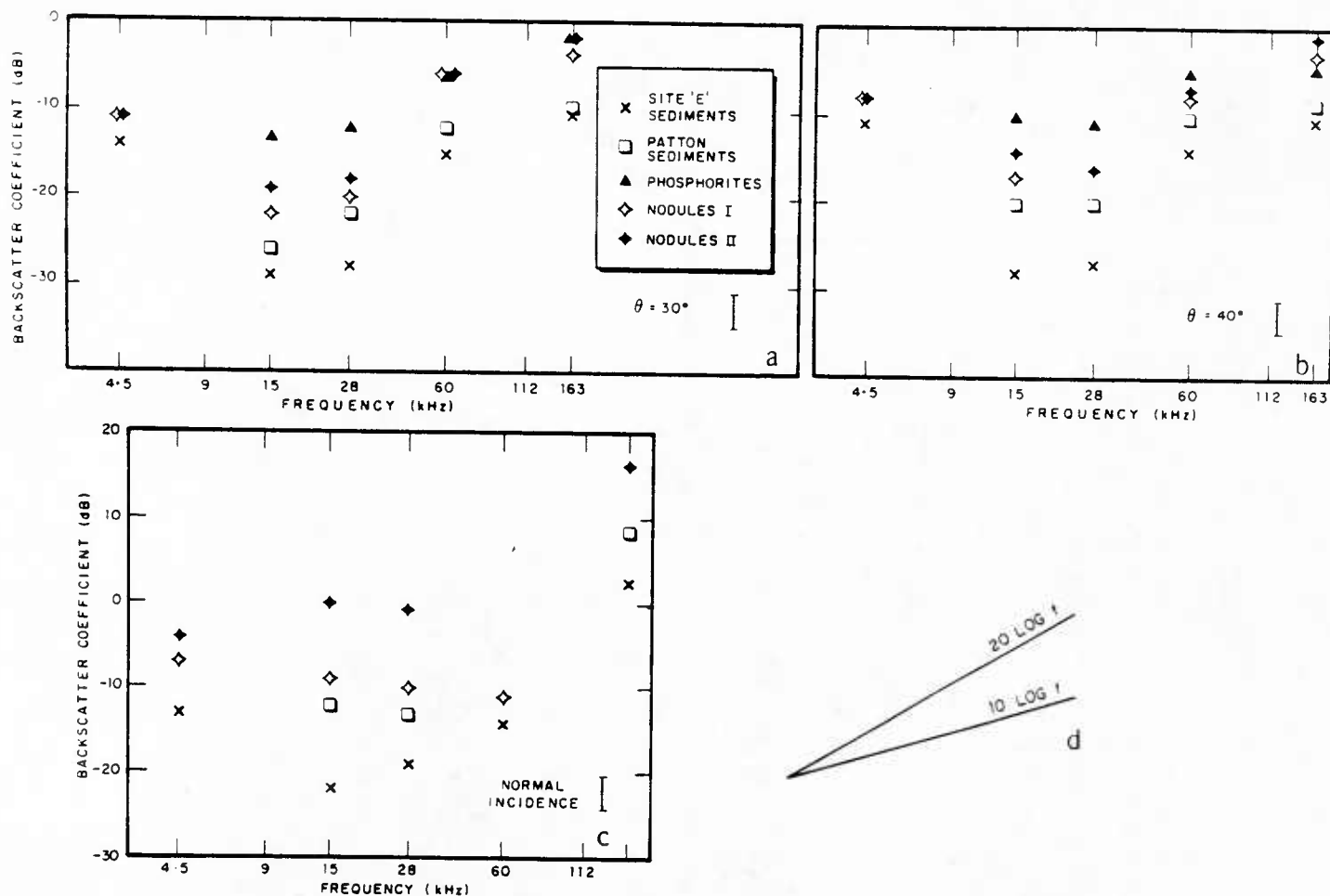


Figure 2-29. Backscatter coefficients as a function of frequency

Backscatter coefficients in dB ref. 1 meter for the sediments, manganese nodules and phosphorites at grazing angles of 30° (a), 40° (b) and normal incidence (c). The lines 10 log f and 20 log f are shown for comparison (d). The error bars correspond to the 68.27% confidence intervals (see text). The major contribution is from the calibration error (compare table 2-7).

Patton Escarpment.

The next higher backscatter coefficients in figure 2-29 are those from the nodule covered areas at site 'E'. The backscatter coefficients from the Thirtymile Bank appear to be the strongest ones. This is not surprising as large parts of the Thirtymile Bank are covered by phosphorite slabs. From figure 2-29 it is clear that the acoustic behaviour varies substantially between the four environments studied i.e. it is possible to identify each one of them by its characteristic acoustic signature.

The standard errors (Spiegel, 1961) were added to and subtracted from the means. Then these values were transformed into dB. The error bars in figures 2-29 to 2-32 show the 68.27% confidence limits. In figure 2-29 the calibration error of ± 1.5 dB has been added to the standard error. The lower limit is 2.3 dB below the mean for the site 'E' sediments in figure 2-29, and 0.8 dB in figures 2-30 to 2-32. The errors for the backscatter coefficients of the sediments at the site of the Patton Escarpment are 0.2 dB smaller (400 pings). The errors for the backscatter coefficients from the manganese nodules (140 pings each) and from the phosphorites (160 pings) fall in between. The standard errors for different frequencies, but the same environment, differ by 0.1 dB or less. Note that in figure 2-29 the major error contribution is a calibration error which is known in dB only (table 2-7).

Figure 2-30 shows the frequency response (relative to the response of the deep sea clay of site 'E') for the four environments and all 7 frequencies. Since the same equipment was used and the vehicle was kept at the same height, these measurements are not subject to calibration errors of the acoustic equipment. Relative changes could be measured within one dB for the sediments and the nodules of site 'E' and for the sediments west of the Patton Escarpment. Small beampattern changes are possible between these three sites and the Thirtymile Bank, since the acoustic wavelength changes when the pressure is increased from 70 bar to 450 bar. Such

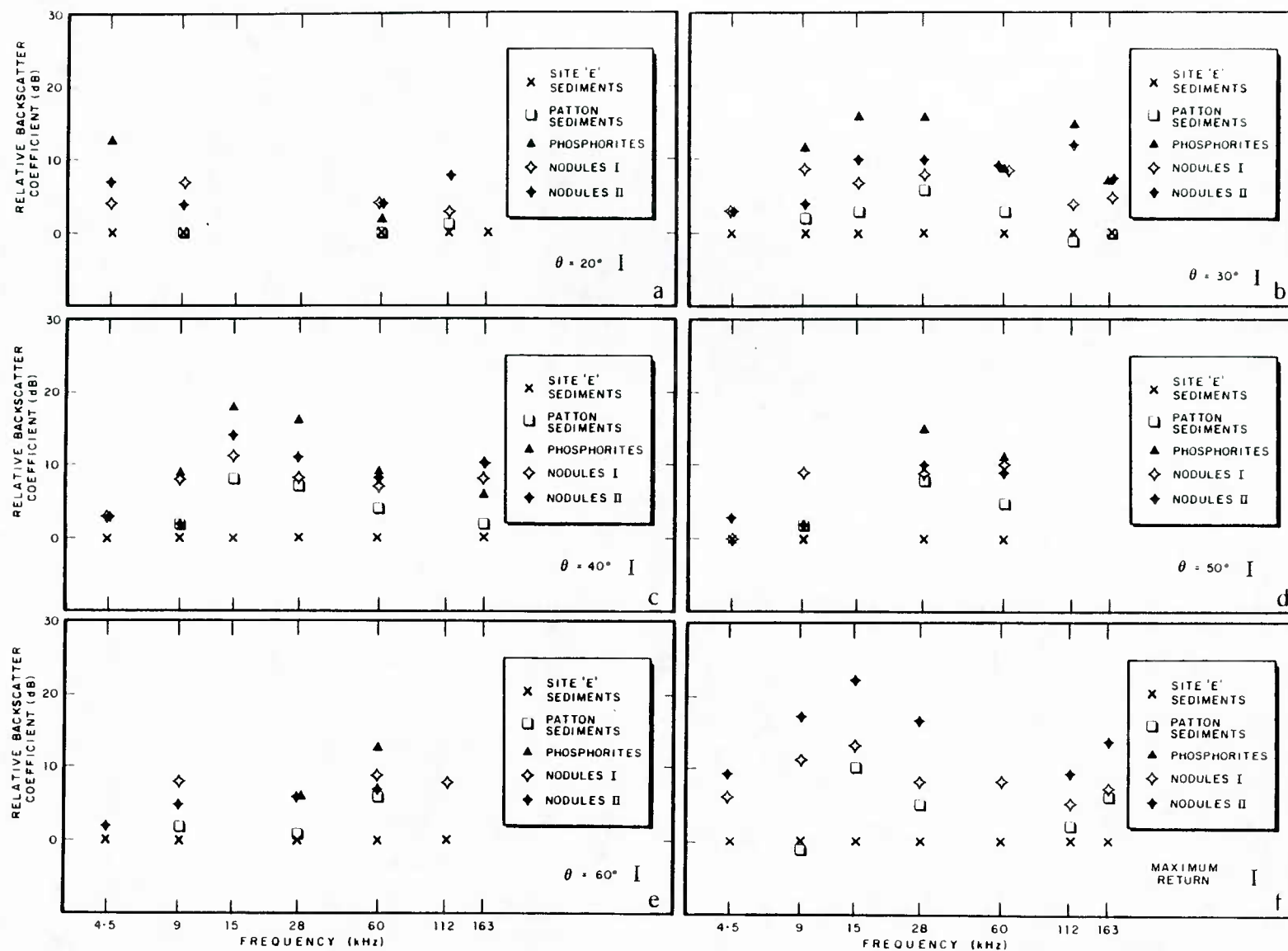


Figure 2-30. Relative backscatter coefficients as a function of frequency

The backscatter coefficients of the four environments are shown relative to the backscatter coefficients of the sediments at site 'E' which have been arbitrarily set equal 0 dB. Since no absolute calibrations are needed, all 7 frequencies can be displayed for grazing angles of 20° (a), 30° (b), 40° (c), 50° (d), 60° (e) and normal incidence (f). The error bars correspond to the 68.27% confidence limits (see text). No calibration errors contribute.

changes do, however, not change the return by more than 2 dB.

At grazing angles different from 90° the backscatter coefficients of the sediments near the Patton Escarpment differ less than 5 dB from those at site 'E' and are always higher at 9, 15, 28 and 60 kHz. Very careful measurements are required to distinguish the two sediment types at 112 kHz and 163 kHz. The Thirtymile Bank phosphorites and the manganese nodules of site 'E' backscatter the acoustic energy much more than the two sediment types. But, again, it is not possible to distinguish between these two types of sea floor at 112 and 163 kHz, but their frequency dependence is different at 9, 15 and 28 kHz.

Using an impedance of 2.010^6 and $2.2 \cdot 10^6 \text{ kg m/m}^2$ for the sediments at site E and at the foot of the Patton Escarpment respectively (from Hamilton, 1974) the first factor in equation (2-60) is nearly 1 dB higher for the sediments at the Patton Escarpment. This suggests that only a fraction of the change in backscattering strength comes from the change in impedance as described by the first factor in equation (2-60), the second part coming from changes in roughness (either correlation area or rms roughness) or local changes in impedance as included in the second factor of (2-60). This hypothesis is supported by the frequency dependence of the backscatter. An alternate explanation would be a frequency dependent impedance which has not been observed to the knowledge of the author.

As already observed at 60 kHz (figure 2-28), the backscatter coefficients vary only slowly at grazing angles above 20° , while the changes below 20° are of the order of 1 dB per degree (figures 2-31 and 2-32). This is in agreement with the measurements made by previous authors and summarized by Urick (Urick, 1983). The relationships between the backscatter from the different environments are conserved as the grazing angle changes. This will allow one to make measurements at any one grazing angle at frequencies of 15 kHz and higher.

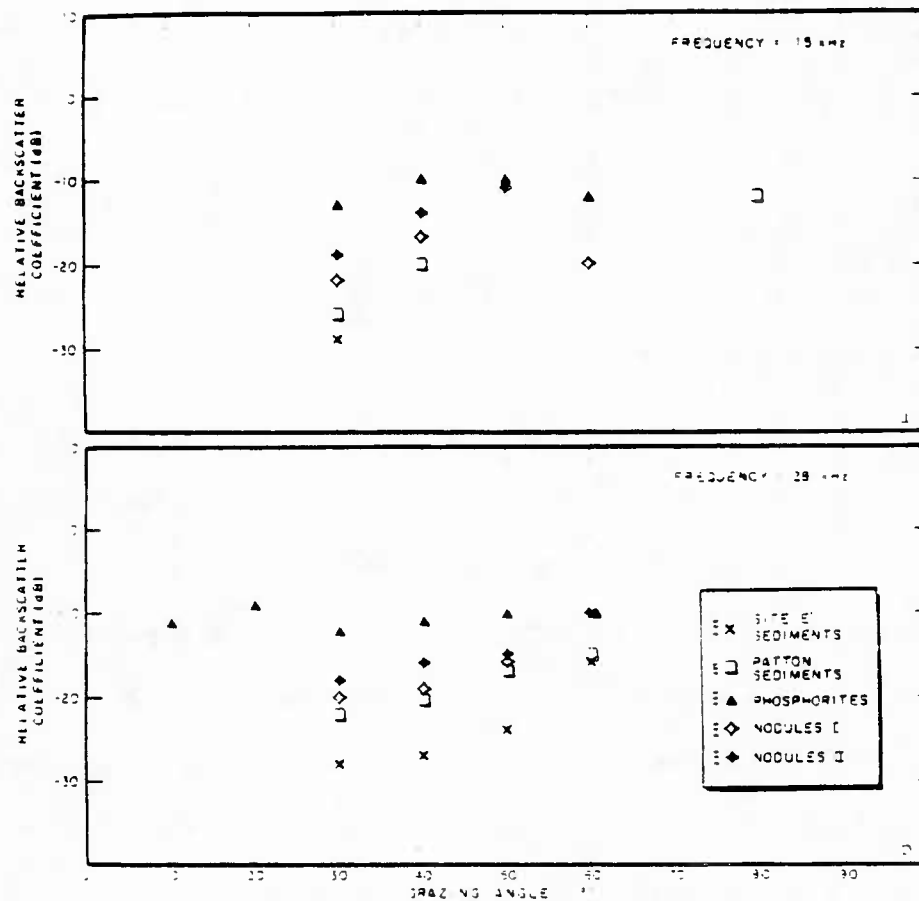


Figure 2-31. Relative backscatter coefficients as a function of the grazing angle

Relative Backscatter coefficients as a function of the grazing angle for 15 kHz (a) and 23 kHz (b) in arbitrary dB. The error bars are the 68.27% confidence limits (see text). Since no absolute calibrations are needed, the errors of the absolute calibrations do not contribute.

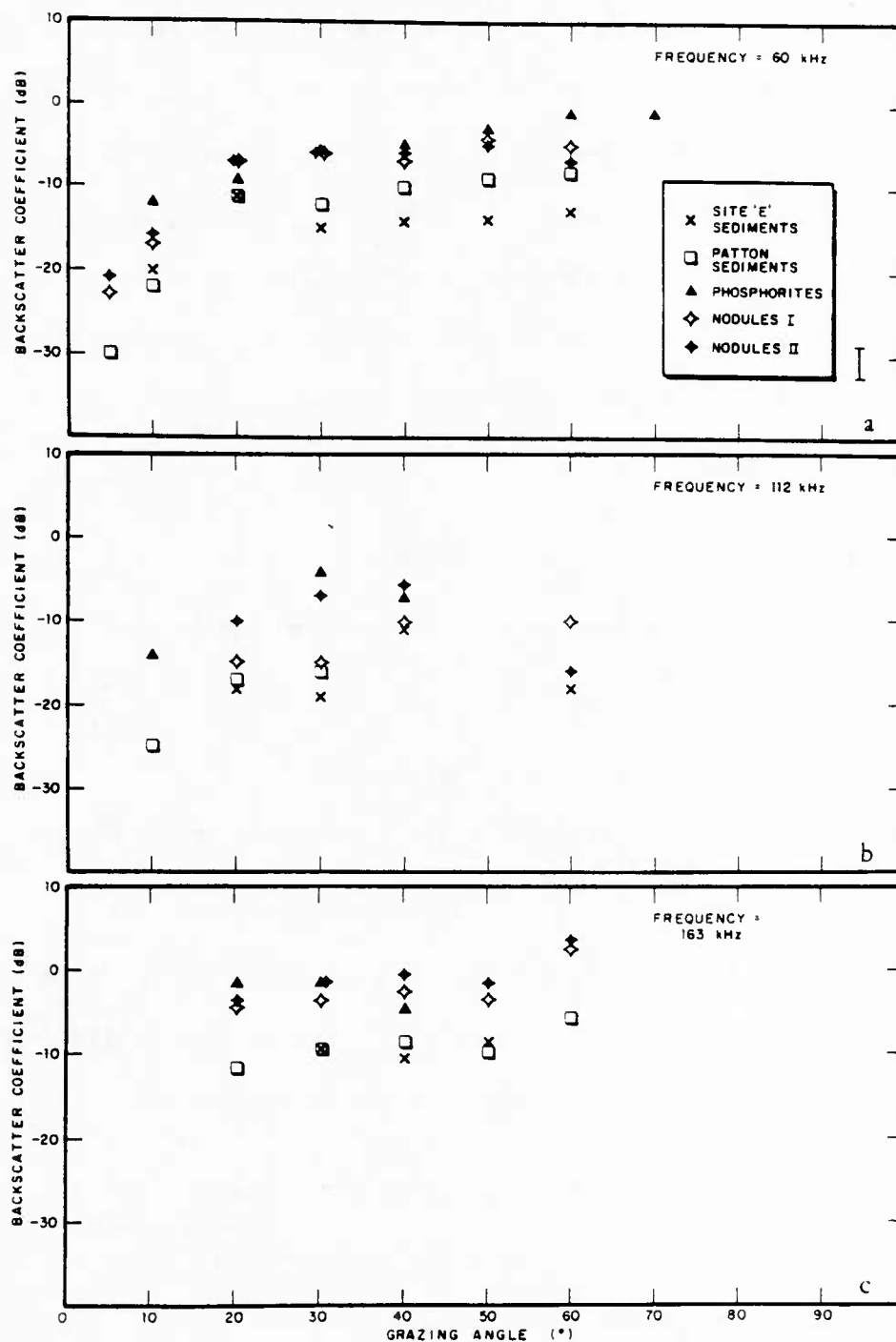


Figure 2-32. Relative Backscatter coefficients as a function of the grazing angle

Relative Backscatter coefficients as a function of the grazing angle for 60 kHz (a), 112 kHz (b) and 163 kHz (c) in arbitrary dB. The error bars are the 68.27% confidence limits (see text). Since no absolute calibrations are needed, the errors of the absolute calibrations do not contribute.

2.5.4 Statistics

The statistics of the envelope of the backscattered signal can be used at all grazing angles to discriminate between various environments. In chapter 2.4.3 first order statistics were used to measure the relative importance of the scattered and reflected signals at normal incidence. In the following, second order statistics of the envelope will be related to changes of the physical characteristics of the sea floor. No absolute calibration is required for this analysis. However, a good knowledge of the beampatterns of the transducers will be useful to prevent the geologist from looking at beampattern artifacts.

2.5.4.1 Covariance function of the envelope

If $s_o(t)$ is the envelope of the transmitted signal, then the harmonic transmitted signal $s(t)$ can be written as

$$s(t) = s_o(t) \cos \omega_o t \quad (2-66)$$

and the more general narrow-band transmitted signal can be represented as

$$s(t) = s_o(t) \cos(\omega_o t + \Phi(t)) \quad (2-66')$$

where ω_o is the center frequency and $\Phi(t)$ is the phase of the signal. Any state of the narrow-band reverberation process $F(t)$ of individual scatterers located at distances $t_i c/2$ (t_i = time of i th scatterer, c = sound velocity) can be written as

$$F_n(t) = \sum_{j=1}^N a_j s(t-t_i) \quad (2-67)$$

where a_i are the stochastic amplitudes of the scattered signal. N is the number of scatterers, and in this context, a stochastic variable. Using the two-dimensional theorem of superposition of stochastic processes, it can be shown (Olchevskii, 1967) that the correlation function $R_r(\tau)$ defined by

$$R_r(\tau) = \frac{\int_{-\infty}^{+\infty} s(t)s(t+\tau)dt}{\int_{-\infty}^{+\infty} s^2(t)dt} \quad (2-68)$$

becomes for quasi-harmonic signals (if δ_{eff} is the effective pulse length)

$$R_r(\tau) = \frac{\cos\omega_o\tau}{\delta_{eff}} \int_{-\infty}^{+\infty} s(t)s_o(t)\cos[\Phi(t+\tau)-\Phi(t)]dt \quad (2-69)$$

For a harmonic pulse

$$\Phi(t) = \Phi(t+\tau) = 0 \quad (2-70)$$

and

$$R_r(\tau) = \frac{\cos\omega_o\tau}{\delta_{eff}} \int_{-\infty}^{+\infty} s_o(t)s_o(t+\tau)dt \quad (2-71)$$

Equation (2-71) means that for harmonic signals the reverberation correlation depends only on the envelope of the transmitted signal. Equation (2-69) can be rewritten as

$$R_r(\tau) = r_r(\tau)\cos\omega_o\tau \quad (2-72)$$

where the beat $r_r(\tau)$ can be called the "correlation coefficient envelope", as it varies slowly compared to $\cos\omega_o\tau$.

If the transmit pulse is of finite duration,

$$s(t) = 0 \text{ for } |t| \geq t_z/2 \quad (2-73)$$

where t_z is the duration of the transmission. Using equations (2-73) and (2-69), and replacing t by $t-\tau/2$,

$$r_r(\tau) \sim \frac{2}{\delta_{eff}} \int_0^{\frac{(t_z-|\tau|)}{2}} s_o(t - \frac{\tau}{2})s_o(t + \frac{\tau}{2})\cos[\Phi(t + \tau/2) - \Phi(t - \tau/2)]dt \quad (2-74)$$

$$r_r(\tau) = \frac{2}{\delta_{eff}} \int_0^{(t_z-\tau)/2} s_o(t - \frac{\tau}{2})s_o(t + \frac{\tau}{2})dt \quad (2-74')$$

for harmonic signals. Olchevskii (Olchevskii, 1967) defines the correlation interval by

$$\tau_r = \int_{-\infty}^{+\infty} |r_r(\tau)|d\tau \quad (2-75)$$

For a rectangular pulse shape $s_o(t) = 1$ for $|t| \leq \delta/2$, where δ is the pulse length, and we can calculate $r_r(\tau)$

$$r_r(\tau) = 1 - \frac{|\tau|}{\delta} \quad \text{for } |\tau| \leq \delta \quad (2-76)$$

and the correlation interval is $\tau_r = \delta/2$.

Olchevskii's results (2-71) and (2-76) were derived for constant mean and constant returned energy. These conditions are obviously not fulfilled for bottom reverberation i.e. where the return varies as a function of the grazing angle. The reverberation process, like any quasi-harmonic stochastic function, can be written as

$$V(t) = E(t)\cos(\omega_o t + \Psi(t)) \quad (2-77)$$

where $E(t)$ is the envelope, ω_o is the center frequency times 2π , Ψ is the phase of the reverberation, and t is the time since the transmission. For zero mean, $\langle V(t) \rangle = 0$, where $\langle \rangle$ is the ensemble average, and the covariance function K_V can be defined as

$$K_V(t_1, t_2) = \langle V(t_1)V(t_2) \rangle \quad (2-78)$$

(Bendat + Piersol, 1971). When the reverberation is stationary, the covariance can be expressed in the narrow-band form

$$K_V(\tau) = K_o(\tau)\cos[\omega_o \tau + \Psi_o(t)] \quad (2-79)$$

where $\tau = t_2 - t_1$ (Plemons, Shooter and Middleton, 1972). K_o and Ψ_o are the envelope and the phase fluctuations. For varying means, the covariance function of the envelope $E(t)$ is best defined as

$$K_E(t_1, t_2) = \frac{\langle E(t_1) - \mu_1 \rangle \langle E(t_2) - \mu_2 \rangle}{(\langle E(t_1) - \mu_1 \rangle^2 \langle E(t_2) - \mu_2 \rangle^2)^{1/2}} \quad (2-80)$$

where $\mu_i = \langle E(t_i) \rangle$. This definition is a generalization of the one given by Olchevskii (Olchevskii, 1967). Olchevskii has shown (Olchevskii, 1967) that for stationary, narrow-band Gaussian reverberation processes, the covariance of the envelope is given by

$$K_E(t_1, t_2) = \frac{\pi}{2} C \gamma_1^2 \left(-\frac{1}{2}, -\frac{1}{2}, 1, \tilde{K}_o(\tau) \right) - \frac{\pi}{2} C \quad (2-81)$$

$$K_E(t_1, t_2) = \frac{\pi}{8} C \tilde{K}_o^2(\tau) + O(\tilde{K}_o^4) \quad (2-81')$$

where γ_1^2 is the hypergeometric function, $C = \langle V^2(t) \rangle$, $\tilde{K}_o(\tau)$ is the normalized envelope and C is the normalization defined by

$$C = (\langle E^2(t_1) \rangle \langle E^2(t_2) \rangle)^{1/2} \quad (2-82)$$

Equation (2-81') means that the correlation coefficient of the reverberation envelope fluctuations is approximately equal to the square of the correlation envelope of its instantaneous values. Olchevskii (olchevskii, 1967) states that if one uses the first 2 terms i.e.

$$K_E(\tau) = 0.91r_r^2(\tau) + 0.09r_r^4(\tau) \quad (2-81'')$$

the error turns out to be less than 1% while the error can reach 10% if one uses the first term only.

Using equation (2-76) in equation (2-81), the covariance of the envelope becomes

$$\tilde{K}_E(\tau) = (1 - \frac{\tau}{\delta})^2 \quad (2-83)$$

where K_E has been normalized so that $\tilde{K}_E(0) = 1$ (figure 2-33). This permits us to compare the theoretical covariance represented by equation (2-81) with the covariance calculated with equation (2-80). Deviations from equation (2-81) express violations of the assumptions made for the derivation of equation (2-81) i.e.

- (1) the reverberation is narrow-band
- (2) the reverberation is Gaussian
- (3) the reverberation is stationary

The equipment (transducers, drivers and filters) and the pulse lengths ascertained that requirement (1) is fulfilled. The reverberation (the stationary part of the signal) is Gaussian if there is a large number of scatterers i.e. $\langle N \rangle \delta \gg 1$, where $\langle N \rangle$ is the average number of scatterers, and δ is the pulse length (for a square transmit pulse). The stationarity is the condition which is most likely to be violated. We shall

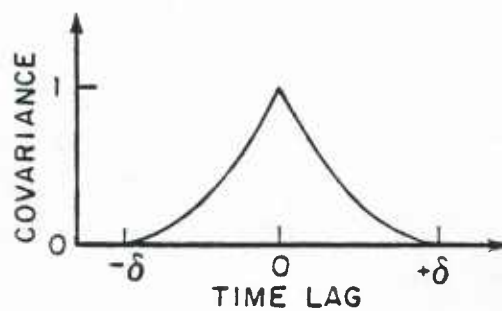


Figure 2-33. Theoretical covariance

Theoretical covariance for a square pulse as calculated with equation (2-83).
Note the symmetry around the time lag 0. The pulse length is equal δ .

therefore interpret deviations from the theoretical curve (figure 2-33) at frequencies from 9 kHz to 163 kHz as deviations from stationarity. At 4.5 kHz, the transmit pulse cannot be considered to be a square pulse as the rise time exceeds 10% of the pulse length.

For frequencies from 15 kHz on upwards, the pulse length was only 1 ms. At a digitizing rate of 2 kHz, this resulted in 2 samples per pulse length on the 30 meter runs. As the covariance of the envelope decreases from 1 to zero over one pulse length, the resolution is very poor and the asymmetry and the width of the covariance can only be measured roughly with the sampled data. In order to increase the accuracy with which the shape of the covariance curve can be determined, it was necessary to increase the digitizing rate. An interpolation of a band-limited signal is possible if it has been sampled at the Nyquist or a higher frequency. As the pulse lengths were 1 ms or more, this was the case. The interpolation was done by inserting three additional samples (zeroes) between any two data points. Then the new samples were low-pass filtered using the Finite Impulse Response (FIR) filter shown in figure 2-34. If h_k are the coefficients of the impulse response of the FIR filter, and x_n are the original samples, then the interpolated signal is given by

$$y_m = \sum_{k=-1}^N v_{m-k-1} h_k \quad (2-84)$$

where

$$\begin{aligned} v_m &= x_m \text{ for } m = 4k \\ &= 0 \text{ otherwise} \end{aligned}$$

and N is the number of taps of the FIR filter. This technique has been described in more detail elsewhere (Peled and Liu, 1976).

Figures 2-26 and 2-27 show the ensemble averaged returns (43 pings each) and the covariances computed with equation (2-80) for 9 and 110 kHz. The time lag

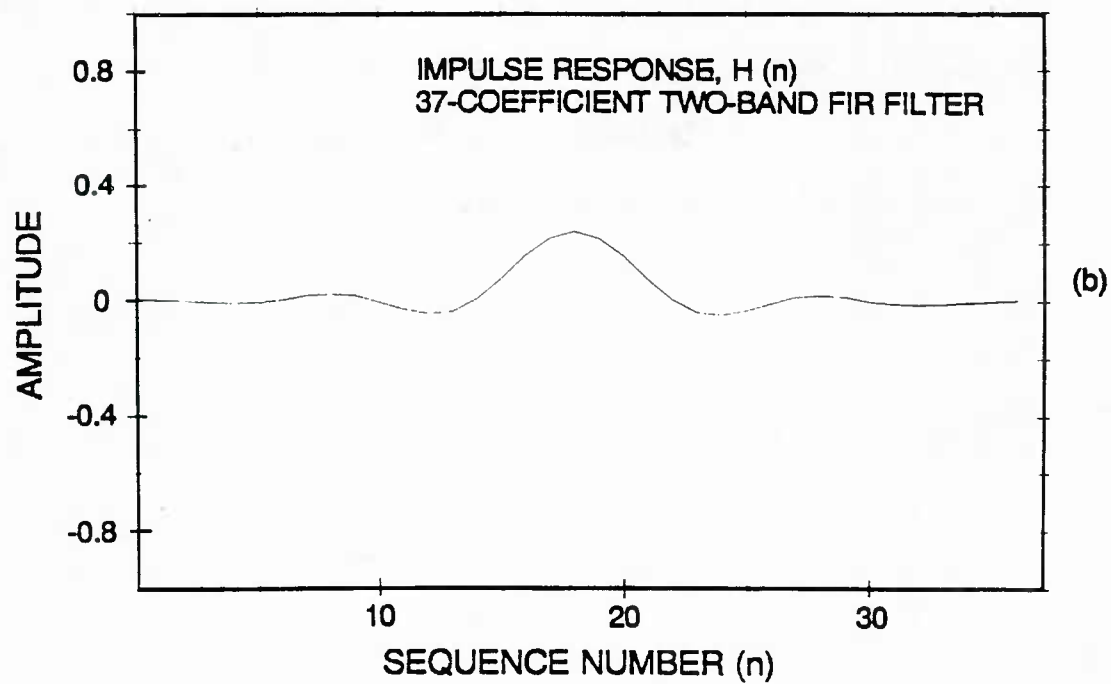
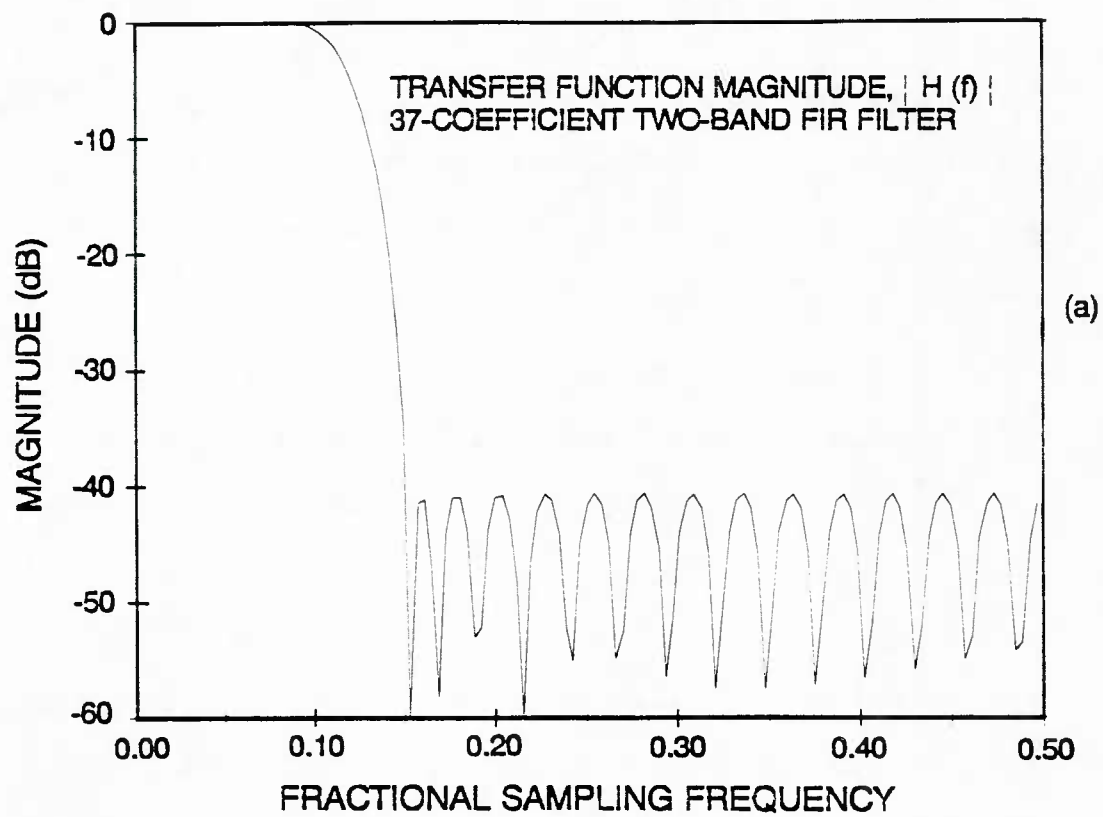


Figure 2-34. FIR filter

Finite Impulse Response filter used for the interpolation of the backscatter data.

zero has been taken as 130 milliseconds after the first return.

The halfwidth of the covariance (ν) has been defined as the time lag between the 0.5 downpoints. A left halfwidth ν_l is defined as the time lag from the left 0.5 point (shorter times) to the time lag zero, similarly a right halfwidth ν_r . The ratio of the left halfwidth over the right halfwidth is the asymmetry η of the covariance i.e.

$$\eta = \frac{\nu_l}{\nu_r} \quad (2-85)$$

Similarly, a quarter-width was defined as the time lag between the 0.25 downpoints.

Figure 2-35 shows the five minute averages of the intensities (arbitrary linear units), the standard deviations, the covariance halfwidths (normalized by the pulse length) and their asymmetries, the covariance quarterwidths (normalized by the pulse length) and their asymmetries for 9 and 110 kHz and a grazing angle of 18° (130 ms since first return) (compare camera run 4 in figure 1-17 for nodule coverage and figure 2-36 for fish track). As already stated earlier, the intensity increases when the nodule coverage increases, except at 9 kHz, the only frequency which is low enough to show a decrease with decreasing nodule size (and increasing coverage). The width of the covariance decreases at all frequencies (it is only slightly frequency dependent) with decreasing nodule coverage, and it appears to be narrowest for nodule free areas. In transition zones the covariance becomes very large as expected. This permits us to distinguish at 9 kHz between the case where the nodule coverage becomes smaller (with constant or increasing nodule size) and the case where the nodule coverage increases but the nodule diameter decreases. This behaviour is even more pronounced for the asymmetry. The theory (Olčevskii, 1967) predicts an asymmetry if the characteristics of the sea floor change. The strong asymmetries observed here correlate with the patchiness of the nodule field. This is most pronounced in densely covered areas.

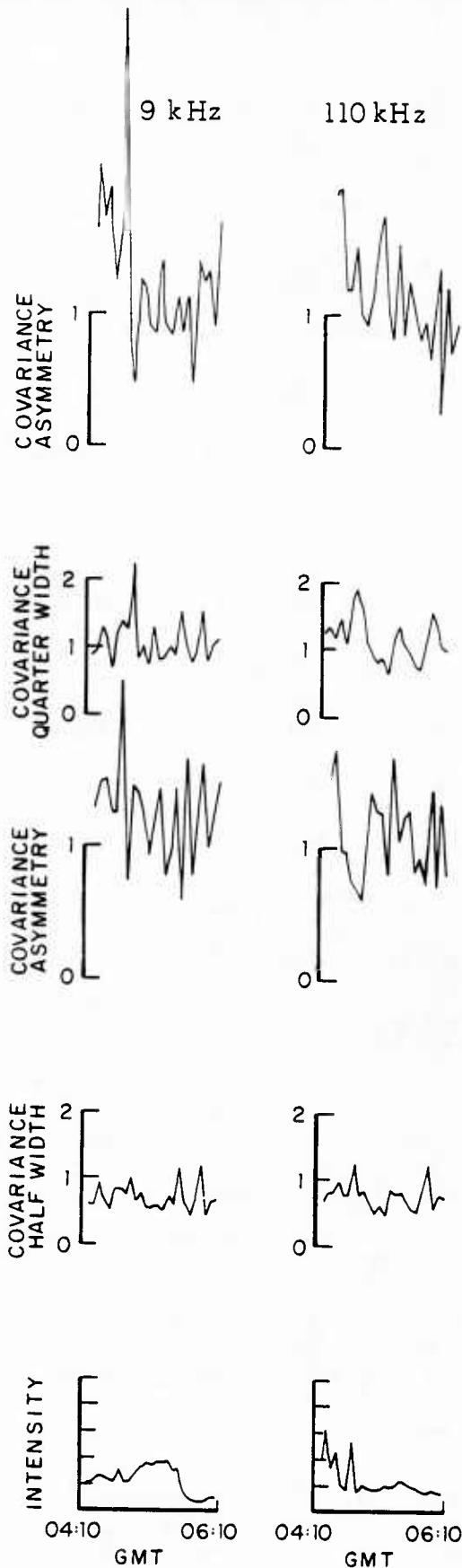


Figure 2-35. Intensities, width and asymmetry of covariances

Intensity (arbitrary linear units), covariance half- and quarterwidths and their asymmetries are shown for the backscatter of 4:10 to 6:00 GMT on 20 June 1983 (compare figure 2-36).

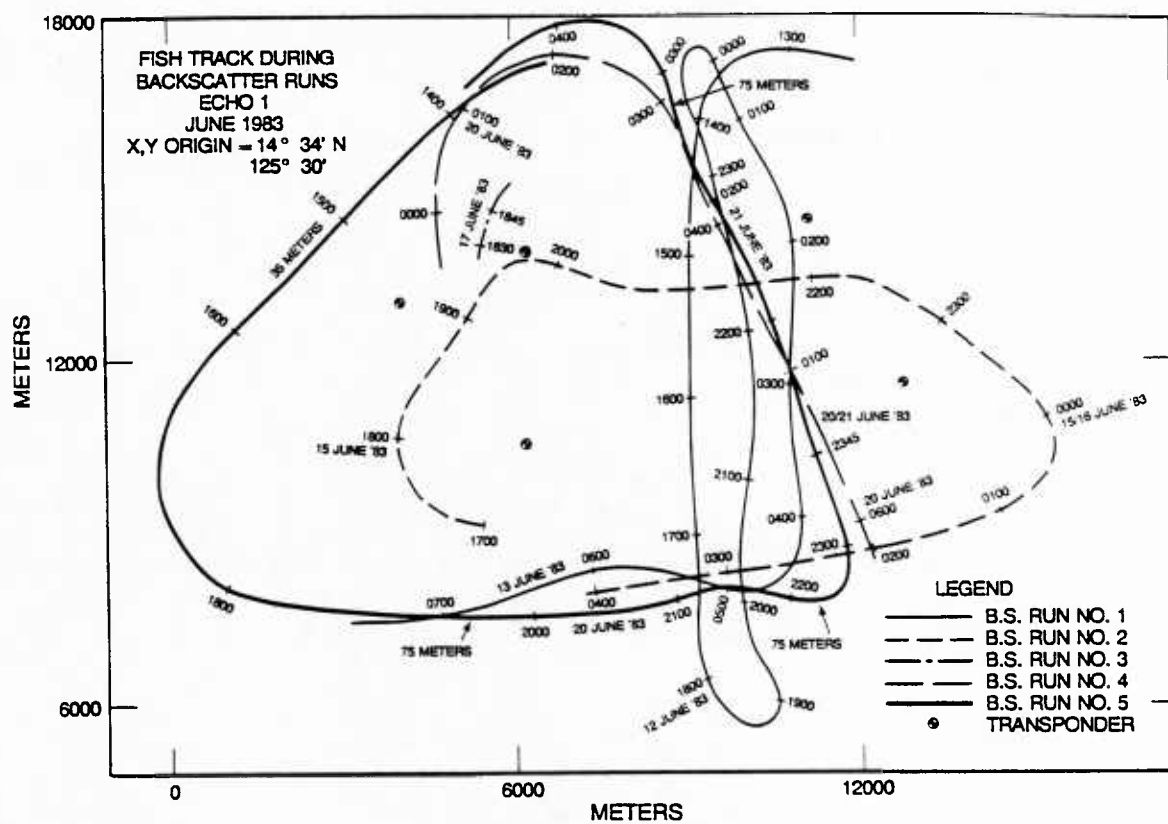


Figure 2-36. Fish track during backscatter measurements at site E

Fish positions and heights above the sea floor during backscatter runs at site 'E' as determined with transponder navigation.

2.6 Relationships between nodule characteristics, reflectivity and backscatter

2.6.1 Background

Let the sound pressure generated by the source be

$$p(t) = E(t)\cos(\omega_c t) \quad (2-86)$$

where p is the pressure, ω_c is the carrier frequency, t is the time since time zero, E is the envelope. Then the backscattered pressure for the i th point scatterer $p_i^{BS}(t)$ is given by

$$p_i^{BS}(t) = G_i E(t) \cos[\omega_c t - \Phi_i] \quad (2-87)$$

where G_i is the backscattering strength of scatterer number i , Φ_i is the phase shift and is given by

$$\Phi_i = 2 k r_i \quad (2-88)$$

where k is the wave number ($2\pi/\lambda$), and r_i is the distance between the source and scatterer number i . The sum of the returns from N scatterers is given by

$$P_{tot}(t) = \sum_{i=1}^N G_i E(t) \cos[\omega_c t - \Phi_i] \quad (2-89a)$$

$$= \text{Real} \left\{ \sum_{i=1}^N G_i E(t) e^{j(\omega_c t - \Phi_i)} \right\} \quad (2-89b)$$

$$= \text{Real} \left\{ E(t) \sum_{i=1}^N G_i e^{j(\omega_c t - \Phi_i)} \right\} \quad (2-89c)$$

where $j = \sqrt{-1}$ and *Real* means the real part only. This is true for all times t . Fresnel discussed the case where the phase varies as a function of the distance (Navy, 1969). If two objects are spaced so that the phase difference less than π ($\lambda/2$), then the backscattered amplitudes add constructively. If the two-way paths differ between π and 2π ($\lambda/2$ and λ), then they interfere destructively. Generalizing this result, the space can be subdivided into zones so that

$$R + (n-1)\frac{\lambda}{4} < r < R + n\frac{\lambda}{4} \quad (2-90)$$

where r is the distance from the source to some point in the zone called "Fresnel zone". The sizes of the first Fresnel zone for the 75 meter backscatter runs are in table 2-12.

frequency	wavelength	height	First Fresnel Zone		insonified area	
			area	radius	area	radius
4.5 kHz	0.33 m	75 m	40.0 m ²	3.6 m	8700 m ²	52.5 m
9 kHz	0.16 m	75 m	20.0 m ²	2.5 m	8700 m ²	52.5 m
15 kHz	0.10 m	75 m	11.8 m ²	1.9 m	870 m ²	16.6 m
30 kHz	0.05 m	75 m	5.9 m ²	1.4 m	230 m ²	8.5 m
60 kHz	0.025 m	75 m	3.0 m ²	1.0 m		
112 kHz	0.014 m	75 m	1.6 m ²	0.7 m	24 m ²	4.0 m
163 kHz	0.009 m	75 m	1.1 m ²	0.6 m	34 m ²	3.3 m

Table No. 2-12: First Fresnel zones for frequencies used on Echo 1.

The Fresnel zone method can be applied to spherical waves which have traveled far enough to be nearly plane. For a transducer insonifying the sea floor, the Fresnel zones are defined by the intersections of the spherical zone defined by (2-90) with the sea floor. If the return comes from the first Fresnel zone only, then the amplitudes add together and

$$A_{tot} = e^{j\phi} \sum_{k=1}^N A_k \quad (2-91)$$

and the intensity becomes

$$I_{tot} = \frac{1}{\rho_o c_o} |\sum A_k|^2 \quad (2-92)$$

where $\rho_o c_o$ is the impedance of the medium of propagation (sea water), and $A_k = G_k E$. A doubling of the number of identical scatterers results in quadrupling the intensity.

If, on the contrary, the phase relationships are random, equation (2-91) leads to

$$I_{tot} = \frac{1}{\rho_o c_o} \left\{ \sum_{k=1}^N A_k e^{j\phi_k} \right\} \left\{ \sum_{l=1}^N A_l e^{j\phi_l} \right\}^* \quad (2-93a)$$

$$= \frac{1}{\rho_o c_o} \sum_{k=1}^N A_k A_k^* \quad (2-93b)$$

$$= \sum_{k=1}^N I_k \quad (2-93c)$$

where * is the complex conjugate. This means that the backscattered intensities add together to yield the total intensity.

Several authors have studied the values of G_i for hard spheres, elastic spheres or manganese nodules (Urlick, 1983; Ma, 1983; Weydert, 1985). Figure 2-37 shows the ratio of backscattering to geometric cross-sections as a function of ka (product of wave number and radius) for hard spheres. For $ka \ll 1$, σ increases as $(ka)^4$ (Rayleigh scattering), while for $ka \gg 1$, $\sigma = 1$ (geometric scattering) i.e. the backscattering cross-section increases as the projected area πa^2 for $ka \gg 1$. Ma obtained numerically similar results for an elastic sphere with the same impedance as the one for manganese nodules (figure 2-37). From this it can be concluded that the backscatter increases with increasing frequency and increasing nodule size for $ka \ll 1$. For $ka \gg 1$ the backscatter is proportional to the geometric cross-section independent of frequency. If the size of the sphere is reduced, the backscatter decreases and vice-versa. This means that nodules of different sizes backscatter the sound differently. So it is possible to determine the nodule sizes using a sonar operating at at least 2 frequencies, either both in the region of Rayleigh scattering or one in the region of Rayleigh scattering, the other one in the region of geometric scattering.

Using elastic nodule like spheres, Ma has shown (Ma, 1983) that on the average the backscatter increases with ka for $ka < 30$. Since the sizes of the nodules in a given area vary around some mean (chapter 1), this result is applicable.

Despite the fact that manganese nodules are not spheres nor ellipsoids, the averaged target strength of a nodule increases as its size increases (Weydert, 1985).

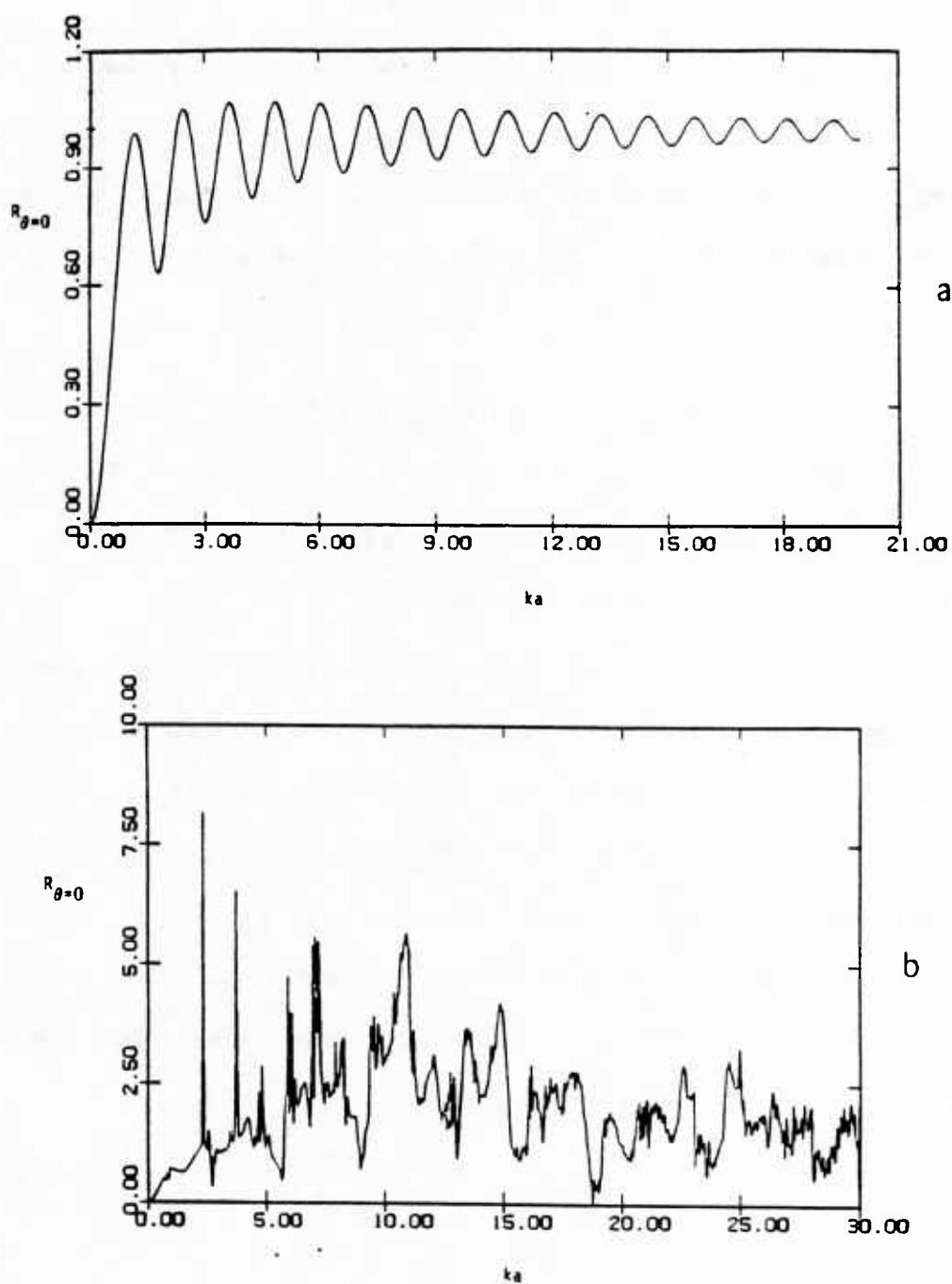


Figure 2-37. Reflectivity of hard and nodule spheres

Backscattered sound pressure for hard spheres (a) and elastic spheres with sound velocity and impedance similar to those of nodules (b). ka is the product of wavenumber and radius. (both from Ma, 1982)

2.8.2 A method for the assessment of nodule resources?

Assuming the nodules are all randomly distributed perfect spheres, and that the sediments are acoustically transparent, the phases of the backscattered intensities sum up to zero and the backscattered intensity of N nodules is the sum of the backscattered intensities (equation 2-93c). If there are M size classes, this sum becomes

$$I_{tot}(f_j) = \sum_{i=1}^M N_i I_i(f_j) \quad j=1, \dots, K \quad (2-94)$$

where N_i is the number of nodules of the i -th size class, and K is the number of frequencies used. This resulting system of equations can be solved if the number of frequencies equals or exceeds the number of size classes.

Now, nodules are not perfect spheres. Neither are fish. It is known, however, that some fish can be represented by equivalent spheres. If this is the case for nodules, or if there is some other unique relationship between the backscattered intensity and the nodule size, this set of equations can be used in principle. From the measurements made on Echo 1, we have learnt that there is an average frequency-dependent difference of 8 - 15 dB at normal incidence between bare mud and areas well covered with nodules. Neglecting the sediments if the nodule coverage exceeds 20% will therefore be all right at normal incidence.

2.8.2 Results

Table 2-13 shows the backscatter coefficients for different nodule coverages at a grazing angle of 30° . For the frequencies exceeding 15 kHz, the backscatter coefficients increase when the nodule coverage increases. At 9 kHz and 15 kHz, the backscatter coefficients first increase, then decrease as the coverage goes up. This decrease coincides with a decrease in the size of the nodules with higher coverage, as

4.5 kHz

coverage	I	$I + \sigma^{(1)}$	$I/I_0^{(2)}$	$I/I_{10}^{(3)}$
mud	-14 dB	-13 dB	0 dB	0.4
10%	-10 dB	-8 dB	4 dB	1
30%	-10 dB	-7 dB	4 dB	1
40%	-11 dB	-9 dB	3 dB	0.8
60%	-10 dB	-8 dB	4 dB	1
80%	—	—	—	—

9 kHz

coverage	I	$I + \sigma^{(1)}$	$I/I_0^{(2)}$	$I/I_{10}^{(3)}$
mud	-21 dB	-20 dB	0 dB	0.5
10%	18 dB	-16 dB	3 dB	1
30%	-12 dB	-9 dB	9 dB	4
40%	-10 dB	-8 dB	11 dB	6
60%	-13 dB	-11 dB	8 dB	3
80%	-17 dB	-15 dB	4 dB	1.2

60 kHz

coverage	I	$I + \sigma^{(1)}$	$I/I_0^{(2)}$	$I/I_{10}^{(3)}$
mud	-15 dB	-14 dB	0 dB	0.4
10%	-11 dB	-8 dB	4 dB	1
30%	-7 dB	-4 dB	8 dB	2.5
40%	-7 dB	-4.5 dB	8 dB	2.5
60%	-5 dB	-3 dB	10 dB	4
80%	-5 dB	-3 dB	10 dB	4

15 kHz

coverage	I	$I + \sigma^{(1)}$	$I/I_0^{(2)}$	$I/I_{10}^{(3)}$
mud	<-29 dB	<-28 dB	0 dB	0.7
10%	-26 dB	-24 dB	3 dB	1
30%	-23 dB	-21 dB	6 dB	2.5
40%	-20 dB	-18 dB	9 dB	5
60%	-21 dB	-19 dB	8 dB	4
80%	-19 dB	-17 dB	10 dB	5

110 kHz

coverage	I	$I + \sigma^{(1)}$	$I/I_0^{(2)}$	$I/I_{10}^{(3)}$
mud	-19 dB	-18 dB	0 dB	0.4
10%	-15 dB	-17 dB	4 dB	1
30%	-9 dB	-6 dB	10 dB	4
40%	-11 dB	-8.5 dB	8 dB	2.5
60%	-8 dB	-6 dB	11 dB	5
90%	-7 dB	-5.5 dB	12 dB	6.5

30 kHz

coverage	I	$I + \sigma^{(1)}$	$I/I_0^{(2)}$	$I/I_{10}^{(3)}$
mud	-29 dB	-28 dB	0 dB	0.7
10%	-27 dB	-24 dB	2 dB	1
30%	—	—	—	—
40%	-21 dB	-18 dB	8 dB	4
60%	-18 dB	-15 dB	11 dB	8
80%	-16 dB	-13 dB	13 dB	13

163 kHz

coverage	I	$I + \sigma^{(1)}$	$I/I_0^{(2)}$	$I/I_{10}^{(3)}$
mud	-12 dB	-11 dB	0 dB	0.5
10%	-9 dB	-6.5 dB	3 dB	1
30%	-5 dB	-2 dB	7 dB	2.5
40%	-5 dB	-2.5 dB	7 dB	2.5
60%	-2 dB	+0.5 dB	10 dB	5
80%	-1 dB	+2 dB	10.5 dB	5.5

Table 2-13: Backscatter coefficients at a grazing angle of 30 degrees

- 1) mean + one standard deviation
- 2) intensity relative mud (arbitrary dB)
- 3) intensity divided by intensity for 10% coverage

4.5 kHz

coverage	I	$I + \sigma^{(1)}$	$I/I_0^{(2)}$	$I/I_{10}^{(3)}$
mud	-13 dB	-12 dB	0 dB	0.7
10%	-11.5 dB	-9.5 dB	1.5 dB	1
30%	-8 dB	-6 dB	5 dB	2.5
40%	-7 dB	-5 dB	6 dB	3.0
60%	-6 dB	-5 dB	7 dB	3.5
80%	-4 dB	-3 dB	9 dB	5.5

9 kHz

coverage	I	$I + \sigma^{(1)}$	$I/I_0^{(2)}$	$I/I_{10}^{(3)}$
mud	-7 dB	-6 dB	0 dB	0.6
10%	-5 dB	-3 dB	2 dB	1
30%	-1 dB	+1 dB	6 dB	2.5
40%	+2 dB	+4 dB	9 dB	5
60%	+5 dB	+6 dB	12 dB	10.0
80%	+8 dB	+9 dB	15 dB	20.0

15 kHz

coverage	I	$I + \sigma^{(1)}$	$I/I_0^{(2)}$	$I/I_{10}^{(3)}$
mud	-22 dB	-21 dB	0 dB	0.3
10%	-17 dB	-14.5 dB	5 dB	1
30%	-9 dB	-7 dB	13 dB	7
40%	-8 dB	-5 dB	14 dB	8
60%	-3 dB	-0.5 dB	19 dB	26.0
80%	0 dB	+2 dB	22 dB	50

110 kHz

coverage	I	$I + \sigma^{(1)}$	$I/I_0^{(2)}$	$I/I_{10}^{(3)}$
mud	-22 dB	-21 dB	0 dB	0.5
10%	-19 dB	-16 dB	4 dB	1
30%	-16 dB	-15.5 dB	6 dB	2
40%	-16 dB	-13 dB	6 dB	2
60%	-12 dB	-15 dB	10 dB	5
80%	-11 dB	-14 dB	11 dB	6.0

30 kHz

coverage	I	$I + \sigma^{(1)}$	$I/I_0^{(2)}$	$I/I_{10}^{(3)}$
mud	-18 dB	-17 dB	0 dB	0.6
10%	-16 dB	-13 dB	2 dB	1
30%	-12 dB	-9 dB	6 dB	2.5
40%	-10 dB	-7 dB	8 dB	4.0
60%	-7 dB	-5 dB	11 dB	8.0
80%	-1 dB	+1.5 dB	17 dB	31.0

163 kHz

coverage	I	$I + \sigma^{(1)}$	$I/I_0^{(2)}$	$I/I_{10}^{(3)}$
mud	+2.5 dB	+3.5 dB	0 dB	0.5
10%	+5 dB	+8 dB	2.5 dB	1
30%	+9 dB	+13 dB	6.5 dB	2.5
40%	+8 dB	+11.5 dB	5.5 dB	2
60%	+13 dB	+16 dB	10.5 dB	6
80%	+16 dB	+19 dB	13.5 dB	12.5

Table 2-14: Normal incidence backscatter

- 1) mean + one standard deviation
- 2) backscatter relative backscatter for mud
- 3) intensity divided by intensity for 10% coverage

one expects from the target strength of individual nodules or spheres ($ka < 1$). The changes in size between 40% and 80% coverage are from 5 to 7 cm down to 4 to 6 cm. The ratio of vertical to longest horizontal axes being 0.50 for all nodule sizes at site 'E', this changes ka only 10 to 20% which is not sufficient to explain both the changes at 9 kHz and at 15 kHz (unless the effective radius is small enough so that $ka < 1$ at 15 kHz for nodules of 6 cm).

Table 2-14 shows the backscatter coefficients for different nodule coverages at normal incidence (maximum return). Although the beampatterns are poorly known at normal incidence and the absolute numbers are therefore suspicious at frequencies above 9 kHz, the relative changes are not affected for a fixed frequency since the height of the fish was maintained. Comparisons of the coverage and the backscatter coefficients show that the backscatter does not increase linearly with the coverage or the number of nodules. At 9 kHz, the product of wavenumber and longest half-axis ($kx/2$) exceeds 1 for all nodule sizes and one would not expect strong changes with nodule size, but rather changes proportional to the changes in coverage. As the backscattered intensity increases 4 times when the coverage is doubled from 30% to 60% at frequencies from 9 kHz to 30 kHz (both 5 to 7 cm nodules), it is concluded that the scattering is coherent at these frequencies and comes mainly from the first Fresnel zone.

The 9 kHz and 15 kHz normal incidence backscatter coefficients increase with coverage for coverages up to 80%, while at a grazing angle of 30° they do not. This cannot be explained by a change of the target strength of the nodules.

The insonified area is on the order of ten square meters at any given instant of time. If the average spacing between the nodules is of the order of $\lambda/2$ or λ , the backscattered wavelets interfere constructively. If the spacing changes, their phase relationships become random and equation (2-93) applies i.e. the total backscattered

intensity decreases substantially. The positions of the nodule centers of several photographs of site 'E' were digitized. Figure 2-38a shows the intensity of a typical two-dimensional Fourier transform of one of those. There is a strong central peak followed several nearly circular ridges with nulls in between. Figures 1-8c, 2-38a and 2-38b show that the spacing between next neighbours is between 10 and 15 cm for 40% coverage and 6 to 8 cm nodules. From figure 2-38a it is also obvious that the positions of the nodules are not random (compare figure 1-8). When the coverage goes up and the nodule size decreases (like at site 'E'), the spacing between the nodule centers tends to reach one nodule diameter in the limit i.e. 5 to 6 cm at site 'E'. This changes both the intensity and the positions of the maxima of the Fourier transform. This is in agreement with the first term in the second factor of equation (2-59) which relates the two-dimensional Fourier transform of the nodule positions to the back-scattered intensity. If this term is not balanced by an appropriate change in the roughness, changes in the nodule distribution pattern will affect the backscatter.

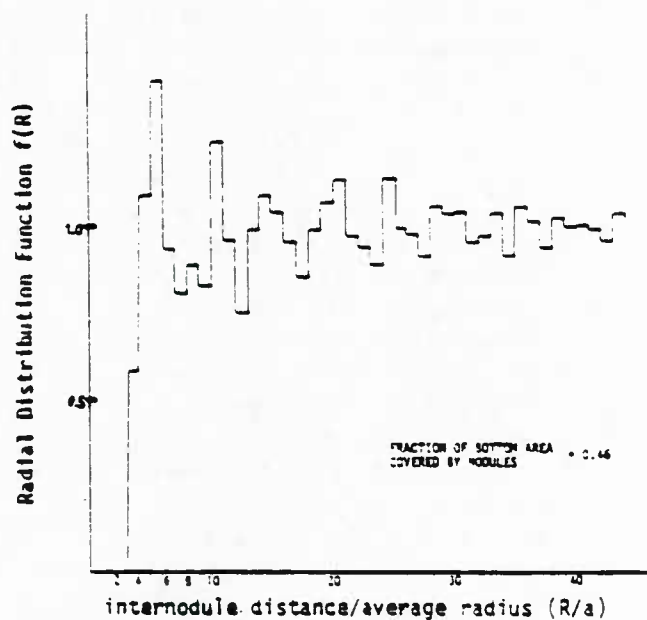
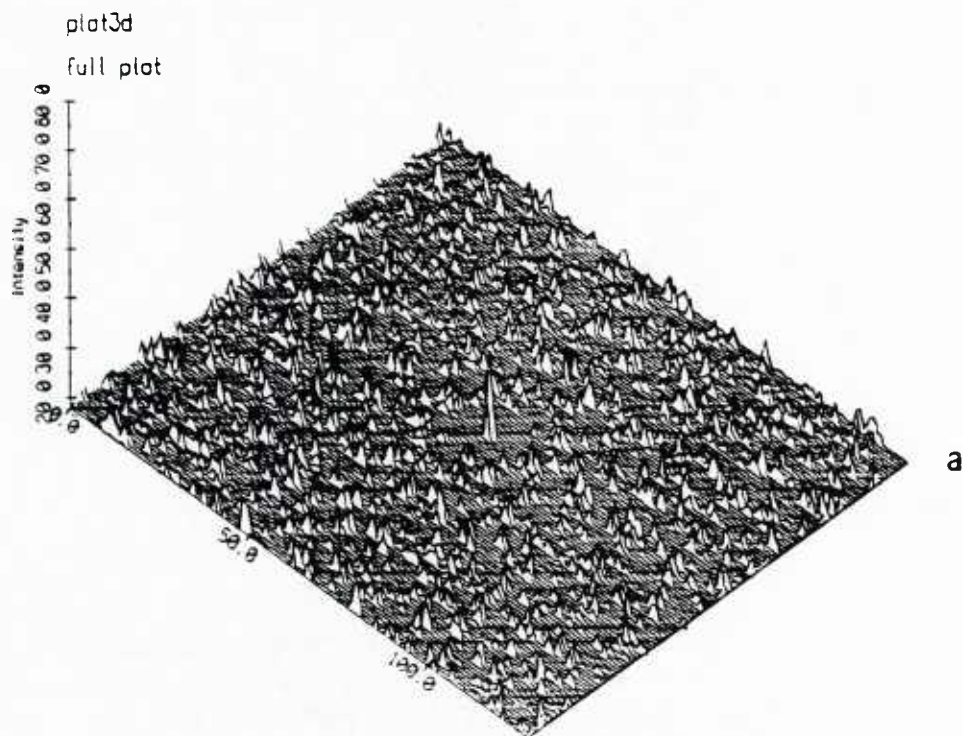


Figure 2-38. Nodule spacing

Sample two-dimensional Fourier transform of the nodule centers (a) and frequency of occurrence of nodule spacing (from Smith, 1981) normalized by the nodule radius (b)

Appendix 2-1

Structure of Identification Record

word number	position or information stored
1	date : year
2	date : month
3	date : day
4	time : hours (GMT)
5	time : minutes
6	time : seconds
7	
8	latitude (degrees)
9	latitude (minutes)
10	longitude (degrees)
11	longitude (minutes)
12	water depth (meters)
13	
14	fish height in cm (cf. word # 47)
15	fish speed (cm/sec)
16	pitch as digitized
17	number of words made at first (high) digitizing rate
18	number as in 17 + date + time + pitch etc...
19	digitizing frequency at beginning (high rate)
20	digitizing frequency after calibration interval (low rate)
21	number of records with data for this second
22	total number of bytes coming from digitizing computer
23	digitizing flag (= 0 , if OK = 1 , if transmitpulse in low rate = 2 , if bottom in both rates = 3 , if transient part of bottom or transmit too long = 4 , if height of fish unreasonable
24	general flag (= 0 ,if everything is OK)
25	frequency in kHz (4,9,15,30,60,110,160)
26	preamp gain (dB)
27	delay of transmission (msec)
28	TVG number (for each frequency)
29	TVG delay (milliseconds)
30	receiver DDTO gain
31	pulselength (number of cycles;cf. word # 64)
32	side scan flag (0 = OK)
33	start of zero reference pulse
34	height of zero reference pulse
35	start of transmit pulse
36	height of transmit pulse
37	start of frequency marker # 1
38	height of frequency marker # 1
39	start of sphere number one
40	height of signal of sphere number one
41	start of signal of sphere number two

42 height of sphere number two
43 start of backscatter from bottom
44 start of frequency marker #2
45 height of frequency marker #2
46
47 height of transducer in millisec (cf. word #14);
48 flag for sphere and reverberation (=0 ,if seperated)
49 number of spheres towed behind fish
50 number of elements used at 160 kHz
51
52 ratio of transmit pulse to reference pulse
53 projector voltage (rms)
54 total-range of pitch (e.g. 15. degrees)(since 16 November 83)
55 ...
56 minimum allowed height in meters
57 maximum allowed height in meters
63 sound speed in m/s (One way)
64 pulse length in microseconds*10 (cf.word #31)

Note that the positions as stored in this record correspond to the time/sampling interval. A zero for a position means that that signal is missing. Note that the heading record is always first i.e. all data are shifted by 64 words.

Appendix 2-2

Interpolation for the input voltages

1.) form the expression $20 \cdot \log(\text{output signal/reference})$ from the digitized back-scatter data : SIGREF

2.) find the next lower ratio RAT0 and the next higher ratio RAT1 from table 'A', and their respective inputs INP0 and INP1, and compute the difference of their inputs

$$BIGA = INP1 - INP0 \quad (A-1)$$

3.) find the exact ratios found sub 2.) and their corresponding inputs INP0' and INP1' in table 'B' (interpolated for the TVG step), and compute the difference of their inputs

$$BIGB = INP1' - INP0' \quad (A-2)$$

4.) find in table 'B' the ratio next lower to SIGREF SIG0 and the next higher one SIG1 (both interpolated for the TVG step), and compute their differences to INP0'

$$\Delta SM0 = SIG0 - INP0' \quad (A-3')$$

$$\Delta SM1 = SIG1 - INP0' \quad (A-3'')$$

5.) rescale and interpolate according to

$$\begin{aligned} INPUT(dB) = & \quad (A-4) \\ = INP0 + & \left[\Delta SM0 + (SIGREF - RAT0) \frac{\Delta SM1 - \Delta SM0}{\Delta x} \right] \frac{BIGA}{BIGB} \end{aligned}$$

where Δx = interval size in table 'B'. The error of the input signal level computed with this method is less than 0.3 dB for receiver gains of 0 and 1 (1/16 and 2/16 of voltage) and output ratios SIGREF with $-10\text{dB} < SIGREF < 5\text{dB}$, and less than 0.7 dB for output ratios with $-30\text{dB} < SIGREF < -10\text{dB}$.

Chapter III Simulations

3.1 Introduction

When carrying out reverberation experiments, it is frequently difficult to determine what is producing the observed phenomena. Simulations can serve to find out if some observation is deterministic or random. Simulations can also be used to estimate the sensitivity of the results to any number of parameters, or, if some inputs are available, to estimate the magnitude and the statistics of the variables to be measured. This reduces the cost of the equipment design and, for oceanographic experiments, the costs of the at sea operations.

Before the sea trials no measurements of the target strength of manganese nodules were available. So it was not possible to add up the echoes from individual nodules to get the total signal received at a transducer (The estimates of the returns were done using backscatter measurements of gravel and of mud). In the meantime, measurements of the backscatter of individual manganese nodules have been published (figure 3-1) (Weydert, 1985). There are also several computer programs available to simulate reverberation and to simulate the return from a number of targets. Version 4 of REVGEN (REVerberation GENeration) developed by Goddard and Princehouse (Goddard and Princehouse, 1985) has been made available to the Marine Physical Laboratory. REVGEN 4 contains a well verified software package for surface, bottom and volume reverberations, as well as for a large range of targets. In addition, it can be used to simulate any beampattern, platform (Deep Tow) trajectory, noise background, etc... Only the built-in reverberation routine and the return from targets will be discussed here. The reader is referred to the user's manual and Goddard and Princehouse 1985 for the description of the trajectories, platforms, beampatterns, etc...

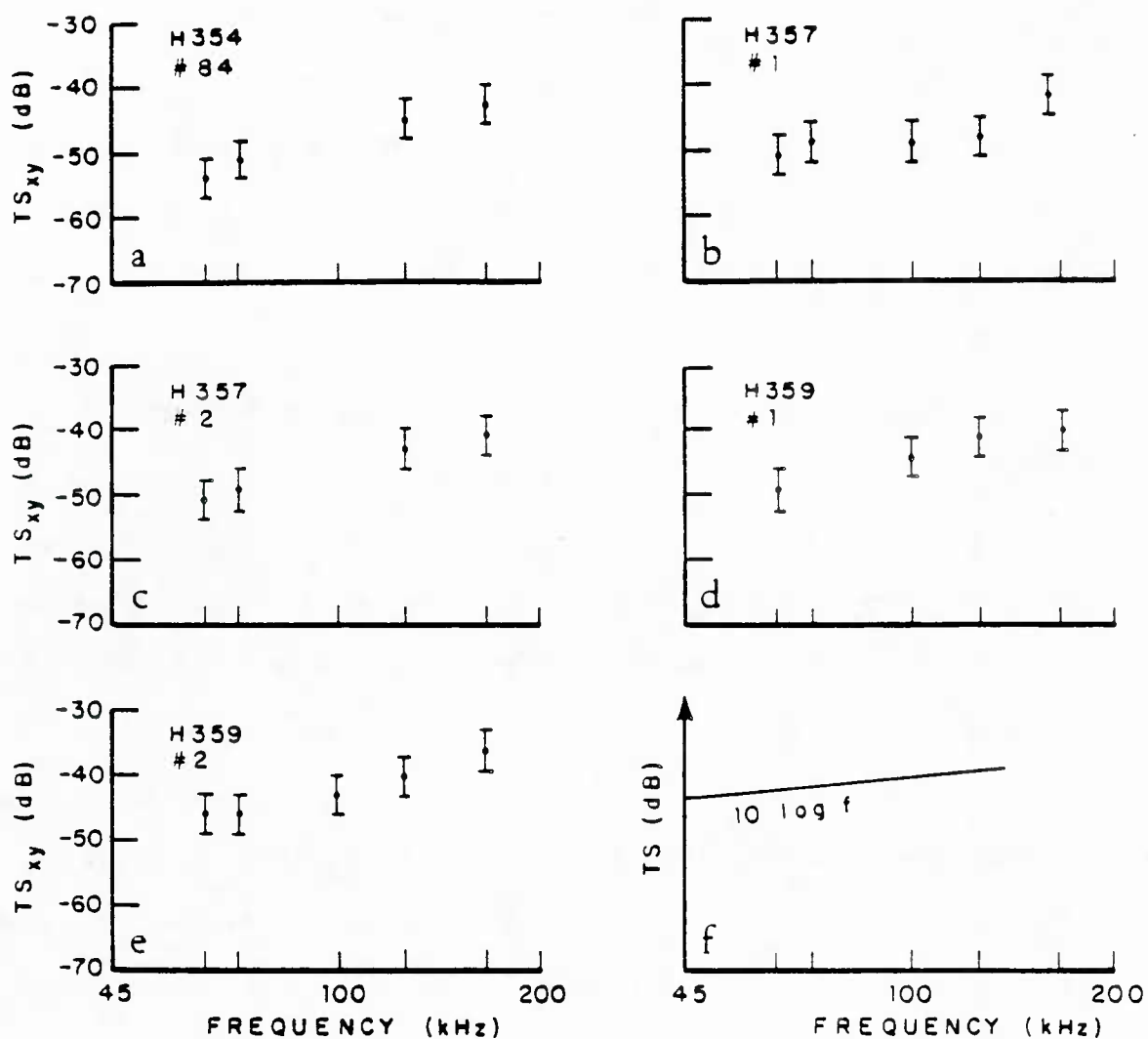


Figure 3-1. Horizontal target strengths of individual nodules

Horizontal target strength (average over echos while the nodules are turned around the x-axis and around the y-axis) as a function of the acoustic frequency. The calibration errors have been indicated. The curve $10 \log_{10} f$ is shown for comparison.

REVGGEN is a linear system, where the return of the targets is given by

$$r(t) = \sum_{i=1}^N a_i G_i(t) s(\alpha_i(t - t_i)) \quad (3-1)$$

where t_i is the two-way travel time between the sonar and the i th target, α_i is the Doppler distortion factor, a_i is the size of the scatterer and

$$G_i(t) = g B_i^2(r_i) h(t) \quad (3-2)$$

where g is the system gain, B_i^2 is the two way transducer response and h represents the two way transmission loss.

In the REVGGEN routine to simulate bottom reverberation, the user defines the reverberation strength as a function of the grazing angle. REVGGEN then places a number of the scatterers into each shell (a layer used to subdivide the calculations into smaller ones so that they can be handled by the computer; this is justified since the system is linear). The sizes of these scatterers are drawn from a Rayleigh distribution, their positions are random.

3.2 Simulation description

In the present study the built-in reverberation routine was only used to simulate the reverberation from bare mud by prescribing idealized reverberation coefficients as a function of the grazing angle. This reverberation was added to the return from the nodules. Runs with and without bottom reverberation showed that the reverberation is negligible compared to the return from the nodules. The nodules themselves were modeled as ellipsoidal targets of given target strengths with 10 to 30 highlights (scatterers) per ellipsoid. The target strengths of the nodules were randomly distributed between -25 dB and -40 dB. Independently of the target strengths, their sizes were randomly chosen between 5 and 10 cm with fixed axes ratios (0.8 for the medium over the longest axis and 0.6 for the vertical over the longest axes). The

vehicle was positioned at a height of 35 meters above the sea floor. A projector with a fan-shaped beampattern with a 1° total beamwidth in the horizontal was chosen to insonify a 4m x 6m patch of nodules at horizontal distances of 50m and 100m with a rectangular pulse (1 ms). This corresponds to grazing angles of 35° and 19° respectively ¹⁾. Thus the insonified area (about 1 m²) was always smaller than the nodule patch. The backscattered signals were computed at the position of the projector i.e. for the case where the same transducer is used as a projector and as a hydrophone (like in the measurements made with the Deep Tow).

Twelve runs were made for 100 nodules per m² at frequencies of 15 kHz and 163 kHz, varying the positions and orientations of the nodules randomly between two consecutive sets of 4 runs (2 grazing angles and 2 frequencies for the same nodule distribution). Figure 3-2 shows examples of the envelopes of the returned signal for a projector source level of 200 dB reference 1 $\mu Pa/Volt$ at 1 m and a digitizing rate of 10 kHz. Note the strong fluctuations within the pings.

Twenty more runs with 200 nodules per m² were made at a grazing angle of 19 degrees and frequencies of 15 and 163 kHz. Figure 3-3 shows 2 examples of individual pings.

In order to check the results, twelve runs with point scatterers were made at both frequencies and a grazing angle of 19° .

¹⁾ Since the 6 Megabytes of memory allocated under UNIX on the computer used were insufficient to do this directly, the 4m x 6m patch was subdivided into 1m x 4m stripes and the complex signals of the returns summed together. This can be done since the system is linear.

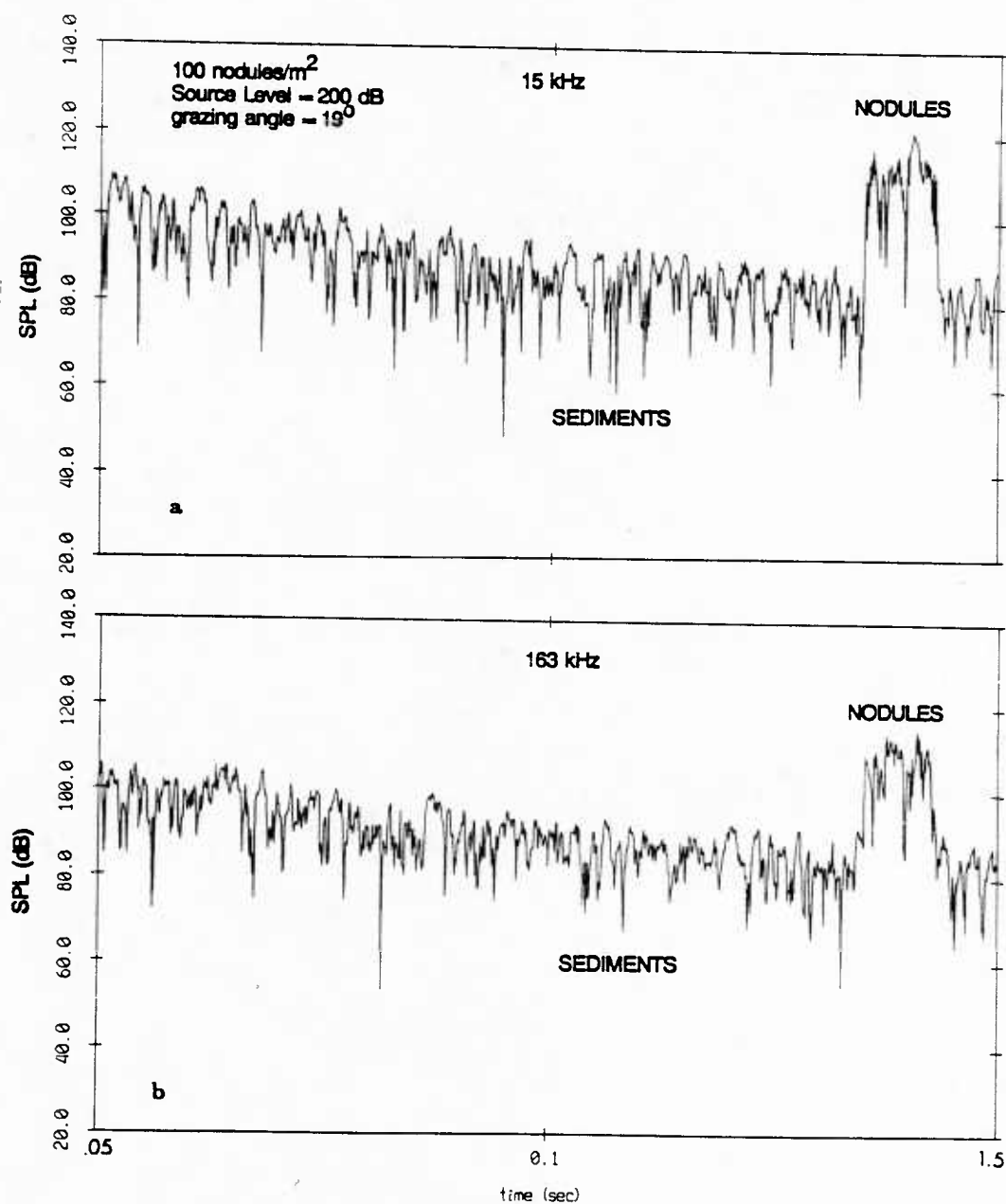


Figure 3-2. Samples of simulated backscatter

Typical envelopes of the return of the simulated backscatter from manganese nodules at 15 kHz (a) and 163 kHz (b), a grazing angle of 19 degrees and 100 nodules per m^2 . The nodule patch coincides with the strong return at 1.4 ms. The level of the background reverberation is one of the input parameters for the program.

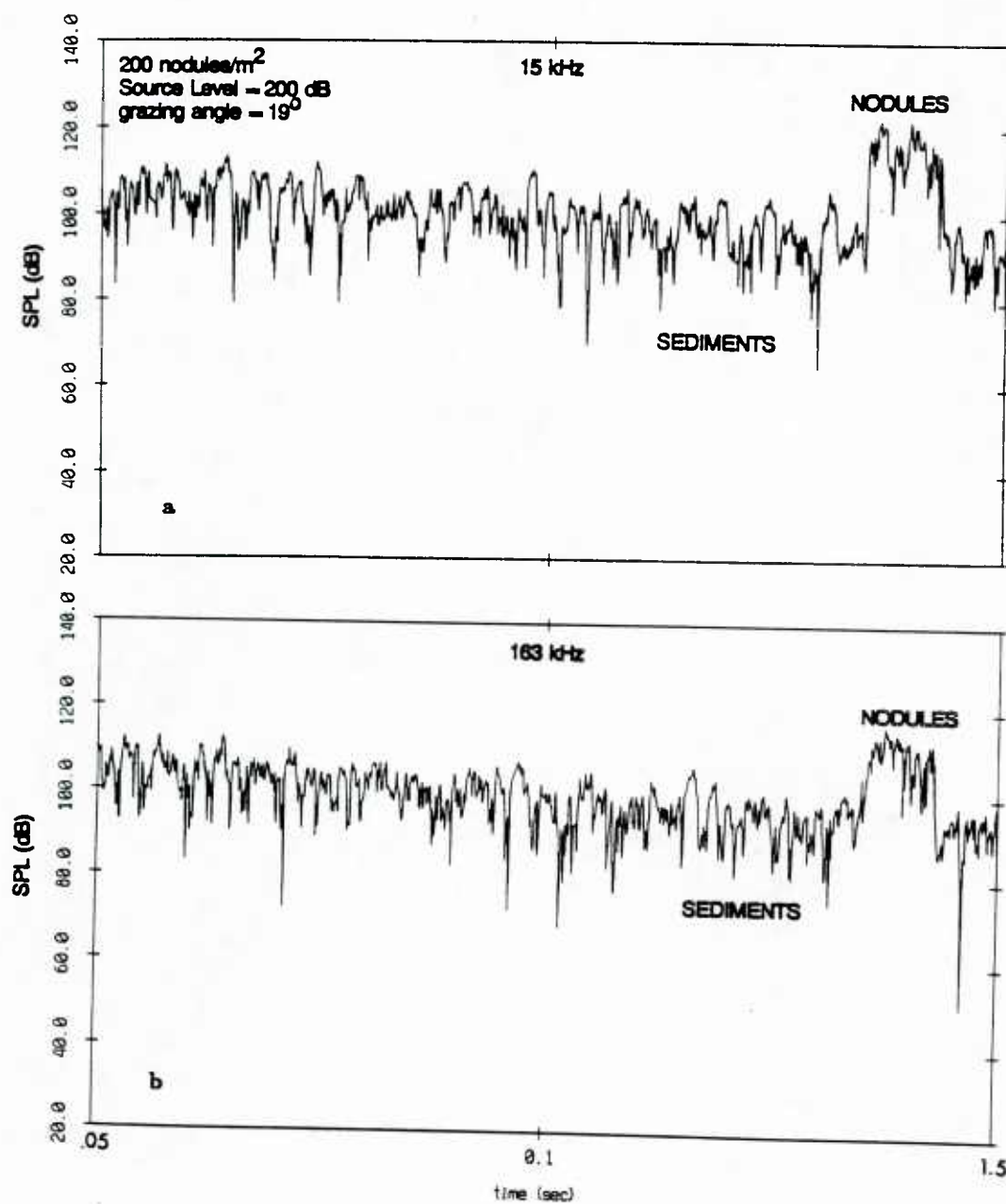


Figure 3-3. Samples of simulated backscatter

Typical envelopes of the return of the simulated backscatter from manganese nodules at 15 kHz (a) and 163 kHz (b), a grazing angle of 19 degrees and 200 nodules per m^2 . The nodule patch coincides with the strong return at 1.4 ms. The level of the background reverberation is one of the input parameters for the program (higher than in figure 3-1).

3.3 Results

The intensity means for each of the two geometries and frequencies were calculated for each ping and then ensemble averaged over all pings in that set. From these averages backscatter coefficients BS were calculated by equation (3-3):

$$BS = SPL - SL + TL - 10 \log A \quad (3-3)$$

where SPL is the sound pressure level in dB at the hydrophone, SL is the source level of the projector (always 200 dB reference 1 μ Pa at 1 m), TL is the transmission loss (spherical spreading and absorption), and A is the insonified area.

angle	number	simulated BS coeff. ¹		in situ BS coeff. ²		calculated TS ³	
		15 kHz	163 kHz	15 kHz	163 kHz	15 kHz	163 kHz
19°	100	-5.5 dB	-8 dB	-23 dB	-6 dB	-50 dB	-34 dB
35°	100	-5.4 dB	-11 dB	-17 dB	-5 dB	-45 dB	-38 dB
19°	200	-3 dB	-6 dB	-21 dB	-5 dB	-51 dB	-33 dB

1) backscatter coefficient for median target strength of -32.5 dB

2) measured backscatter coefficients

3) target strength derived by matching 1) and 2)

Table 3-1: Backscatter coefficients and target strength

Backscatter coefficients as a function of the grazing angle, frequency and number of nodules per m^2 as calculated with REVGEN and as measured in situ on Echo 1. The third column shows the target strengths calculated by matching the measured and the simulated backscattering strength.

With the inputs as described above the means lead to the backscatter coefficients in table 3-1. An increase of 2 to 2.5 dB is observed when the number of nodules per m^2 is doubled. The return at 163 kHz is several dB lower than the return at 15 kHz although exactly the same nodules (same target strengths and same highlights) were positioned with the same orientations on the same points of the sea floor. Since a similar difference is observed when the nodules are replaced by point scatterers, it is concluded that the different phase relationships for the different wavelengths lead to

this difference. For 100 nodules per m^2 , the average spacing between nodule centers is 10 cm, which is less than a wavelength at 15 kHz, but several wavelengths at 163 kHz. When the number of nodules is doubled, the spacing between the centers of next neighbours decreases by $\sqrt{2}$, which changes the spacing to wavelength relationships by $\sqrt{2}$. The situation is complicated by the fact that our nodules are ellipsoids and the spacing between nodules decreases much faster than the spacing of their centers when the number of nodules is increased. Thus the phases of the backscattered wavelets change with the nodule distribution. This also explains why a doubling of the number of nodules does not always lead to a doubling of the backscattered energy.

Since the system is linear, a change in the target strengths in the input file (uniform distribution from -40 dB to -25 dB) translates itself to the mean. From this it is possible to determine the median target strength TS^{calc} for the manganese nodules on the sea floor with equations (3-4) i.e. by matching the measured backscattering strength.

$$TS^{calc} = -32.5 - BS^{calc} + BS^{meas} \quad (3-4)$$

where -32.5 is the median target strength used for the simulations, BS^{calc} is the backscatter coefficient as calculated with REVGGEN, and BS^{meas} is the backscatter coefficient as measured in situ. Nodules comparable to those described in the input file were observed in the Control Area and just south of the Mining Area at site 'E' (table 3-1). This leads to median target strengths of -51 to -45 dB at 15 kHz and -38 to -33 dB at 163 kHz (table 3-1). The measured "horizontal target strength" is -38 ± 3 dB for a nodule of 8 cm length and a frequency of 163 kHz (figure 3-1). Using a $10\log f$ relationship, the results from figure 3-5 can be extrapolated to yield a target strength of -52 ± 3 dB at 15 kHz. It is not surprising that the agreement is not better. The "horizontal target strength" is an average over the echo at all angles

while the nodule is rotated around the x-axis and around the y-axis (one at a time). At least some of the angular variation observed in the tank experiment is not well modeled or averaged out by REVGGEN. Otherwise there should be a difference in the return at different grazing angles and all frequencies. The target strength of the nodules in the tank was determined at a pressure of 1 bar, while at site 'E' the pressure is 450 bar. Only the target strengths of a few nodules have been measured i.e. the average target strength of the nodules of a given area is unknown. In addition, the target strength was extrapolated from 45 kHz ($ka = 6$) to 15 kHz ($ka = 2$). The model used in these simulations is strongly simplified, especially the model for the nodules (a set of point scatterers distributed within an ellipsoid the size of a nodule). The accuracy of a model using a random positioning on the sea floor must be questioned as the nodules tend to be locally aligned by the benthic activity.

Figures 3-4a and 3-4b shows typical covariances as computed by equation (2.70) (12 ping average). The covariances follow closely the theoretical shape for a rectangular transmit pulse (Olchevskii, 1967). The halfwidth and the quarterwidth are somewhat narrower than those measured in situ (figure 2-38). This discrepancy is attributed to the patchiness of the nodule field on the scale of a few meters.

Figure 3-4c shows the covariance when the nodules change abruptly from 100 nodules per m^2 to 200 nodules per m^2 . This was possible by ensemble averaging over both sets of pings at a grazing angle of 19 degrees. The covariance is strongly asymmetric around the center (zero time lag). This is in agreement with the covariances observed at sea when the nodule coverage changes or when the nodules disappear (chapter 2.5).

Twelve runs were made with point scatterers having a target strength of -25 dB. No bottom reverberation was included. This allowed to study the varying phase relationships between the Huygens wavelets when the number of nodules is increased

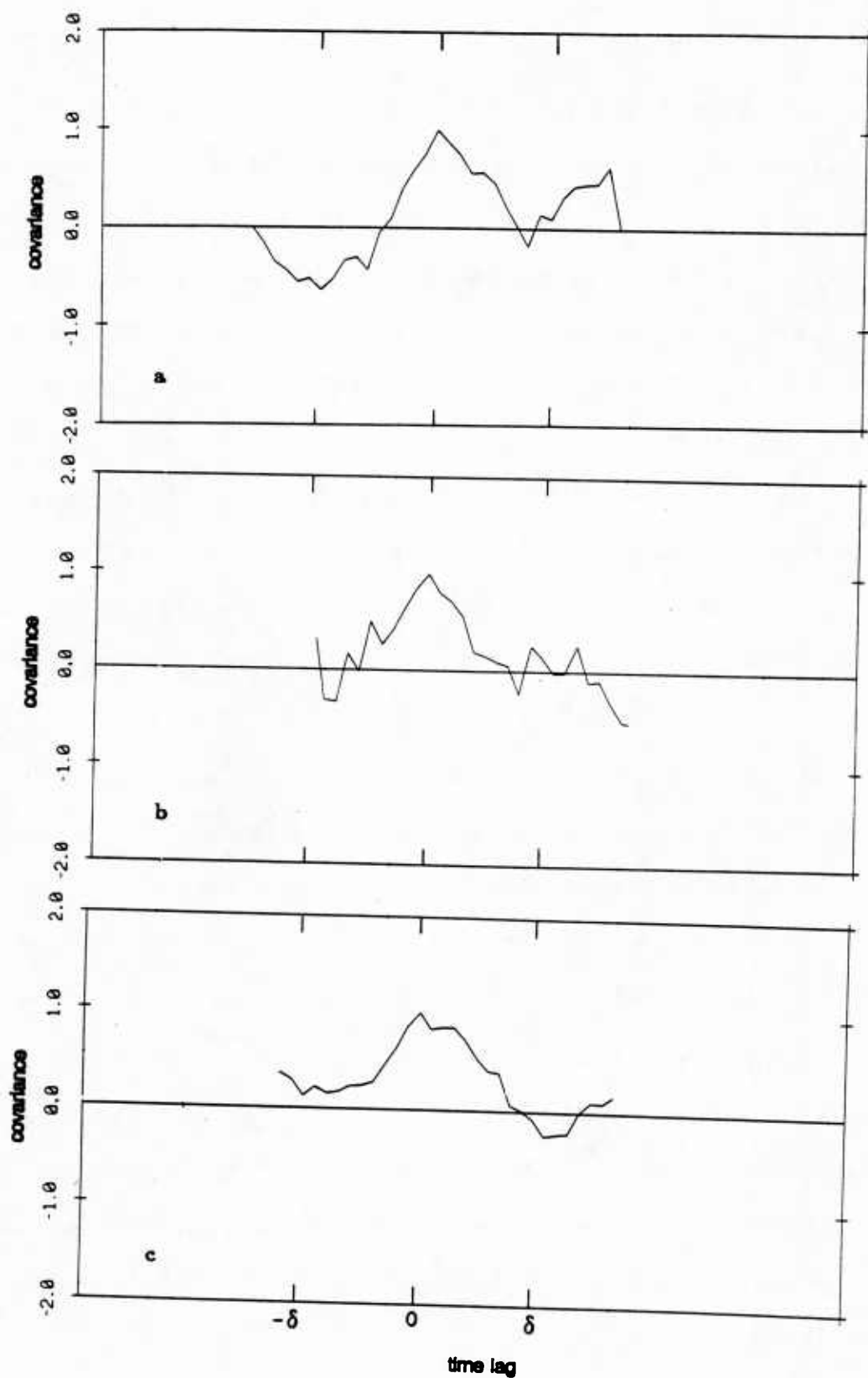


Figure 3-4. Covariances

Covariances as computed with equation (2.70) for a pulse length δ of 1 ms and 100 nodules per m^2 (a), 200 nodules per m^2 (b), and for a sharp transition zone from 100 nodules per m^2 to 200 nodules per m^2 (c).

from 100 to 400 nodules per m^2 . The results (table 3-2) show that after a peak at 300 to 350 nodules per m^2 , the backscatter drops again. With the random distributions used, the drop is insufficient to explain the drop in backscattering strength observed at 9 kHz at site 'E' (Note that for point scatterers a denser nodule coverage is equivalent to a longer acoustic wavelength i.e. the results of the REVGGEN simulation at 15 kHz can be applicated to 9 kHz).

<i>nodules/m²</i>	100	200	300	350	400
backscatter	0 dB	1.8 dB	2.4 dB	2.1 dB	1.3 dB

Table 3-2: Return from different nodule concentrations.

3.4 Conclusion

The backscatter from manganese nodules on the sea floor has been simulated using the computer program REVGGEN. It was shown that the return is strongly sensitive to the phase relationships between the wavelets generated at the nodules. By matching the backscattering strength measured in situ and the backscattering strength from the simulations, target strengths of the manganese nodules of -51 to -45 dB at 15 kHz and -38 to -33 dB at 163 kHz were derived. These are roughly in agreement with those measured in an earlier experiment (Weydert, 1985). The asymmetry of the covariance observed in situ when the nodule coverage changes was reproduced by changing the number of nodules from 100 to 200 nodules per m^2 , while the covariance of a uniform distribution follows closely the theoretical function.

CONCLUSION

During the Echo 1 expedition an area of Cu-Ni rich manganese nodules was intensively studied and with a deeply towed instrument package and a box coring technique. The geology of this area has been described in detail and it has been shown that the nodule size distributions are best modeled by a Gaussian. The three main nodule axes are related to each other as 1:0.8:0.5. The nodule density is $2.00 \pm 0.04 \text{ g/cm}^3$ and the volumes increase on the average with the 2.4th power of the longest length. The nodule coverage varies from bare sediment to 80% and the sizes range from 2 cm to 13 cm. It was found that the changes of the thickness of the upper acoustic unit of the sediment column correlate with changes in nodule coverage and concentration.

The acoustic backscatter has been determined for frequencies of 4.5 to 163 kHz for 4 different environments, namely the deep sea sediments at site 'E', the deep sea sediments at the foot of the Patton Escarpment, the manganese nodules at site 'E' and the phosphorites at the Thirtymile Bank. The acoustic backscatter is different for different deep sea sediments, depends on the manganese nodule coverage and the presence or absence of phosphorites. At frequencies of 30 kHz and higher the backscatter increases with increasing nodule coverage at all grazing angles. At normal incidence, the backscatter increases with nodule coverage for all 7 frequencies. For frequencies below 60 kHz, the backscatter increases as the square of the nodule coverage i.e. the return comes from the first Fresnel zone only (normal incidence). These results show that it is possible to distinguish acoustically between different types of deep sea sediments and between different amounts of nodule coverage of the sea floor. It is therefore possible to use acoustic techniques to identify different types of deep sea floor and to determine nodule coverage. These results will strongly facili-

tate the exploration of the sea floor, especially prospective deep sea mining sites.

REFERENCES

- Allman, R.L., and Igarashi, Y., 1984, In situ sediment attenuation and sound velocity ratio measured in shallow water at the Quinault Range, Naval Ocean Systems Center, San Diego, California, Technical Report 982.
- Anderson, V. C., 1950, Sound scattering from a fluid sphere, *Journal of the Acoustical Society of America*, vol. 22, p.426-431.
- Anderson, V.C., 1984, EECS 142C laboratory notes, University of California San Diego.
- ANSI, 1972, Procedures for calibration of underwater electroacoustic transducers, American National Standards Institute, S1.20-1972.
- Arrhenius, G., 1952, Sediment cores from the East Pacific, Repts. of the Swedish Deep-Sea Expedition No. 5.
- Arrhenius, G., Jasievicz, J. and Weydert, M., 1985, Crystal structures in manganese nodules from the Pacific Ocean floor, in prep.
- Bendat, J.S. and Piersol, A.G., 1971, Random data: analysis and measurement procedures, Wiley, New York, 1971.
- Berlincourt, D.A., and Krueger, H.H.A., 1964, Behavior of piezoelectric ceramics under various environmental and operational conditions of radiating sonar transducers, Clevite (Ohio) technical paper TP-228.
- Bischoff, J. L. and Piper, D. Z., 1979, Marine Geology and Oceanography of the Pacific Manganese Nodule Province: Marine Science, v. 9., New York, Plenum Press.
- Bobber, R., 1970, Underwater electroacoustic measurements, Naval Research Lab Florida.
- Breaker, L. C. and Winokur, R. S., 1967, The variability of bottom reflected signals using the Deep Research Vehicle Alvin: USN Oceanographic Office, IR No. 67-92.
- Breslau, L.R., 1967, The normally incident reflectivity of the sea floor at 12 kHz and its correlation with physical and geological properties of naturally occurring sediments. WHOI Reference 67-16.
- Breslau, L., 1967, Classification of of sea-floor sediments with a shipborne acoustical system: WHOI Contribution No. 1678.
- Clay, C.S. and Medwin, H., 1977 *Acoustical Oceanography*, John Wiley and Sons
- Clay, C. S. and Leong, W. K., 1973, Acoustic estimates of the topography and roughness spectrum of the sea floor southwest of the Iberian Peninsula, in *Physics of Sound in Marine Sediments*: L. Hampton, Ed., New York, Plenum Press.

- Clay, C.S., and Rona, P.A., 1965, Studies of seismic reflections from thin layers of the ocean bottom in the western North Atlantic, *Journal of Geophysical Research*, vol. 70, p.855-869.
- De Moustier, C., 1985, Inference of manganese nodule coverage from sea beam acoustic backscattering data, *Geophysics*, vol. 50, No 6, pp. 989-1001.
- Emery, K.O., 1960, *The sea off Southern California*, John Wiley and Sons.
- Finney, B., Heath, R.G., and Lyle, M., 1984, Growth rates of manganese-rich nodules at MANOP Site H (Eastern North Pacific), *Geochimica et Cosmochimica Acta*, vol.48, pp.911-919.
- Goddard, R.P. and Princehouse, D.W., 1985, REVGEM, high fidelity simulations of sonar signals, Applied Physics Lab, University of Washington, Technical Report, APL-UW8505.
- Goldberg, E., and Arrhenius, G., 1958, Chemistry of Pacific Pelagic Sediments, *Geochimica et Cosmochimica Acta*, vol.13, pp.153-212.
- Greenslate, J., 1977, Manganese concentration wet density : a geochemistry constant, *Marine Mining*, vol. 1, pp. 125-148.
- Hamilton, E.L., Shumway, G., Menard, H.W., and Shippek, C.J., 1956, Acoustic and other physical properties of shallow-water sediments off San Diego, *Journal of the Acoustical Society of America*, vol. 28, p.1-15.
- Hamilton, E. L., 1970a, Sound velocity and related properties of marine sediments, North Pacific: *J. Geophysical Research*, v.75, p.4423-4446.
- Hamilton, E. L., 1970b, Reflection coefficients and bottom losses at normal incidence computed from sediment properties: *Geophysics*, v.35, p.995-1004.
- Hamilton, E.L., 1974, Prediction of deep sea sediment properties: state-of-the-art, in *deep-sea sediments : physical and mechanical properties*, A.L. Inderbitzen, editor, Plenum Press, New York.
- Harris, B., 1966, *Theory of probability*, Addison Wesley, 291p.
- Hewlett Packard, 1979, Sonar transducer calibration, Application Note 205-2.
- Hastrup, O.L., 1970, Digital analysis of acoustical reflectivity in the Tyrrhenian abyssal plain, *Journal of the Acoustical Society of America*, vol. 70, p.181-190.
- Heath, R.G., 1979, Burial rates, growth rates, and size distributions of deep-sea manganese nodules, *Science*, vol. 205, p.903-904.
- Heath, R.G. and Van Andel, T., 1973, Initial Reports of the Deep Sea Drilling Project, volume 16, site 159, p.231-264, Washington, D.C., US Government Printing Office, Washington, D.C.

- Heath, R.G. and Van Andel, T., 1973, Initial Reports of the Deep Sea Drilling Project, volume 16, site 160, p.265-299, Washington, D.C., US Government Printing Office, Washington, D.C.
- Hill, M.N., 1952, Seismic refraction shooting in an area of the eastern Atlantic, Phil. Trans. Royal Society London(A), vol.244, p. 561-569.
- Hiroe, T., Keiji,H., Kenji, I., and Eiji, K., 1984, Research and development project of manganese nodule mining system in Japan, Offshore Technology Conference, Houston (Texas), 1984.
- IEEE, 1979, Programs for digital signal processing, Chapter 5.1, IEEE Press, The Institute of Electric and Electronics Engineers, Inc. New York.
- Ishimaru, A., 1978, Wave propagation and scattering in random media, Academic Press, New York, 1978, volumes 1 and 2.
- Jitkovskii, Y.Y. and Volovova L.A., 1965, Sound scattering from the ocean bottom, paper E67, Proceedings of the Fifth International Acoustics Congress, Liège, Belgium.
- Johnson, D.A., 1971, Studies of deep sea erosion using deep-towed instrumentation, Ph.D. thesis, Scripps Institution of Oceanography Reference 71-24.
- Jones, J.L., Leslie, C.B., and Barton, L.E., 1964, Acoustic characteristics of underwater bottoms, Journal of the Acoustical Society of America, vol.36, p. 154-157.
- Karas, M.C., Studies of manganese nodules using Deep-Tow photographs and side-looking sonars, Scripps Institution of Oceanography Reference 78-20.
- Katsuya, T., Fukuo, I., and Tetsuo, Y., 1984, Development of in situ measuring apparatus of geotechnical elements of sea floor images, Offshore Technology Conference, Houston, 1984.
- Keane, J.J., 1968, Volume reverberation as a function of single frequency pulse lengths and frequency modulated sweep rates, Journal of the Acoustical Society of America, vol 43, pp.566.
- Leroy, C.C., 1969, Development of simple equations for accurate and more realistic calculations of the speed of sound in sea water, Journal of the Acoustical Society of America, 46, pp. 216-226.
- Lieberman, L.N., 1948, Reflection of sound from coastal sea bottom, Journal of the Acoustical Society of America, 20, p.305-309.
- Lovett, J.R., 1978, Merged seawater sound-speed equations, Journal of the Acoustical Society of America, 63(6), 1978, pp.1713-1718.
- Ma, Y., 1982, Acoustic scattering analysis for remote sensing of manganese nodules, Ph.D.-thesis, Virginia Polytechnic Institute and State University, Blacksburg, Virginia.

- Mackenzie, K. V., 1960, Reflection of sound from coastal bottoms: J. Acoustical Society of America., v. 32, p.221-231.
- Magnuson, A. H., 1983, Manganese nodule abundance and size from bottom reflectivity measurements: Marine Mining, v. 4, p.265-296.
- Magnuson, A. H., Sundkvist, K., Ma, Y., and Smith, K., 1981, Acoustic soundings for manganese nodules: Proc.13th Annual Offshore Technology Conf., OTC 4133, p.147-161.
- Magnuson, A. H., Sundkvist, K., Ma, Y., Riggins, D., and Sen, R., 1982, Remote acoustic sensing of manganese nodule deposits: Proc. 14th Annual Offshore Technology Conf., OTC 4260, p. 431-444.
- McKinney, C.M., and Anderson, C.D., 1964, Measurements of backscattering of sound from the ocean bottom, Journal of the Acoustical Society of America, vol. 36, p158-163.
- Mitsui, T., Gomi, T., Ito, T., Ushitani, M., and Yamaguchi, M., 1984, Development of composite fiber-optic electric-power umbilical cable and optical feedthrough for deep ocean mining, Offshore Technology Conference, Houston, 1984.
- Mizuno, A. and Moritani, T., 1976, Manganese nodule deposits of the Central Pacific Basin, in World Mining and Metals Technology, p. 267 -281.
- Morse, P.M., and Ingard, K.U., 1968, Theoretical Acoustics, Mc Graw-Hill Book Company, New York.
- Nafe, J.E., and Drake, C.L., 1963, Physical properties of marine sediments, in: The Sea, vol. III, M.N. Hill, editor, Interscience Publishers, New York, p.794-815.
- Navy, US, 1946, The application of oceanography to sub-surface warfare Summary technical report of the National Defence Research Committee.
- Navy, US, 1969, Bergman, P. G., Yaspan, A., Gerjuoy, E., Major, J. K., and Wildt, editors, Physics of sound in the sea, Department of the Navy, Washington, D.C.
- Ol'shevskii, V.V., 1967, Characteristics of sea reverberation, Consultants Bureau, New York.
- Patterson, R. B., 1967, Relationships between acoustic backscatter and geological characteristics of the deep ocean floor: J. Acoustical Society of America, vol. 46, p. 756-761.
- Peled, A. and Liu, B., 1976, Digital signal processing, Theory, design and implementation, John Wiley & Sons.
- Piper, D. Z., Leong, K., and Cannon, W. F., 1979, Manganese nodule and surface sediment compositions: Domes sites A, B, and C, in Marine Geology and Oceanography of the Pacific Manganese Nodule Province, Marine Science: vol. 9, New York, Plenum Press, p. 437-473.

- Rayleigh, Lord, 1896, *The Theory of Sound*, London, G.B.
- Richards, A.F., 1962, Investigations of deep sea sediment cores, part 2: mass physical properties, US Navy Hydrographic Office, Technical Report 106.
- Sarmiento, R., and Kirby, R.A., 1962, Recent sediments of Lake Maracaibo, *Journal Sed. Petr.*, vol. 32, p.698-724.
- Shumway, G., 1960, Sound speed and absorption studies by a resonant method, *Geophysics*, vol. 25, p. 451-457 and p. 659-682.
- Smith, K.D., 1981, Properties of oceanic manganese nodule fields relevant to a remote acoustical sensing system, Master's thesis, Virginia Polytechnical Institute and State University, Blacksburg, Virginia, USA.
- Spiegel, M.R., 1961, *Statistics*, McGraw-Hill Book Company.
- Spiess, F. N. and Greenslate, J., 1976, Pleiades expedition leg 4, Scripps Institution of Oceanography, Manganese Nodule Project Technical Report No. 15.
- Spiess, F., N. and Tyce, R. C., 1973, Marine Physical Laboratory Deep Tow instrumentation system: Scripps Institution of Oceanography Reference 73-4.
- Spiess, F. N., Hessler, R., Wilson, G., Weydert, M., and Rude, P., 1984, Echo I cruise report: Scripps Institution of Oceanography Reference 84-3.
- Spiess, F. N. and Lonsdale, P. F., 1982, Deep Tow rise crest exploration techniques : *Marine Technology Society Journal*, vol. 16, p. 67-75.
- Spiess, F. N and Weydert, M. : Cruise report: Rama Leg 1, MANOP sites C & R, March 1984, in Scripps Institution of Oceanography Reference 84-4
- Stanton, T.K., 1984, Sonar estimates of microroughness, *Journal of the Acoustical Society of America*, vol. 75, p.809-818.
- Sumitomo Metal Mining Co., LTD., 1982, Multi-frequency exploration system (MFES): Technical Information 24-8, 4-Chome Shimbashi, Minato-ku, Tokyo, Japan.
- Urick, R.J., 1954, The backscattering of sound from a harbour bottom, *Journal of the Acoustical Society of America*, 26, p.231-235.
- Urick, R. J., 1983, *Principles of Underwater Sound*, 3rd edition, New York, McGraw-Hill Book Co., Inc.
- Urick, R.J., and Saling, D.S., 1962, Backscattering of explosive sound from the deep sea bed, *Journal of the Acoustical Society of America*, vol. 34, p. 1721-1724.
- Varadan V.K. and Varadan V.V., 1980, (editors) *Acoustic, electromagnetic and elastic wave scattering - focus on the T-matrix approach*, Pergamon, New York, 1980.

- Waterman, P.C., 1969, New formulation of acoustic scattering, *Journal of the Acoustical Society of America*, 45, p.1417-1429. p.1417.
- Weydert, M., 1985, Measurements of the acoustic backscatter of manganese nodules, *Journal of the Acoustical Society of America*, volume 78.
- Weydert, M., and Zampol, J., 1985, Relationships between manganese nodule abundance and bathymetry at MANOP sites H, R and S, in prep.
- Yeats, R.S. and B.U. Haq, 1978, Initial Reports of the Deep Sea Drilling Project, volume 63, site 469, p.173-226, Washington, D.C., US Government Printing Office, Washington, D.C.

ONR/MPL GENERAL DISTRIBUTION LIST

Chief of Naval Research
Department of the Navy
Arlington, Virginia 22217
Code 12, 122(2), 102C
111, 112, 113,
1122PO, 425-AC, 460

ONRDET
NSTL Station
Bay St. Louis, Mississippi 39529
Code 112, 1121, 1122CS, 422CB,
1122PO, 1125GG

Director
Office of Naval Research
Branch Office
1030 East Green Street
Pasadena, California 91101

Commander
Naval Sea Systems Command
Washington, D. C. 20362
Code 63, 63R, 63R-23

Defense Advanced Res. Proj. Agency
TTO - Tactical Technology Office
1400 Wilson Boulevard
Arlington, Virginia 22209
Atten: CDR Kirk Evans

Commander
Naval Air Systems Command
Washington, D. C. 20361
Code 370

Commander
Naval Ship Res. & Dev. Center
Bethesda, Maryland 20084

Director
Strategic Systems Proj. Ofc. (PM-1)
Department of the Navy
Washington, D. C. 20361
Code NSP-2023

Commander
Naval Surface Combat Systems Center
White Oak
Silver Spring, Maryland 20910

Commanding Officer
Civil Engineering Laboratory
Naval Construction Battalion Center
Port Hueneme, California 93043
Code L40, L42

Director of Research
U.S. Naval Research Laboratory
Washington, D. C. 20375
Code 2620, 2627, 5000, 5100, 5800

Commanding Officer
Naval Ocean Research and
Development Activity (NORDA)
NSTL Station
Bay. St. Louis, Mississippi 39529
Code 100, 110, 300, 330,
340, 350, 360, 500

Commander
U.S. Naval Oceanographic Office
NSTL Station
Bay St. Louis, Mississippi 39522
Bill Jobst

Commander
Submarine Development Group ONE
Fleet Post Office
San Diego, California 92152

Commander
Naval Space and Warfare
Systems Command
Washington, D.C. 20360
Code PME-124, 320A

Commanding Officer
U.S. Naval Air Development Center
Attention: Jim Howard
Warminster, Pennsylvania 18974

Executive Secretary, Naval Studies
Board
National Academy of Sciences
2101 Constitution Avenue, N.W.
Washington, D.C. 20418

Commander
Naval Ocean Systems Center
San Diego, California 92152
Code 00, 01, 16, 94, 531
5301, 71, 72

Commanding Officer
Naval Underwater Systems Center
Newport, Rhode Island 02844
John D'Albora

Officer in Charge
Naval Underwater Systems Center
New London Laboratory
New London, Connecticut 06320
Code 900, 905, 910, 930, 960

Assistant Secretary of the Navy
(Research Engineering & Systems)
Department of the Navy
Washington, D. C. 20350

Commanding Officer
Naval Coastal Systems Laboratory
Panama City, Florida 32401

Director
Defense Documentation Center
(TIMA), Cameron Station
5010 Duke Street
Alexandria, Virginia 22314

Institute for Defense Analyses
400 Army-Navy Drive
Arlington, Virginia 22202

Chief Scientist
Navy Underwater Sound Reference Div.
U.S. Naval Research Laboratory
P.O. Box 8337
Orlando, Florida 32806

Supreme Allied Commander
U.S. Atlantic Fleet
ASW Research Center, APO
New York, New York 09019
Via: ONR 100 M, CNO OP092D1,
Secretariat of Military,
Information Control, Committee

Director
College of Engineering
Department of Ocean Engineering
Florida Atlantic University
Boca Raton, Florida 33431

Director
Applied Research Laboratory
Pennsylvania State University
P.O. Box 30
State College, Pennsylvania 16802

Director
Lamont-Doherty Geological Observatory
Torrey Cliff
Palisades, New York 10964

Director
The Univ. of Texas at Austin
Applied Research Laboratory
P.O. Box 8029
Austin, Texas 78712

Director
Woods Hole Oceanographic Institution
Woods Hole, Massachusetts 02543

National Science Foundation
Washington, D. C. 20550

STOIA
Battelle Columbus Laboratories
505 King Avenue
Columbus, Ohio 43201

National Oceanic & Atmospheric
Administration
Ocean Engineering Office
6001 Executive Boulevard
Rockville, Maryland 20852

Superintendent
U.S. Naval Postgraduate School
Monterey, California 93940

Director
Institute of Marine Science
University of Alaska
Fairbanks, Alaska 99701

Director
Applied Physics Laboratory
Johns Hopkins University
Johns Hopkins Road
Laurel, Maryland 20810
Atten: J. R. Austin

Director
Marine Research Laboratories
c/o Marine Studies Center
University of Wisconsin
Madison, Wisconsin 53706

Director
Applied Physics Laboratory
University of Washington
1013 East 40th Street
Seattle, Washington 98105

Director
Inst. of Ocean Science Engineering
Catholic University of America
Washington, D.C. 20017

Office of Naval Research
Resident Representative
c/o Univ. of California, San Diego
La Jolla, California 92093

University of California, San Diego
Marine Physical Laboratory
La Jolla, California 92093

December 1985

U223761